Development and Characterization of a Self-Stressing Shape Memory Alloy (SMA)-Fiber Reinforced Polymers (FRP) Composite Patch for Repair of Cracked Steel Structures

A Dissertation

Presented to

The Faculty of the Department of Civil and Environmental Engineering

University of Houston

In Partial Fulfillment

Of the Requirements for the Degree

Doctor of Philosophy

in Civil Engineering

By

Mossab W. El-Tahan

Doctoral Dissertation

May 2015

Development and Characterization of a Self-Stressing Shape Memory Alloy (SMA)-Fiber Reinforced Polymers (FRP) Composite Patch for Repair of Cracked Steel Structures

Mossab W. El-Tahan

Approved:

Chair of the Committee
Mina Dawood, Assistant Professor,
Civil and Environmental Engineering

Committee Members:

Qianmei Feng, Associate Professor,
Industrial Engineering

Bora Gencturk, Assistant Professor,
Civil and Environmental Engineering

Gangbing Song, Professor
Mechanical Engineering

Kaspar Willam, Professor,
Civil and Environmental Engineering

Suresh Khator, Associate Dean,
Cullen College of Enginerring

Roberto Ballarini, Professor and Chair,
Civil and Environmental Engineering

Acknowledgements

I would like to express my deepest gratitude to my advisor Dr. Mina Dawood. Without his guidance, support, and constructive comments this dissertation would not have been possible. Dr. Dawood has not only influenced my research skills, but also gave me endless advices to enhance my personal skills. During my PhD journey he was always supportive in all means. I am very fortunate to have Dr. Dawood as my advisor.

I would like to thank Dr. Qianmei Feng, Dr. Bora Gencturk, Dr. Gangbing Song and Dr. Kaspar Willam for accepting to be in my dissertation committee. I would like to extend my thanks to Dr. Gangbing Song for supporting the experimental efforts of this research. The support by Dr. Cumaraswamy Vipulanandan is also appreciated.

The financial support from the National Science Foundation (Award number 1100954) and the Civil and Environmental Engineering department is acknowledged. The generous material donation by Fyfe and Huntsman Advanced Materials is appreciated.

The help from the department staff is highly acknowledged. Special thanks to Betsy Roguer, Cherish Wallace, Gerald McTigret, Jeffery Miller, Jose Rodriguez, Maria Trasancos, Stephanie Davis and Stephanie Woods.

The technical support from the engineering computing center (ECC) and the high performance computing center (HPCC) is acknowledged. Special thanks to Diem Tran, Eric Stern, Jeffrey Sarlo, and Kiet Luong.

Mehmet Sahin cannot be thanked enough for his assistance in the lab. I wish to express my acknowledgements to my dear colleagues Ahmed Elhasani, Aram Raheem, Hazem Amer, Jeannot Ahossein, Leo Peirick, Oswaldo Russian and Shahriyar Beizaee. Their help and support is highly appreciated. Special thanks to my colleagues Botong Zheng, Hossein Karagah and Reza Mousavi for the constructive discussion and sharing their knowledge.

I also want to thank my amazing helpers Andres Aranzales, Evan White, Felix Vergara, Juan Macias, Sebastian Hernandez, William Sagastizado and Xavier Everette for their tremendous help during my research.

I would like to extend my sincere gratitude to my friends Ahmed Elhasani, Emane Elhasani and Usama Salem for bringing their joy and laughter.

My words cannot express my gratitude to my dear parents, Dr. Wahba El-Tahan and Karima Eldissouky, for their continuous support and prayers. Special thanks go to my sister Mariam El-Tahan for her short visit.

At last but never the least, I would like to thank my beloved wife, Khadiga Elkafrawy, for her patience, support, unyielding love and prayers. You are always my biggest supporter and encourager. I thank God for having you and my son Hamza in my life.

Development and Characterization of a Self-Stressing Shape Memory Alloy (SMA)-Fiber Reinforced Polymers (FRP) Composite Patch for Repair of Cracked Steel Structures

An Abstract

Of a

Dissertation

Presented to

the Faculty of the Department of Civil and Environmental Engineering

University of Houston

In Partial Fulfillment

Of the Requirements for the Degree

Doctor of Philosophy

in Civil Engineering

By

Mossab W. El-Tahan

May 2015

Abstract

Prestressed carbon fiber reinforced polymer (CFRP) patches are emerging as a promising alternative to traditional methods to repair cracked steel structures and civil infrastructure. However, existing prestressing methods require the use of heavy and complex fixtures to apply prestressing forces, which is impractical in many applications. In this research a self-stressing shape memory alloy (SMA)-fiber reinforced polymer patch is presented that can be used to prestress civil infrastructure, with a target application of repairing cracked steel structures. The self-stressing patch consists of nickel titanium niobium (NiTiNb) SMA wires embedded in a fiber reinforced polymer (FRP). The self-stressing patch can be bonded to the steel member in the vicinity of a crack. The prestressing force is generated by restraining the shape memory effect of the embedded NiTiNb SMA. The self-stressing patch is thermally activated and therefore does not require heavy equipment, but rather only a heat source or electrical power supply during the activation of the wires.

This dissertation presents the development of the self-stressing patch and the characterization of the static and fatigue behavior of the patch. Different SMA and epoxy materials were tested to identify their thermomechanical properties and to select suitable materials for the patch. The bond behavior between two different types of SMA wires, superelastic Nitinol and NiTiNb, and FRP was evaluated experimentally. Based on the experimental observations an empirical model is proposed to quantify the minimum required embedment lengths between superelastic Nitinol and CFRP. The debonding mechanism between the NiTiNb and FRP was examined numerically using the finite element method (FEM). A trilinear cohesive zone model (CZM) was established, which incorporates cohesive and frictional components, to predict the pull-out behavior of NiTiNb wires embedded in FRP. The monotonic and fatigue behavior of the self-stressing patch were also characterized experimentally. This dissertation presents an empirical model that can be used to predict the fatigue degradation of the prestressing force in the patch. The research findings indicate that the self-stressing patch is able to generate a sustained recovery stress of 390 MPa. Patches for which the maximum applied loads in a fatigue cycle did not cause debonding of the SMA wires from the FRP exhibited fatigue lives up to 2 million cycles with less than 20% degradation of the prestressing force. The results suggest that the patch is a promising alternative to traditional methods of repairing structures with prestressed FRP patches.

Table of Contents

List of Figures

List of Tables

Chapter 1: Introduction

Fatigue cracks in steel structures typically initiate at stress concentrations in fatigue-sensitive details. Although the magnitude of the far-field stresses due to applied cyclic loads is low, the localized stresses may be much higher. Under cyclic loading cracks initiate, propagate, and may ultimately lead to member rupture and complete failure of the structure. Some examples of the fatigue related failures are the catastrophic failure of the Alexander L. Kielland platform which killed 123 persons (Almar-Naess et al., 1984), the failure of the high mast poles in Colorado (Goode and Van de Lindt, 2008), Wisconsin (Foley et al., 2004), and Iowa (Chang et al., 2009).

Repairing cracked steel members with fiber reinforced polymers (FRP) patches or overlays, is emerging as an effective means to repair cracked steel structures. Using this technique an FRP patch is bonded across the crack using a structural adhesive. This bridges the crack and reduces the stress intensity factor at the crack tip due to the change in the load path. The effectiveness of this repair method can be improved by prestressing the patches. This induces compressive stresses at the crack tip. These compressive stresses at the vicinity of the crack tip reduce the stress ratio, which can increase the fatigue life of the repaired members, and may even halt the crack completely (Bassetti et al., 2000; Taljsten et al., 2009). However, the current prestressing techniques require heavy equipment to apply the prestressing force and complex fixtures to anchor the FRP materials to the structure. Moreover, many systems require drilling holes into the substrate structure which requires permanent modification of the structure and may act as a site for re-initiation of cracking.

1.1. Research objectives and outline

The objectives of this research are to: (a) develop a self-stressing SMA/FRP composite patch that can be used to repair cracked steel members or other civil infrastructure, (b) establish a technique to model the bond of SMA wires that are embedded in FRP, (c) quantify the magnitude of the prestressing force that can be achieved by the proposed patch, and (d) quantify the degradation of the prestressing force in the self-stressing patch due to fatigue loading.

In the proposed system the prestressing force is generated by restraining the shape memory effect of NiTiNb wires. An FRP overlay can subsequently be applied to bridge the crack. This study presents the development of the self-stressing patch with an emphasis on repair of cracked steel members. This research presents the efforts spent to develop the self-stressing patch. The complexity of developing the patch comes from the different thermomechanical properties of the constituents.

The prestressing force generated by the SMA wires is transferred to the composite through the bond interface. Effective bond between the SMA wires and the FRP composite is essential to ensure the stability of the prestressing force. The bond between SMA wires and FRP is studied with a focus on identifying the debonding mechanisms to prevent a premature pull-out failure of the SMA wires from the FRP composite.

The performance of the self-stressing patches during activation and under monotonic tensile loading is evaluated to quantify the magnitude of the prestressing force that can be achieved using the proposed patches and to identify suitable methods to activate the patch. The fatigue behavior of the patch is studied to examine the stability of the prestressing force under cyclic loading during the life of the patch which is an important consideration in the design of the patch.

1.2. Scope and organization of the dissertation

This dissertation is organized into seven chapters, including this introductory chapter, and three appendices.

Chapter 2 presents a review of the relevant literature related to repair of cracked steel structures, structural applications of shape memory alloys, and bond between SMA and FRP.

The remainder of the research effort was conducted in two phases. The first phase is described in three chapters, which present the experimental and analytical development of the self-stressing patch.

Chapter 3 summarizes the conceptual development of the self-stressing patch and the details of material tests that were conducted to study the behavior of the patch constituents. The chapter summarizes the test results of three types of SMA wires and four different types of epoxy adhesives. Appendix A presents the comprehensive details of the experimental results for completeness.

The bond between two types of SMA wires, namely superelastic nickel titanium (NiTi) and shape memory nickel titanium niobium (NiTiNb), and carbon FRP composites is discussed in Chapter 4. Pull-out tests were conducted to evaluate the bond strength. An empirical model is presented to predict the development length for the tested configuration of NiTi wires embedded in FRP. Appendices B and C present the comprehensive set of experimental results for the pull-out tests of NiTi wires and NiTiNb wires, respectively, embedded in FRP.

Chapter 5 presents the details of the finite element analysis that was conducted to evaluate the bond behavior between NiTiNb SMA and FRP.

Chapter 6 summarizes the findings of the second phase of the research. The chapter describes the behavior of the SMA/FRP patches under monotonic loading and fatigue loading. The degradation of the prestress force of the SMA wires is quantified and an empirical model is presented to predict the degradation of the prestressing force due to fatigue loading.

The conclusions of the work conducted in this dissertation are presented in Chapter 7 followed by recommendations for future work.

Chapter 2: Background

This chapter presents a review of the relevant literature related to repair of cracked steel structures, SMAs and their applications in structural engineering and bond between SMA and FRP. The chapter concludes by outlining the research needs and presents the significance of this dissertation.

2.1. Repair of cracked steel elements

Fatigue cracks usually form in steel structures due to cyclic loads such as wind, traffic, or machinery vibration. Some examples of structures that are susceptible to fatigue loads are bridges, cranes, offshore structures, and structures supporting machinery. Although the magnitude of the applied cyclic loads is lower than the ultimate capacity, under repeated loading cracks can form at stress concentration locations and propagate if the stress intensity factor exceeds the threshold stress intensity factor, ΔK_{th}, leading to member rupture. Several methods are commonly used to repair cracked metallic structures. One of the repair methods is to attach cover plates over both sides of the crack by pretensioned high strength bolts (Fisher et al., 1998). By doing so the load path is changed and the propagation of the crack is halted. Another alternative is to drill a crack-stop hole at the tip of the crack and fill it with a steel pin (Domazet, 1996). This method provides localized compression stress at the crack tip and reduces the stress concentration by changing the crack tip geometry. A third alternative is to apply residual compressive stresses by peening (Sharp et al., 1994). Repair welding is an alternative, however, cracks can re-initiate at the weld location (Domazet, Z., 1996). These conventional methods require complex heavy equipment and experienced labor in confined areas which typically have limited accessibility. Additionally in some situations, welded repairs are infeasible due to the risk of explosions. Thus alternative repair methods are required which can be easily implemented in areas with limited accessibility.

Patching cracked steel members with fiber reinforced polymers (FRP) materials, is emerging as an effective means to repair cracked steel structures (Tavakolizadeh and Saadatmanesh, 2003; Jones and Civjan, 2003; Lam et al., 2007; Nakamura et al., 2009; Fam et al., 2009; Jiao et al., 2012; Wu et al., 2012; Wu et al., 2013; Wang et al., 2014; Colombi et al., 2015). Using this technique an FRP patch is bonded across the crack with a structural adhesive. This bridges the crack and reduces the stress intensity factor at the vicinity of the crack tip.

The effectiveness of this repair method can be improved by prestressing the patches which induces compression stresses at the crack tip resulting in a further increase in the fatigue life (Bassetti et al., 2000; Taljsten et al., 2009; Huawen et al., 2010; Ghafoori et al., 2012a,b; Ghafoori and Motavalli, 2013; Koller et al., 2014; Emdad and Al-Mahaidi, 2015; Ghafoori et al., 2015).

Bassetti et al. (2000) studied the application of prestressing CFRP perpendicular to the fatigue crack path to repair riveted bridge members. Steel plate specimens with a center crack with two notches were tested under fatigue loading with a stress range of 80 MPa and a stress ratio of 0.4. It was found that the prestressed CFRP plates were able to reduce the crack opening displacement at the crack front, and increase the fatigue life by 20 times compared to the unrepaired plates. Full scale testing was also performed on riveted cross girder with prestressed CFRP plates. The results of the full scale test indicated that prestressing method was able to completely halt the crack even after 20 million cycles of fatigue loading.

Taljsten et al. (2009) tested 10 steel plates with a center hole repaired with prestressed and non-prestressed CFRP composite. The length width and thickness of each plate was 670 mm, 205 mm and 8 mm, respectively. The plates were repaired with four CFRP plates, two on each side of the hole on both faces of the steel plate. The study was conducted to evaluate the effectiveness of using prestressed CFRP plates system to repair steel plates with a center notch. The applied stress range was 97.5 MPa and the stress ratio was 0.086. The results indicated that the fatigue lives of the specimens repaired with non-prestressed CFRP plates were 2.45 to 3.74 times the fatigue lives of specimens with no repair. However, specimens with prestressed CFRP plates did not fail even after 6 million cycles.

An experimental and analytical study was carried out by Huawen et al. (2010) to study the fatigue behavior of steel plates repaired with prestressed CFRP plates. A fracture mechanics based model was presented that can predict the fatigue life of the specimen. The results indicated that using prestressed CFRP specimens can increase the fatigue life by four times compared to the unrepaired specimens. The proposed analytical model was in good agreement with the experimental results.

Ghafoori et al. (2012a,b) investigated the effectiveness of a new unbonded prestressing repair system. The fatigue behavior of notched steel beams strengthened with bonded and unbonded prestressed CFRP plates were compared. A fracture mechanics based model was presented to calculate the minimum prestressing force required to arrest the crack growth in retrofitted beams. In order to arrest the crack, the level of prestressing can be found by solving the following equation:

$$K_1^{overall} = K_1^{CFRP} + K_1^{M} \leq 0\,, \tag{2.1}$$

where, K_1^{CFRP} and K_1^{M}, are the stress intensity factors at the vicinity of the crack due to the prestressing force, and the applied moment, respectively. K_1^{CFRP}, is a negative value, indicating that the prestressing force tends to close the crack, while K_1^{M} is a positive value indicating that the external applied moment tends to open the crack. A finite element analysis was conducted to verify the proposed model. The results indicated that beams with bonded repair system exhibited a strain concentration at the crack location while the unbonded repair system exhibited a uniform strain distribution along the length of the CFRP plate. It was noticed in the case of the unbonded repair system that the CFRP plate slipped at the mechanical anchor system prior to failure. The results of the proposed model and the finite element analyses were in good agreement. The results indicated that designing the beam with the proposed model resulted in a complete arrest of the fatigue crack even after 400,000 fatigue cycles. No change in the stiffness and strain distribution along the CFRP plate were observed.

In the studies by Ghafoori et al. (2015a,b) the authors repaired a 120 year old metallic bridge using the unbonded prestressed system described in Ghafoori et al. (2012a). This method overcomes the surface preparation problems required for bonded methods, and is suitable for the uneven surfaces like riveted surface. In this study the authors presented the concept of constant fatigue life diagram which was used to determine the minimum prestress level required to repair the metallic bridge. The model, shown in Figure 2.1, is based on the models by Goodman (1899) and Johnson (1899). The Goodman model is more accurate but requires the knowledge of the endurance stress limit, S_e, (which is usually difficult to determine for an existing structure) and the ultimate strength, S_{ut}, of the repaired metal. While Johnson's model requires less knowledge about the repaired metal (the ultimate strength, S_{ut}, only). In this research the authors discussed that introducing a prestressed system does not influence the stress amplitude (σ_a) as the increase in stiffness of the repaired structure is usually small. However, the application of the prestressing force reduces the stress ratio and the mean stress (σ_m) as shown in the figure. According to the proposed model shown in Figure 2.1, the fatigue life of a metallic member can be shifted from the finite life (point A, which lies outside of the curve) to the infinite life (point B, which lies inside the curve).

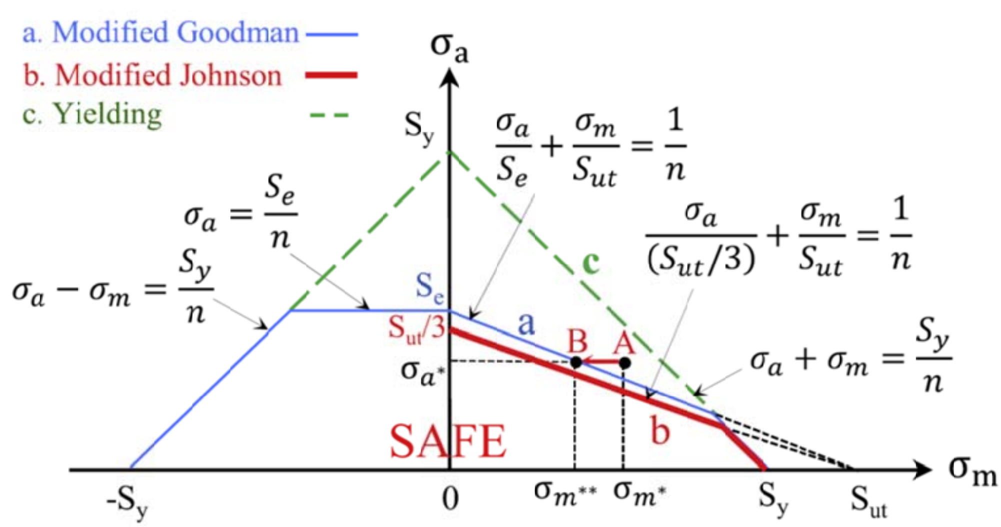

Figure 2.1. Constant fatigue life diagram (Ghafoori et al., 2015a,b)

2.2. Shape memory alloys

Shape memory alloys (SMA) exhibit a unique behavior in which the crystals of the material reorient and transform between two different phases, martensite and austenite, when subjected to certain conditions. Figure 2.2 shows the stress-strain curves of SMA at the martensitic and austenitic phases. It can be seen in the figure that the SMA is fully in the martensitic phase while the material is below its martensitic finish temperature (M_f). Below this temperature the atoms arrange in a twinned orientation as shown in the figure. This structure is called twinned martensite. Upon loading of the SMA while the temperature is less than M_f, the atoms in the twinned martensite will reorient and form a detwinned martensite formation. This causes the material to experience a permanent residual deformation. As illustrated in Figure 2.2, when the material is heated above the austenitic start temperature (A_s) the crystals start to reorient into the austenitic phase as shown in the figure. When the temperature of the material reaches the austenitic finish temperature (A_f) the material is fully in the austenitic phase, and the built-in residual strain is relieved. Upon cooling, the material undergoes another transformation, from the austenitic phase to the twinned martensitic phase with no built in strain. This phenomenon is referred to as the shape memory effect. When SMA is loaded and unloaded at temperature below M_f the material exhibits a residual strain. If the SMA is restrained before heating it to a temperature over A_f, the material will reorient and transform into the austenitic phase. But, since the material is restrained the transformation will generate a recovery force.

Another phenomenon occurs when the SMA is deformed at temperatures above A_f. It can be seen in the Figure 2.2 that if the material is loaded over a critical stress limit, it experiences a stress induced martensitic transformation. Upon unloading the SMA material, the martensite becomes unstable and the material returns to the austenite phase and its original shape. It can be seen in the figure that the SMA material exhibits a hysteretic behavior during the transformation from the austenite to martensite in the loading part and the transformation from martensite to austenite in the unloading part. This phenomenon is referred as the superelasticity effect or pseudoelasticity.

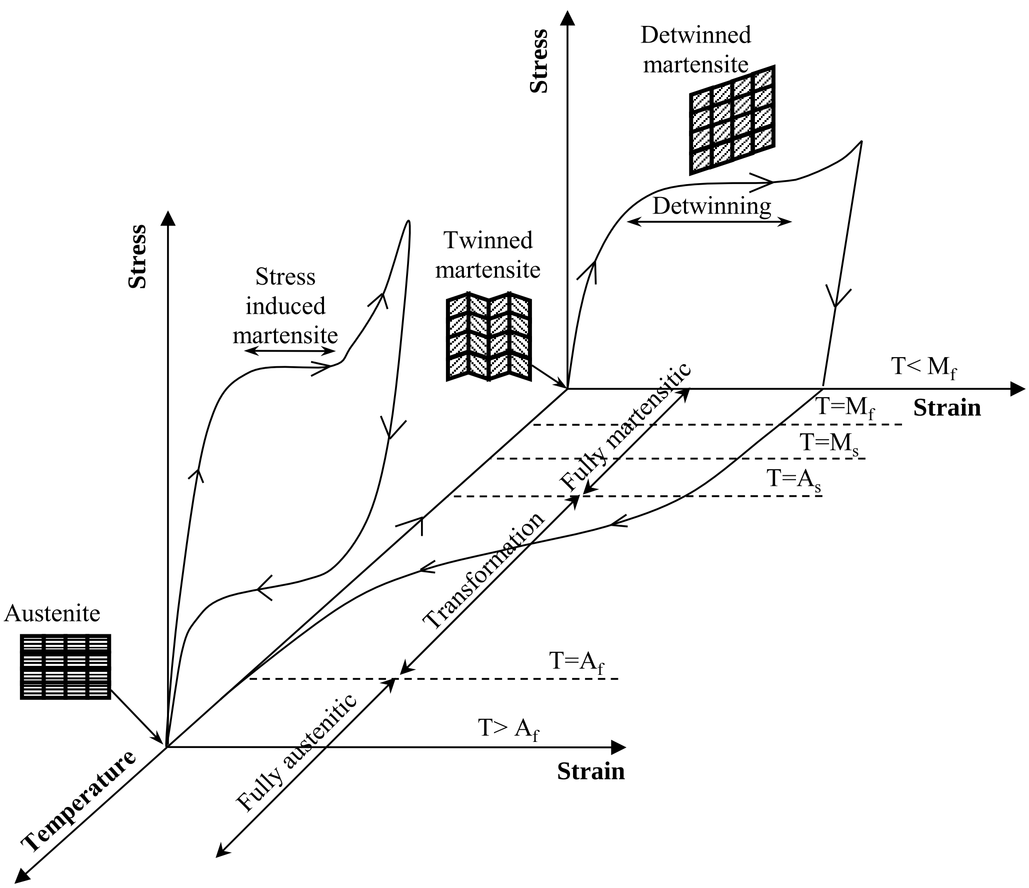

Figure 2.2. Stress-strain relationship for SMA in martensite and austenite phases (Adapted from Alam et al., 2007)

Another property to define the SMA behavior is called the thermal hysteresis width. The hysteresis width is defined by Melton et al. (1989) as

$$A_{50} - M_{50}, \tag{2.2}$$

where A_{50} and M_{50} are the temperatures at which 50% of the strain change has occurred during the heating and cooling, respectively.

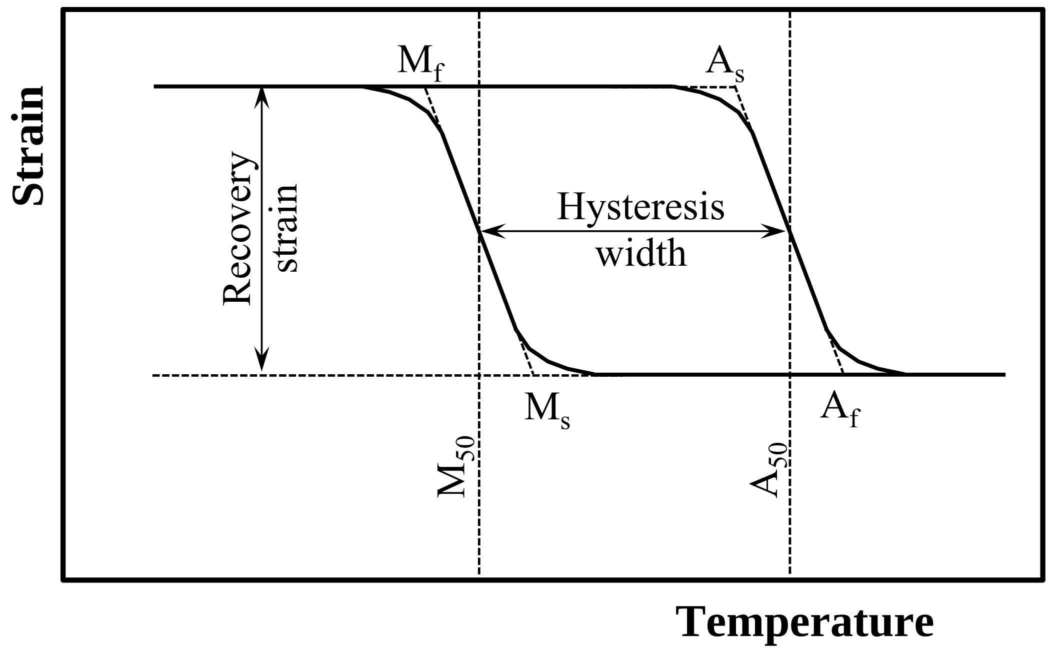

Figure 2.3. The definition of the SMA thermal hysteresis width (Adapted from Melton et al., 1989)

The complex behavior of the Nitinol has been utilized in different applications. By restraining the shape memory effect of the SMA, a recovery force is generated which allows the SMA to be used as solid state actuators. The SMA actuators can achieve high-force-to-size ratio compared to other types of actuators. Researchers have exploited SMAs to create devices that could not have been possible with regular actuators. Some examples are: variable area exhaust nozzle (Song et al., 2007); ultra-deep water subsea blowout prevention system (Song et al. 2008), robotic fish (Rossi et al., 2011), mimicking a jet propeller inspired by the cuttlefish (Gao et al., 2014).

Nitinol SMA has been embedded in composites to actively tune the properties of FRP composites (Epps and Chandra, 1997; Baz et al., 2000; Sittner and Stalmans, 2000; Song et al., 2000b; Loughlan et al., 2002; Yuse and Kikushima, 2005; Sippola and Lindroos, 2007). SMAs have also been embedded in FRP composites to increase their energy dissipation capacity (Lagoudas et al., 2001; Turner 2005; Liu et al., 2007, Raghavan et al., 2010; Wierschem and Andrawes, 2010; Heller et al., 2012). While binary NiTi alloys are well established, they have relatively narrow thermal hysteresis in the range of 30^{o}C to 50^{o}C (Melton and Mercier, 1980). This limits their suitability for applications which require sustained recovery forces at or near room temperature. Iron based SMAs have been developed and used for prestressing applications (Czaderski et al., 2005; Moser et al., 2005; Janke et al., 2005; Dong et al. 2009; Cladera et al.,2014; Czaderski et al, 2014). The iron based SMAs exhibit a wide thermal hysteresis with high activation temperature, have higher elastic modulus compared to others NiTi alloys. However, the corrosion behavior of the iron based SMAs is still questionable (Maji et al., 2006; Rovere et al., 2012).

Other alloys like the ternary NiTiNb SMA have been developed (Zhao et al., 1989; Melton et al., 1989; Ying et al. 2011). The ternary alloy exhibits a wide hysteresis which allows the alloy to remain austenitic at temperatures below room temperature. The martensitic start temperature of the alloy is in the range of -50^{o}C. This means that by utilizing the shape memory effect a recovery (presstressing) force can be maintained at room temperature, which is suitable for the civil applications where continuous heat of the wires is not economically feasible (as in the case of binary NiTi alloys). The increase in the thermal hysteresis is achieved by the addition of the soft deformable particles of the niobium which increased the thermal hysteresis width and the activation temperatures. The NiTiNb SMA is well suited for applications that require sustained recovery forces at or near room temperature as in the case for hydraulic couplers (Melton et al., 1986) and in the structural engineering applications.

2.3. Applications of NiTiNb SMAs in structural engineering

Andrawes and Shin (2008) studied analytically the effectiveness of using SMA for active confinement of concrete columns. The study compared between the effectiveness of using active confinement and conventional passive confinement to improve the ductility of reinforced a concrete column subjected to an earthquake. The results of this study indicated that the column with active confinement exhibited a reduction in the maximum strain as well as in the drift compared to the column retrofitted by passive confinement when subjected to the same ground motion. The same authors then expanded their research and studied the experimentally effectiveness of using NiTiNb SMA spirals for active confinement of concrete (Shin and Andrawes, 2010). The study started by investigating the thermo-mechanical behavior of the NiTiNb wires to examine the maximum recovery stress that can be obtained from a single wire. Specimens wrapped with SMA spirals only, with GFRP only and SMA/GFRP were tested in this research to investigate the effectiveness of using NiTiNb wires for active confinement of concrete cylinders. It was shown that the individual wires provided a stable recovery stress that can reach 460 MPa. Research results indicated that the strength and ultimate strain of the concrete cylinders confined with SMA spirals increased by 21% and 24 times compared to the unrepaired specimens. It was found that specimen with SMA jacket with a pitch of 13 mm and four layers of GFRP jacket exhibited an increase in the concrete strength and ultimate strain by 1.2 and 10 times, respectively, compared to specimens with 8 layers of GFRP.

Shin and Andrawes have gone further applying their NiTiNb/FRP system to a whole column (2011). In this study the authors evaluated the lateral cyclic behavior of reinforced concrete columns retrofitted with NiTiNb/FRP system. Four 1/3 scale columns were tested, the first one served as a control specimen. The second, third and fourth specimens were retrofitted with NiTiNb SMA spirals, GFRP jacket, and SMA/GFRP jacket, respectively. The three retrofitting schemes were designed to have the same confining pressure. It was found that the SMA and SMA/GFRP schemes increased the concrete strength slightly by 1.06 and 1.03, respectively, compared to the unrepaired column. However the flexural ductility and dissipated energy of the column repaired with SMA jacket was 2.85 and 4.71, respectively, compared to the unrepaired column. Whereas, the flexural ductility and dissipated energy of the column repaired with SMA/GFRP was 2.39 and 3.85, respectively, compared to the unrepaired column. It was found that the column repaired with GFRP jacketing only exhibited moderate enhancement in the ductility by 1.18 compared to the unrepaired one. It was noticed that the columns repaired with SMA spirals exhibited less damage than the column repaired with GFRP jacket only, despite the fact that the former exhibited 75% increase in the maximum drift compared to the later.

Choi et al. (2010) compared between the performance of NiTi and NiTiNb SMA wires for active confining of concrete elements. Five concrete cylinders were tested under compression, while three reinforced concrete columns were tested under flexural loading. It was found that the concrete cylinders with either NiTiNb or NiTi SMA jackets were able to increase the peak strength and the ductility of concrete cylinders compared to those without a jacket. However, the NiTiNb SMA jacket was more effective in increasing the peak strength of the concrete cylinder compared to the one with NiTi jacket. A significant improvement in the strength and ductility were observed in both systems. However, the column with NiTiNb jacket exhibited a higher maximum strength.

Choi et al. (2011) evaluated the effect of active confinement using NiTiNb wires on the bond behavior between steel rebars and concrete. A total of 10 push-out specimens were tested in the study by pushing an embedded steel rebar out of the concrete. Five unconfined cylinders served as control specimens, two of them were tested under monotonic loading while three were tested under cyclic loading. Five cylinders were confined with NiTiNb SMA wires, two of them were tested under monotonic loading while three specimens were tested under cyclic loading. Based on the results of this study it was found that the active confinement was able to change the failure mode from splitting failure to push-out failure. The bond strength and slip increased by 42% and 500%, respectively, for samples with active confinement compared to the unconfined specimens when subjected to monotonic loading. The load-slip envelopes of the confined specimens tested under cyclic loading matched the load-slip responses of the confined specimens tested under monotonic loading.

Dommer and Andrawes (2012) investigated the long term behavior and the effect of the ambient temperature on the effectiveness of the NiTiNb SMA/FRP system. Tests on the SMA wire were conducted to evaluate the residual recovery stress variation under temperatures ranging from -10^{o}C to 50^{o}C. The results of the wire testing indicated that the wires were able to develop about 50% of the recovery stress at freezing temperature in the range of -10^{o}C. The test results showed that there was no indication of relaxation in the NiTiNb wires for 36 hours even when the ambient temperature increased up to 50^{o}C. The wires tested under cyclic loading showed an increasing unrecoverable strain after unloading with increasing maximum strain values. The authors expected that this reduction in the recovery stress will be minimal due to the plastic deformations of the concrete in the transverse direction. The authors concluded that the NiTiNb SMA can produce stable recovery force within the normal service temperature of the structures which is desirable in civil applications.

Chen et al. (2014) investigated the active confinement of non-circular columns. The confinement was applied using NiTiNb SMA wires. A total of 13 concrete columns with a square cross section were tested in this study, four of them were unconfined to serve as control specimens. Five of the tested specimens were passively confined with GFRP while four were actively confined with NiTiNb SMA wires. One column out of each group was tested under cyclic loading, while the rest were tested under monotonic loading. The variables considered in this study were the number of GFRP layers, and spacing and confining scheme of the SMA wires. Based on the results of this study, the lateral strain of the specimen repaired with active SMA confinement was 53% of the lateral strain for the specimen repaired with GFRP only at the same stress level. This indicated that the SMA repair system was able to delay the damage and dilation of concrete compared to the unrepaired specimens, which in turn increase the ductility of the columns.

2.4. Bond behavior between SMAs and composites

FRP composites have been widely used as load carrying members due to their light weight and versatility. SMAs are embedded in FRP components to actively tune the properties of the composites (Epps and Chandra, 1997; Baz et al. 2000; Song et al., 2000a; Song et al., 2000b; Icardi, 2001; Loughlan et al., 2002). Similarly, SMAs are embedded in FRP components to increase the energy dissipation capacity of the composites (Turner 2005; Liu et al., 2007, Wierschem and Andrawes, 2010; Raghavan et al., 2010). In both cases the effectiveness of the SMA/FRP composite relies on establishing an effective bond between the two materials. Several researchers have studied the effect of surface treatment methods on the bond behavior of SMA. Jonnalagadda et al. (1997) investigated the effect of the surface treatment of SMA wires embedded in an epoxy matrix on the bond strength using pull-out tests. Different surface treatments were investigated: untreated, acid-etched, hand sanded, and sandblasted. Sandblasting provided the highest bond strength, while acid etching and hand sanding were less effective methods of enhancing the bond properties. Jang and Kishi (2005) examined different methods of acid etching to increase the bond strength between NiTi SMA wires and CFRP. They found that the bond strength increased 3% to 18% compared to the untreated wires. Acid etching with a 3% hydrofluoric acid and 15% nitric acid solution produced the highest bond strength of the treatment methods studied. The increase in the interfacial bond strength was attributed to the surface roughness caused by the acid etching. Sadrnezhaad et al. (2009) evaluated the bond behavior between NiTi SMA and a silicone-based matrix for medical applications. SMA wires with different surface treatments were investigated under scanning electron microscopy and pull-out tests were conducted to determine the morphological and bonding interactions with the silicone matrix. Acid etching and oxidization increased the frictional forces at the interface which led to an increase in the bond strength.

Using scanning electron microscopy Lau et al. (2002) examined the debonding failure mechanism of prestrained martensitic SMA wires embedded in an epoxy matrix. Debonding occurred at the SMA-epoxy interface for wires that were prestrained up to 8% when the wires were heated beyond the austenitic finish temperature, A_f. Heating caused the surrounding epoxy to expand while the SMA wires contracted due to the shape memory effect. This induced large shear stresses which led to debonding of the highly prestrained wires. As such, it was recommended to prestrain the SMA wires to less than 8% to reduce the interfacial shear stresses.

Poon et al. (2005a,b) studied the interfacial bond behavior of prestrained martensitic SMA wires embedded in an epoxy matrix. A model was developed to predict the debonding behavior, initial debonding stress, and critical bond length (Poon et al., 2005a). The maximum debonding stresses at different activation temperatures were predicted and compared with experimental results. The model captures the change in the embedment length with the increase of the activation temperature. Also, a phase-stress-displacement diagram was developed that can be used to determine the critical pull-out stress of prestrained martensitic SMA wires embedded in an epoxy matrix during activation (Poon et al., 2005b). Wang et al. (2011) developed a closed-form solution to analyze the stress distribution along the SMA-epoxy interface when the shape memory effect of a SMA wire embedded in cylindrical epoxy matrix is activated. A finite element analysis was also conducted to validate the closed-form model. Both the closed-form solution and the finite element analysis indicate that the maximum interfacial shear stress is located at the ends of the SMA wire while the maximum axial stress is at the midpoint of the embedded SMA wire. Both the axial stress and the interfacial shear stress increased with the increase of the actuation temperature. The maximum interfacial shear stresses were proportional to the prestrain level, while the maximum axial stress in the SMA increased nonlinearly.

Payandeh et al. (2009) examined the bond behavior of martensitic NiTi wires embedded in a cylindrical epoxy matrix by pull-out tests. Three heat treatments were applied to the NiTi wires in order to achieve three martensitic transformation characteristics. The embedded wires were loaded in a displacement control until failure complete occurred. The effect of the loading rate on the debonding behavior was also studied. A digital camera behind a polariscope was used to observe the debonding process during the test. Based on the test results it was concluded that the bonded part of the wire cannot experience transformation since transformation induces large strains. Debonding occurred if the debonding load was smaller than the transformation load. In a companion study the effect of the martensitic transformation on the debonding initiation of martensitic SMA wires embedded in an epoxy matrix was investigated (Payahdeh et al., 2010). It was found that the maximum interfacial shear stress depends on the wire's elastic modulus. The interfacial shear strength for specimens with SMA wires was less than that of specimens with steel wires. Based on the experimental observations the interfacial shear strength was about 9 MPa for specimens that exhibited no phase transformation, and 14 MPa when martensitic transformation occurred. Payandeh et al. (2012) studied the effect of the martensitic transformation on the debonding initiation in non-prestrained SMA wire-epoxy matrix composites at different temperatures. SMA wires were embedded in an epoxy coupon to achieve 6% and 12% SMA volume fractions. Epoxy coupons with SMA volume fractions of 6% were tested in tension at 20^{o}C, 80^{o}C, and 90^{o}C, while specimens with SMA volume fractions of 12% were tested at 80^{o}C and 90^{o}C. Increasing the test temperature increased the tensile strength of the composites while the tensile strength of the epoxy decreased. The martensitic transformation occurred in multiple locations in the embedded wires causing a bonded/debonded pattern.

2.4.1. Anchorage of SMA wires in FRP composites

Epps and Chandra (1997) studied experimentally and numerically the active tuning of composite beams with embedded SMA wires. The SMA wires inserted into embedded sleeves in the composite beam then clamped at both ends of the composite. This approach eliminated the problems associated with the adhesive softening during activation of the wires. It was found that one SMA wire with a diameter of 0.5 mm was able to increase the first frequency of the composite by 22%. Extending this study numerically suggested that the frequency of the composite could be increased by 276% when embedding 25 SMA wires with a diameter of 0.5mm. Yuse and Kikushima (2005) proposed the SMA-FRP system shown in Figure 2.4 which can be bonded to other elements for vibration control. The proposed system relies on the interlock between the SMA and the adhesive to transfer the recovery force. Hence, overcame the challenges associated with debonding while activating the wires. The authors demonstrated experimentally that the partial embedment of the SMA wires allowed for faster response during cooling compared to the systems with full embedment as the wires are exposed and cooled by the ambient air.

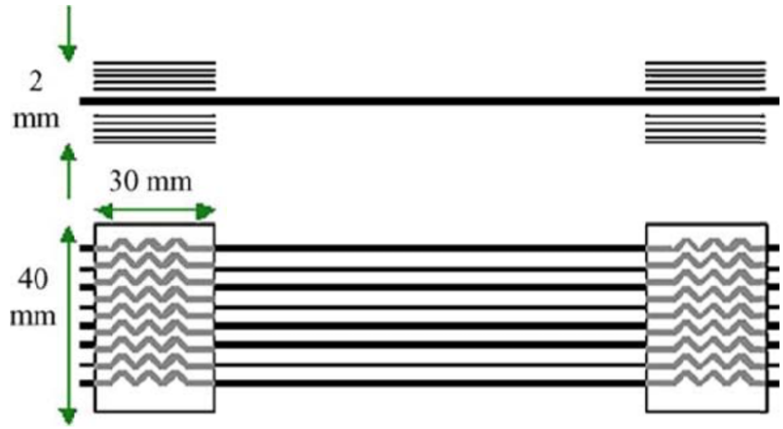

Figure 2.4. SMA-FRP system developed by Yuse and Kikushima (2005)

2.5. Research significance

The previous studies showed that the application of prestressing FRP systems can increase the fatigue life of the repaired members by up to 20 times (Bassetti et al., 2000), and may even halt the crack completely (Taljsten et al., 2009). However, FRP prestressing systems commonly require heavy fixtures to clamp the ends of the FRP plate and heavy equipment to apply the prestress force to the FRP material. Figure 2.5 shows some of the examples of the prestressing fixtures and rigs that have been reported in the technical literature. Moreover, the application of the prestressing system often requires permanent modification of the repaired structure, such as by drilling holes. This highlights the need for an alternative method that is easy to apply and requires minimal use of equipment. The research conducted to date further indicates that the bond behavior of SMA wires that are embedded in FRP composites is dominated by multiple complex mechanisms that require careful consideration in the early design stages to help ensure satisfactory performance. This dissertation describes the development, bond behavior, monotonic response, and fatigue degradation of a SMA/FRP self-stressing patch. The target application of this new patch is for repair of cracked metallic structures, with a focus on civil infrastructure applications, but with further development could potentially be used on non-metallic structures or in non-civil applications.

(a)

(b)

(c)

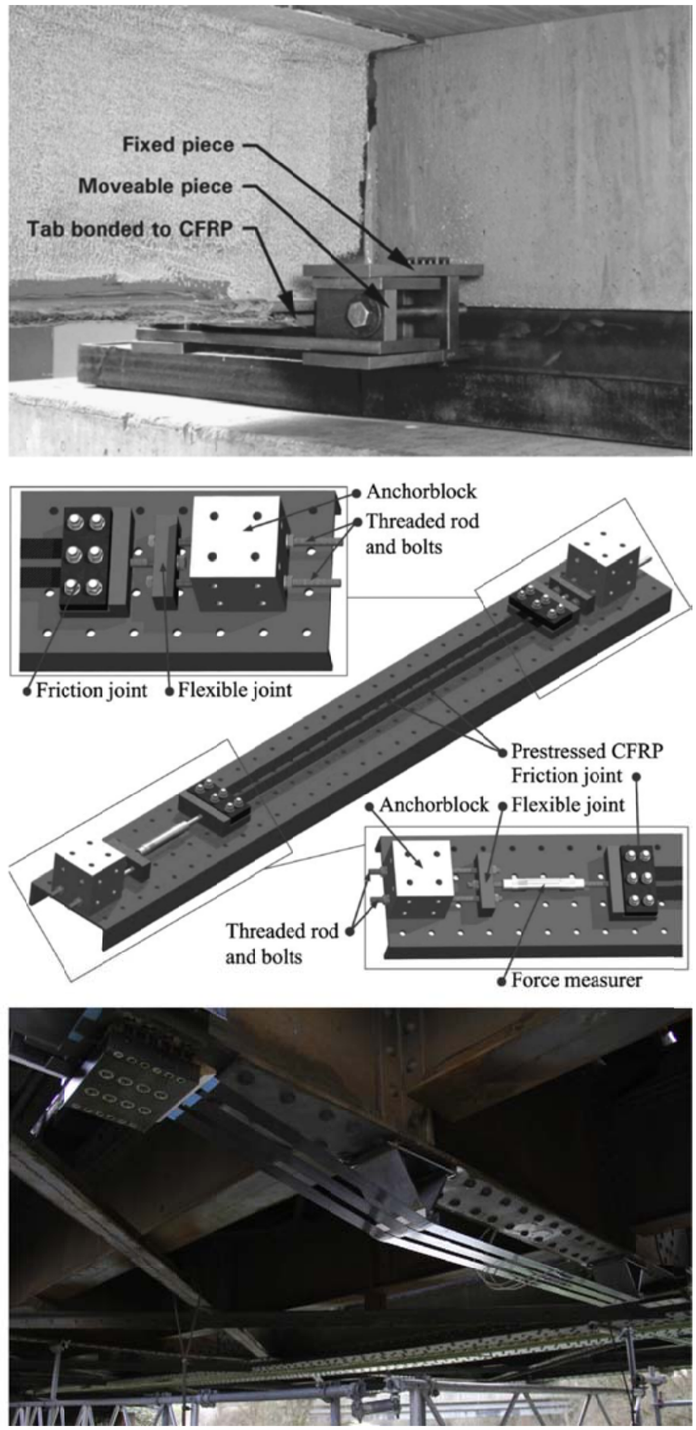

Figure 2.5. Prestressing rigs and fixtures: (a) Schnerch and Rizkalla, 2008; (b) Taljsten et al., 2009; and (c) Ghafoori et al., 2015

Phase I: Patch Development

Chapter 3: Conceptual Development and Materials Selection

In this chapter the conceptual development of the self-stressing patch is discussed. Three different SMA wires were tested as well as two structural adhesives to determine their thermomechanical properties. Based on the results the most suitable materials were selected. Based on the work conducted in this chapter a discussion is presented at the end of the chapter to summarize configurations of the proposed self-stressing patch.

3.1. Conceptual development

The self-stressing SMA/FRP composite patch consists of three main constituents: SMA wires to apply the prestress force, fibers to bridge the fatigue cracks, and adhesive to bond and protect the fibers and the SMA wires. The prestressing force is generated by utilizing the unique thermomechanical properties of the SMA. The concept of the self-stressing patch is to embed prestrained SMA wires into two FRP tabs as shown in Figure 3.1. The cured tabs can be bonded to a cracked steel element using a structural adhesive to anchor the SMA wires to the structure on either side of the crack. The SMA wires can then be activated by application of direct heat or electrical current thereby providing a prestressing force. An FRP overlay is subsequently bonded to the repaired member to bridge the crack. The self-stressing patch applies a prestressing force directly to the repaired element with neither heavy equipment nor fixtures.

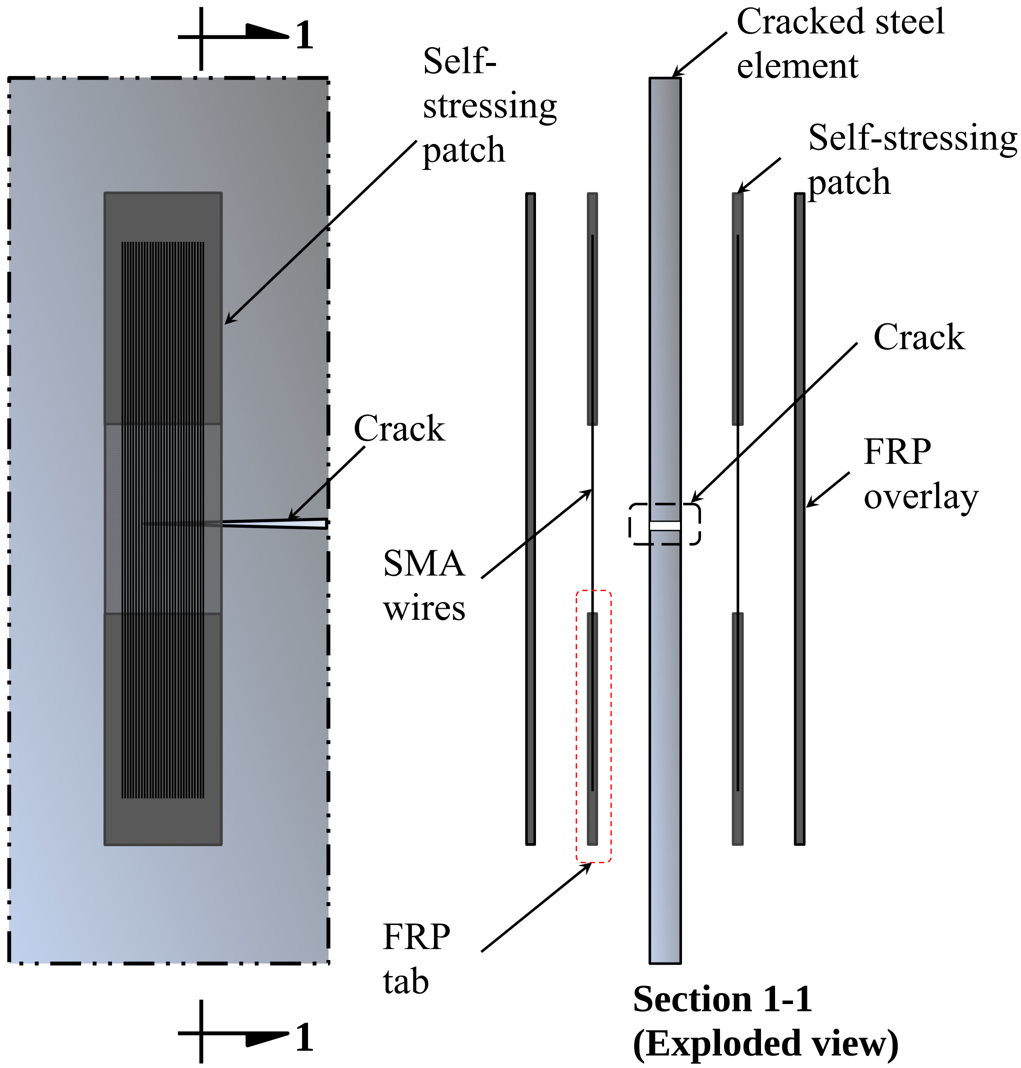

Figure 3.1. A schematic drawing showing the application of the proposed self-stressing SMA/FRP patch to a cracked steel element

An effective prestressing force can be as small as 12 kN to 15 kN (Taljesten et al, 2009) or as high as 165 kN (Bassetti et al., 2000). The effectiveness of the prestressed repair system does not depend on the prestressing level only but also depends on the geometry and properties of the repaired element, and the dimensions and material properties of the FRP material. To design a prestressing system one needs to determine the minimum prestressing level required to halt a fatigue crack, which allows the structure to have an infinite fatigue life. The prestressing level can be determined based on either a fracture analysis based model as presented by Huawen et al. (2010) and Ghafoori et al. (2012a,b) or a constant fatigue life diagram concept (Goodman, 1899; Johnson, 1899) as presented by Ghafoori et al. (2015a,b). In this study it is required to demonstrate that the self-stressing patch is capable of generating a prestressing force in the same order of magnitude as other prestressing systems available in the literature which can reach an infinite fatigue life.

3.2. Materials

The complexity of developing the self-stressing patch comes from the different mechanical and thermomechanical properties of each of the constituents. As the SMA wires are heated, the surrounding adhesive may heat up, leading to possible degradation of its mechanical properties and debonding of the SMA wires from the FRP tabs. Thus, a complete loss in the recovery force could occur. The thermomechanical properties of three SMA wires and two structural adhesives were studied to determine the suitable materials for the proposed self-stressing patch.

3.2.1. Shape Memory Alloys

Three SMA materials were tested to evaluate their thermomechanical properties and to quantify the maximum recovery stress that can be achieved using each alloy. These include: a binary NiTi alloy that was martensitic at room temperature and exhibits the shape memory effect upon heating; NiTi alloy that was austenitic at room temperature and exhibits the superelastic effect at room temperature; and a ternary NiTiNb alloy that is martensitic at room temperature, with a wide thermal hysteresis. The NiTiNb SMA exhibits the shape memory effect upon heating. In this research the first is called shape memory NiTi, the second is called the superelastic NiTi, and the last is called NiTiNb.

The shape memory SMA and superelastic SMA were tested in this research for comparison purposes.

3.2.1.a Shape memory NiTi

The shape SMA wire was supplied by NDC Inc. It is known commercially as alloy SM495 and was provided with an oxidized surface. The chemical composition of the alloy (by weight) is 54.5% nickel, oxygen ≤ 0.05%, carbon ≤ 0.02%, titanium balance, and inclusion area fraction ≤ 2.8% (NDC, 2015a). The reported maximum tensile strength and ultimate strain of the material is ≥ 1070 MPa and ≥ 10%, respectively. Two specimens, each was 305 mm long, were tested in tension up to failure to obtain the stress-strain relationships. Figure 3.2 shows the test setup and instrumentation used in this test.

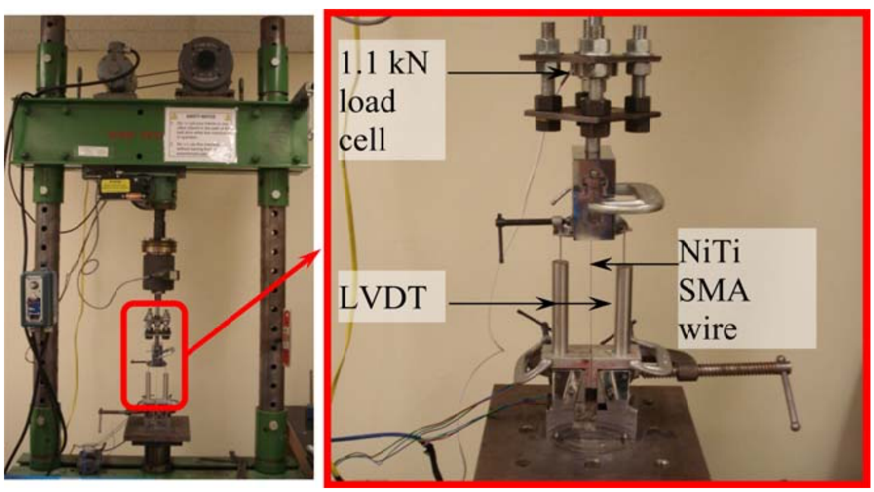

Figure 3.2. Test setup and instrumentation for the shape memory NiTi SMA wire tested in tension

An electromechanical self-reacting frame with a total capacity of 44.5 kN was used to load the specimen at a rate of 0.2 mm/minute. A load cell with a capacity of 1.1 kN (Omega Engineering, model number LC8200-625-250) was used to measure the load, while two linear variable displacement transformer (LVDT) (Trans-Tek, model number 0244-0000) were used to determine the strain in the wire. The data were collected using a data acquisition system, shown in Figure 3.3, (Micro-Measurements, system 7000) at a frequency of 1 Hz.

Figure 3.3. Data acquisition system (Micro-Measurements, system 7000)

Figure 3.4 shows the stress-strain relation for the tested specimens. The average ultimate tensile strength and the total elongation for the shape memory NiTi wires were 1195 MPa and 0.145 mm/mm, respectively.

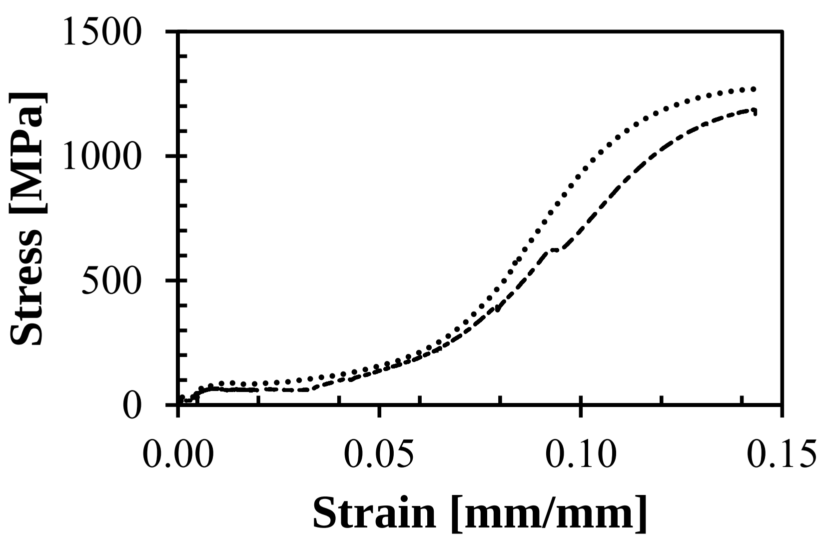

Figure 3.4. Stress strain relationship for shape memory NiTi SMA

The shape memory effect of NiTi wires was evaluated by prestraining the 0.5 mm diameter wire to a strain of 0.08 mm/mm using the same setup shown in Figure 3.2. The wire was clamped to a testing frame. A tensile load of 8.9 N, which corresponds to a stress of 45 MPa, was applied to seat the wire and the wire was subsequently heated using an electrical current to characterize the temperature versus recovery stress response. Electrical current was applied to the wire in increments of 0.5 volts. The temperature of the wire exceeded 75°C when 5.4 volts were applied to the wire.

A load cell with a capacity of 1.1 kN (Omega Engineering, model number LC8200-625-250) was used to measure the force while two thermocouples (Omega Engineering, model number SA1-T-120), were used to monitor the temperature of the wire. Figure 3.5 shows the power supply (BK Precision, model number 9122A) used in this research. The power supply can supply a maximum current of 5 amps and a maximum voltage of 10 volts.

Figure 3.5. Power supply used for the recovery force test

Figure 3.6 shows the relationship between the recovery stress and the temperature for the shape memory NiTi wire. It can be seen that the recovery stress in the wire remained zero until the wire temperature reached 30°C. After the wire temperature exceeded 30°C, increasing the temperature resulted in a corresponding increase of the recovery stress until the temperature reached 75°C at which point the stress reached 415 MPa and remained constant. Inspection of the figure suggests that the austenitic start (A_s) and finish (A_f) temperatures of the wire were 30°C and 75°C, respectively. Upon removing the electric current the wire started to cool immediately and the recovery stress decreased until it reached zero stress at a temperature of 40°C. By observing the hysteretic behavior of the shape memory NiTi SMA wire it can be seen that removal of the heat sources results in a rapid loss of recovery force. This indicates that in the case of heating the SMA wires using an electrical current, this would require a continuous reliable power supply. This is not a feasible solution if the shape memory NiTi SMA wire is to be used in applications requiring a sustained recovery. The wire was partially cooled to simulate either change of the ambient temperature or intermittent loss of electric current as shown in Figure 3.6. The figure illustrates that partial cooling of the wire causes partial loss of the recovery force.

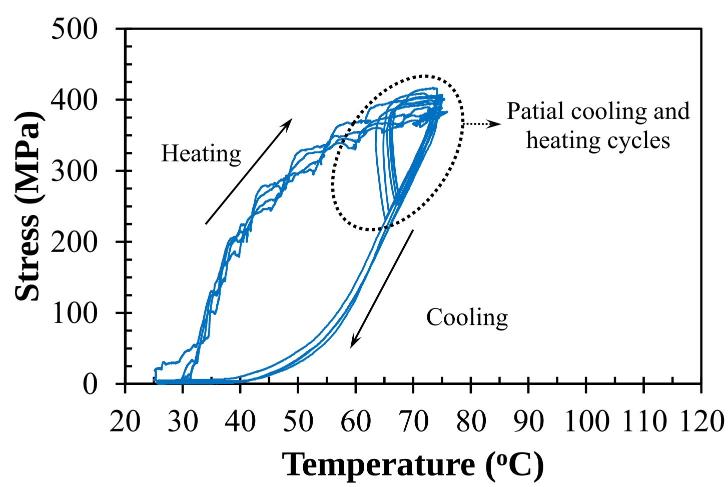

Figure 3.6. Stress temperature relationship for shape memory NiTi wire

3.2.1.b Superelastic NiTi

The superelastic NiTi SMA wire was supplied by NDC Inc. It is known commercially as alloy SE495 and was provided with grit blasted surface. The superelastic NiTi SMA wires have a nominal composition by weight of 55.8% nickel, oxygen ≤ 0.05%, carbon ≤ 0.02%, titanium balance, and inclusion area fraction ≤ 2.8% (NDC, 2015b). The reported ultimate tensile strength and ultimate strain is ≥ 1070 MPa and ≥ 10%, respectively. The alloy is austenitic at room temperature and hence, it exhibits the superelastic effect. Three wire diameters were evaluated in this research: 0.47 mm, 0.66 mm, and 0.89 mm. Three samples of each wire diameter were tested in tension according to ASTM F2516 (ASTM International, 2014). The test setup and the instrumentations used in this test are shown in Figure 3.8. A load cell with a capacity of 1.1 kN (Omega Engineering, model number LC8200-625-250) was used to measure the force. An extensometer with an initial gage length of 13 mm (Epsilon Technology., model number 3442-0050-050-HT1) was used to measure the elongation of the wire. The data acquisition shown in Figure 3.3 was used to collect the data at a frequency of 1 Hz.

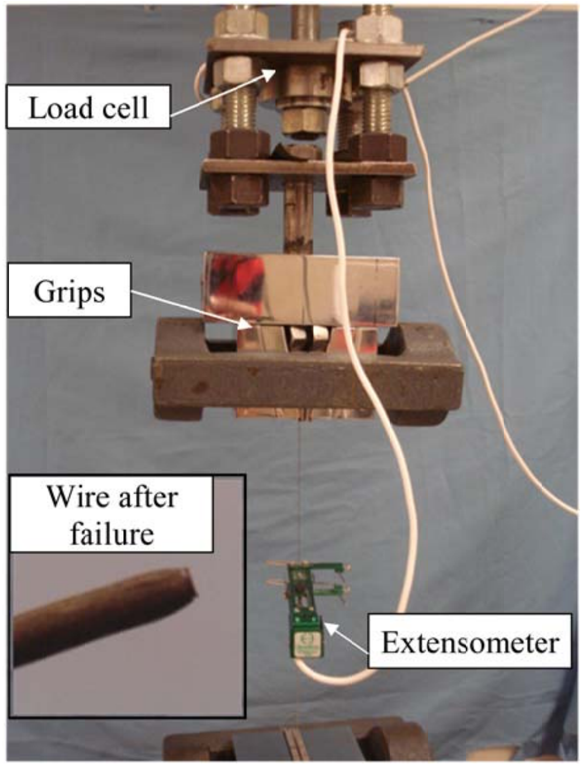

Figure 3.7. Test set of the tensile test of the superelastic NiTi SMA wire

The SMA wires were strained up to 0.06 mm/mm, unloaded to a stress less than 7.0 MPa, and reloaded to failure. The stress-strain curves of the wires are shown in Figure 3.8. According to the ASTM F2516, the upper plateau stress, σ_{UPS}, is defined as the stress value at 0.03 mm/mm strain during the initial loading of the specimen, while the lower plateau stress, σ_{LPS}, is defined as the stress value at 0.025 mm/mm strain during unloading. The mechanical properties of the wires are summarized in Table 3.1.

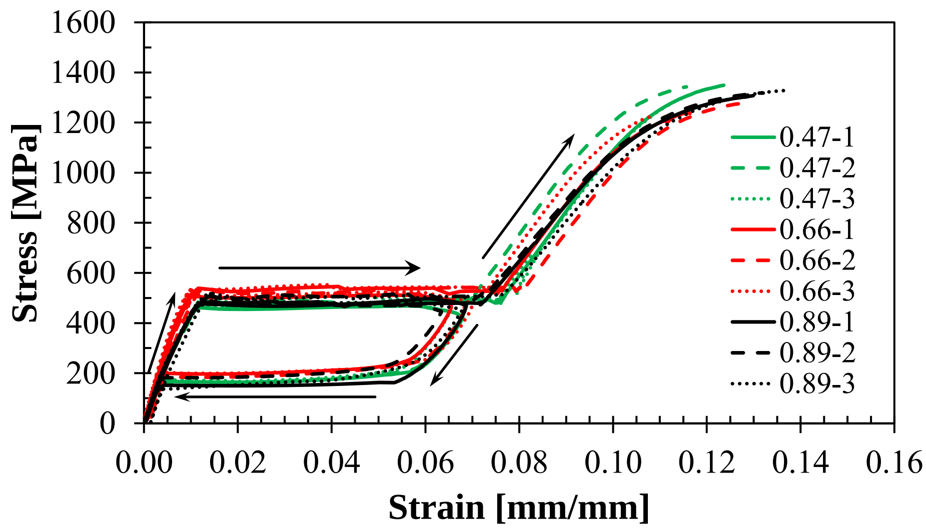

Figure 3.8. Stress strain curves for the superelastic NiTi SMA wires

Table 3.1. Mechanical properties of the superelastic NiTi SMA

Diameter [mm]	**Test #**	σ_u **[MPa]**	ε_u **[mm/mm]**	σ_{UPS} **[MPa]**	σ_{LPS} **[MPa]**
	1	1350	0.124	485	180
0. 47	2	1345	0.116	490	180
	3	1315	0.117	500	185
	1	1240	0.116	505	205
0. 66	2	1280	0.128	505	195
	3	1225	0.108	515	190
	1	1310	0.130	470	150
0. 89	2	1320	0.132	475	190
	3	1330	0.137	485	165
	Average	1300	0.123	490	180
	Standard Deviation	44	0.009	14	16
	COV[1] (%)	3.4	7.6	3.0	8.8

[1] Coefficient of variation (COV) = Standard deviation/average x 100

A prestressing force can be generated utilizing the superelastic effect following similar procedure to pretensioned prestressed concrete. The wires can be affixed to a suitable prestressing fixture, then prestrain the superelastic NiTi SMA to 6%. Saturated fibers can be applied sandwiching the wires to fabricate the patch. Upon curing of the patch the wires can be released from the prestressing frame and the patch can be installed to the cracked structure. A superelastic NiTi SMA wire is expected to generate a force of 490 MPa per wire, which is 18% higher compared to the 415 MPa recovery stress in the case of the shape memory NiTi wire. However, it requires a heavy prestressing frame. Hence, it has no advantage over the conventional FRP prestressing techniques.

3.2.1.c NiTiNb

The NiTiNb SMA is a ternary alloy that exhibits the shape memory effect upon heating from room temperature and maintains a recovery force at room temperature. NiTiNb SMAs are known for their wide thermal hysteresis. As per the manufacturer, the A_s, A_f, M_s and M_f of the alloy is 47^{o}C +/-5^{o}C, 165^{o}C, -65^{o}C and -120^{o}C, respectively. The NiTiNb SMA wires were received in a prestrained condition and with a grit blasted surface. The diameter of the wires after grit blasting was 0.77 mm. The wires were provided in 1370 mm long ± 100 mm discrete pieces. The wires were prestrained to 0.11 mm/mm prior to delivery with a recoverable strain of 0.056 mm/mm upon heating. More details about the prestraining technology can be found in US Patent 4631094 (Simpson et al., 1986). The manufacturer recommends heating the wire up to 165^{o}C to ensure full transformation of the wires and to maximize the recovery force. Six samples of the NiTiNb wire were tested in tension to evaluate the mechanical properties of the wire. Three wires were tested at room temperature in as-delivered condition (with no activation). Three other wires were activated by heating to 165^{o}C while unrestrained then cooled to room temperature and tested after cooling. The test setup and instrumentation used in this test are identical to what described in section 3.2.1.b. Table 3.2 summarizes the test results, while Figure 3.9 shows the stress-strain relationships of the tested wires.

Table 3.2. Mechanical properties of the prestrained NiTiNb SMA

		σ_u [MPa]	ε_u^* [mm/mm]
Not activated	Test #1	1160	0.317
	Test #2	1165	0.411
	Test #3	1160	0.351
	Average	1160	0.360
	Standard Deviation	2.9	0.048
	COV (%)	0.3	13.2
Activated	Test #1	1120	0.477
	Test #2	1155	0.481
	Test #3	1142	0.444
	Average	1140	0.467
	Standard Deviation	17.7	0.020
	COV (%)	1.6	4.4

* The wires were received in prestrained condition with recoverable strain of 0.056 mm/mm

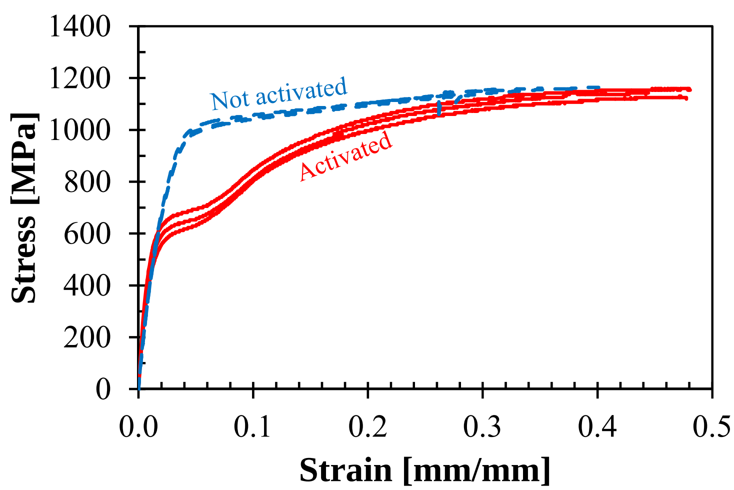

Figure 3.9. Stress-strain curves of the NiTiNb SMA wires

The recovery force that can be generated by the NiTiNb SMA is evaluated. Figure 3.10 illustrates the test setup that was used to measure the recovery force of restrained NiTiNb wires. Individual 250 mm long wires were restrained in a rigid test frame and heated to measure the maximum recovery force. A power supply (Agilent, model number 6542A) capable of supplying a maximum current of 10 amps and maximum voltage of 20 volts was used to heat the wires. As shown in the figure, two electrodes were installed 76 mm apart near the center of the wire. Two thermocouples (Omega Engineering, model number SA1-T-120) were bonded between the two electrodes to monitor the temperature of the wire. A load cell with a maximum capacity of 1.1 kN (Omega Engineering, model number LC8200-625-250) was used to measure the recovery force. A data acquisition system (Micro-Measurements, system 7000) was used to collect the data at a frequency of 1 Hz.

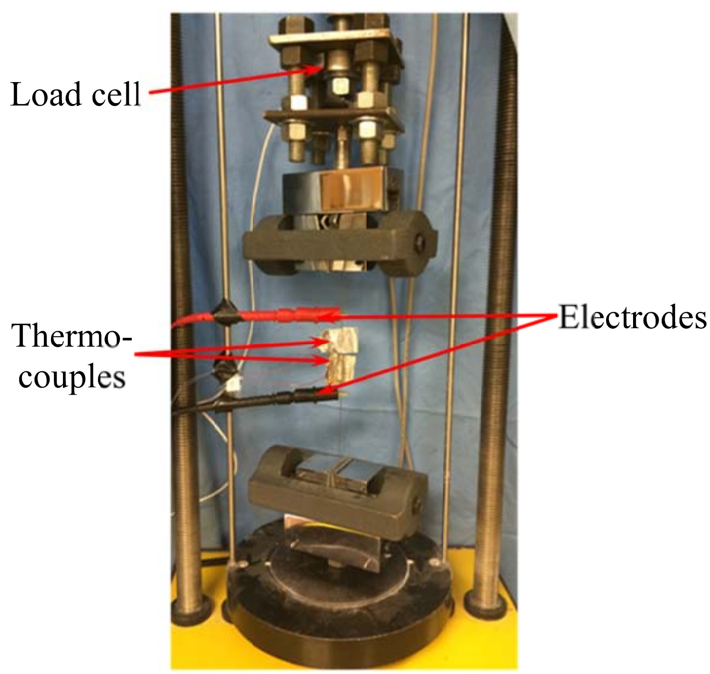

Figure 3.10. Test setup and instrumentation for the recovery stress test of the NiTiNb SMA wire

The NiTiNb was activated by passing an initial current of 3 amps through the wire, and increasing the current in increments of 0.5 amps until the recovery force stabilized at 7.5 amps. A seating load of 8.9 N was applied prior to heating of the wire. Figure 3.11 shows the relationship between the SMA recovery stress and the wire temperature. The A_s temperature range is indicated on the figure as well as the recommended temperature for full activation of the wire. The figure shows the response of the NiTiNb wires and the response of a shape memory NiTi wires for comparison purposes. Inspection of Figure 3.11 indicates that the recovery stress in the NiTiNb wire increased continuously with the increase of temperature up to a temperature of 51^{o}C (A_s). After that temperature the recovery stress increased at a higher rate until the temperature of the wire reached 113^{o}C. The recovery stress remained constant at 390 MPa after this temperature. Upon cooling of the wire to room temperature, the wire stress remained essentially constant. Inspection of the figure indicates that the NiTiNb and the shape memory NiTi generated a prestressing stress of 390 MPa and 415 MPa, respectively. However, upon cooling down the NiTiNb SMA was able to maintain the recovery force unlike the shape memory NiTi which lost all the recovery force. This illustrates the ability of the NiTiNb wire to sustain significant recovery stresses at room temperature.

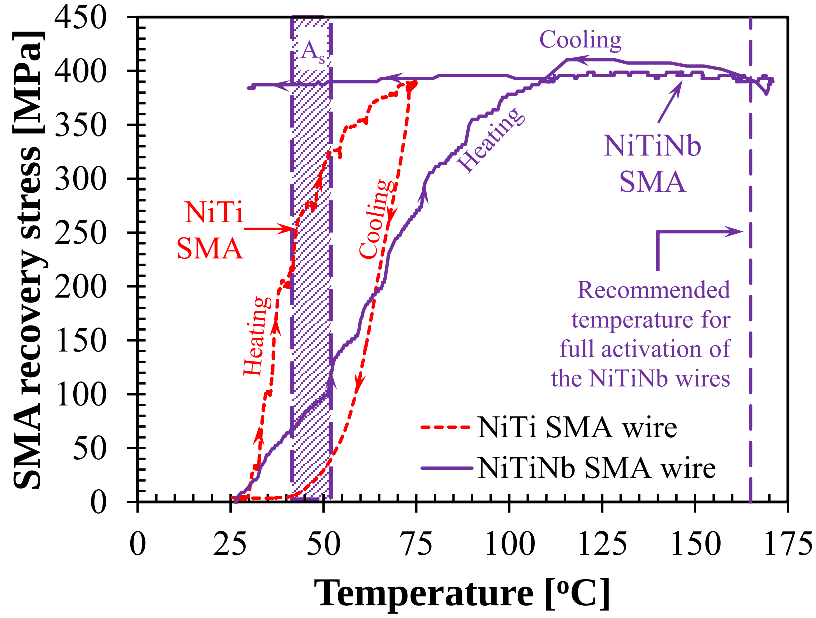

Figure 3.11. The relation between the NiTiNb recovery stress and wire temperature

The stability of the recovery force during repeated extreme heating is investigated. The same wire used in the recovery force test was subjected to 12 thermal cycles. In each cycle, the wire was heated to 165°C then cooled to room temperature. The applied temperature profile and the corresponding recovery stresses are shown in Figure 3.12(a) while the degradation of the room-temperature recovery stress with the number of thermal cycles is presented in Figure 3.12(b). Inspection of Figure 3.12 indicates that the wire maintained a stable recovery stress during the first four thermal cycles with gradual relaxation during the fifth and sixth cycles. The test was stopped after 12 heating cycles as no significant reduction was observed after the 7th heating cycles. It is expected that the recovery stress would remain stable at 315 MPa afterwards. It can be concluded that the wire can maintain over 80% of the recovery force after extreme heating cycles. The maximum temperatures experienced by most civil structures during service are typically below 40°C, and are not expected to cause any significant degradation of the recovery stress.

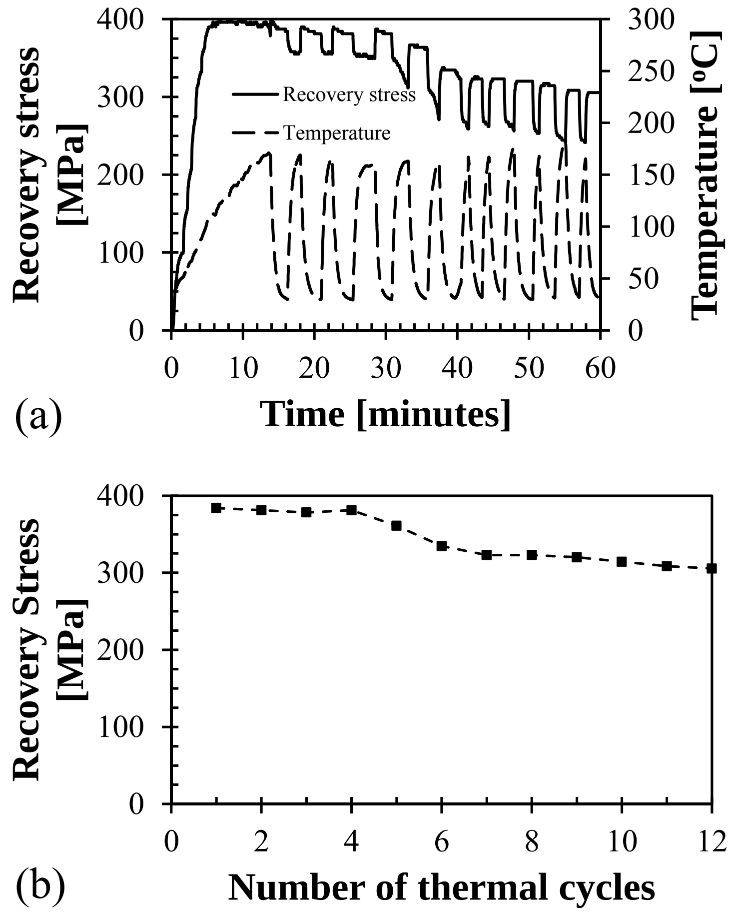

Figure 3.12. (a) Thermal loading protocol with corresponding recovery stress, and (b) Recovery stress of NiTiNb measured after cooling to 25°C

3.2.2. Saturating resin

The self-stressing patch is comprised of SMA wires embedded in FRP. To generate a prestressing force the SMA wires are heated to a temperature higher than the A_f which is 165°C as in the case of NiTiNb. At this temperature the adhesive would heat and soften. The softening of the adhesive would cause a partial or complete loss in the prestress. Hence, evaluating the thermomechanical properties of the saturating resin is essential to prevent any loss in the repair system. There are standard tests available to determine the so called glass transition temperature (T_g) of the adhesive. The T_g is the temperature at which the adhesive transition from the glassy to the rubbery state. However, the value of the T_g varies between different test methods. The interest of this study is to determine the temperature at which the tensile stiffness of the adhesive is substantially reduced which would cause a loss in the prestressing force. In this section the thermomechanical properties of two structural adhesives are evaluated by plotting the relation between the tensile modulus of the adhesive tested at various temperatures.

Two commercially available structural adhesives were evaluated: Tyfo S (By Fyfe Co.) and Araldite LY 5052 / Aradur 5052 (by Huntsman Advanced Materials). Both adhesives were low-viscosity, two-part components with ambient temperature cure cycles and optional elevated temperature post-cure treatments. Throughout the rest of this dissertation the first adhesive is called Tyfo S, while the second is called Araldite. A total of 60 cured resin coupons were tested according to ASTM D638-14 (ASTM International, 2014) to evaluate their tensile moduli and strengths at different temperatures. Figure 3.13 shows the details of the epoxy coupons. The epoxy coupons were prepared by mixing, by weight, 100 parts of component A to 34.5 parts of component B for the Tyfo S adhesive, and 100 parts of component A to 38 parts for component B for the Araldite adhesive. The mixed epoxies were then cast into a machined plastic mold shown in Figure 3.14.

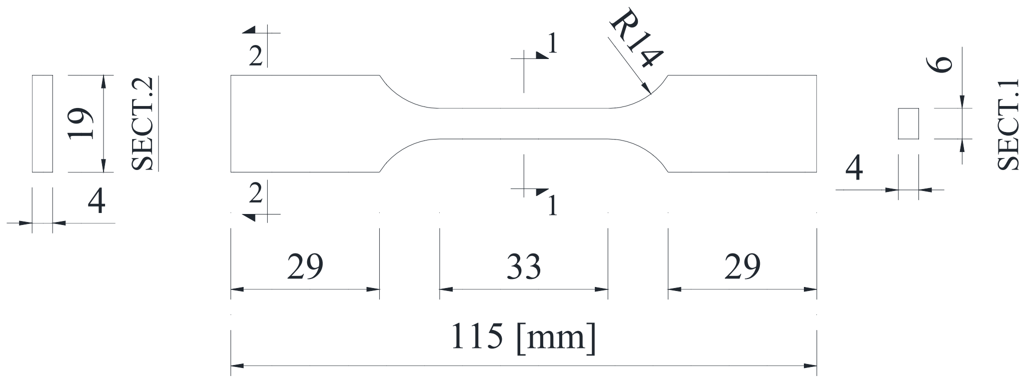

Figure 3.13. Dimension details of the epoxy coupon

Table 3.3 shows the test matrix of the epoxy tensile tests. Tyfo S was cured at 25^{o}C for seven days then tested in tension at 25^{o}C and 45^{o}C. Four sets of specimens were made from Araldite. The first set was cured at 25^{o}C for 7 days and tested at 25^{o}C, 45^{o}C, and 60^{o}C. The second, third and fourth sets were cured at 25^{o}C for 24 hours then post cured at 45^{o}C, 60^{o}C, and 75^{o}C for 24 hours, respectively. Samples from each set were tested at 25^{o}C, 45^{o}C, 60^{o}C, 75^{o}C, and 100^{o}C. These test temperatures were selected to represent the ranges of activating temperatures of the SMA wires.

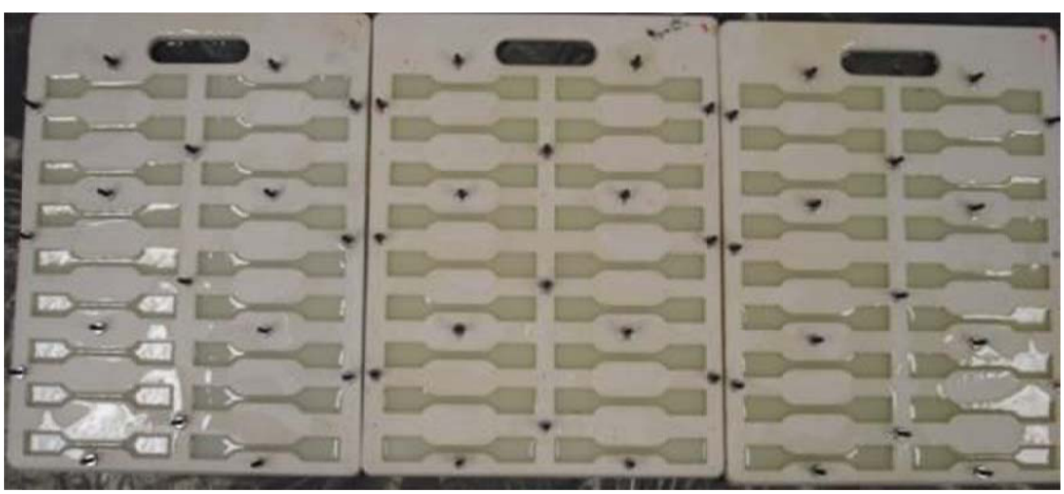

Figure 3.14. The machined plastic molds used in fabricating the epoxy coupons

Table 3.3. Epoxy test matrix

	Curing temperature[1] [°C]	Post cure temperature[2] [°C]	Testing temperature [°C]
Tyfo S	25	---	25, 45
Araldite	25	---	25, 45, 60
	25	45	25, 45, 60, 75, 100
	25	60	25, 45, 60, 75, 100
	25	75	25, 45, 60, 75, 100

[1] Specimens were cured for 7 days

[2] Specimens were post cured for 1 day

Figure 3.15 shows the test setup of the epoxy coupons test. A 22-kN load cell (Tovey Engineering, model number SW10-5K-B000) was used to measure the applied load, while an extensometer with an initial gage length of 13 mm (Epsilon Technology., model number 3442-0050-050-HT1) was used to measure the elongation of the epoxy. The coupons were heated in a frame-mountable environmental chamber (Instron, model number 3111) with a maximum temperature capacity of 204°C. The chamber was set to the desired testing temperature and the internal temperature was allowed to achieve a steady state. The epoxy coupon was gripped from one end and the extensometer was affixed to the specimen inside the environmental chamber. The specimens along with the extensometer were left for 20 minutes to allow for both. Then the other end of the specimen was gripped and the gage length of the extensometer was reset. The specimen was re-soaked for another 10 minutes to overcome any drop in the temperature inside the chamber during the gripping process.

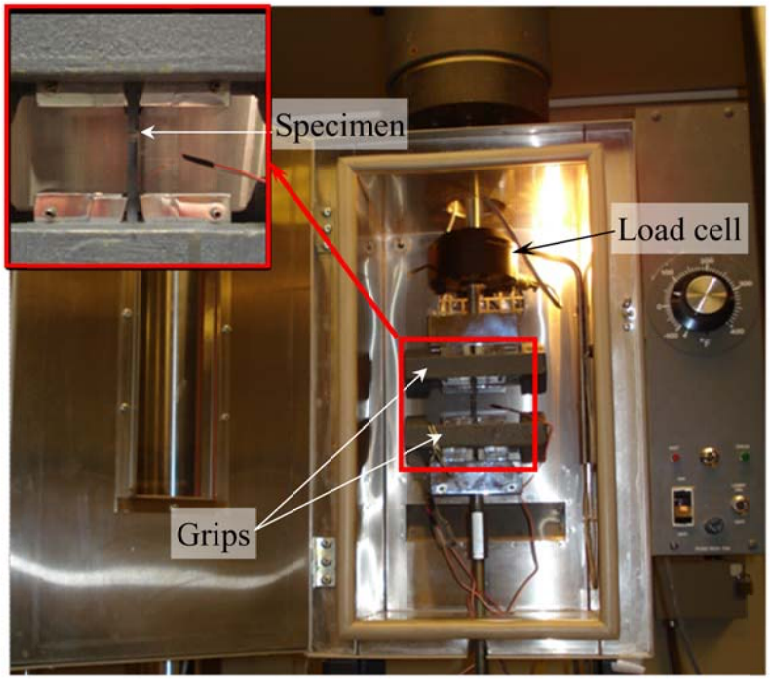

Figure 3.15. Test setup for the epoxy coupons test

Figure 3.16 plots the relationship between the tensile modulus of the two tested adhesives versus the testing temperature. The stress-strain curves and the mechanical properties are presented in Appendix A. Inspection of the figure indicates that a substantial degradation in the tensile modulus was observed as the ambient testing temperature increased. The Tyfo S tensile coupons that were cured at 25^{o}C and tested at 45^{o}C deformed excessively when the extensometer was mounted on the specimens. As such, the elastic modulus of Tyfo S was taken as zero for temperatures above 45^{o}C. The tension coupons of the Araldite adhesive that were cured at 25^{o}C and tested at 60^{o}C exhibited a similar behavior and thus the elastic modulus of Araldite specimens which were cured at 25^{o}C was taken as zero for temperatures greater than 60^{o}C. Inspection of Figure 3.16 indicates that at the austenitic finish temperature both adhesives were completely softened. It can be seen in the figure that the specimens cured at 25^{o}C and tested at 60^{o}C exhibited an elastic modulus of zero MPa, while the specimens post cured at 45°C and tested at 60°C exhibited an elastic modulus of 1820 MPa. This shows that post curing of the Araldite adhesive resulted in an increase in the elastic moduli of the adhesive at elevated temperatures. Since the post-cure temperatures were above the austenitic start temperature of the SMA, the curing regimens would likely cause partial activation of the SMA wires in the patch. As such, elevated temperature post-cure cycles are not recommended for the proposed application. The Araldite adhesive was selected for further consideration in the patch development as the Araldite adhesive retained higher tensile modulus at room temperature and within the austenitic start temperature range compared to the Tyfo S adhesive.

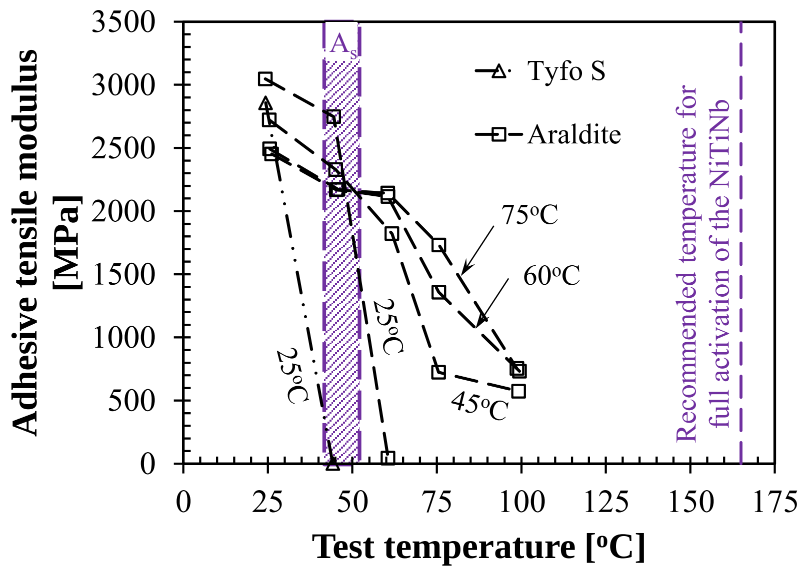

Figure 3.16. The relation between the tensile modulus of adhesives versus temperature

3.2.3. Fibers

Throughout this research two fiber types were used: carbon fibers and glass fibers. Both fibers were supplied by Fyfe. The reported tensile strength, tensile modulus, elongation, density, and aerial weight of the dry fibers are summarized in Table 3.4

Table 3.4. Carbon and glass fibers properties

	Carbon fibers	Glass fibers
Tensile strength [MPa]	3790	3240
Tensile modulus [MPa]	230,000	72,400
Elongation [mm/mm]	0.017	0.045
Density [gm/cm^3]	1.79	2.55
Aerial weight [gm/m^2]	644	915

3.3. Wire activation and thermal transfer

To ensure complete activation of the wires, the manufacturer recommends heating the wires to 165^{o}C. This temperature is well above the softening temperatures of the two adhesives tested in the previous section. The testing reported in section 3.2.2 further indicates that the softening temperature, the temperature at which the elastic modulus drops to 50% of its room temperature value, of commonly used ambient-temperature cure structural adhesives is within the range of 45^{o}C to 60^{o}C. Softening of the adhesive during activation of the SMA wires would allow the SMA wires to slip during activation resulting in partial to no restraint of the transformation process and subsequently little to no recovery forces developed in the wires. Therefore, the activation process of the patches must be carefully considered to prevent the temperature in the FRP patch from exceeding the softening temperature of the saturating resin, thereby maximizing the recovery forces in the wires and the compressive stresses transferred to the substrate.

To overcome the adhesive softening problem the self-stressing shown in Figure 3.17 can be activated by heating only the exposed portion of the wires to generate the prestressing force. This eliminates the challenges associated with softening of the epoxy.

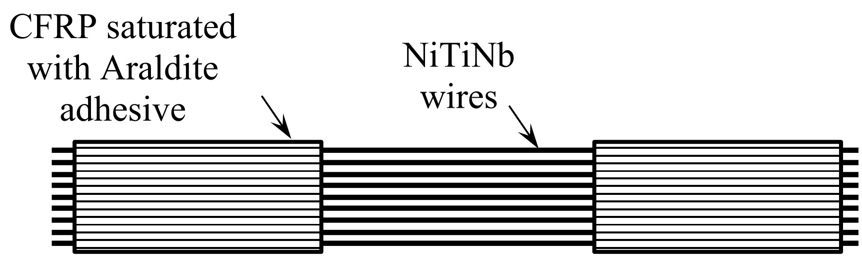

Figure 3.17. Proposed configurations for the self-stressing patch

3.3.1. Localized electrical heating of NiTiNb wires

A 255-mm long, 0.81 mm diameter NiTiNb wire was tested to study the possible epoxy softening in the bonded region due to heat transfer by thermal conduction through the SMA wire. The temperature along the wire was measured using electrically insulated thermocouples (Omega Engineering, model number SA1-T-120), as shown in Figure 3.18(a). Two electrodes were attached to the wire with a spacing of 125 mm. The distance between the electrode and the thermocouple outside the heated area was 20 mm as shown in the figure. The measured temperature profiles along the length of the wire are plotted in Figure 3.18(b) at different heating time intervals. Inspection of the figure indicates that the temperature of the wire between the two electrodes reached nearly 120^{o}C. However, immediately outside of the electrodes, the temperature of the wire remained constant after 10 minutes of continuous heating. This indicates that electrically heating the central exposed portion of the SMA wires is a viable alternative for the proposed configuration.

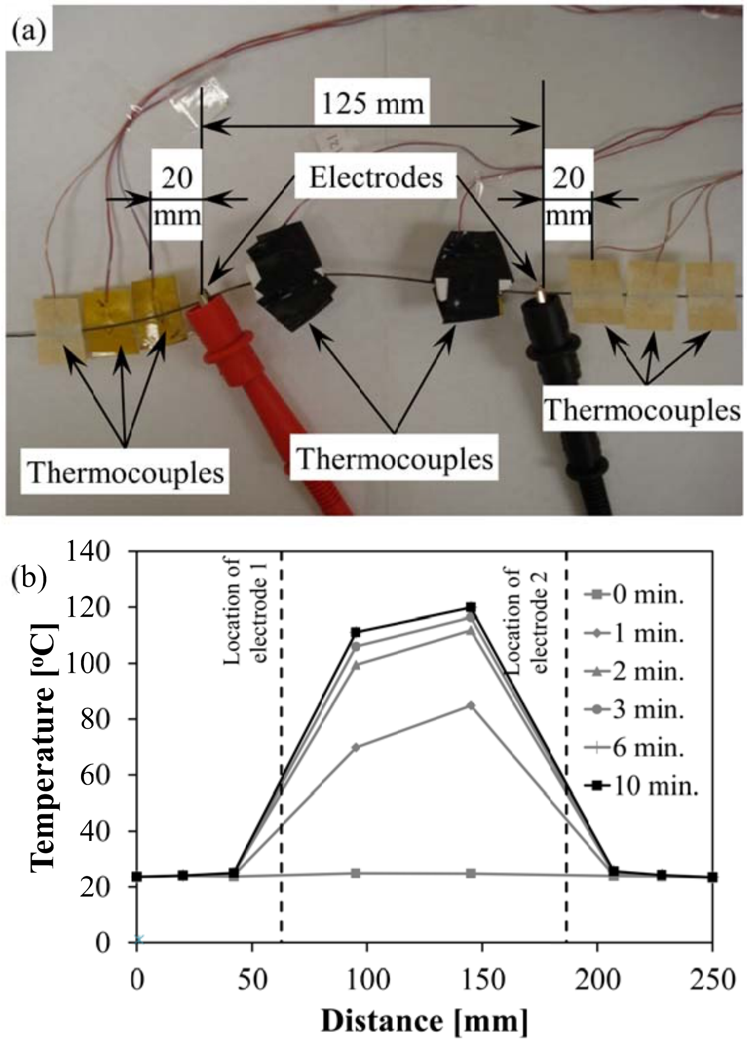

Figure 3.18. Thermal transfer test: (a) test setup, and (b) results

3.4. Discussion

The ternary wide thermal hysteresis NiTiNb SMA was able to generate a recovery stress of 390 MPa, while the binary shape memory NiTi SMA was able to generate a prestressing stress of 415 MPa. However, upon cooling down the NiTiNb SMA was able to maintain the recovery force unlike the shape memory NiTi which lost all the recovery force. Thus, the NiTiNb SMA is suitable to be used in the self-stressing patch. Cyclic heating and cooling of NiTiNb wires up to 165^{o}C results in an 18% reduction of the sustained recovery force at room temperature after 12 cycles. However, cycling heating and cooling in the expected service temperature range for most civil infrastructure (up to 40^{o}C) is not expected to have any significant impact on the recovery force.

Post curing of the Araldite adhesive resulted in an increase in the elastic moduli of the adhesive at elevated temperatures. However, post-cure temperatures above the austenitic start temperature of the NiTiNb SMA would likely to cause partial activation of the SMA wires in the patch. As such, elevated temperature post-cure cycles are not recommended for the proposed application. The Araldite adhesive was selected as it retained higher tensile modulus at room temperature and 45^{o}C. The maximum temperatures experienced by most civil structures during service are typically below 40^{o}C, and are not expected to cause any significant degradation of either the recovery stress or the tensile modulus of the Araldite adhesive. Activating the central exposed portion of the wire, 20 mm away from the patch would eliminate the possible softening of the epoxy at the embedded part the SMA wires in the patch configuration presented.

Chapter 4: Bond Behavior of Superelastic NiTi and NiTiNb SMA Wires Embedded in FRP Composites

Effective bond between SMA wires and FRP materials is essential to ensure that composites with embedded SMA wires perform as intended. The research conducted to date predominantly studied the bond behavior of martensitic Nitinol wires, which exhibit the shape memory effect, embedded in epoxy cylinders (Lau et al, 2002; Poon et al, 2005a,b; Payandeh et al., 2009; Wang et al., 2011 Payandeh et al., 2012). Comparably little is known about the bond behavior between other types of SMA wires, such as superelastic Nitinol or NiTiNb, embedded in thin FRP composites. The complexity of bond behavior between superelastic NiTi and FRP comes from the abrupt change of modulus caused by the stress-induced martensitic transformation, which may lead to debonding. Understanding the debonding behavior is essential in the design of FRP composite systems with embedded superelastic NiTi such as ductile FRP rebars (Wierschem and Andrawes, 2010) and composites with embedded SMA damping (Liu et al, 2007; Raghavan et al., 2010).

The self-stressing patch proposed in this dissertation is composed of NiTiNb wires embedded in FRP composite. The prestressing force generated by the NiTiNb wires is transferred to the FRP composite through the bond interface. The stability of the prestressing force relies on effective bond between the NiTiNb wires and the FRP. Debonding between the two could lead to partial or full loss of the pretress force which could compromise the effectiveness of the repair.

This chapter outlines and presents the experimental work conducted to study the bond behavior between two SMA wires: superelastic NiTi and NiTiNb to FRP composites. A total of 60 pull-out specimens were fabricated and tested in this study. Table 4.1 presents the test matrix for the pull-out specimens with superelastic NiTi wires embedded in CFRP. The factors considered in this study were the wire diameter (0.47 mm, 0.66 mm and 0.89 mm) and the embedment length (13 mm, 25 mm, 51 mm, 102 mm and 127 mm). Three repetitions of each configuration were tested.

Table 4.1. Test matrix for the pull-out specimens with superelastic NiTi

d_b [mm]	L_d [mm]	Number of repetitions
0.47	13 (28d_b)	3
	25 (53 d_b)	
	51 (109 d_b)	
	102 (217 d_b)	
	127 (270 d_b)	
0.66	13 (20 d_b)	
	25 (38 d_b)	
	51(77 d_b)	
	102(155 d_b)	
	127(193 d_b)	
0.89	13(15 d_b)	
	25(28 d_b)	
	51(57 d_b)	
	102(115 d_b)	
	127(143 d_b)	

Table 4.2 summarizes the test matrix for the NiTiNb pull-out tests. The test parameters for the specimens with NiTiNb wires include the embedment length (25 mm, 51 mm and 102 mm) of the SMA wires, fiber type in the FRP composite, and the number of wires per specimen. The pull-out specimens were divided into three groups, as summarized in the table. The specimens in the first group consisted of a single NiTiNb wire embedded in CFRP with embedment lengths of 25 mm, 51 mm and 102 mm. The specimens were tested to evaluate the minimum embedment length required to develop the maximum interface strength. The second group consisted of three NiTiNb wires embedded in CFRP with embedment length of 102 mm. The specimens of the second group were tested to examine the possible interaction between the adjacent wires. In the third group, the effect of the FRP type on the pull-out behavior of a single wire was examined. Three repetitions were tested of each configuration.

Table 4.2. Test matrix for the pull-out specimens with NiTiNb

	Fiber type	Adhesive type	Embedment length [mm]	Number of embedded wires	Number of repetitions
Group 1	Carbon	Araldite	25 (33 d_b)	1	3
			51 (66 d_b)		
			102 (132 d_b)		
Group 2	Carbon	Araldite	102 (132 d_b)	3	
Group 3	Glass	Araldite	102 (132 d_b)	1	

4.1. Specimen details

Figure 4.1 shows the dimensions and details of the pull-out specimens. All the pull-out specimens were fabricated using a hand lay-up method. The specimens with superelastic NiTi SMA wires were fabricated by embedding a single wire between two layers of unidirectional carbon fiber fabric. Tyfo S was used as a saturating resin as the superelastic wire does not require activation, hence, the softening of the adhesive is not expected to be an issue. The specimens with NiTiNb SMA wires were fabricated using either glass and carbon fibers, and saturated using the Araldite resin. The properties of fibers, resins, and SMA wires are presented in details in Chapter 3.

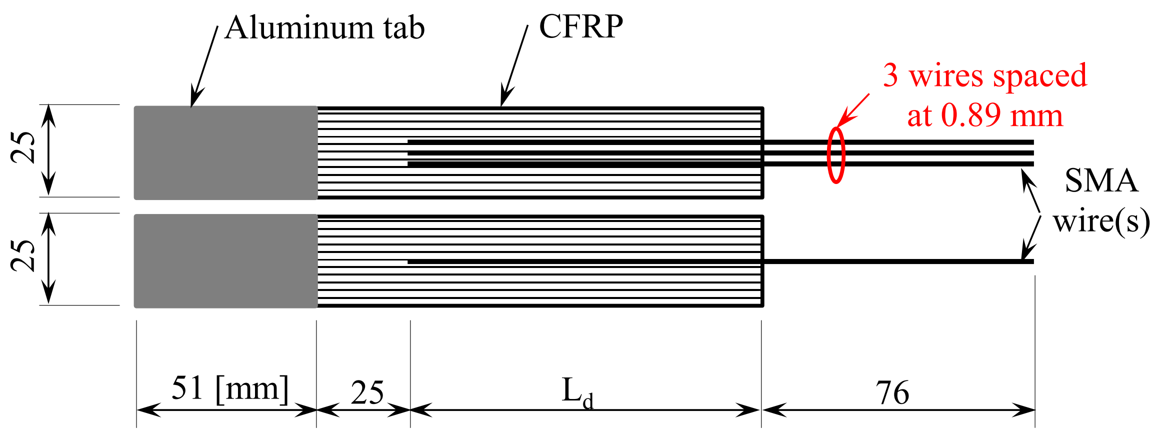

Figure 4.1. Pull-out specimen dimensions

As shown in Figure 4.1, the SMA wires extended 76 mm outside the FRP to provide room to grip the wire and affix the instrumentation. Aluminum tabs were bonded to the end of the FRP patch and gripped in the load frame during testing. A clear distance of 25 mm was provided between the end of the embedded SMA wire and the tabs to prevent interference in the bonded portion of the wire. Figure 4.2(a) and (b) show the pull-out specimens with superelastic NiTi and NiTiNb SMA wires, respectively. The specimens were mounted in an electromechanical test frame and the wires were pulled out of the patches by applying an axial tension force in displacement control. The pull-out specimens with superelastic NiTi and NiTiNb SMA were tested at a rate of 2.5 mm/minute, and 0.4 mm/minute, respectively.

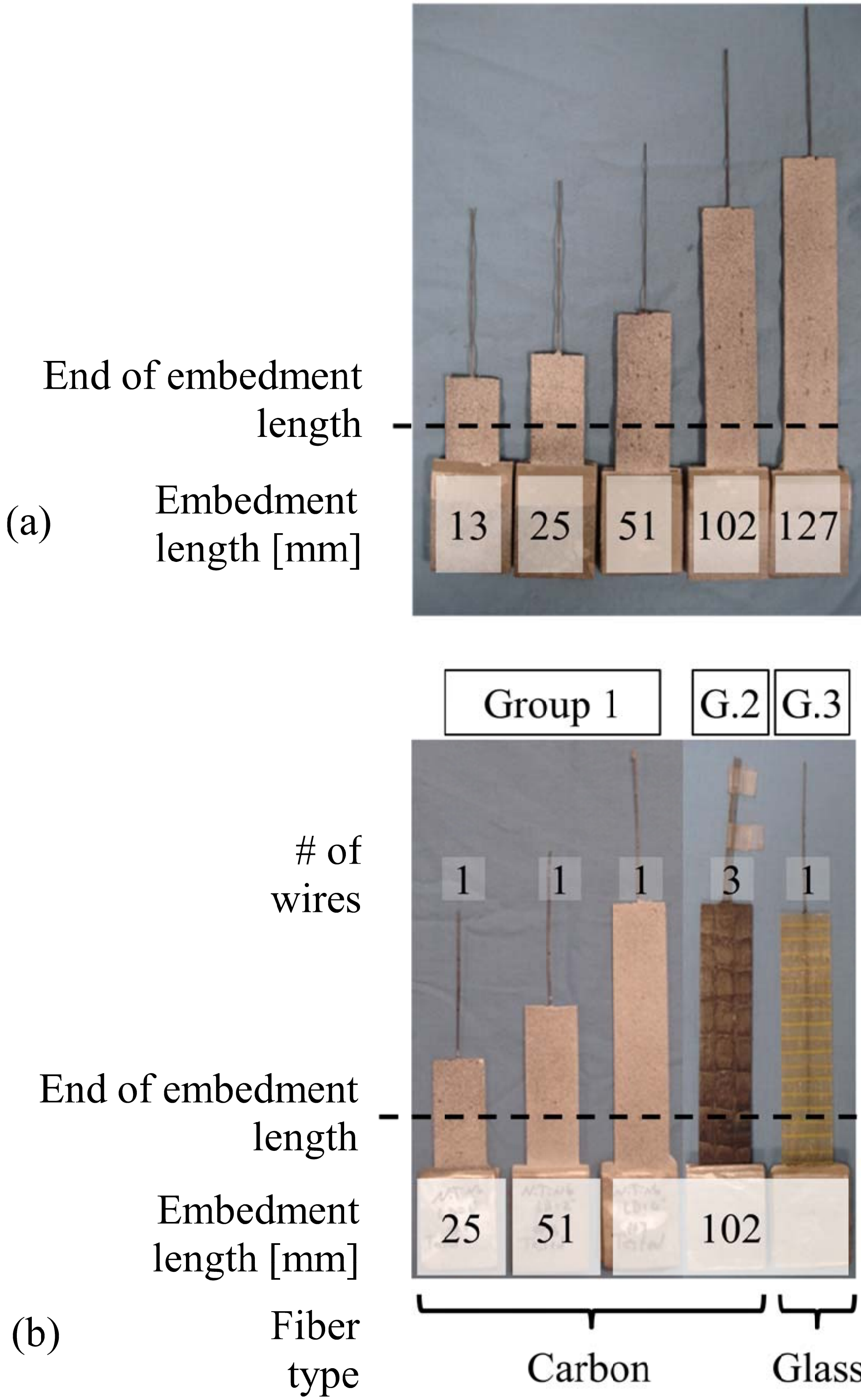

Figure 4.2. Pull-out specimens with (a) superelastic NiTi wires, and (b) NiTiNb SMA wires

4.2. Test setup and instrumentation

Figure 4.3 shows the test setup and instrumentations used for the pull-out tests. Two sets of instrumentations were used: conventional instrumentation and a digital image correlation system (DIC). The DIC was used to help identifying the onset and propagation of debonding. The conventional instrumentations consisted of (a) two load cells with capacity of 22 kN (Tovey Engineering, model number SW10-5K-B000) and 1.1 kN (Omega Engineering, model number LC8200-625-250) which were used to measure the load; (b) two extensometers with initial gage lengths of 13 mm (Epsilon Technology., model number 3442-0050-050-HT1), and 51 mm (Epsilon Technology., model number 3542-0200-050-ST) were used to measure the elongation of the wire, and the relative displacement between the wire and the FRP, respectively; and (c) a data acquisition system (Micro-Measurements, system 7000) to record the readings from the conventional instruments. The data acquisition system recorded at a frequency of 1 Hz.

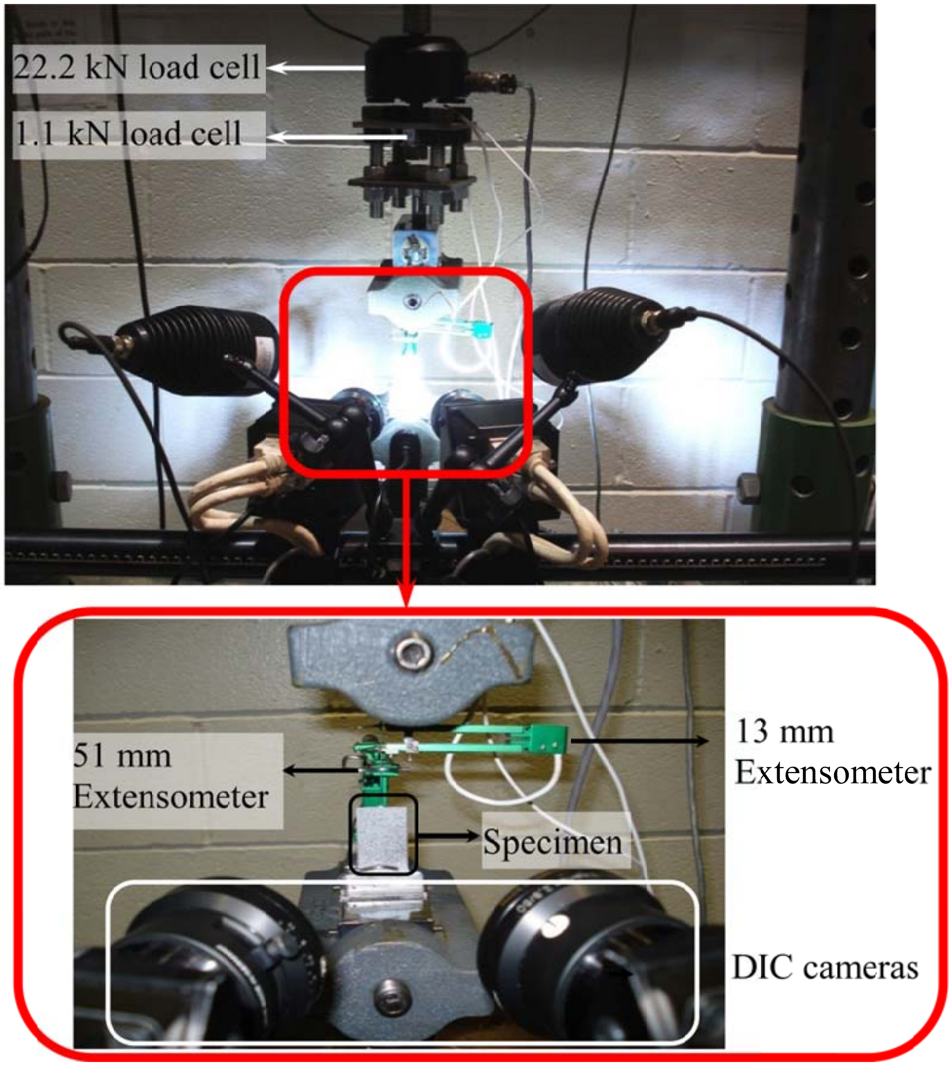

Figure 4.3. Test setup of the pull-out test

The DIC system consists of: (a) two cameras each with a resolution of 12 mega pixels, each equipped with a lens with a 50 mm focal length; (b) a digital control unit; and (c) a data acquisition system that is capable of recording images from the DIC system and digital signals from up to eight conventional sensors with signals of +/- 10 VDC. A random black and white speckled pattern was applied to the surface of the specimen. The system recorded images at a frequency of 1 Hz. The ARAMIS software calculated displacements and strains on the surface of the CFRP by tracking sets of pixels called facets as illustrated in Figure 4.4. The facets are tracked in subsequent sets of images (GOM mbH, 2011) and the coordinates of each facet is computed. Based on the coordinates of the facets the displacements and strains are calculated. In this study facet size and step were 35 pixels and 28 pixels, respectively. To eliminate possible noise of the strain readings the strain readings were filtered using the built-in averaging filter in ARAMIS software. Each 7 adjacent facets were averaged based on the median strain. The filter was run three times on all the facets.

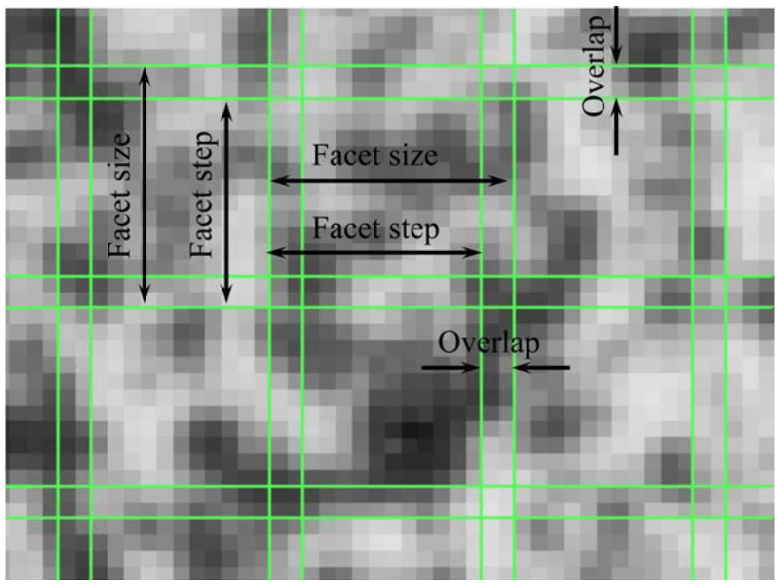

Figure 4.4. An example of facet size and step (adapted from ARAMIS manual, 2011)

Both data acquisition systems were connected together to synchronize the data as shown in Figure 4.5. The 1.1 kN load cell, 13 mm extensometer and 51 extensometer were connected to the Micro-Measurements data acquisition only. The 22.2 kN load cell was connected to a special card on the Micro-Measurements data acquisition that passes through the input signal as an output, with a gain of 50.3, which can be sent to another data acquisition system for data synchronization. The signal was passed through a load cell conditioner (Omega Engineering, model number DRF-LC-115VAC-20MV-0/10) with an output voltage of 10 VDC for an input of 20 mV to amplify the signal which was subsequently connected to the data acquisition system on the DIC controller.

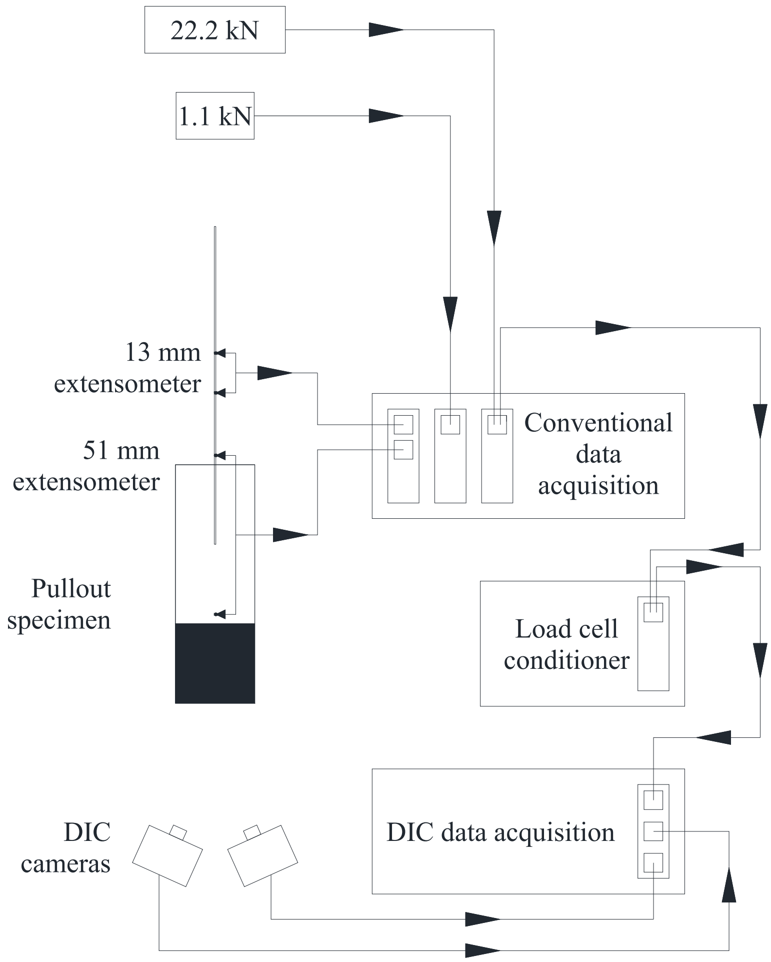

Figure 4.5. Schematic drawing of the instrumentation used for the pull-out test

4.3. Results and discussion of the pull-out specimens with superelastic NiTi SMA wires

All of the tested pull-out specimens failed by debonding. Figure 4.6 shows a typical specimen after failure. The figure indicates that the debonded part of the wire had no epoxy attached to it suggesting that an adhesive failure occurred at the wire-adhesive interface. All the specimens failed by complete debonding after transformation of the SMA wire except for three sets of specimens. These other three sets, including samples with 0.66 mm diameter wire with 13 mm embedment length, and 0.89 mm diameter wire with 13 mm and 25 mm embedment lengths, failed by complete debonding of the SMA wires prior to the initiation of the transformation of the wire.

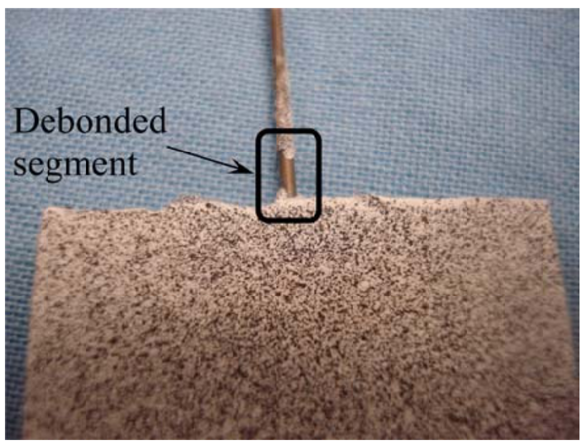

Figure 4.6. A typical specimen after complete debonding

Figure 4.7 presents the combined results from both measurement systems for the specimen with an embedment length of 25 mm and a wire diameter of 0.47 mm. This specimen failed by complete debonding after transformation of the wire. A similar trend of behavior to that shown in the figure was observed for all of the specimens that failed by debonding after transformation of the wire as shown in Appendix B. The time histories of the load, wire elongation (measured by the 13 mm extensometer), and relative displacement between the CFRP and SMA (measured by the 51 mm extensometer) are shown on a single plot to facilitate comparison. Longitudinal strain contours obtained from the DIC system are plotted above the time histories. The values of the time, load, relative displacement between the CFRP and SMA, and wire strain at the times when each strain contour was captured are shown above the strain contours. Dotted lines on the time histories indicate the time when each strain contour was captured by the DIC system. The legend located at the bottom of the figure indicates key points during testing.

Time [s]	23	28	34	93	94	95	111	134	145	155	156
Load [N]	47	64	79	81	82	81	82	82	82	82	23
Disp. [mm]	0.015	0.029	0.041	0.395	0.412	0.432	0.768	1.163	1.482	1.842	1.786
Strain [mm/mm]	0.005	0.008	0.011	0.035	0.036	0.037	0.048	0.069	0.07	0.07	0.064

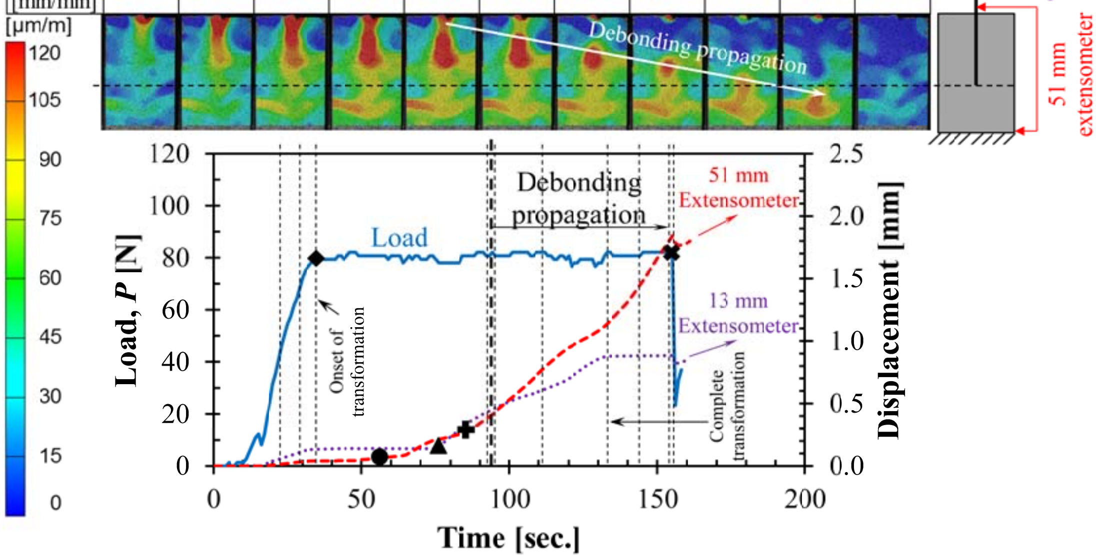

◆ Initiation of martensitic transformation
● Initiation of martensitic transformation within the gage length of the 51 mm extensometer
▲ Initiation of martensitic transformation within the gage length of the 13 mm extensometer
✚ Initiation of debonding
✖ Completion of debonding

Figure 4.7. Load and displacement histories and DIC contours for a specimen with an embedment length of 25 mm, and a wire diameter of 0.47 mm

The strain contours shown in Figure 4.7 indicate the presence of a localized strain concentration at the location where the SMA wire exited the CFRP patch. As loading continued the size and intensity of the strain concentration increased until a time of 94 seconds. At that stage a clear shift of the strain concentration away from the edge of the CFRP patch was observed. This indicates the initiation of observable debonding of the wire. The debonding propagated along the embedment length of the SMA wire as indicated by the shift of the location of this strain concentration.

Inspection of the load and displacement histories shown in Figure 4.7 reveals that initially the applied load increased up to 79 N, at a test time of 34 seconds (indicated by ◆ in Figure 4.7). The corresponding stress in the wire was 456 MPa which is consistent with the upper plateau stress of the SMA. This suggests that the initiation of the martensitic transformation occurred in the wire. The DIC system indicated that the wire remained completely bonded to the CFRP patch up to that stage. Inspection of the wire elongation history (obtained by the 13 mm extensometer) indicates that the corresponding strain in the wire was 0.011 mm/mm which is consistent with the transformation strain of the wire. After this stage the displacement remained constant for 33 seconds as the transformation initiated and propagated outside of the extensometer gage length. At a test time of 76 seconds (indicated by ▲ in Figure 4.7) the strain in the wire within the gage length of the 13 mm extensometer started to increase again. This indicates propagation of the transformation of the wire within the gage length of the extensometer. The wire strain increased up to 0.069 mm/mm which is consistent with the measured complete transformation strain of the wire.

Inspection of the displacement history (obtained by the 51 mm extensometer) indicates that the relative displacement between the SMA wire and the CFRP patch was negligible up to a test time of 54 seconds (indicated by ● in Figure 4.7). At that stage the relative displacement increased gradually due to transformation of the unbonded SMA wire within the gage length of the 51 mm extensometer and very close to the edge of the CFRP patch. At test time of 86 seconds (indicated by ✚ in Figure 4.7) the relative displacement rate increased noticeably. This increase of the displacement rate was attributed to the onset of debonding which is consistent with the DIC observations. Failure was observed as a sudden drop of the applied load at a test time of 155 seconds (indicated by ✖ in Figure 4.7) which corresponded to complete debonding of the wire from the patch.

For specimens with wire diameters of 0.66 mm and 0.89 mm and embedment lengths up to 13 mm and 25 mm, respectively, complete debonding of the wire was observed prior to the onset of the martensitic transformation in the SMA wire. This was due to the relatively large diameters of these wires and the relatively short development lengths. Figure 4.8 shows the debonding sequence for a specimen with a wire diameter of 0.89 mm and an embedment length of 25 mm in a similar format to that of Figure 4.7. The figure shows a similar strain concentration to that shown in Figure 4.7. The shift of the strain concentration was observed after the load reached 252 N at a test time of 25 seconds. This indicates that debonding initiated and propagated along the embedment length of the SMA wire. Complete debonding occurred at an applied load of 318 N which corresponds to wire stress of 512 MPa. The measured stress in the wire at failure suggests that the transformation of the wire was imminent. Inspection of the figure indicates that although debonding initiated the wire was able to carry additional load as the debonding propagated until complete debonding occurred.

Appendix B provides the detailed test results of all the pull-out tests of the superelastic NiTi SMA wires embedded in CFRP composite.

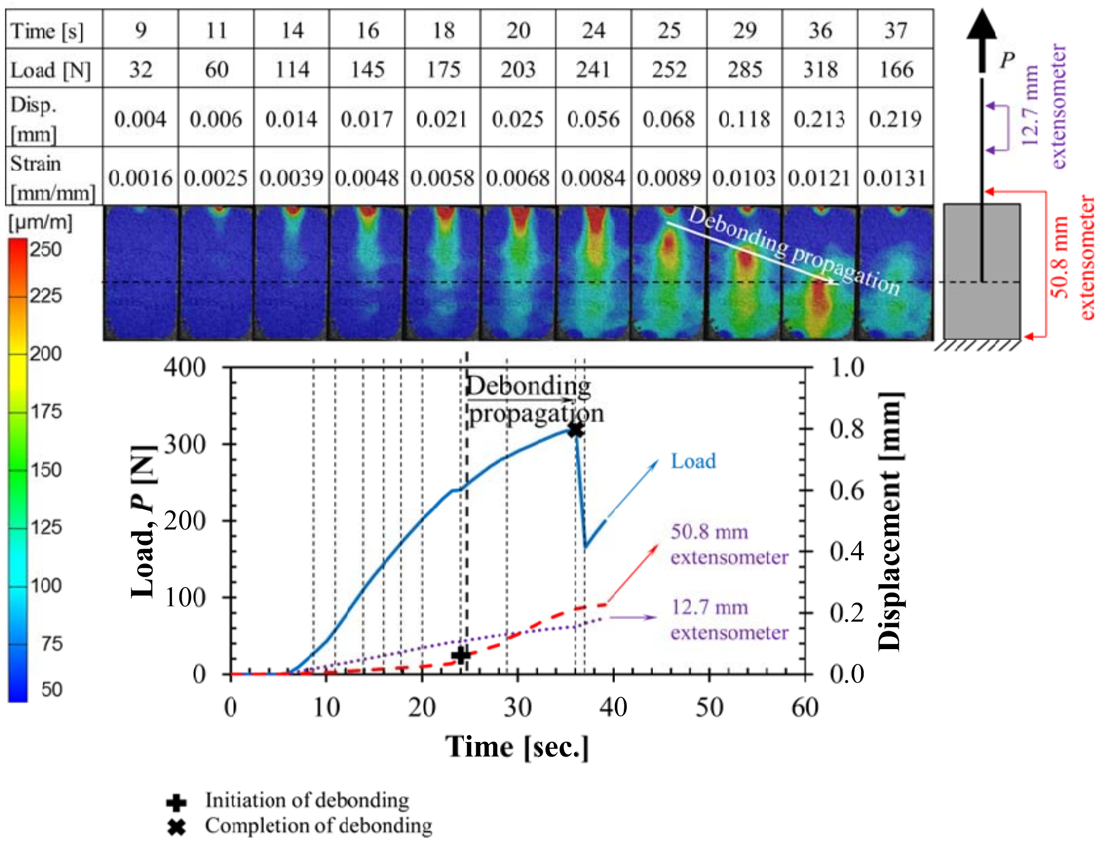

Figure 4.8. Load and displacement histories and DIC contours for a specimen with an embedment length of 25 mm and a wire diameter of 0.89 mm.

Table 4.3, Table 4.4 and Table 4.5 summarize the maximum stress, ultimate strain and maximum slip measured before failure for all of the pull-out specimens with wire diameters of 0.47 mm, 0.66 mm and 0.89 mm, respectively. The coefficient of variation is also presented in the table. The coefficient of variation of the load was less than 6% in most cases although they it was as high as 10% in specimens with embedment lengths of

51 mm and wire diameters of 0.47 mm. The coefficient of variation of the strain was less than 10% in most cases although it was as high as 11% and 20% in specimens with embedment lengths of 25 mm and 13 mm and wire diameters of 0.47 mm and 0.89 mm, respectively. The coefficient of variation of the slip was less than 9% in most cases although they were as high as 20% and 25% in specimens with embedment lengths of 13 mm and wire diameters of 0.66 mm and 0.89 mm, respectively.

Table 4.3. Pull-out test results of NiTi Superelastic wire with diameter 0.47 mm

L_d [mm]	Test #	Failure mode	Maximum stress [MPa]	Ultimate strain [mm/mm]	Maximum slip [mm]	Median (COV[4]) Stress	Median (COV[4]) Strain	Median (COV[4]) Slip
13	1	1	475	0.069	1.45	470 (2%)	0.070 (2%)	1.72 (14%)
	2		475	0.071	1.94			
	3		460	0.069	1.78			
25	1	1	530	0.059	---[3]	520 (8%)	0.068 (11%)	0.52 (5%)
	2		475	0.070	1.84			
	3		560	0.073	1.73			
51	1	1	445	0.068	3.51	500 (10%)	0.070 (4%)	3.42 (8%)
	2		545	0.068	3.65			
	3		505	0.073	3.10			
102	1	1	---[2]	0.070	7.04	---	0.072 (3%)	7.13 (1%)
	2		---[2]	0.070	7.16			
	3		545	0.074	7.19			
127	1	1	500	0.073	8.70	505 (2%)	0.067 (9%)	8.68 (1%)
	2		513	0.061	8.66			
	3		505	0.065	8.67			

[1] Debonding after complete transformation of the wire

[2] Error in the load cell signal

[3] The 51 mm extensometer slipped

[4] Coefficient of variation = standard deviation / average x 100

Table 4.4. Pull-out test results of NiTi Superelastic wire with diameter 0.66 mm

L_d [mm]	Test #	Failure mode	Maximum stress [MPa]	Ultimate strain [mm/mm]	Maximum slip [mm]	Median (COV[5]) Stress	Median (COV[5]) Strain	Median (COV[5]) Slip
13	1	1	495	0.010	0.41	500 (4%)	0.010 (2%)	0.32 (25%)
	2		525	0.010	0.27			
	3		485	0.010	0.27			
25	1	2	550	0.076	1.16	575 (4%)	0.080 (13%)	1.29 (9%)
	2		575	0.091	1.34			
	3		600	0.072	1.37			
51	1	2	545	0.076	---[4]	540 (1%)	0.075 (1%)	2.91 (5%)
	2		545	0.075	3.01			
	3		530	0.074	2.81			
102	1	2	590	0.076	6.71	585 (2%)	0.072 (4%)	6.77 (1%)
	2		570	0.077	6.82			
	3		590	0.072	---[4]			
127	1	2	570	---[3]	---[4]	565 (3%)	0.076 (1%)	8.67 (1%)
	2		550	0.076	8.69			
	3		570	0.076	8.65			

[1] Debonding prior to transformation of the wire

[2] Debonding after complete transformation of the wire

[3] The 13 mm extensometer slipped

[4] The 51 mm extensometer slipped

[5] Coefficient of variation = standard deviation / average x 100

Table 4.5. Pull-out test results of NiTi Superelastic wire with diameter 0.89 mm

L_d [mm]	Test #	Failure mode	Maximum stress [MPa]	Ultimate strain [mm/mm]	Maximum slip [mm]	COV[5] [%] Stress	Strain	Slip
13	1	1	315	0.007	---[4]	290 (8%)	0.006 (20%)	---
	2		280	0.006	0.19			
	3		270	0.005	---[4]			
25	1	1	510	0.012	0.21	495 (3%)	0.012 (7%)	0.19 (18%)
	2		490	0.011	0.21			
	3		480	0.011	0.15			
51	1	2	535	0.071	2.68	510 (6%)	0.071 (1%)	2.46 (13%)
	2		515	0.070	---[4]			
	3		480	0.071	2.23			
102	1	2	555	0.072	4.55	560 (1%)	0.072 (1%)	4.86 (6%)
	2		560	0.072	5.11			
	3		560	0.072	4.93			
127	1	2	535	0.068	7.14	540 (2%)	0.070 (3%)	7.00 (3%)
	2		540	---[3]	---[4]			
	3		550	0.071	6.85			

[1] Debonding prior to transformation of the wire

[2] Debonding after complete transformation of the wire

[3] The 13 mm extensometer slipped

[4] The 51 mm extensometer slipped

[5] Coefficient of variation = standard deviation / average x 100

Figure 4.9 (a) and (b) show the maximum measured stress and strain in the wires, respectively, as a function of the embedment length for the three tested wire diameters. The figure also shows the measured upper plateau stress, σ_{UPS}, the strain at the onset of transformation, and the upper transformation strain of the SMA wires. Inspection of the figure indicates the presence of two critical embedment lengths, $L_{d,\sigma}$ and $L_{d,\varepsilon}$, respectively, for each of the wire diameters. The first critical length, $L_{d,\sigma}$, is the embedment length required for the wire to achieve its upper plateau stress, σ_{UPS}, and begin transformation. It can be seen in Figure 4.9(a) that $L_{d,\sigma}$ for the wires with diameters of 0.66 mm and 0.89 mm is 13 mm and 25 mm, respectively. All the specimens with wire diameters of 0.47 mm failed after complete transformation of the wire. Therefore, the first development length, $L_{d,\sigma}$ could not be identified from the tests, but should be less than 13 mm. It can be seen in the figure that increasing the embedment length of the wires beyond $L_{d,\sigma}$ did not increase the debonding load for the wires since, in these cases, the peak load was limited by the transformation stress of the wire. However, increasing the development length beyond $L_{d,\sigma}$ did increase the maximum strain that developed in the wires prior to complete debonding.

The second critical embedment length, $L_{d,\varepsilon}$, is the embedment required for the wire to achieve the complete transformation strain of the SMA. Inspection of Figure 4.9(b) indicates that the second development length, $L_{d,\varepsilon}$, for the 0.47 mm, 0.66 mm, and 0.89 mm diameter wires is 13 mm, 25 mm, and 51 mm, respectively. Increasing the development length beyond these lengths did not increase the maximum strain in the wire. For the specimens with wire diameter of 0.47 mm and 0.89 mm diameter wires the measured strain at complete transformation was less than the average value that was obtained from the individual wire tests. However, the difference was within the experimental scatter of the results and was attributed to inherent inter-specimen variability.

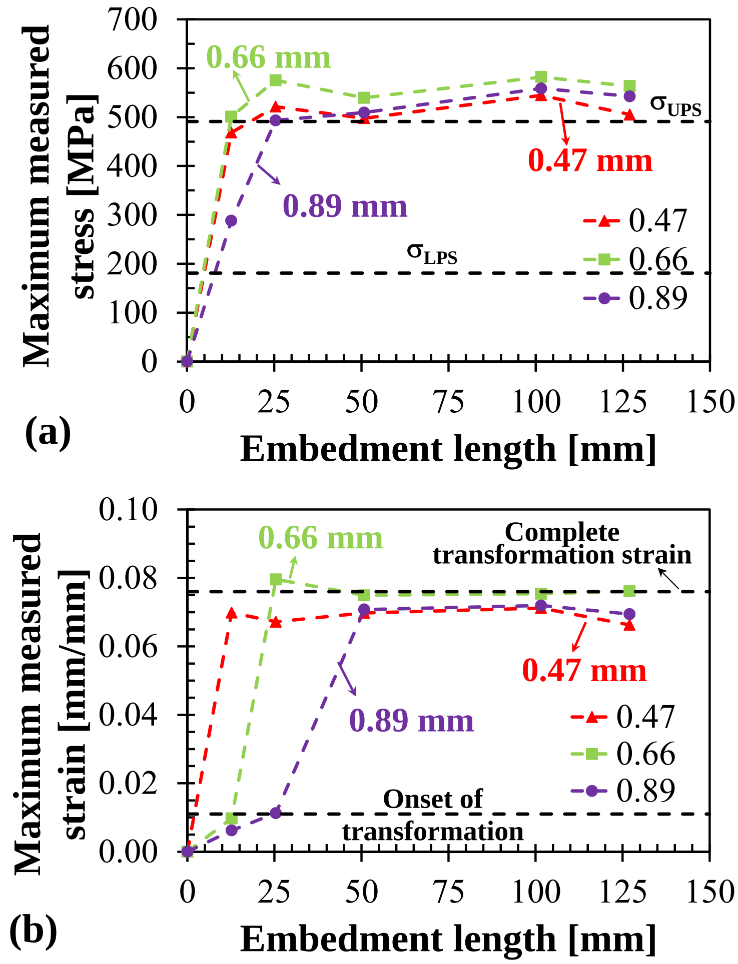

Figure 4.9. The relation between (a) Maximum measured stress versus embedment length, and (b) Maximum measured strain in the wire versus embedment length.

Figure 4.10 presents the minimum development lengths, $L_{d,\sigma}$ and $L_{d,\varepsilon}$, as a function of the square of wire diameter, d_b^2. Inspection of the figure indicates that the minimum development lengths are proportional to the square of the wire diameter, d_b^2. Based on a regression analysis, the minimum development lengths, $L_{d,\varepsilon}$, and $L_{d,\sigma}$ was found to be

$$L_{d,\varepsilon} = 64 \times d_b^2 \text{ and} \tag{4.1}$$

$$L_{d,\sigma} = 32 \times d_b^2 . \tag{4.2}$$

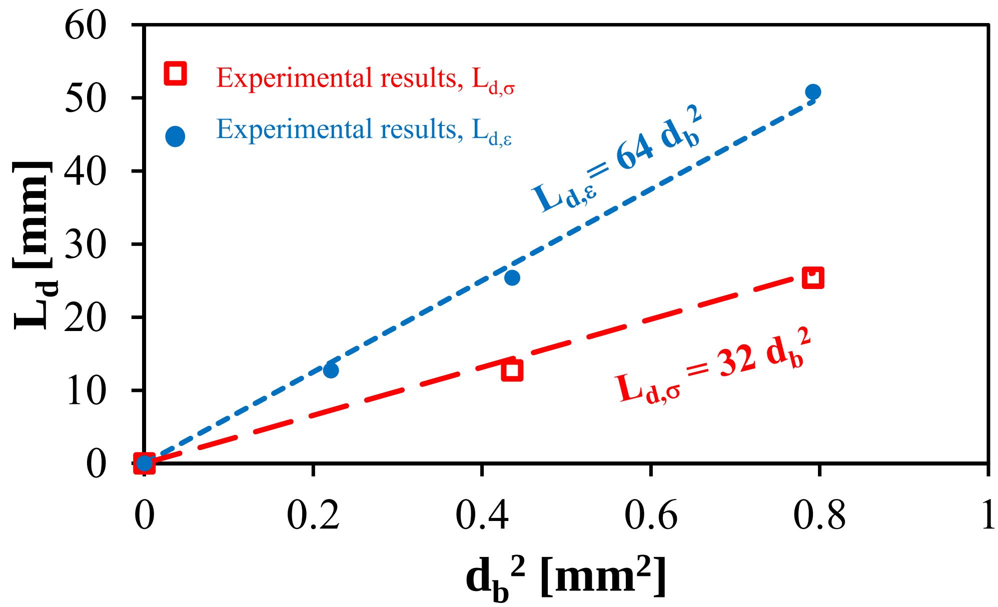

Figure 4.10. Comparison between the proposed empirical equation to predict the minimum $L_{d,\sigma}$ and $L_{d,\varepsilon}$ and the experimental results

Equation 4.2 predicts that the first development length, $L_{d,\sigma}$, for the 0.47 mm diameter wire is 7 mm. This embedment length is likely too small to verify experimentally.

4.4. Results and discussion of the pull-out specimens with NiTiNb SMA wires

All of the tested specimens failed by complete debonding of the NiTiNb SMA wires from the FRP patches. The debonded part of the wire had no epoxy bonded to it suggesting that an adhesive failure occurred at the wire-adhesive interface. The debonding was characterized by a sudden drop in the load. Table 4.6 summarizes the maximum recorded load and slip values just before complete deboning occurred for all of the tested specimens. The mean and coefficient of variation of each group are also presented in the table. The coefficient of variation of the debonding load was less than 7% in all cases except for specimens in group 1 with an embedment length of 51 mm. The coefficient of variation of the slip was less than 3% in all cases except for the specimens in group 1 with an embedment lengths of 25 mm and 51 mm.

Table 4.6. Pull-out test results of NiTiNb wires embedded in FRP composite

Group #	# of wires	FRP type	L_d [mm]	Test #	σ_{max} [MPa]	Maximum slip [mm]	Mean		COV[3] [%]	
							Stress	Slip	Stress	Slip
1	1	C[1]	25	1	555	0.38	265	0.37	2	14
				2	570	0.41				
				3	577	0.31				
			51	1	890	1.48	365	1.15	13	25
				2	750	1.05				
				3	695	0.92				
			102	1	675	1.80	330	1.78	4	2
				2	715	1.71				
				3	735	1.84				
2	3	C[1]	102	1	770	2.57	1115	2.49	7	3
				2	865	2.23				
				3	765	2.68				
3	1	G[2]	102	1	665	1.64	305	1.61	5	2
				2	610	1.58				
				3	690	1.62				

[1] CFRP

[2] GFRP

[3] Coefficient of variation= standard deviation / average x 100

Figure 4.11 shows the combined test results from the DIC and conventional measurement systems for a specimen with a single NiTiNb SMA wire embedded 25 mm into a CFRP patch. A similar trend was observed for all of the tested specimens as shown in Appendix C. Figure 4.11 presents the relationship between the applied load and the relative displacement between the SMA wire and the CFRP patch. The figure also shows the longitudinal strain contours obtained from the DIC system. Square markers on the load-displacement curve indicate the stages at which the DIC system captured each strain contour image.

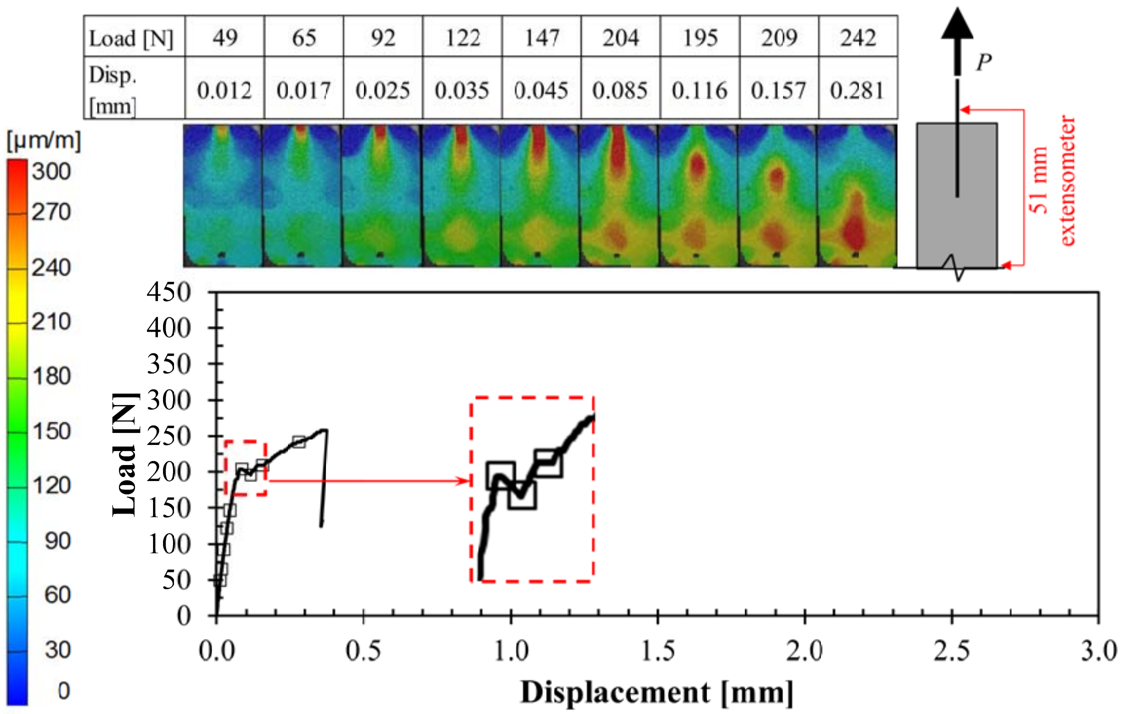

Figure 4.11. Load-relative displacement curve and DIC strain contours for pull-out specimen with a NiTiNb wire with L_d of 25 mm embedded in CFRP patch

Inspection of the strain contours indicates the presence of a localized strain concentration at the location where the SMA wire exited the FRP. As loading continued, the size and intensity of the strain concentration increased, up to a load of 204 N. After that stage a clear shift of the strain concentration away from the edge of the CFRP patch was observed. This indicates the initiation of observable debonding of the wire. The debonding propagated along the embedment length of the SMA wire, as indicated by the shift of the location of this strain concentration. The load-displacement relationship indicates that response was linear until debonding initiated at a load of 204 N, after which the applied load decreased slightly as the displacement increased. This is consistent with the DIC observation of debonding. Loading the specimen after the onset of debonding resulted in an increase in the load until failure occurred at a load of 260 N and relative displacement of 0.38 mm. The increasing load after debonding suggested that the force transferred through the bond is transferred through cohesion before the initiation of debonding and friction after debonding.

4.4.1. Effect of embedment length

Figure 4.12 shows the load versus the relative displacement between the NiTiNb wire and the CFRP for the specimens in group 1 with embedment lengths of 25 mm, 51 mm and 102 mm. The figure indicates that all the specimens tested in this group exhibited a similar behavior. The specimens initially exhibited a linear response before the initiation of debonding. After debonding initiated the specimens exhibited a hardening response during which the load continued to increase until failure occurred. The increasing load after the initiation of debonding suggested that the force transferred across the wire-adhesive interface was transferred through cohesion before the initiation of debonding and friction after debonding.

It should be noted that the specimens with L_d = 51 mm had the highest scatter in both the load and relative displacement at complete debonding. Moreover, the failure load for those specimens was higher than the failure load for specimens with L_d of 102 mm.

This increase in the failure load may have been due to the curvature of the embedded portion of the wire due to fabrication errors. The curvature induced interlocking component to the bond strength which increased the complete failure load. This suggests that the fabrication method requires modification to ensure the straightness of embedded portion of the wire.

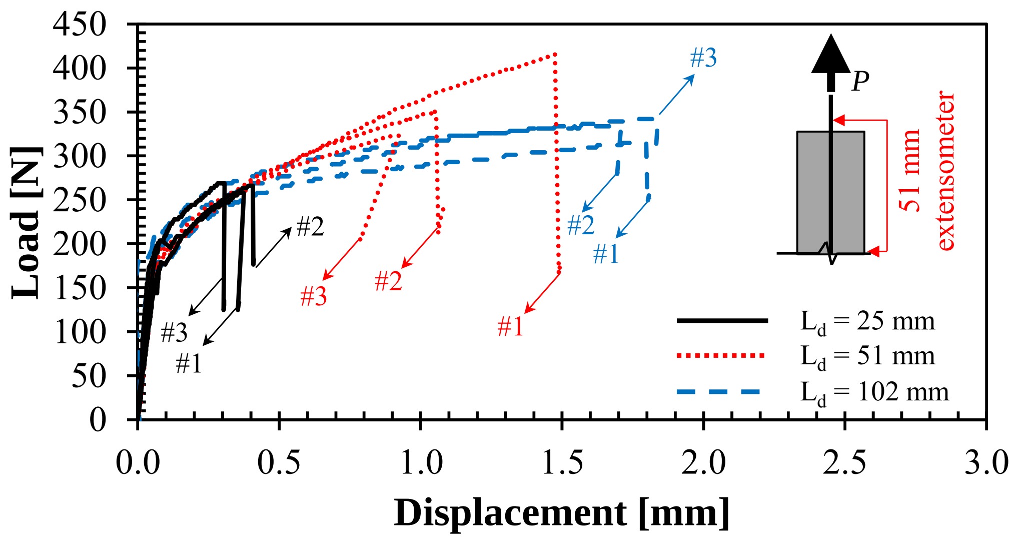

Figure 4.12. Load versus relative displacement for all pull-out specimens tested in Group 1 with NiTiNb embedded in CFRP

4.4.2. Effect of multiple NiTiNb wires

Specimens of the second group consisted of three NiTiNb wires spaced at 0.89 mm that were embedded in CFRP with an embedment length of 102 mm. The specimens in the second group were tested to examine the possible interaction between the adjacent wires. No special precautions were taken to grip the wires as the diameter of the wires were small. Figure 4.13 shows the load (per wire) versus relative displacement for the specimens with 3 wires. The responses of similar specimens with a single embedded NiTiNb wire and the same embedment length are also plotted for comparison purposes. Inspection of the figure indicates that the specimens with a single NiTiNb wire and those with three NiTiNb wire exhibit similar responses and failure loads. This suggests that a wire spacing of 0.89 mm, or 1.2 times the wire diameter, is sufficient to prevent any adverse interactions between the wires.

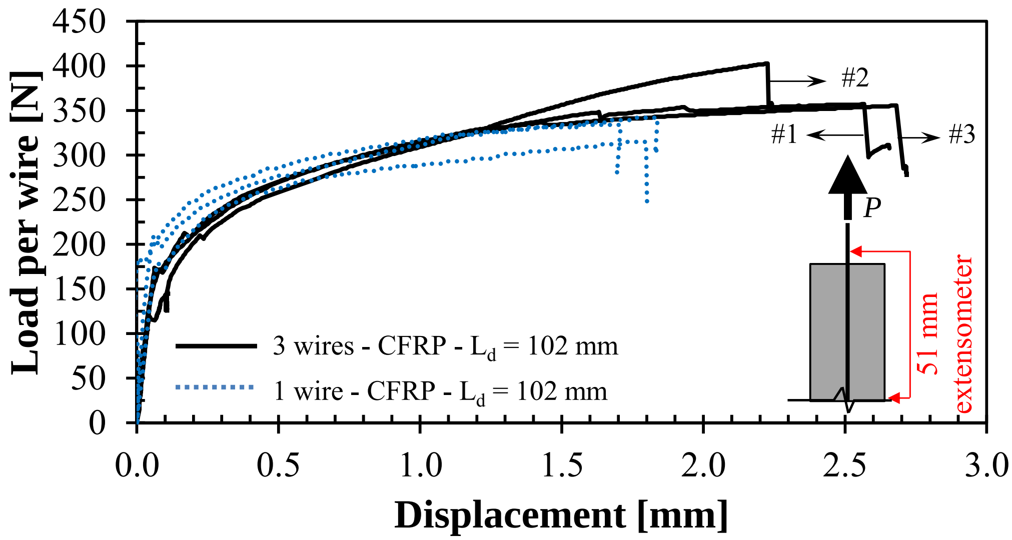

Figure 4.13. Comparison between load-displacement responses of pull-out specimens with 1 NiTiNb wire with L_d of 102 mm versus 3 NiTiNb wires with L_d of 102 mm embedded in CFRP patch

4.4.3. Effect of FRP Type

In the third group of specimens a single NiTiNb wire was embedded in a GFRP patch to examine the effect of the FRP type on the pull-out behavior. Figure 4.14 illustrates the effect of the FRP type on the load-displacement response of pull-out specimens with a single NiTiNb wire embedded in CFRP and GFRP and a 102 mm embedment length. It can be seen in the figure that the specimens with SMA wires embedded in GFRP exhibited a similar behavior to the specimens with CFRP. However, complete debonding for specimens with wires embedded in GFRP occurred when the load dropped by 4%, after the drop the load remained constant while the wire is pulled out.

Visual inspection of the translucent GFRP specimen confirmed that the wire was completely pulled out as seen in Figure 4.15. Inspection of the Figure 4.14 indicates that the maximum stress achieved in NiTiNb wires embedded in GFRP patches was 8% lower than that for NiTiNb wires embedded in CFRP patches. This is within the experimental scatter, hence, there no evidence that the pull-out behavior depends on the FRP type.

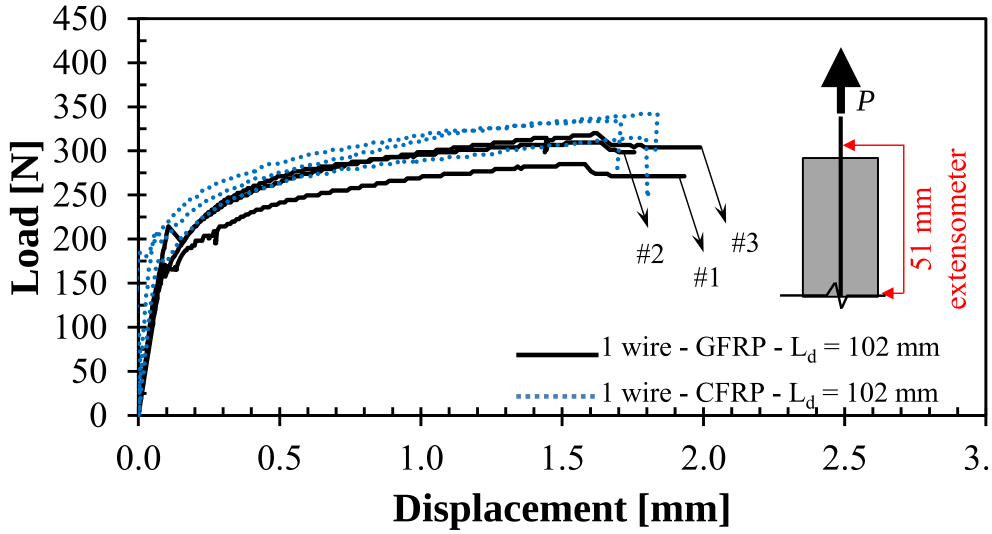

Figure 4.14. Comparison between load-displacement responses of pull-out specimens with 1 NiTiNb wire with L_d of 102 mm embedded in GFRP versus CFRP

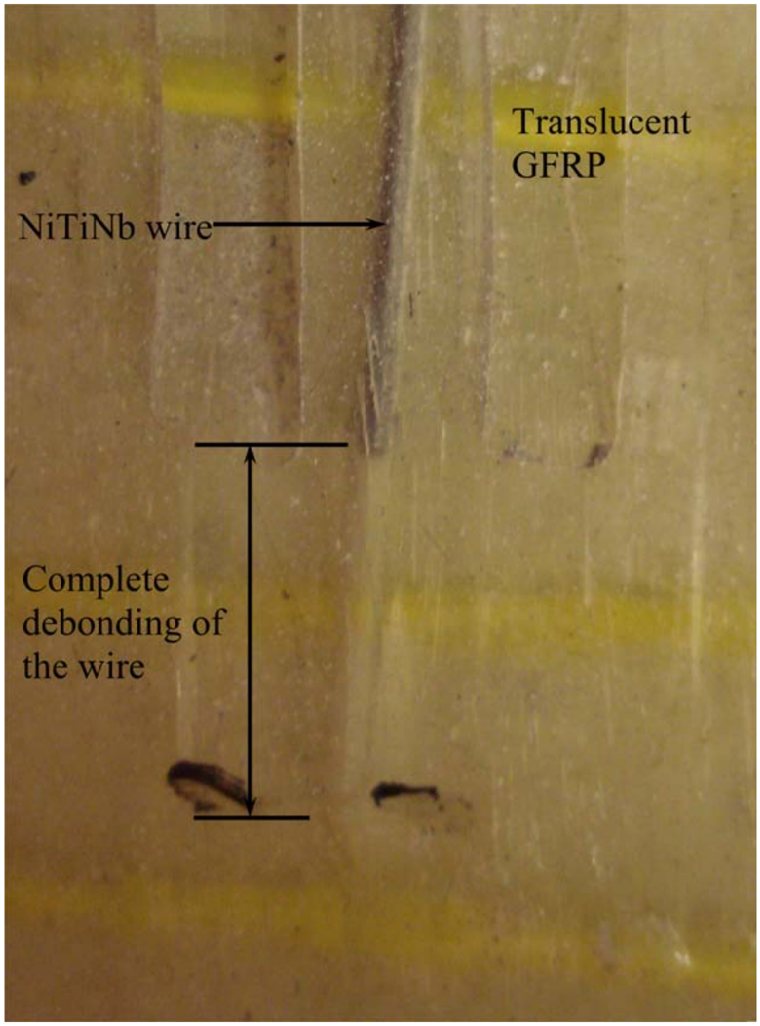

Figure 4.15. Complete debonding of the pull-out specimen with NiTiNb wire embedded in GFRP composite

Figure 4.16 shows the maximum measured wire stress as a function of the embedment length of the wires for the tested pull-out specimens embedded in CFRP. Each point on the figure represents the average of the maximum measured wire stress at the time of complete debonding for three similar samples. The error bars in the figure indicate the range of the measured results. The onset of debonding is also indicated in the figure for each group of pull-out specimens. It can be seen in Figure 4.16 that the average stress at the onset of debonding is 400 MPa for all of the tested specimens. The stress at the onset of debonding does not depend on either the embedment length or the number of wires. However, increasing the embedment length increased the load at complete debonding. This suggests that the interface strength is composed of two components: cohesion (before the onset of debonding) and friction (after the onset of debonding). The cohesion component does not increase by increasing the embedded length. However, the frictional component depends on unbonded length.

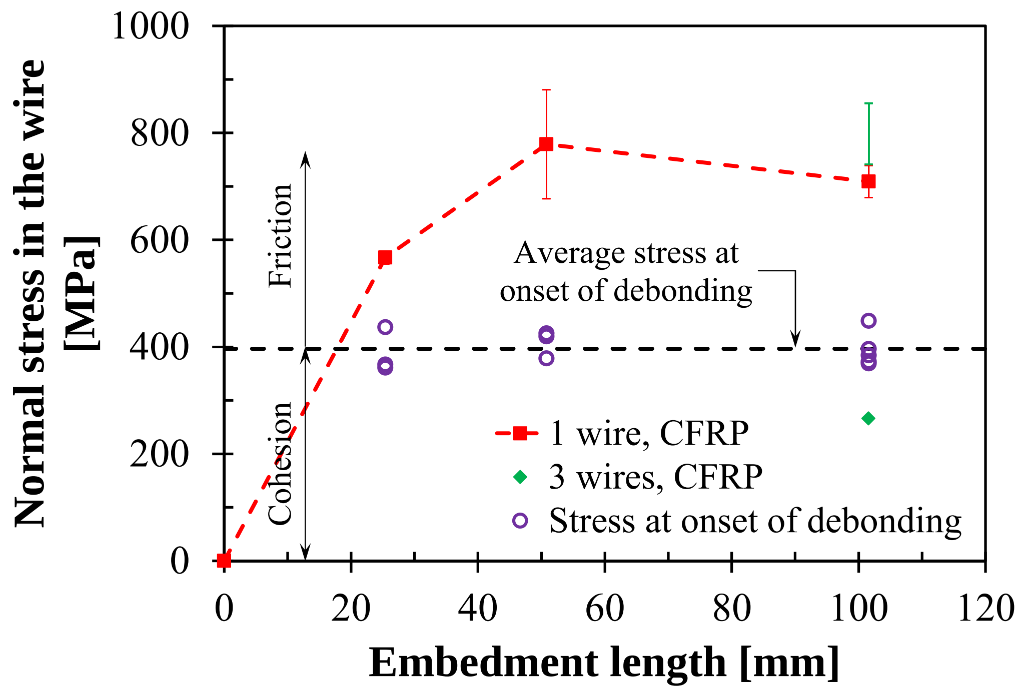

Figure 4.16. Maximum measured stress per wire versus embedment length for all pull-out specimens

The pull-out behavior during activation of the exposed part of the wire is expected to be similar to those pulled to failure as the bonded part in both cases remain not activated.

Chapter 5: Finite Element Analysis of Pull-out Specimens with NiTiNb SMA Wires Embedded in CFRP

A 3-D nonlinear finite element analysis (FEA) was conducted using the commercial software package ABAQUS v6.12 to investigate the debonding mechanism of a NiTiNb SMA wire embedded in CFRP fabricated with Araldite adhesive. The results obtained experimentally for pull-out specimens with L_d of 25 mm were used to quantify the interface parameters. The FEA results were then then validated versus the experimental results obtained from specimens with L_d of 51 mm and 102 mm. The same procedure used in this bond study can be used to model the pull-out behavior when other combination of SMA and adhesive are used.

5.1. Description of the 3-D finite element model

Figure 5.1 illustrates the geometry and boundary conditions of the finite element (FE) model. The model consisted of the NiTiNb SMA wire, the CFRP patch, and the interfacial region. Symmetry boundary conditions were applied and one quarter of the specimen was modeled. A displacement of 5 mm, 7 mm and 10 mm was applied at the tip of the SMA wire for models with embedment lengths of 25 mm, 51 mm and 102 mm, respectively. Both the NiTiNb wire and the CFRP were meshed using 8-node continuum elements (element C3D8R) with three translational degrees of freedom at each node, linear shape functions, reduced integration and hourglass control. The mesh size was chosen similar to what was presented in Dawood et al. (2015). The auto mesh feature of the software was used to mesh the model. The NiTiNb wire was meshed to 480, 960 and 1440 elements along the length for the models with embedment lengths of 25 mm, 52 mm and 102 mm, respectively. Three elements through the diameter of the wire were used. The CFRP part close to the interface was meshed to a number of elements of 80 times the embedment length, while it was meshed away from the interface and at the free end of the patch to a number of elements of 20 times the embedment length. The CFRP patch was meshed to two elements through the thickness. The total number of elements for the models with L_d of 25 mm, 51 and 102 mm was 5600, 10060 and 35470, respectively.

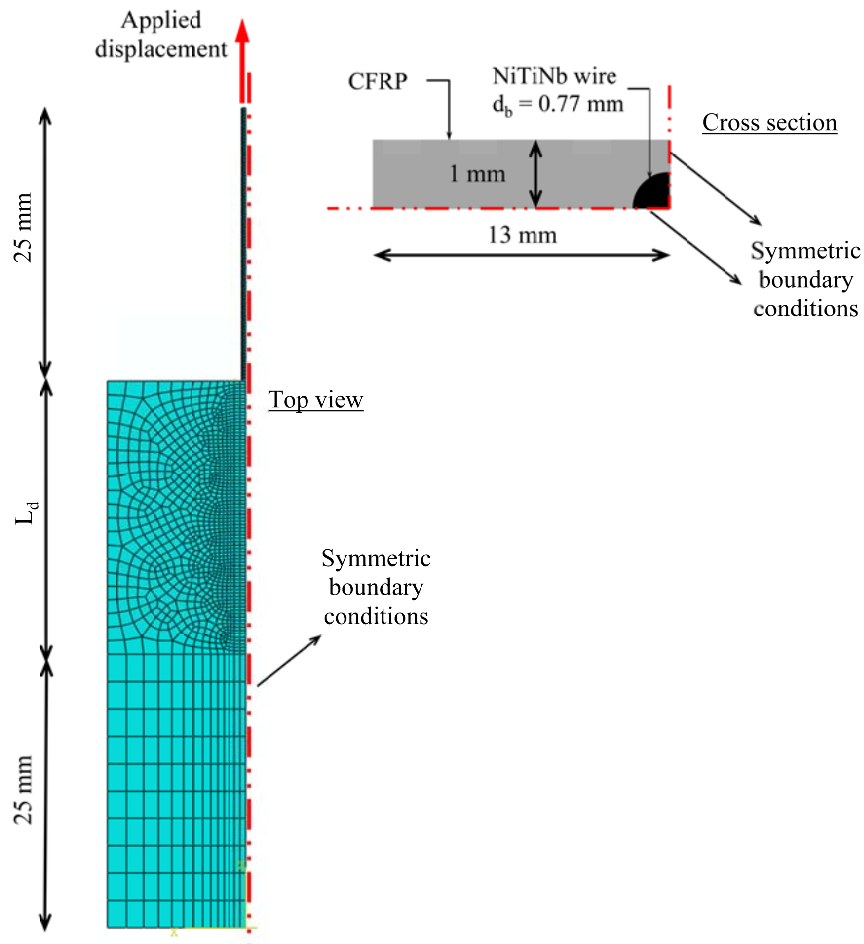

Figure 5.1. FE model details: (a) Boundary conditions and load, (b) Mesh details showing the number of elements used in the model

The NiTiNb SMA wire was modelled as linear elastic with tensile modulus of 45,770 MPa and poisons ration of 0.3 up to a stress of 200 MPa. After that point the material was modeled with hardening which was defined in the form of a table using the stress and plastic strains obtained from the experiments in section 3.2.1.c. Figure 5.2 compares the stress-strain curve obtained from the FE model to the stress-strains obtained experimentally.

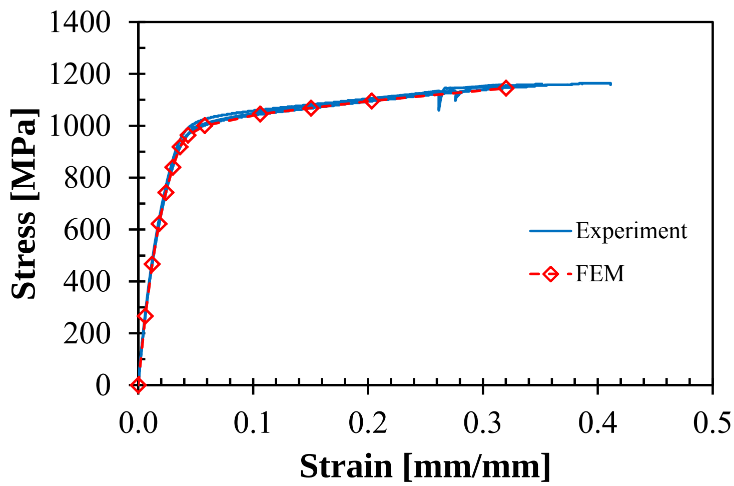

Figure 5.2. Stress-strain curve for the NiTiNb SMA wire obtained from the FEM with comparison to the experimental results

The CFRP material was modeled as a transverse isotropic, elastic material with five independent elastic constants: longitudinal modulus (E_1) of 86.6 GPa, transverse moduli ($E_2 = E_3$) of 4.98 GPa, shear moduli in the transverse plane ($G_{12} = G_{13}$) of 1.82 GPa, and Poisson's ratios ($\nu_{12} = \nu_{13}$, and ν_{23}) of 0.3, and 0.3, respectively. E_1 was determined experimentally by testing a trimmed part of the pull-out specimen in uniaxial tension according to ASTM D3039 (ASTM international, 2014). The tensile modulus of the fibers E_f was obtained from the manufacturer data sheet while the tensile modulus of the epoxy, E_m, was determined experimentally according to ASTM D638 (ASTM international, 2014) as described in chapter 3. Knowing E_1, E_f, and E_m the fiber volume fraction, v_f, and E_2 were calculated using the rule of mixtures (Jones, 1999) as

$$E_1 = E_f\, v_f + E_m\,(1\text{-}v_f) \text{ and} \tag{5.1}$$

$$\frac{1}{E_2} = \frac{v_f}{E_f} + \frac{(1 - v_f)}{E_m}. \tag{5.2}$$

Assuming $\nu_f = \nu_m = \nu_{12} = 0.3$, the remaining parameters required to define the mechanical properties of the FRP were calculated as

$$G_f = \frac{E_f}{2(1 + \nu_f)}, \tag{5.3}$$

$$G_m = \frac{E_m}{2(1 + \nu_m)}, \tag{5.4}$$

$$G_{23} = \frac{E_2}{2(1 + \nu_{23})}, \tag{5.5}$$

$$\frac{\nu_{12}}{E_1} = \frac{\nu_{21}}{E_2}, \tag{5.6}$$

$$\frac{\nu_{13}}{E_1} = \frac{\nu_{31}}{E3}, \tag{5.7}$$

$$\frac{\nu_{23}}{E_2} = \frac{\nu_{32}}{E_3}, \text{ and} \tag{5.8}$$

$$\frac{1}{G_{12}} = \frac{v_f}{G_f} + \frac{(1 - v_f)}{G_m}. \tag{5.9}$$

Full Newton technique was used with unsymmetrical matrix storage option to improve the convergence rate of the equilibrium iterations (Dassault Systèmes Simulia Corp., 2012). An initial step size was selected corresponding to a displacement at the tip of the SMA wire of 0.005 mm per step. The step size was automatically subdivided up to 1000 times until convergence was reached in each step. Complete debonding was reached between 30 to 95 steps.

The computations were conducted using the Maxwell cluster available by the Center for Advanced Computing and Data Systems at the University of Houston. The cluster has a total of 3712 cores (114 – 8 GB, 4 cores AMD 2.2 GHz; 125 – 16 GB, 8 cores AMD 2.2 GHz; 4 – 64 GB, 32 cores AMD 2.3 GHz; 28 – 64 GB, 32 cores AMD 2.2 GHz; 4 – 128 GB, 32 cores AMD 2.2 GHz; and 2 – 512 GB, 64 cores AMD 2.2 GHz). The FEM with embedment lengths of 51 mm and 102 mm were run on a desktop computer (4 GB, 4 core Intel i5 3.20 Ghz). The computation time on the desktop computer was 20 minutes and 90 minutes for the models with embedment length of 51 mm and 102 mm, respectively.

5.2. Cohesive Zone Model

In this research the traction-separation behavior of the CZM was defined by a linear elastic behavior followed by damage initiation and evolution (Dassault Systèmes Simulia Corp., 2012) as

$$\tau = \begin{Bmatrix} \sigma_n \\ \tau_1 \\ \tau_2 \end{Bmatrix} = \begin{bmatrix} k_{nn} & k_{n1} & k_{n2} \\ k_{n1} & k_{11} & k_{12} \\ k_{n2} & k_{12} & k_{22} \end{bmatrix} \begin{Bmatrix} \delta_n \\ \delta_1 \\ \delta_2 \end{Bmatrix} = k\delta, \tag{5.10}$$

where τ is the nominal traction stress which consisted of three components: σ_n the normal traction, τ_1 the traction along the length of the interface and τ_2 the tangential traction. The corresponding separations are δ_n, δ_1 and δ_2. The normal and tangential tractions are not coupled in this study (k_{ij} = zero, where $i \neq j$). The normal and tangential separations were assumed to be negligible compared to the separation along the interface based on the nature of the applied loading and the geometry of the specimen. Hence the traction-separation law reduced to

$$\tau_1 = k_{11}\, \delta_1 . \tag{5.11}$$

In the following discussion the subscripts in the notation have been eliminated unless necessary for clarity. A maximum nominal stress criterion was used in which the damage initiated when the tangential shear stress τ exceeds a critical value τ_{max}. A scalar damage variable, D, was introduced to represent the load induced damage of the interface. The value of D ranges from initially 0 for undamaged interface to 1 when the interface is completely damaged. Hence the traction-separation law reduced to

$$\tau = \begin{cases} (1-D)\,\tau_e , & \text{when } \tau > \tau_{max} (\text{damage criterion is met}) \\ \tau_e , & \text{otherwise} \end{cases} \tag{5.12}$$

where τ_e is the interfacial shear stress predicted by the elastic traction separation law defined as

$$\tau_e = k\, \delta . \tag{5.13}$$

The traction-separation relationship that describes the CZM behavior used to model the interface in this study is shown in Figure 5.3. The CZM shown in the figure consists of two parts: elastic behavior when the damage criterion is not met, and bilinear damage evolution which otherwise. The CZM model was defined using six parameters: the initial interface stiffness, k, the interfacial shear strength, τ_{max}. The bilinear damage evolution was defined by two points (τ_1, δ_1) and (τ_2, δ_2) in terms of the corresponding slip, δ, and damage parameter, D, as shown in Figure 5.3.

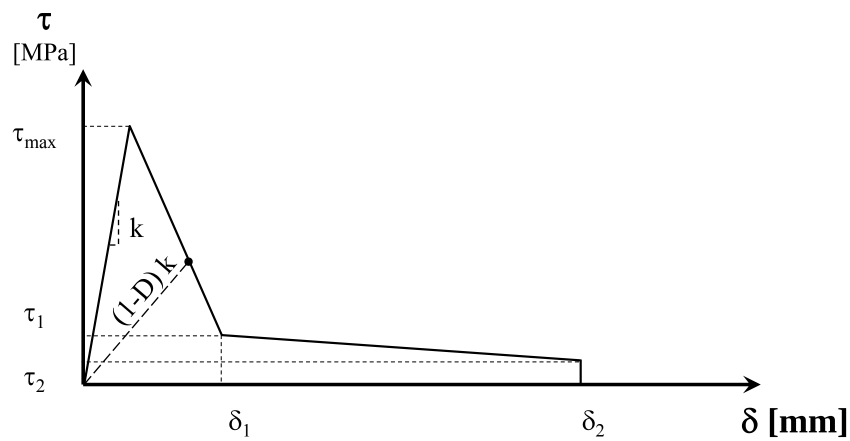

Figure 5.3. Cohesive zone model (CZM) used to model the wire-adhesive interface

A bilinear damage evolution was used rather than the classical linear evolution model to take into account the cohesive and friction components of the post bond initiation behavior. It can be seen in Figure 4.11 that the pull-out specimens exhibited a hardening behavior after the initiation of debonding. This suggests a non-negligible contribution from a load transfer mechanism at the interface other than by cohesion alone. The proposed CZM can be conceptualized as representing a friction contribution at the interface along the debonded portion of the wire. In the proposed model, the friction component is allowed to degrade as the slip increases. This can be attributed to abrasion of the relatively soft composite due to pulling out of the SMA wire.

The elastic part of the CZM was defined in ABAQUS as mechanical cohesive behavior with an interface stiffness of 1000 MPa/mm. Damage criterion with a maximum nominal stress of 15 MPa was defined in the program. Once the damage criterion was met and the evolution was defined with the damage coefficient, D, and the corresponding plastic displacement in a table format. Ten points were used to define each line of the bilinear damage evolutions.

5.3. Quantification of the parameters of the CZM

A sensitivity analysis was carried out to calibrate the CZM parameters of a specimen with L_d of 25 mm and a wire diameter of 0.77 mm. Once the parameters were identified, the model was verified by comparison with experimental results for pull-out specimens with L_d of 51 mm and 102 mm.

The value of each of the six parameters of CZM were determined independently from the other five parameters; that is, interdependencies between the parameters were neglected. Thus, six groups of FE models, summarized in Table 5.1, were considered to quantify each of the six parameters of the CZM. The values given in the table were selected based on a series of preliminary analyses to determine the expected range of parameters. In group 1 the CZM was modeled as linear elastic with no damage to quantify the interfacial stiffness, k, of the CZM. In this group k was varied from 200 MPa/mm to 1250 MPa/mm. In group 2, τ_{max} was varied from 10 MPa to 20 MPa while k, τ_1 , τ_2 , δ_1 and δ_2 were fixed at 1000 MPa/mm, 2.5 MPa, 1.0 MPa, 0.04 mm and 0.4 mm, respectively. Similarly, FEA were carried out in groups 3, 4, 5 and 6 to quantify τ_1 , τ_2 , δ_1 and δ_2, respectively as summarized in Table 5.1.

Table 5.1. Ranges of values considered to quantify the CZM parameters

Group	k [MPa/mm]	τ_{max} [MPa]	τ_1 [MPa]	τ_2 [MPa]	δ_1 [mm]	δ_2 [mm]
1	200, 400, 500, 1000, 1250	--	--	--	--	--
2	1000	10, 12.5, 15, 17.5, 20	2.5	1.0	0.04	0.4
3	1000	15	1, 1.5, 2.0, 2.5, 3.0	1.0	0.04	0.4
4	1000	15	2.0	0.5, 1.0, 1.5, 2.0	0.04	0.4
5	1000	15	2.0	1.0	0.02, 0.03, 0.04, 0.05, 0.06	0.4
6	1000	15	2.0	1.0	0.04	0.2, 0.3, 0.4, 0.5, 0.6

Figure 5.4 shows the load-displacement relationships that were obtained from the FEA for different values of the CZM elastic stiffness, k. The experimental results for three similar specimens with 25 mm embedment lengths are also plotted for comparison purposes. A root square error (RSE) method was used to determine the k that best fit the experimental results. The RSE was calculated as

$$\mathrm{RSE} = \sqrt{(K_{exp,AVG} - K_{FEA})^2}\,, \qquad (5.14)$$

where $K_{exp,AVG}$ is the average pull-out stiffness obtained experimentally from all the pull-out specimens, while K_{FEA} is the pull-out stiffness predicted by FEA.

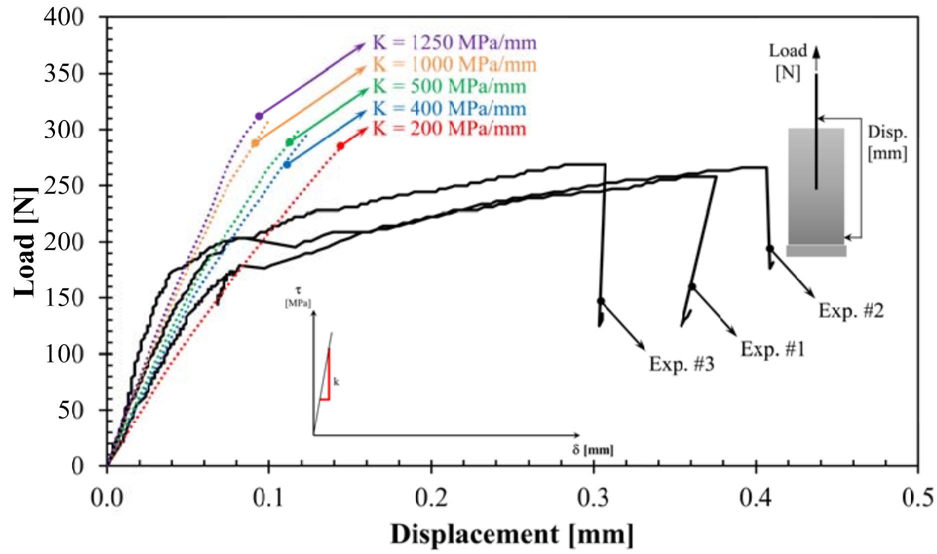

Figure 5.4. Calibration of the interface stiffness, k, based on the comparison between the predicted and the experimental results.

Figure 5.5 shows the effect of varying the CZM elastic stiffness, k, on the RSE. Among the values considered in this study, a CZM stiffness of 1000 MPa/mm minimized the RSE. Therefore, this value was chosen to represent the interface stiffness. It should be noted that all of the FEA predictions of stiffness are within the experimental scatter. This suggests that the uncertainty in the experimental data is greater than that associated with the interface stiffness k of the CZM.

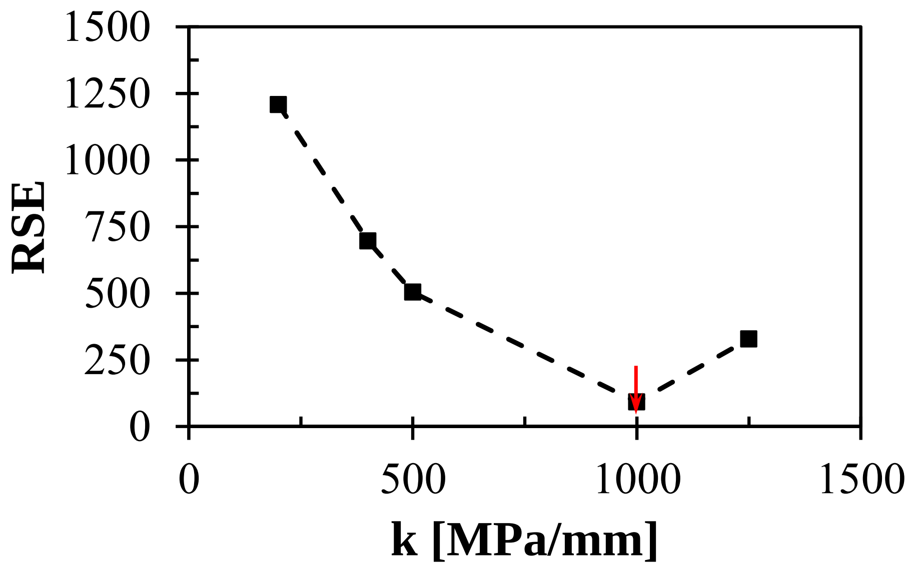

Figure 5.5. The RSE of the FEA observed by varying k.

Figure 5.6 shows the effect of varying the interfacial shear strength, τ_{max}, on the load-displacement relationship of the pull-out specimens. The load-displacement relationships obtained experimentally are also shown for comparison purposes. It can be seen in the figure that the response was initially linear until debonding initiated after which the model predicted a hardening behavior until complete pull-out of the wire occurred. Inspection of the figure indicates that the predicted response was similar to that exhibited experimentally. This suggests that the CZM model with a bilinear damage evolution is suitable and can capture the frictional component of the pull-out behavior. Inspection of Figure 5.6 reveals that by increasing τ_{max} the load at the initiation of debonding, the ultimate load and ultimate slip increased.

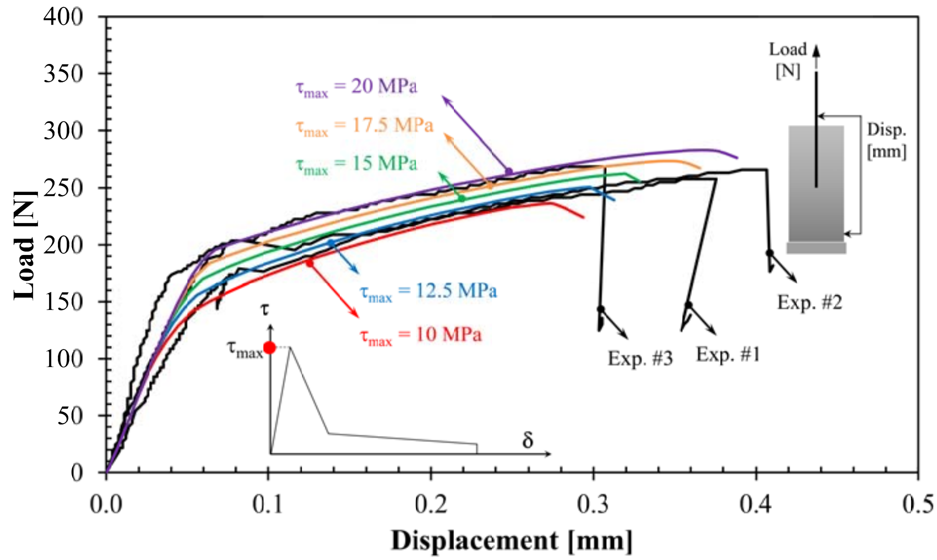

Figure 5.6. Calibration of the maximum shear stress, τ_{max}, based on the comparison between the predicted and the experimental results.

A root mean square error (RMSE) method was used to determine the value of τ_{max} that best fit the experimental results. The RMSE was calculated as

$$\mathrm{RMSE} = \sqrt{\frac{\sum_{i=1}^{n} (P_{exp} - P_{FEA})^2}{n}} \,, \tag{5.15}$$

where P_{exp} and P_{FEA} are the loads obtained from experiments and FEA, respectively, at a given value of the displacement, and n is the number of points (in the range of 28 to 48) for which the RMSE was evaluated. Figure 5.7 shows the RMSE of the FEA prediction for different values of the interfacial shear strength, τ_{max}. Each point on the curve represents the average RMSE calculated based on the three experimental repetitions. Among the values considered, the value of 15 MPa for τ_{max} reached 15 MPa resulted in the lowest average RMSE and was thus selected as the interfacial shear strength.

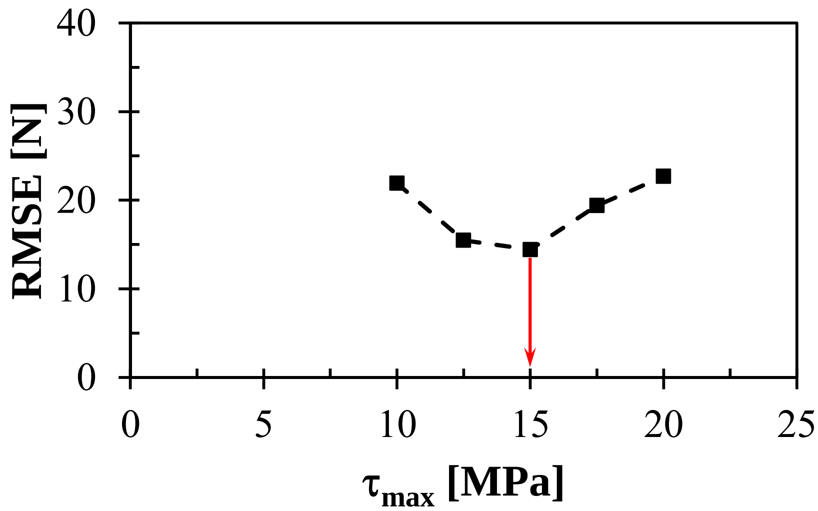

Figure 5.7. The effect of varying τ_{max} on the RMSE calculated between the load obtained from FEA and the experimentally.

The same approach was adopted to quantify the rest of the CZM parameters. Figure 5.8(a) – (d) presents the predicted load-displacement responses while Figure 5.9(a) – (d) plots the calculated RMSE versus the experimental results for the different values of τ_1, τ_2, δ_1 and δ_2, respectively. It should be noted that the error calculation for the load was stopped at either the ultimate displacement obtained by the finite element analysis or the experimental results, whichever is smaller.

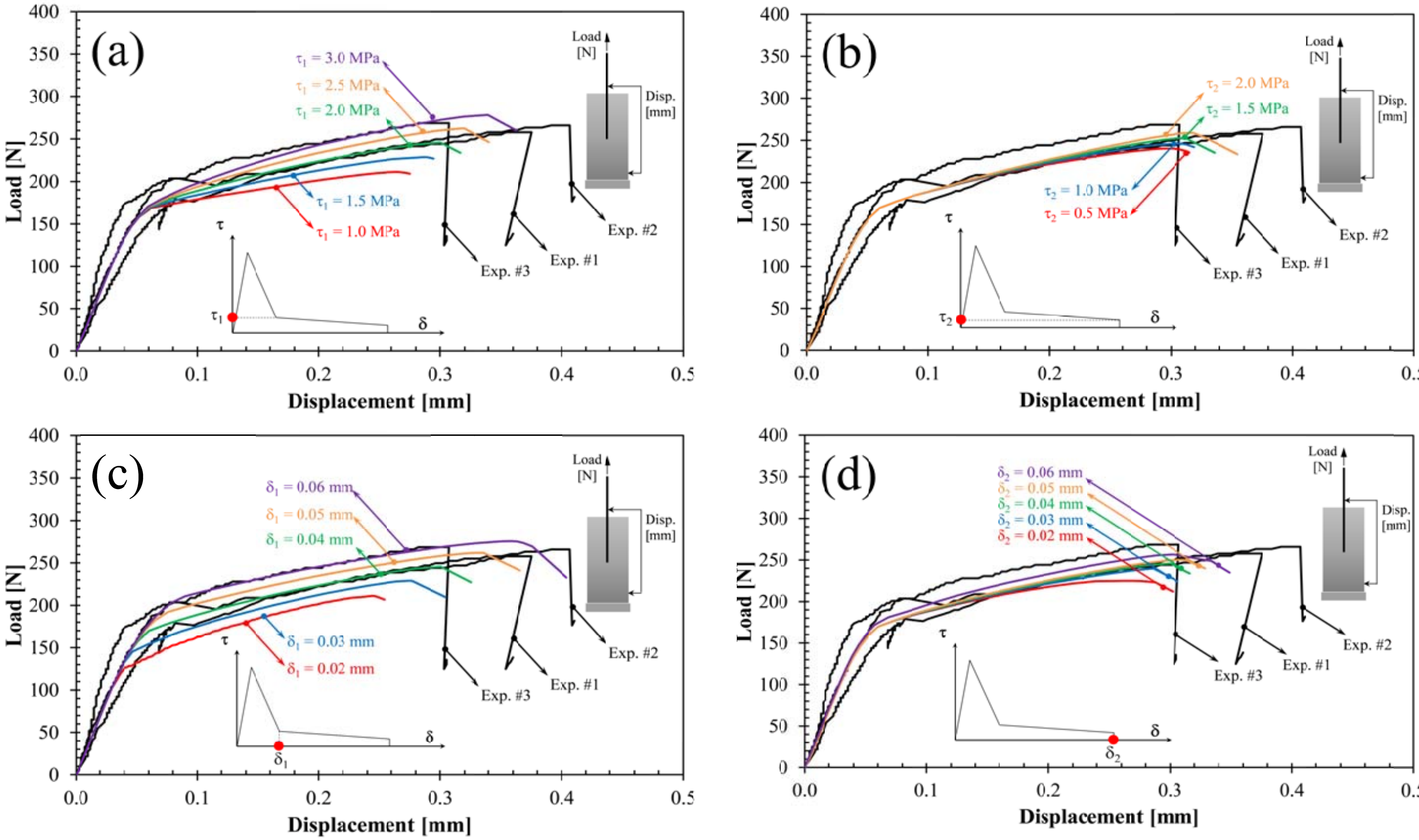

Figure 5.8. Calibration of the: (a) τ_1, (b) τ_2, (c) δ_1 and (d) δ_2 based on the comparison between the predicted and the experimental results

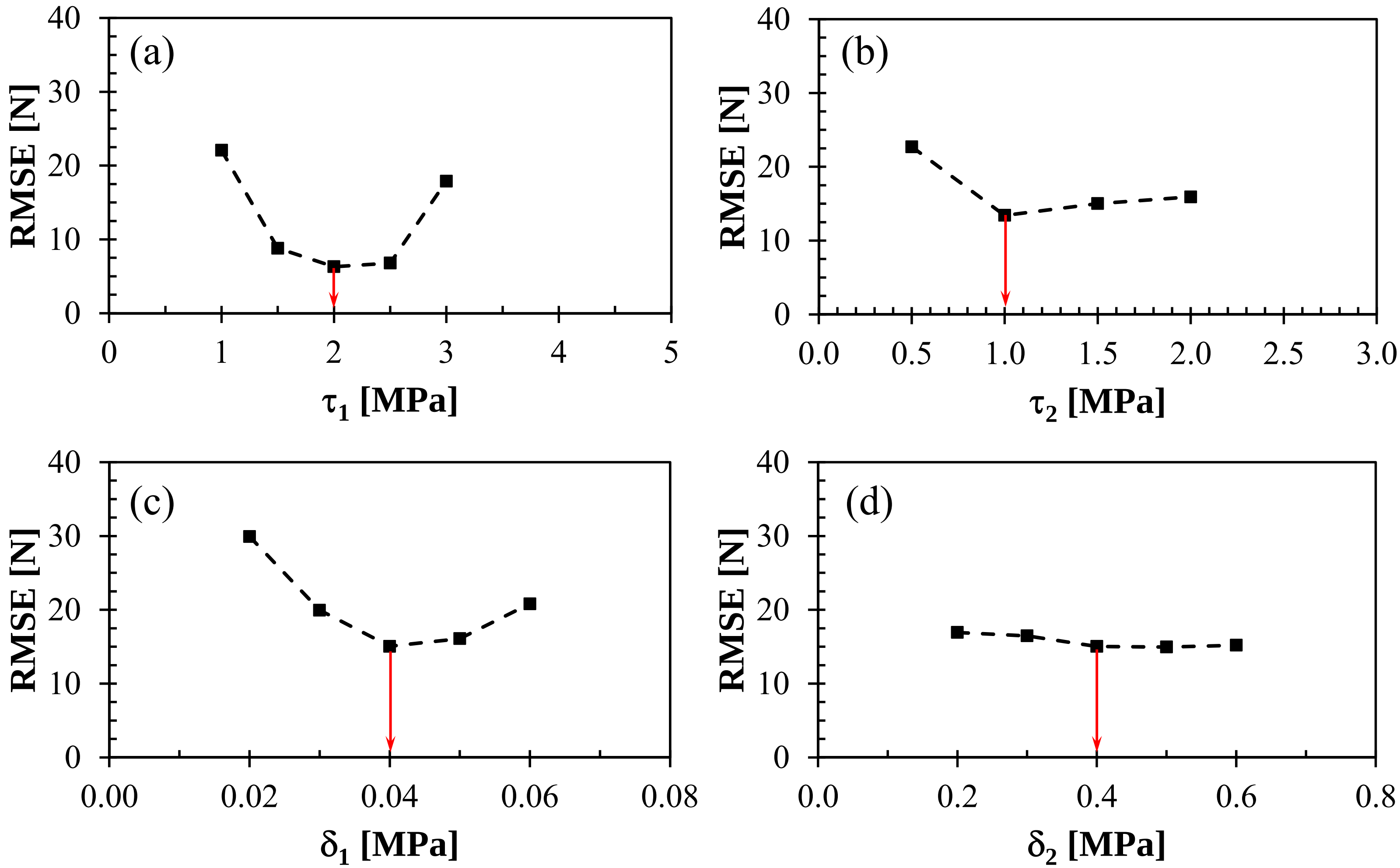

Figure 5.9. The RMSE values with varying: (a) τ_1, (b) τ_2, (c) δ_1 and (d) δ_1

It can be seen in Figure 5.8(a) that increasing τ_1 increases the pull-out stiffness after the onset of debonding. A value of τ_1 of 1.0 MPa under predicted the ultimate load by 16% while a value of 3.0 MPa over predicted the ultimate load by 6%. Figure 5.9(a) plots the RMSE calculated for the different values of τ_1. Among the values considered, the value of 2.0 MPa for τ_1 resulted in the lowest average RMSE and was thus selected. Inspection of Figure 5.8(b) indicates that changing τ_2 had a smaller effect on the load-displacement response than when varying τ_1. When τ_2 equals to 1.0 the RMSE is minimal according to Figure 5.9(b). Among the values considered, the value of 1.0 MPa for τ_2 resulted in the lowest average RMSE and was thus selected.

Inspection of Figure 5.8(c) indicates that increasing the value of δ_1 increased the load at which the debonding initiated. This is expected as the point ($\tau_{1,}$ δ_1) on the traction-separation relationship defines the interface toughness, G, at which complete damage of the cohesive behavior initiates and starts to propagate. Once the debonding initiated the load-displacement curves were parallel for the different values of δ_1. Figure 5.9(c) indicates that a value of 0.04 mm for δ_1 provides the best approximation of the experimental data among the values considered. Inspection of Figure 5.8(d) shows that changing the value of δ_2 has a negligible effect on the load at which the debonding initiates, while it has a slight effect on the ultimate load. Figure 5.9(d) shows that the predicted response was relatively insensitive to the selected value of δ_2. The maximum predicted RMSE among the different values of δ_2 that were considered was 1.9 N compared to between 8 N and 15.8 N for the other parameters. However the same approach was adopted and a value of 0.4 mm was selected for δ_1. Table 5.2 summarizes selected values of the different parameters of the optimized CZM.

Table 5.2. Calibrated CZM parameters

Parameter	Calibrated value
k	1000 MPa/mm
τ_{max}	15 MPa
τ_1	2.0 MPa
τ_2	1.0 MPa
δ_1	0.04 mm
δ_2	0.4 mm

5.4. Interfacial stresses and debonding mechanism

The finite element model that was developed in this study provided the opportunity to investigate features of the SMA/CFRP debonding process that could not be observed experimentally. Specifically, the numerical simulations provided insight into the distribution of stresses at the SMA/CFRP interface. Investigation of the evolution of the stress distribution with increasing load sheds light on the importance of key features in the global load-displacement response and also the mechanisms that drive the propagation of debonding and the stress transfer at the SMA/CFRP interface. These features are discussed in this section.

Figure 5.10(a), (b) and (c) plot the load-displacement curve obtained from the FEA, the interfacial shear stress along the bond length, and the interface damage coefficient, respectively, along the SMA/CFRP bond length. Seven key points were highlighted in the Figure 5.10(a). It can be seen in Figure 5.10(a) that up to point 2 the global load-displacement response exhibited linear, elastic behavior. Loading the wire beyond point 2 resulted in a non-linearity of the global response. At point 1, which is representative of any point within the elastic region, the maximum shear stress occurred near the end of the CFRP patch where the SMA exited the CFRP and decayed rapidly along the interface. The maximum value of the shear stress was less than the interfacial shear strength. At this stage the damage parameter was equal to zero along the entire interface indicating a completely elastic response and no debonding. At point 2 the shape of the interfacial shear stress distribution was similar to that at point 1. The peak interfacial shear stress reached the interfacial shear strength, τ_{max}, of 15 MPa. Correspondingly, the damage parameter at the same point obtained a maximum value of 0.25 indicating the initiation of damage at the SMA/CFRP interface. As the applied load increased further to point 3, the peak shear stress shifted away from the end of the CFRP patch and the magnitude of the damage parameter increased. After this point the area under the cohesive portion of the shear stress distribution remained essentially constant. Beyond this stage, at points 4 and 5, the interfacial shear stress distribution exhibited distinct cohesive and frictional components indicating the onset and propagation of debonding along the interface. As the applied load increased from point 3 to point 6, the contribution of the cohesive component of the interfacial stress remained constant but propagated away from the end of the CFRP patch. Correspondingly, the area under the frictional component of the distribution continued to increase which resulted in the hardening slope of the global response. The damage parameter in Figure 5.10(c) indicates that in the debonded region the damage parameter remained essentially constant and equal to 1 and decreased to zero at the end of the cohesive region. The location where the damage parameter is equal to zero coincides with the elastic portion of the cohesive shear stress distribution at the interface. At point 6, the remaining bonded length of the SMA/CFRP interface was less than the length required to develop the complete cohesive shear stress distribution. Consequently the global response began to exhibit a softening response as shown in point 7. Beyond this stage complete debonding occurred and the finite element model indicated full debonding failure as the wire continued to slip with no corresponding load in the wire.

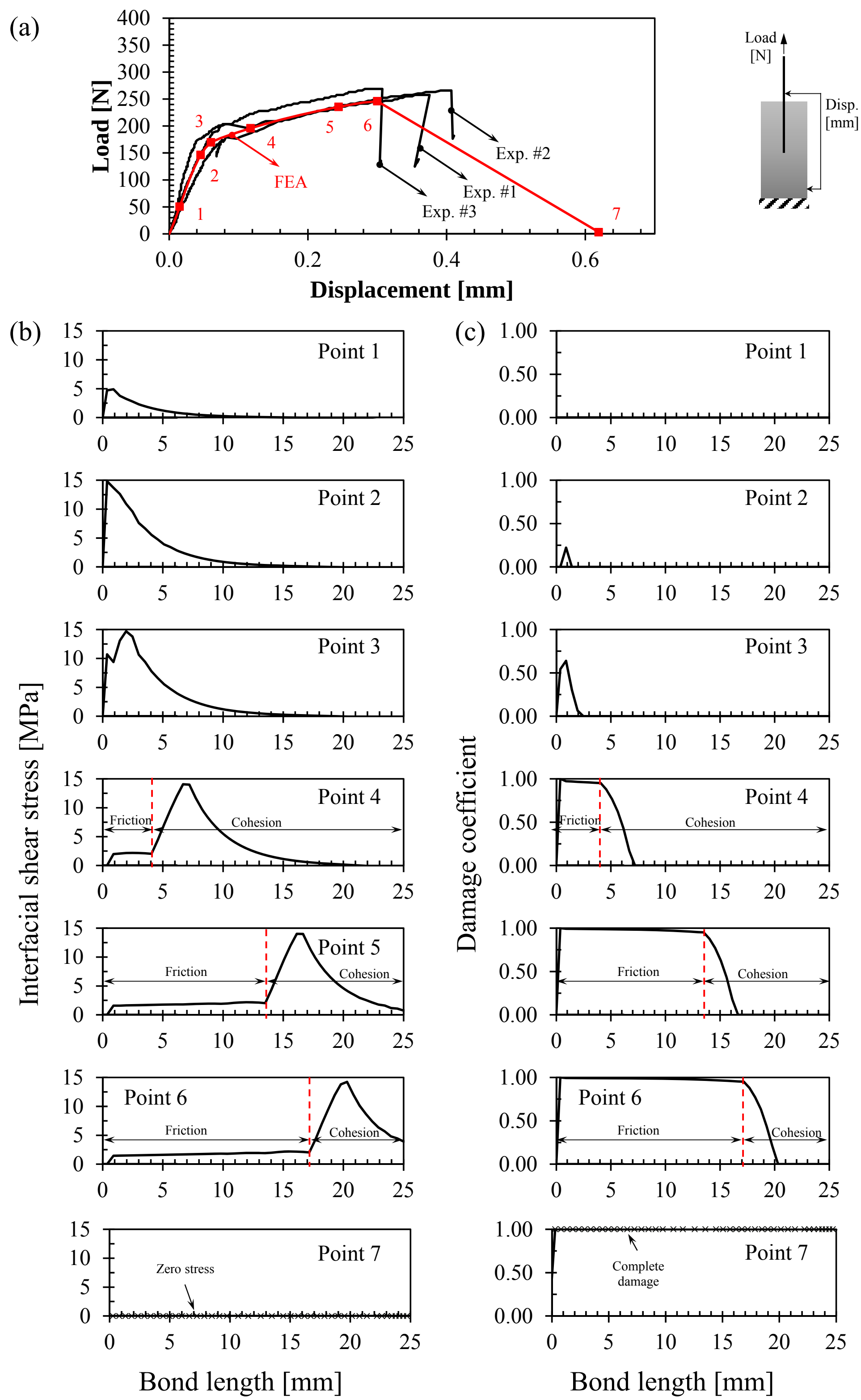

Figure 5.10. (a) Load-displacement response, (b) Interfacial shear stress distribution along the bond length, and (c) The interface damage coefficient along the bond length

5.5. Model validation

Once the parameters of the CZM were quantified, the response of the pull-out specimens with L_d of 51 mm and 102 mm were modeled. The predicted load-displacement curves were compared with those obtained experimentally to validate the FEA.

Figure 5.11 shows the predicted load-slip response compared to the experimental results for an NiTiNb SMA wire embedded in a CFRP patch with an embedment length of 51 mm. The figure also presents the results of three similar tests. Inspection of the figure indicates that the predicted response matches very well the response obtained experimentally until the load reached 275 N. beyond this point, the displacement continued to increase without any further increase in load. The figure further indicates that the experimental response did not exhibit this behavior. Comparison of the experimental and numerical results indicates that the FEA underestimated the ultimate pull-out load and slip of the interface by 24% and 35%, respectively. This was attributed to the truncation of the frictional component of the CZM as illustrated in Figure 5.12.

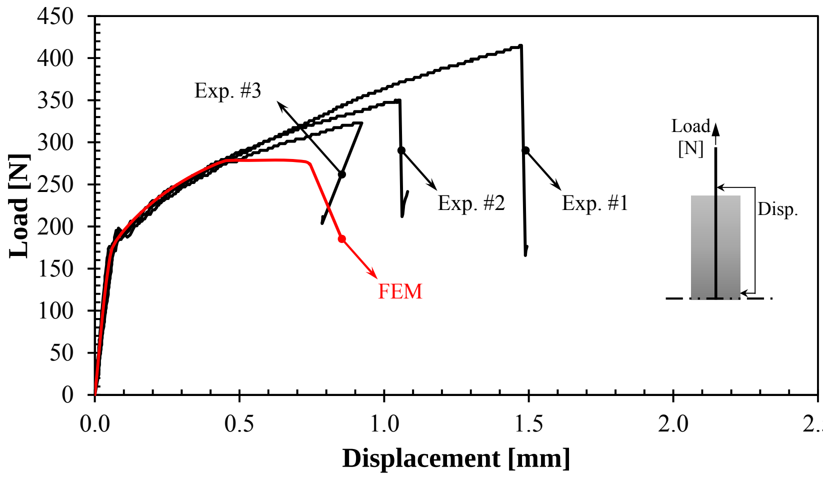

Figure 5.11. Comparison between the predicted and measure load-displacement for pull-out specimen with one NiTiNb SMA wire embedded in CFRP with L_d of 51 mm

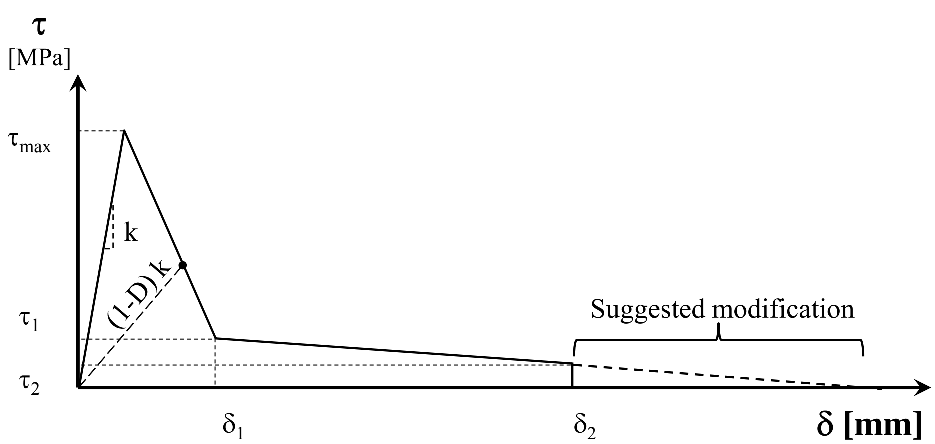

Figure 5.12. Suggested modification to the CZM

The CZM model was refined to extend the frictional component until the residual stress was negligible as illustrated in the figure. The effect of this revision is illustrated in Figure 5.13. The extension of the frictional component of the CZM resulted in larger predicted loads and displacements of the pull-out specimens at failure. However, the FEA still under predicted the failure load and displacement by 17% and 24% respectively.

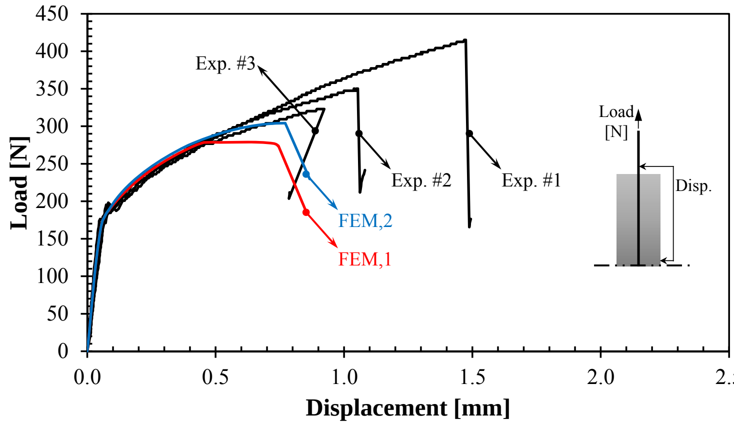

Figure 5.13. Load-displacement curve after tweaking the CZM parameters for pull-out specimen with one NiTiNb SMA wire embedded in CFRP with L_d of 51 mm

It should be noted that the specimens with L_d = 51 mm had a high scatter in experimental results. Moreover, the failure load and displacement for those specimens was higher than the failure load and displacements for specimens with L_d of 102 mm. This increase in the failure load may have been due to the curvature of the embedded portion of the wire due to fabrication errors. The curvature induced interlocking component to the bond strength which increased the failure load. Hence, the prediction of FEA will be considered as satisfactory.

The refined CZM model was implemented in the FEA to predict the response of the pull-out specimens with SMA embedment lengths of 102 mm. Figure 5.14 presents the predicted and measured load-displacement responses. The figure shows that the predicted load-displacement response is in good agreement with the experimental results.

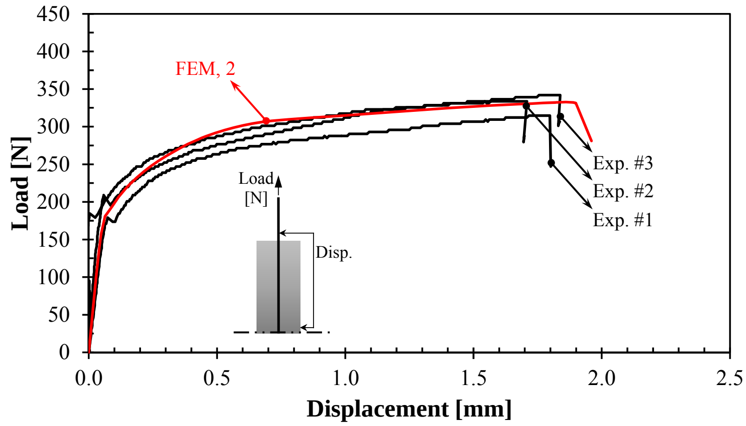

Figure 5.14. Comparison between the predicted and measure load-displacement for pull-out specimen with one NiTiNb SMA wire embedded in CFRP with L_d of 102 mm

Phase II: Behavior of the Self-stressing Patch Under Monotonic and Fatigue Loading

Chapter 6: Patch Response Under Monotonic and Fatigue Tensile Loading

Two self-stressing patches were fabricated and tested to evaluate: (a) the maximum recovery force that the patches can be generated upon activation, and (b) the monotonic tensile response of the activated patches. These tests provided an opportunity to evaluate whether or not the prestressing force that can be achieved is proportional to the number of wires in the patch or if there are unanticipated losses in the system. The method used to fabricate the self-stressing patch is also discussed in detail in this chapter.

A total of 14 self-stressing patches were fabricated and tested to evaluate the stability of the prestressing force when the self-stressing patch is subjected to fatigue loading. The factors considered in this study are the prestress level in the NiTiNb SMA wires and the applied force range. A model that predicts the degradation in the prestress is also presented.

6.1. Patch response under monotonic tensile loading

6.1.1. Specimen details

Figure 6.1 shows the details and dimensions of the self-stressing patch. The tested patches consisted of 10 NiTiNb SMA wires embedded into two CFRP tabs. As seen in Figure 6.1 each wire was 306 mm long and the clear distance between the adjacent wires is 0.89 mm. The wires were embedded in CFRP at both ends with embedment length of 102 mm. The embedment length of 102 mm was selected as it exhibits the highest failure load among the tested pull-out specimens. The central 102 mm long portion of the wires was exposed to allow room to activate the SMA wires. The CFRP consisted of unidirectional carbon fibers embedded in Araldite epoxy. The cured CFRP tabs where 2 mm thick. The properties of the wires, adhesive, and fibers are given in sections 3.2. Aluminum tabs were bonded to the CFRP tabs to prevent damage to the patches when gripped in the testing frame. A clear distance of 25 mm was provided between the end of the embedded wires and the aluminum tabs to prevent interference with the test.

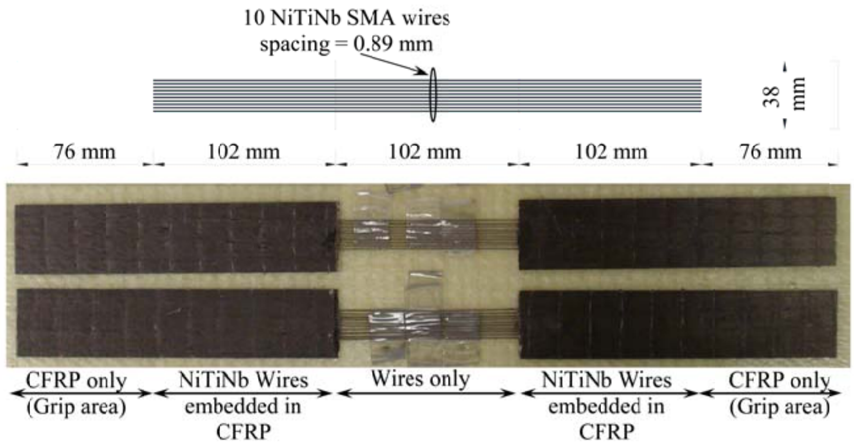

Figure 6.1. Specimen details and dimensions of the self-stressing patch

6.1.2. Self-stressing patch fabrication

To maximize the efficiency of the patches, the NiTiNb wires should be carefully aligned to avoid slack in the wires. Any slack in the wires would result in unrestrained shrinkage of the wires during activation, thereby reducing the total prestressing force that could be achieved. As such, during fabrication of the patches care was taken to minimize the amount of slack in the wires and to carefully align the wires to ensure that they were as parallel as possible.

Figure 6.2 shows the main steps in fabricating the patches. Superleastic Nitinol spacer wires with a diameter of 0.89 mm were placed between the NiTiNb wires to maintain straightness and uniform spacing of the NiTiNb wires. The NiTiNb wires and the spacer wires were cut to lengths of 306 mm and taped together as shown in Figure 6.2. Cotton threads were used to affix the NiTiNb wires to the carbon fabric at four locations as shown in the figure. After affixing the NiTiNb wires to the carbon fabric the spacer wires were removed. The carbon fibers along with the NiTiNb wires were saturated with epoxy and placed between four molds (two bottom molds and two top molds). Only the carbon fiber end tabs were inside the molds while the 102 mm central portion of the wires was exposed. This approach was adopted to prevent the low viscosity epoxy resin from flowing onto the central portion of the NiTiNb wires. A pressure of 690 Pa was placed on top of the molds to squeeze the entrapped air bubbles and excess epoxy out of the fibers to achieve a higher volume fraction. The specimens were left for 7 days before demolding. After demolding, the edges of the CFRP tabs were trimmed using a wet-cut tile saw.

It should be noted that the specimens were fabricated with the available resources in the lab to produce prototype specimens. The current fabrication method is labor intensive and time consuming. The time for a trained person to prepare one specimen is around 2 hours. However, if the fabrication method is automated, the fabrication time is expected to be less.

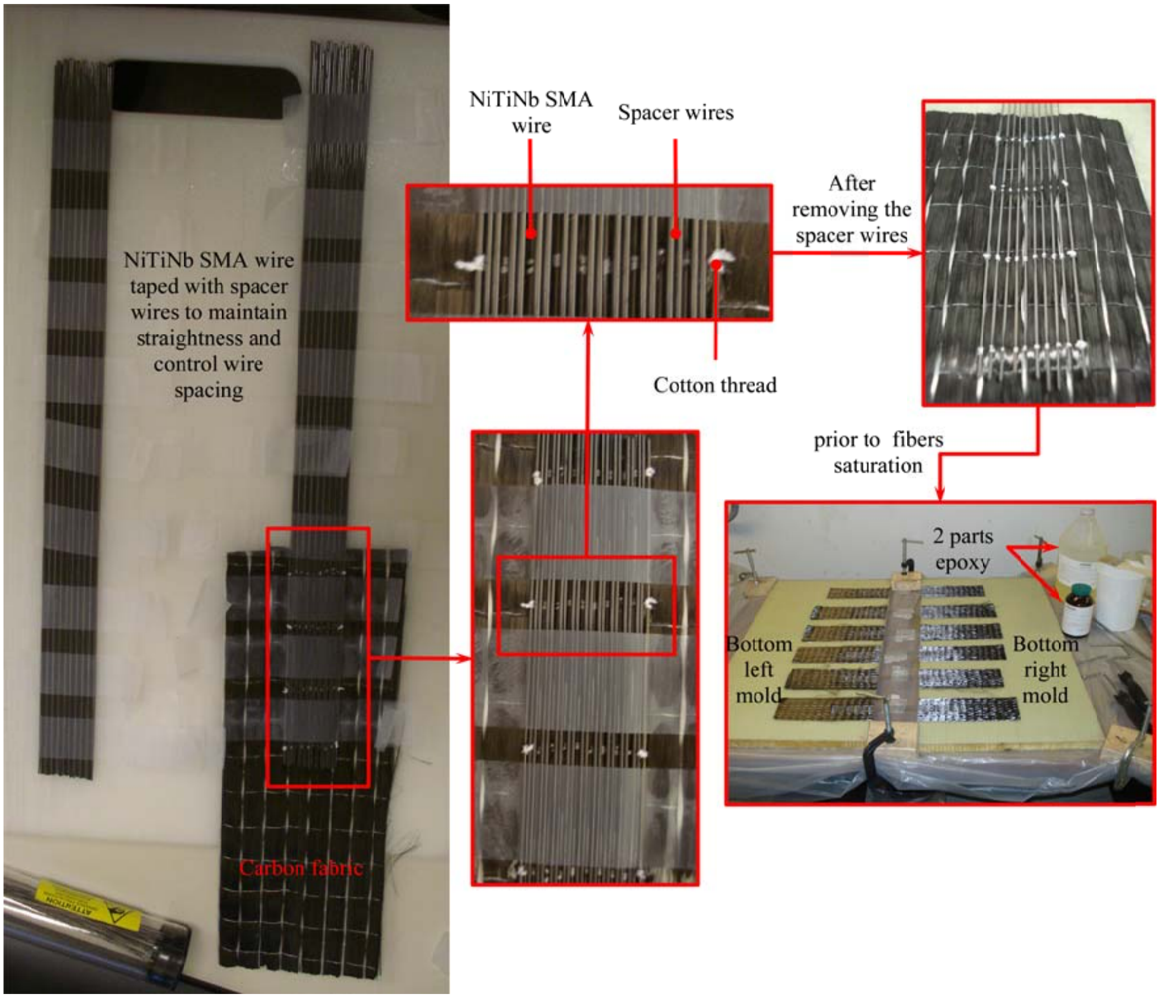

Figure 6.2. The self-stressing patch during fabrication

6.1.3. Test setup and instrumentation

Figure 6.3 shows the test setup and instrumentation used to measure the recovery force that was generated by the self-stressing patch upon activation. A 22 kN load cell (Tovey Engineering, model number SW10-5k-B000) used to measure the recovery force and the applied load. Two thermocouples (Omega Engineering, model number SA1-T-120) were mounted on the NiTiNb wires to monitor the temperature during activation.

The SMA wires were activated directly using forced hot air as an alternative to electrical heating. Fiber glass insulation was placed around the CFRP tabs to prevent softening of the epoxy. The thickness and the R value of the fiberglass were 51 mm and 6.7, respectively. An electromechanical self-reacting frame with a total capacity of 44.5 kN was used to load the specimen at a rate of 0.4 mm/minute. Thermocouples were also installed underneath the insulation to monitor the temperature of the CFRP surface during activation. A data acquisition system (Micro-Measurements, system 7000) was used to collect the data at a frequency of 1 Hz.

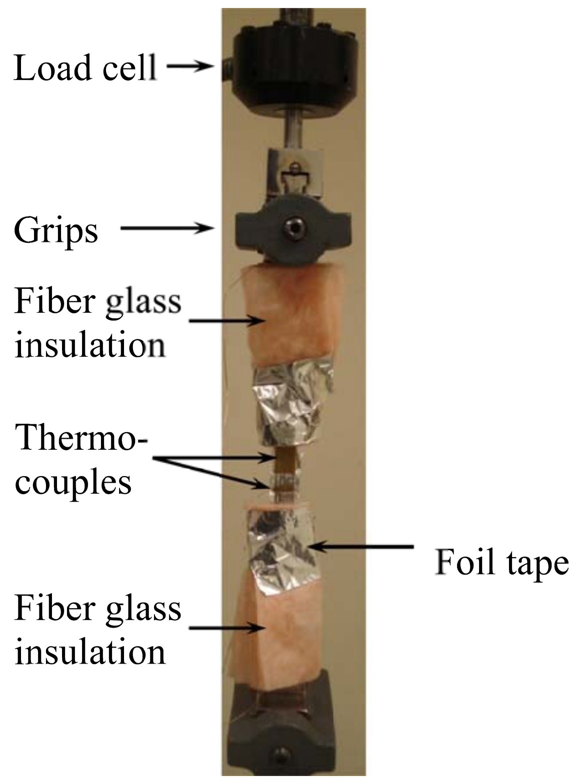

Figure 6.3. Test setup and instrumentation of self-stressing SMA/FRP patch

6.1.4. Results and discussion

Figure 6.4 shows the thermomechanical response of the two tested patches. The figure also presents the transformation temperatures of the NiTiNb wires as reported by the manufacturer. A seating load of 89 N was applied to the specimens prior to heating the wires. Upon heating, recovery forces of 1927 N and 2035 N were measured for the first and the second patches, respectively. During heating of the first patch the thermocouples debonded from the SMA wires when the temperature reached 158°C. However, the results indicate that the wires were fully activated at this stage. After the patches cooled down to room temperature, sustained recovery forces of 1710 N and 1750 N were measured. These correspond to recovery stresses of 367 MPa and 375 MPa for the first and second patches, respectively. During activation of the self-stressing patch it was noticed that the temperature on the surface of the CFRP increased from 26°C to 31°C. Thermomechanical testing of the adhesive indicated that the adhesive had a softening temperature between 45°C and 60°C above which the elastic modulus of the adhesive droped dramatically as described in Chapter 3. Therefore, direct heating of the NiTiNb wires while insulating the CFRP tabs was a practical way to activate the SMA wires without causing significant softening of the CFRP tabs. This is important since softening of the CFRP tabs could result in relaxation of the prestressing force over time.

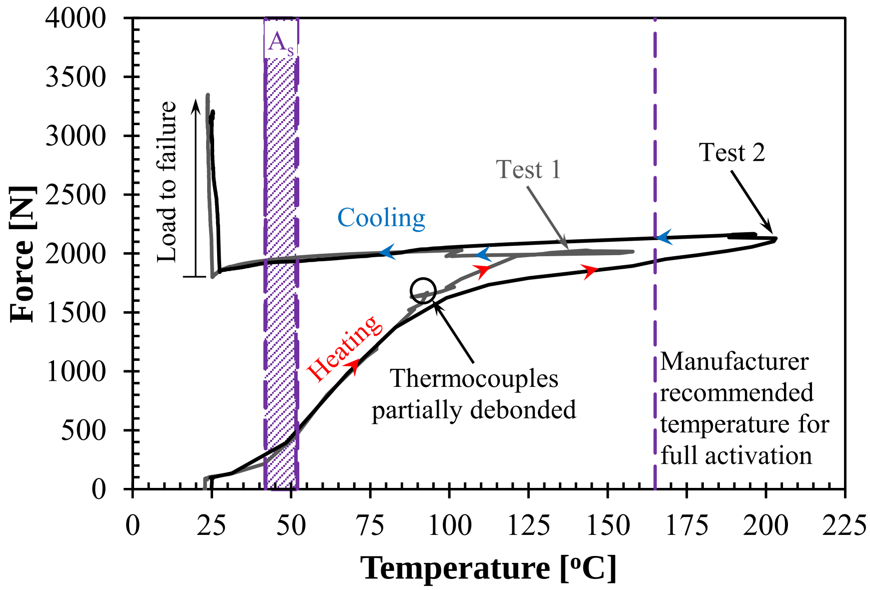

Figure 6.4. Force measured upon heating the self-stressing SMA/FRP patch before loading to failure

After activation of the wires the patches were subsequently loaded monotonically in tension to failure. The measured failure loads were 3350 N and 3210 N for the first and second patches, respectively. These correspond to a failure stress in the wire of 720 MPa and 690 MPa, respectively. Both patches failed by progressive debonding of the NiTiNb wires from the CFRP tabs. The measured failure loads of the patches were 195% and 180% of the measured recovery forces of the two patches respectively, indicating a substantial margin of safety against debonding.

During activation the behavior of the self-stressing patch is similar to the behavior of a single wire described in section 3.2. The recovery stress was 370 MPa and 390 MPa for the self-stressing patch and a single wire, respectively. The pull-out behavior of the self-stressing patch is similar to the behavior of pull-out specimens with one and three wires. The stress that caused complete debonding was 705 MPa, 710 MPa and 800 MPa for the self-stressing patch, the pull-out specimen with one wire, and pull-out specimen with three wires, respectively. Inspection of the results suggests that no loss of prestress occurred during activation. The results suggest that the prestressing force was proportional to the number of NiTiNb wires in the patch.

Accordingly, scaling up the patch to achieve a double-sided repair using two 85 mm wide patches with 37 wires each would generate prestressing force of 12 kN, which is comparable to the configuration that has been previously used to extend the fatigue life of cracked steel elements by Taljsten et al. (2009). It should be noted that FRP overlay is still needed to increase the stiffness of the repaired member and to bridge the crack.

6.2. Patch response under fatigue tensile loading

6.2.1. Specimen details

Figure 6.5 presents the dimensions of the fatigue specimens. The specimens consisted of ten 0.77 mm NiTiNb SMA wires that were embedded into two CFRP tabs at each end. Each wire was 306 mm long and was embedded 102 mm into each CFRP tab leaving a 102 mm clear length in the center of the specimen. The clear distance between the wires was 0.89 mm. The CFRP consisted of a unidirectional carbon fiber fabric embedded in the Araldite adhesive. The properties of both materials can be found in section 3.2. The central 102 mm long portion of the wires was exposed to allow activation of the SMA wires. Steel tabs were bonded to the CFRP tabs and gripped in the testing frame. A clear distance of 25 mm was provided between the end of the embedded wires and the steel tabs to prevent any interference in the bonded portion of the wire. The self-stressing patches tested in this research were fabricated using the same approach described in section 6.1.

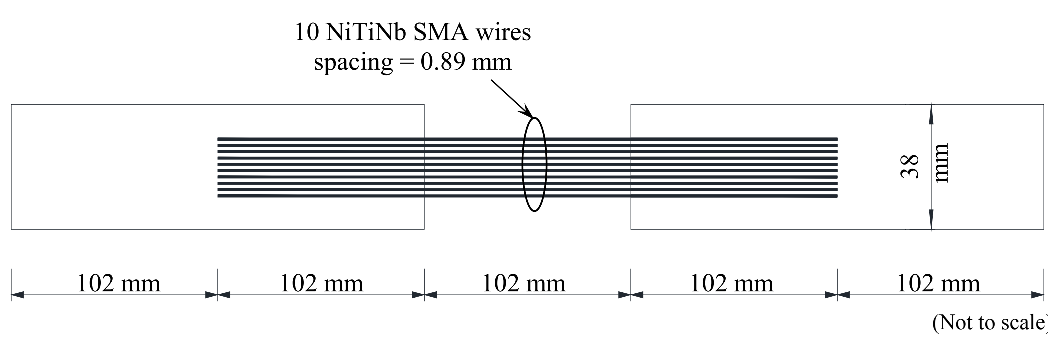

Figure 6.5. Specimen details and dimensions of the fatigue specimens

Table 6.1 summarizes the test matrix of the fatigue specimens. The test specimens were divided into three groups. In the first two groups the NiTiNb wires were partially activated to generate a recovery stress of 250 MPa. Based on the pull-out tests that were described in chapter 4, the stress in the NiTiNb wires at the onset of debonding was 400 MPa. The recovery stress level of 250 MPa was selected to prevent debonding of the NiTiNb wires during activation. In the third group the wires were fully activated up to a stress level of 390 MPa which induced debonding of the SMA wires from the CFRP tabs. Three or four similar tests were conducted for each configuration in the first group, while two similar tests were conducted for each configuration in the second and third groups. Figure 6.6 illustrates the parameters considered in the three test groups. For the coupons in the first group, the SMA wires were partially activated to a stress of 250 MPa and subjected to stress ranges of 20 MPa, 50 MPa or 80 MPa. The maximum stress in the wires in this group was less than the stress required to cause debonding of the SMA wires from the CFRP tabs. In the second group the SMA wires were partially activated to the same level as in Group I but the applied stress range in the SMA wires was 200 MPa. In this case the maximum stress in the wires during the fatigue cycling was greater than the stress required to cause debonding. In the third group, the SMA wires were fully activated to a stress level of 390 MPa in the SMA wires. At this stress level debonding of the SMA wires from the CFRP tabs would be initiated. The applied fatigue stress range in the wires was 200 MPa for this group.

Table 6.1. Test matrix for the specimens tested under fatigue loading

	Target prestress level [MPa]	Stress range [MPa]	Number of repetitions
Group I	250	20	4
		50	3
		80	3
Group II	250	200	2
Group III	390	200	2

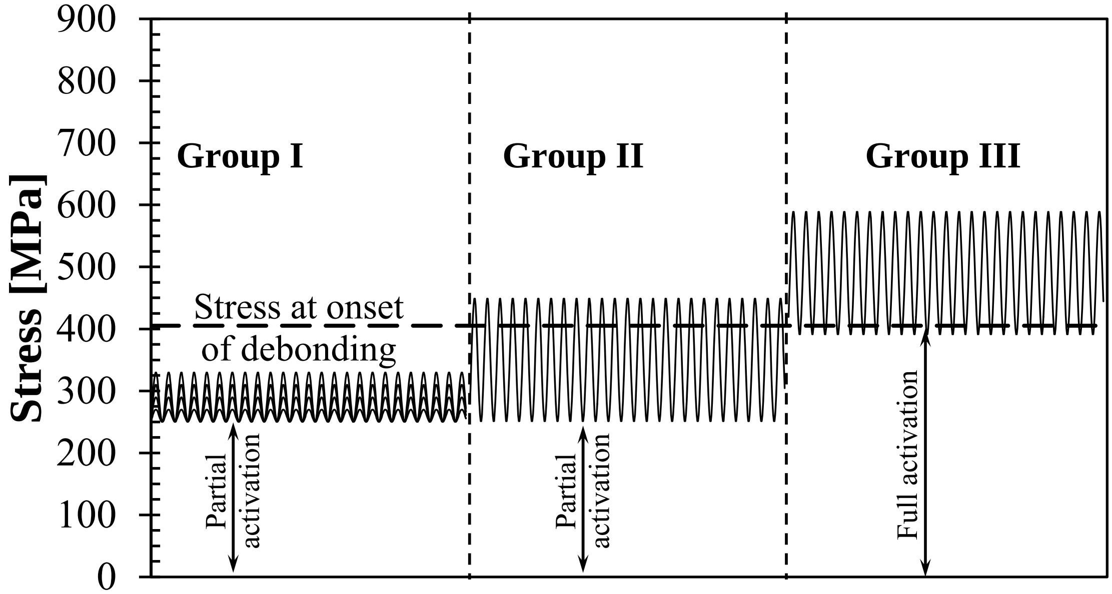

Figure 6.6. A schematic drawing illustrating different stress ranges and activation levels for the three groups considered in this research.

6.2.2. Test setup and instrumentation

Figure 6.7 shows the test setup used to test the self-stressing patches under fatigue loading. The specimens were tested in a 490 kN MTS servo-hydraulic testing frame (model number 370.50) which is equipped with a digital controller and a data acquisition system. The testing frame is equipped with an in-line low capacity loading system with a capacity of 22 kN.

A heat gun was used to fully activate the SMA wires while a power supply was used to partially activate the wires through electrical conduction. The details of the power supply used in this research are described in section 3.2.1.c.

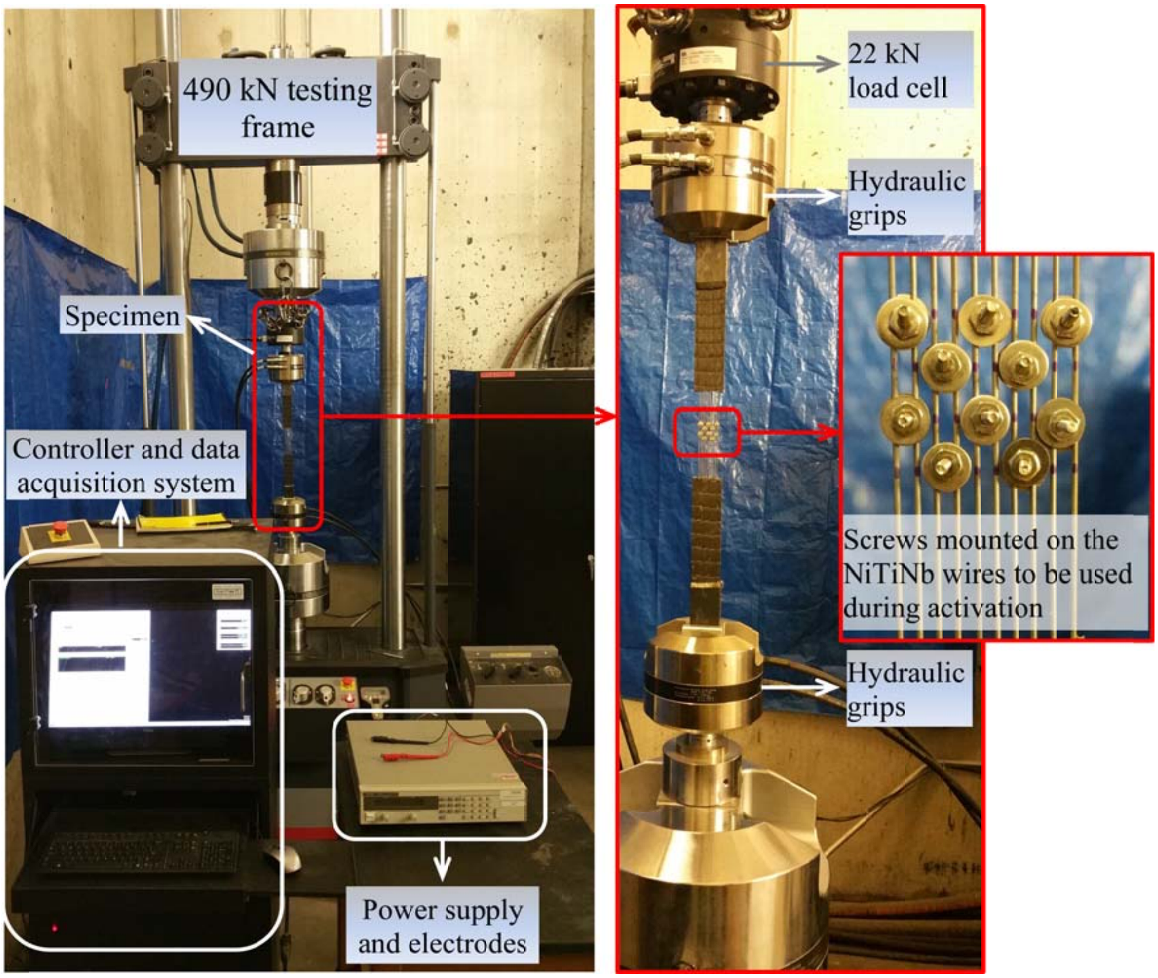

Figure 6.7. Test setup of the fatigue specimens

6.2.3. Test protocol

The upper end of the specimen was placed in the upper grip with a hydraulic gripping pressure in the hydraulic lines of 10 MPa. Then actuator was switched to a load control mode before gripping the lower end of the specimen using the same pressure. A seating load of 89 N was applied to the specimen and the SMA wires were activated to the desired level. Once the wires are activated fatigue loading was applied.

A heat gun was used to fully activate the SMA wires in Group III, similar to the procedure described in section 6.1. An electrical power supply was used to partially activate the specimens in Group I and Group II while the force was monitored by the load cell of the testing frame. Figure 6.8 shows a close view of the wires prior to partial activation. It can be seen in the figure that each pair of adjacent wires were connected in a parallel configuration using screws, washers, and nuts. The screws were used as electrodes to activate the two adjacent wires simultaneously. Electrical tape was used to insulate the other wires before connecting the power supply to the screws. Electrical current was applied to each pair of wires until the recovery stress reached 125 MPa. Before activating the next pair of wires the first two wires were allowed to cool for four minutes to allow the recovery stress to stabilize. This process was repeated twice, with the recovery stress reaching 250 MPa after the second stage of activation. The wires were activated following the activation sequence shown by the numbering in Figure 6.8.

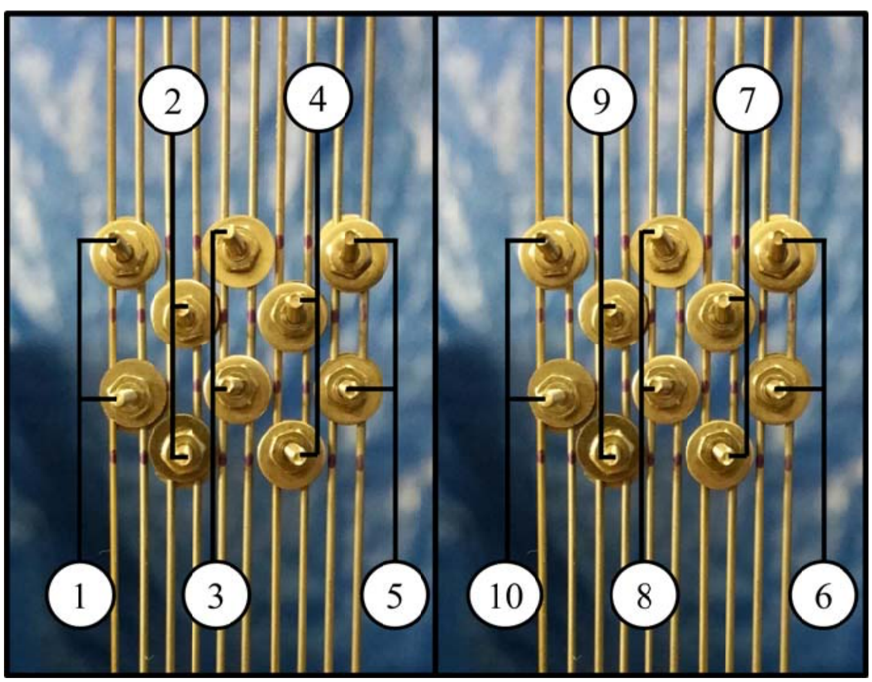

Figure 6.8. The sequence used to partially activate the SMA wires

Figure 6.9 shows the loading protocol used in this test. A cyclic load was applied in load control mode at the target load range level for 500 cycles at a frequency of 10 Hz. The actuator was then repositioned to its set point (zero displacement location) in displacement control to measure the residual prestressing force in the self-stressing patch. The load was measured and recorded for 10 seconds. The cyclic loading resumed for another 500 cycles and the process was repeated up to 2 million loading cycles or until failure as shown in Figure 6.9. Failure was defined when the actuator displaced 20 mm from the set point indicating pull-out or rupture of the SMA wires.

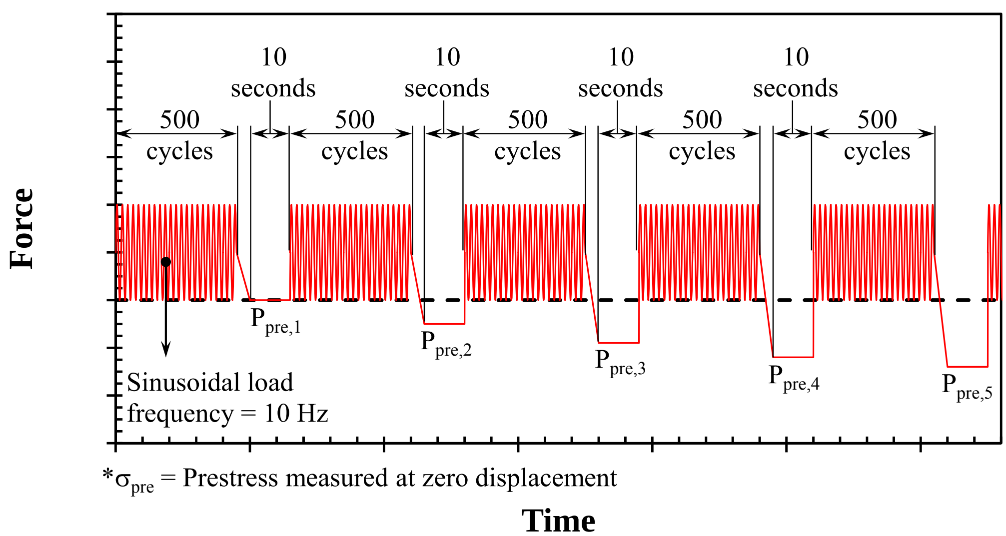

Figure 6.9. Loading protocol for the fatigue specimens

6.2.4. Results and discussion

Table 6.2 summarizes the results of the tested specimens. Each specimen was assigned a three part identifier. The first part indicates the target prestress level in MPa. The second part indicates the stress range in MPa, while the third part is a serial number to differentiate multiple repetitions of the same configuration. The specimens in Group I were tested up to 2 million cycles with no sign of failure and were categorized as run-out specimens. Due to unexpected power failure during testing, the test was terminated at 680,858 cycles and 900,296 cycles for specimens 250-20-3 and 250-20-4, respectively. All the specimens of Group II and Group III failed by rupture of one or more of the NiTiNb wires followed by a pull-out of the remaining wires as shown in Figure 6.10. It should be noted that the wires in specimens tested under a stress range between 20 MPa and 80 MPa did not exhibit a rupture failure. While wire rupture was observed for the specimens tested under a stress range of 200 MPa. The rupture of the wires could be due to fatigue loading. The fatigue behavior of a single wire was not evaluated in this research.

Table 6.2. Results summary of the self-stressing patch when subjected to fatigue loading

	Specimen ID	Target Prestress [MPa]	Actual Prestress [MPa]	Stress range [MPa]	Cycles to failure
Group I	250-20-1	250	235	20	2,000,000[a]
	250-20-2	250	250	20	2,000,000[a]
	250-20-3	250	255	20	680,859[b]
	250-20-4	250	250	20	900,297[b]
	250-50-1	250	260	50	2,000,000[a]
	250-50-2	250	255	50	2,000,000[a]
	250-50-3	250	255	50	2,000,000[a]
	250-80-1	250	250	80	2,000,000[a]
	250-80-2	250	250	80	2,000,000[a]
	250-80-3	250	255	80	2,000,000[a]
Group II	250-200-1	250	250	200	117,504
	250-200-2	250	250	200	115,189
Group III	390-200-1	390	375	200	58,860
	390-200-2	390	390	200	49,584

[a] Specimen run out at 2 million cycles

[b] The test was stopped due to unexpected power failure

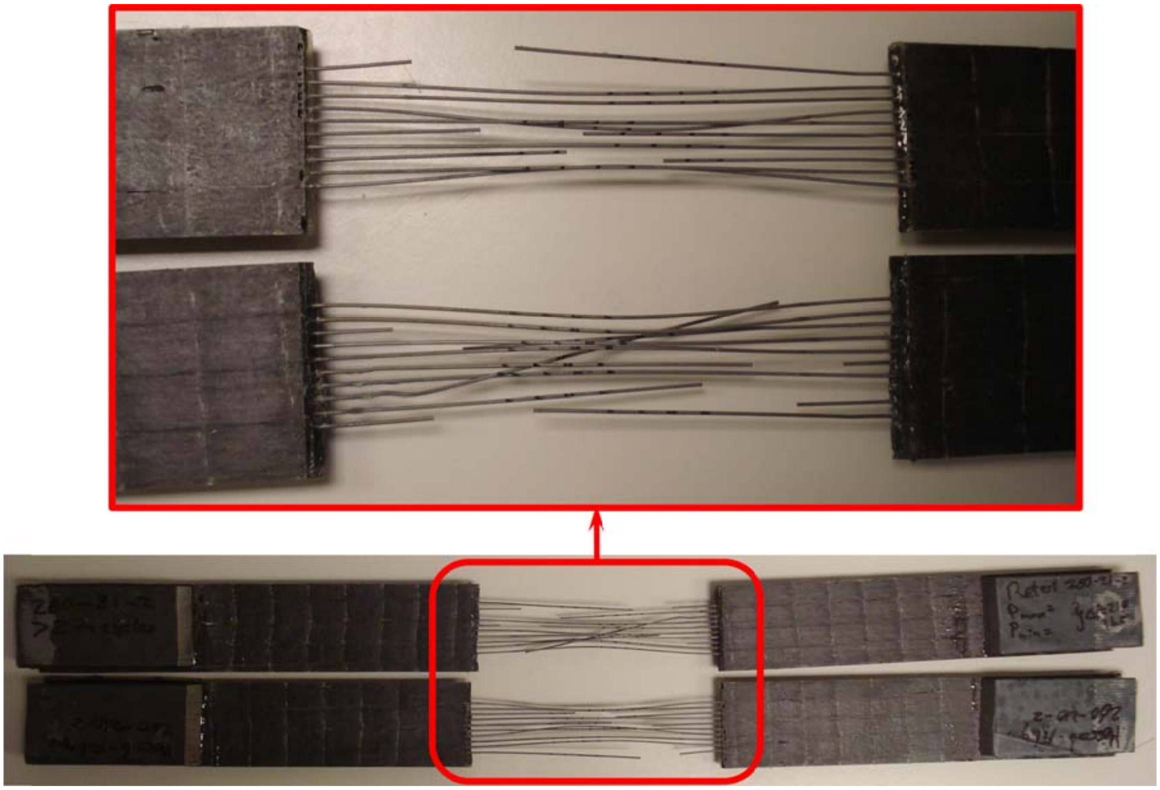

Figure 6.10. Failed fatigue specimens

Figure 6.11 shows the degradation of the normalized prestress ($\sigma_{pre,500,i}/\sigma_{pre,0}$) with increasing number of loading cycles for the Group I. The normalized prestress is calculated by dividing the stress in the wire after the application of the i^{th} 500 loading cycles, $\sigma_{pre,500,i}$, by the initial prestress $\sigma_{pre,0}$. Inspection of Figure 6.11(a) indicates that for the patches that were partially activated and tested at the lowest force range the prestress decreased by 8% within the first 500,000 cycles (most of which occurred within the first 100,000 cycles) after which the residual prestress remained constant up to 2 million cycles.

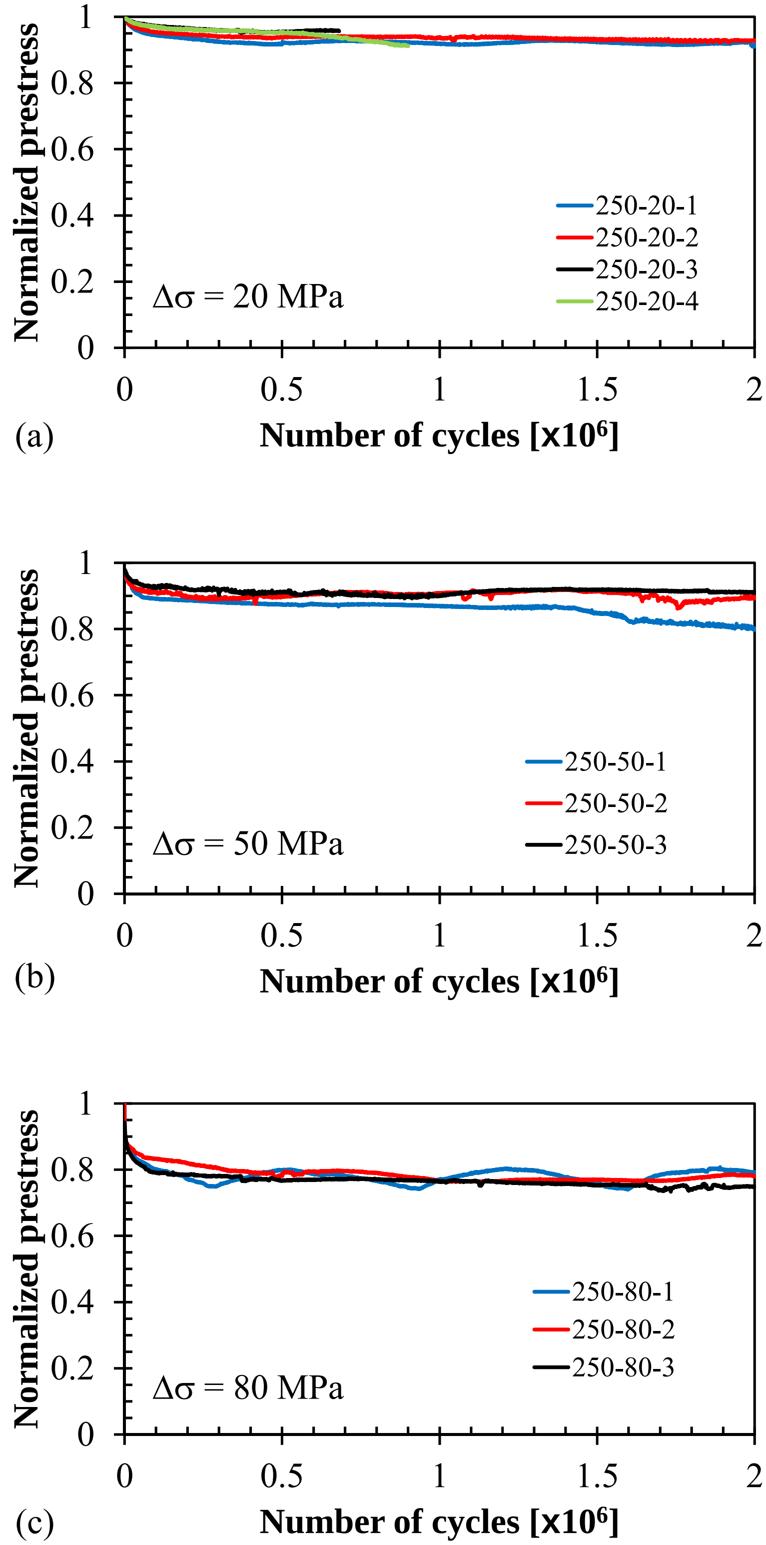

Figure 6.11. The normalized prestress versus the number of fatigue cycles for Group I for specimens with stress range of: (a) 20 MPa, (b) 50 MPa and (c) 80 MPa

A similar trend can be observed from Figure 6.11(b) and (c), with prestressing losses of 12% and 23% occurring within the first 500,000 cycles for specimens that were tested at 50 MPa and 80 MPa stress ranges, respectively. Subsequently the residual prestressing force remained constant up to 2 million cycles. For specimen 250-80-1 a cyclic fluctuation in the prestress force with a period of 24 hours was observed. This fluctuation was due to temperature fluctuations in the lab due to failure of the HVAC system in the lab.

Figure 6.12 presents the results for specimens of Group II which was partially activated and tested at the highest load range, 200 MPa. Inspection of the figure indicates that after the application of the first 500 fatigue cycles the prestressing forces in the patches decreased to 60% of their initial values. Afterwards, the prestress force gradually decreased and stabilized at 60,000 cycles at 40% of the original prestress force. Rupture of the first SMA wire was observed after 106,000 and 109,000 cycles for specimens 1 and 2, respectively. Rupture of the wires was accompanied by a sudden decrease of the residual prestressing force, initiation of debonding of the SMA wires and rupture of subsequent wires due to the increased demand on the intact wires. Failure, defined as 20 mm deformation of the actuator, was observed after 117,000 and 115,000 cycles for specimens 1 and 2, respectively.

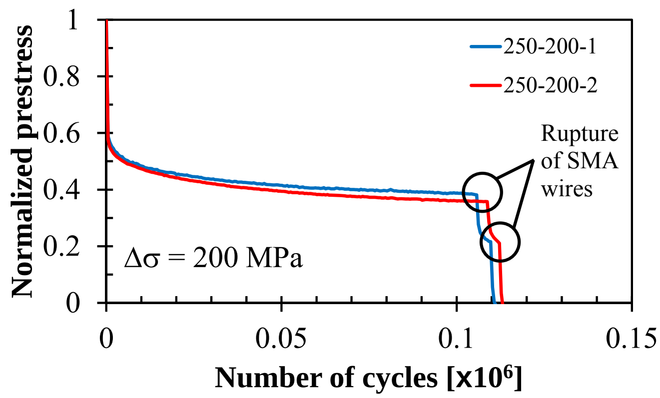

Figure 6.12. The normalized prestress versus the number of fatigue cycles for Group II

Figure 6.13 presents the test results of Group III which was fully activated and tested at the highest load range, 200 MPa. As soon as the fatigue loading was applied debonding initiated and was observed and a faint cracking sound was heard. Inspection of Figure 8.8 indicates that after the application of the first 500 fatigue cycles the prestress force decreased by 60% of its initial value. The prestressing force continued to decrease with continued cyclic loading until it was totally lost after 24,000 and 33,000 loading cycles for specimens 1 and 2, respectively. Failure of the patches occurred at 58,900 and 49,600 cycles for specimens 1 and 2, respectively.

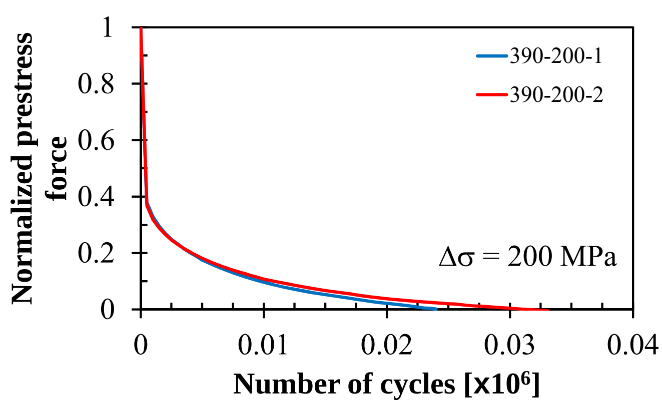

Figure 6.13. The normalized prestress versus the number of fatigue cycles for Group III

Figure 6.14 presents the normalized prestress versus the fatigue life for all the tested specimens. Inspection of the figure indicates that the specimens that were partially activated achieved a longer fatigue life compared to the fully activated specimens. In Group I minimal loss of prestress and no indication of failure were observed after 2 million loading cycles. While in Groups II and III an immediate and significant loss of prestress occurred after the first 500 cycles. The prestress loss in the latter two cases is believed to be attributed to interface damage as the applied load exceeded the load required to initiate debonding. The debonding caused relaxation in the SMA wires and hence a loss in the prestress occurred. The test results indicate that in the case of Group I the interface remained intact for the duration of the 2 million applied fatigue cycles.

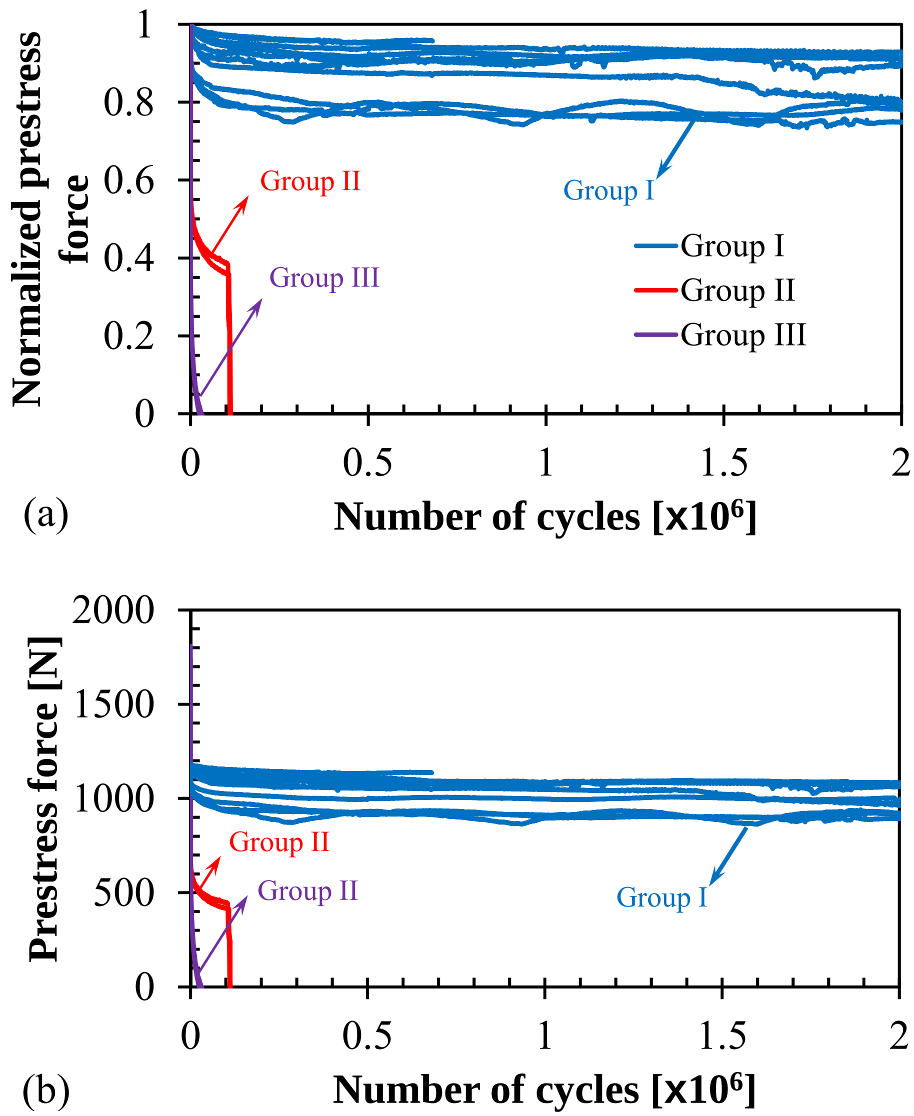

Figure 6.14. Relation between number of cycles to failure and: (a) normalized prestress force, (b) prestress force for the three groups

Considering a fatigue damage accumulation law such as the commonly used Miner's rule (Miner, 1945)

$$\sum_{i=1}^{N} \frac{n_i}{N_i} = 1 , \tag{6.1}$$

where n_i is the number of cycles accumulated at stress σ_i, and N_i is the number of cycles to failure at the same stress σ_i. There is no further accumulated damage as shown in Figure 6.14, suggesting that the Group I specimens will exhibit an infinite fatigue life.

The specimens in Group I, which survived 2 million load cycles, were retested at a stress range of 200 MPa and the fatigue lives of those specimens were compared with those of the specimens that were tested directly at a stress range of 200 MPa (i.e. specimens of Group II). Table 6.3 summarizes the fatigue lives of the retested specimens.

Table 6.3. Results summary of fatigue specimens of Group I retested at a stress range of 200 MPa

Specimen ID	Stress range [MPa]	Cycles to failure
Retest 250-20-1	200	98,697
Retest 250-20-2	200	99,899
Retest 250-80-1	200	119,238
Retest 250-80-2	200	142,785

The specimens were retested as soon as the 2 million cycles were finished. The same loading protocol was used in this test. The retested specimens of Group I exhibited similar failure modes to those of the virgin specimens that were tested in Group II. Figure 6.15 compares the degradation of the prestressing force of the retested samples in Group I to that of the virgin samples of Group II that were tested at the same stress range. Inspection of the figure indicates that the first 500 fatigue cycles the prestressing forces for the specimens that were initially tested at a stress range of 20 MPa decreased by 35% while the prestressing force in the specimens that were initially tested at a stress range of 80 MPa decreased by 15%. Afterwards, the prestress force gradually decreased and stabilized after 50,000 cycles. Rupture of the first SMA wire was observed and accompanied by a sudden decrease of the residual prestressing force at fatigue life ranging from 98,000 to 143,000 cycles. It can be seen in Figure 8.10 that the fatigue lives of the retested specimens were similar to those of the specimens that were tested directly at a stress range of 200 MPa (i.e. specimens of Group II).

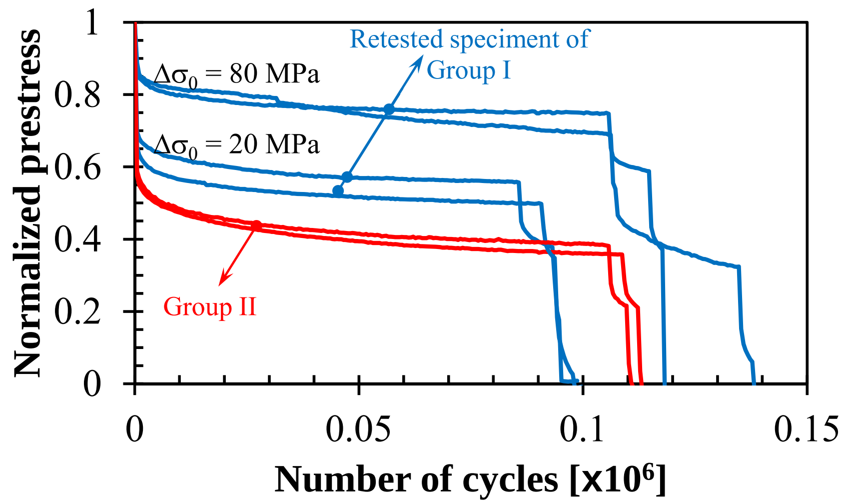

Figure 6.15. The normalized prestress versus the number of fatigue cycles for the retested specimens of Group I versus Group II

Based on the experimental results of the fatigue study, the self-stressing patch should be designed such that the maximum expected stress in the wire due to the combined effect of activation and fatigue loading is less than the stress to initiate debonding. In this case the fatigue life of the patch is at least 2 million cycles. In this case, the expected loss of the prestressing force during the service life of the patch depends on the applied stress range on the SMA wires.

6.2.5. Proposed Model to predict the degradation of the prestress stress

Figure 6.16 presents the final prestress, $\sigma_{pre,f}$, versus the maximum applied fatigue stress, σ_{max}, for all of the tested specimens. The stress at the onset of debonding is highlighted in the figure. Inspection of the figure indicates that the final prestress is proportional to the maximum applied stress when the maximum stress is less than the stress at the onset of debonding. Whereas the prestress is completely lost when the maximum stress is higher than the onset of debonding stress. Using a linear regression, the final prestress can be expressed as

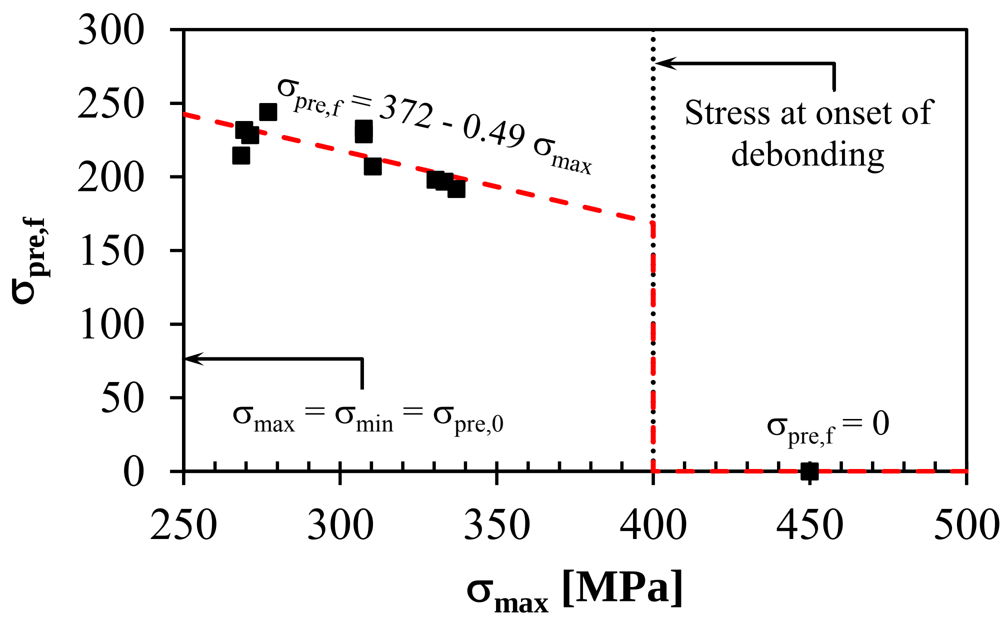

Figure 6.16. Comparison between the proposed empirical equation to predict the loss of prestress and the experimental results

$$\sigma_{pre,f} = \begin{cases} 372 - 0.49\,\sigma_{max} & , \quad \text{when } \sigma_{max} < \sigma_{onset\ of\ debonding} \\ 0 & , \quad \text{when } \sigma_{max} > \sigma_{onset\ of\ debonding} \end{cases} . \tag{6.2}$$

Inspection of Figure 6.16 indicates that the prestressing system should be designed such that the maximum stress in the wire due to the combined effect of activation and fatigue loading is less than the stress at the onset of debonding. This enables the self-stressing patch to reach an infinite fatigue life.

It should be noted that more specimens need to be tested to validate the model when the wires are partially activated to a stress other than 250 MPa and the applied maximum stress is less than the onset of debonding stress.

Chapter 7: Conclusions, Limitations and Future Work

An experimental and numerical study was conducted to develop and characterize the behavior of a self-stressing SMA/FRP patch for repair of civil infrastructure with a target application of repairing cracked steel structures. This research is divided into two phases. In the first phase the thermomechanical response of different shape memory alloys and saturating resins was quantified to select suitable materials for the development of the self-stressing patch. The bond behavior of SMA wires to FRP patches was investigated experimentally and numerically. In the second phase the performance of the patch during activation, monotonic tensile loading, and tensile fatigue loading was characterized. The conclusions of each phase of this research and the recommendations for future work are summarized in the following sections.

7.1. Conceptual development and material selection

Three different SMA wires and two structural adhesives were tested to determine their thermomechanical properties. Based on the results the most suitable materials were selected. Based on the research finding the following conclusions were drawn:

- NiTiNb SMA wires are more suitable to be used as actuators for the self-stressing patch over either shape memory NiTi or superelastic NiTi. Prestrained NiTiNb SMA wires are capable of generating recovery stresses of 390 MPa even after cooling the wire to room temperature. The shape memory NiTi was able to generate a recovery stress of 415 MPa, however, a continuous heating of the wire is required in applications requiring a sustained recovery at or near room temperature. The tested superelastic NiTi SMA wires could generate a recovery stress of 490 MPa. However, the prestressing concept using these wires requires the use of a heavy prestressing frame. Hence, it has limited advantage over the conventional FRP prestressing techniques.

- Cyclic heating and cooling of NiTiNb wires between 165^{o}C and room temperature resulted in an 18% reduction of the sustained recovery force at room temperature after 12 cycles. However, cycling heating and cooling in the expected service temperature range for most civil infrastructure (up to 40^{o}C) is not expected to have any significant impact on the recovery force.
- Two saturating resins, Tyfo S and Araldite, were tested to evaluate their thermomechanical properties when cured and tested at different ambient temperatures. The softening temperature of Tyfo S adhesive when cured at 25^{o}C for 7 days was between 25^{o}C and 45^{o}C, while for Araldite the softening temperature was between 45^{o}C and 60^{o}C. Elevated temperature post-cure cycles increased the softening temperature of the Araldite adhesive up to 75^{o}C depending on the post-cure temperature. However, elevated temperature post-cure cycles are not recommended for the proposed self-stressing patch as the curing regimens would likely cause partial activation of the SMA wires thereby reducing the efficiency of the patch. Based on these results the Araldite adhesive was selected for further investigation since the Araldite adhesive retained a higher percentage of its room-temperature tensile modulus at elevated temperatures than the Tyfo S adhesive.
- Activating the central exposed portion of the NiTiNb SMA wires by either electrical conduction or direct heating using forced air did not result in softening

of the epoxy in the FRP tabs. This resulted in more effective transfer of the recovery stresses to the anchorage region of the proposed patches and maximized the efficiency of the utilization of the SMA wires for prestressing.

7.2. Bond behavior between superelastic NiTi SMA wires and FRP

The pull-out behavior of specimens with superelastic NiTi wires embedded in FRP was tested. The factors considered in this study were the wire diameter (0.47 mm, 0.66 mm and 0.89 mm) and the embedment length (13 mm, 25 mm, 51 mm, 102 mm and 127 mm). The research findings lead to the following conclusions:

- Two debonding mechanisms were observed for the tested superelastic NiTi wires embedded in CFRP patches: debonding prior to wire transformation, and complete debonding after transformation. Debonding after transformation was the dominant failure mode for smaller diameter wires with longer embedment lengths while debonding before transformation was the dominant failure mode for larger diameter wires with shorter embedment lengths.
- Two critical embedment lengths, $L_{d,\sigma}$ and $L_{d,\varepsilon}$, were defined for the tested NiTi wires embedded in CFRP patches. These are the required embedment lengths to achieve the upper plateau stress and the complete transformation of the tested wires, respectively. $L_{d,\sigma}$ was found to be 12.7 mm and 25.4 mm, for wires with diameter of 0.66 mm and 0.89 mm, respectively, while for wires with a diameter of 0.47 mm, $L_{d,\sigma}$ was found to be less than 12.7 mm. $L_{d,\varepsilon}$ was found to be 12.7 mm, 25.4 mm and 50.8 mm for specimens with wire diameter of 0.47 mm, 0.66 mm and 0.89 mm, respectively.

- Both embedment lengths, $L_{d,\varepsilon}$ and $L_{d,\sigma}$ were found to be proportional to the square of the wire diameter, d_b^2 but with different constants of proportionality.
- The digital image correlation system ARAMIS proved to be an effective tool to identify the initiation and propagation of debonding of SMA wires from FRP composites. The DIC system enabled the development of longitudinal strain contours on the surface of the FRP which could be used to monitor the propagation of strain concentrations along the SMA wires during the debonding process.

7.3. Bond behavior between NiTiNb SMA wires to FRP

Pull-out specimens with embedded NiTiNb wires were tested to investigate their bond behavior. The test parameters considered were the embedment length of the SMA wires, the fiber type in the FRP composite, and the number of wires per specimen. Based on the test observations the following conclusions can be drawn:

- The load-displacement response of the pull-out specimens with NiTiNb wires was linear until debonding initiated. The pull-out specimens exhibited a hardening behavior after the initiation of debonding. This suggests a non-negligible contribution from a load transfer mechanism at the interface other than cohesion alone.
- The average stress at the onset of debonding was 400 MPa for all of the tested specimens. The stress at the onset of debonding does not depend on either the embedment length or the number of wires. However, increasing the embedment length increased the load at complete debonding. This suggests that the interface

strength is composed of two components: cohesion (before the onset of debonding) and friction (after the onset of debonding). While the cohesive component does not increase by increasing the embedded length, the frictional component does.

- The specimens with three NiTiNb wires embedded in CFRP, with a clear distance of 0.89 mm between the wires exhibited similar behavior to the specimens with one wire. This suggests that the wire spacing of 0.89 mm or 1.2 times the wire diameter is sufficient to prevent any adverse interactions between the wires.
- The maximum stress achieved in NiTiNb wires embedded in GFRP patches was 8% lower than that for NiTiNb wires embedded in CFRP patches which was within the experimental scatter. Accordingly, there is no evidence of a strong dependence of the pull-out strength on the fiber type although the effect of the adhesive type was not investigated in detail.

7.4. Finite element analysis of pull-out specimens with NiTiNb SMA wires embedded in CFRP

Finite element analyses were conducted to investigate the debonding mechanism of a NiTiNb SMA wire embedded in CFRP. A cohesive zone model was used to model the interface between the SMA wire and the FRP. The results obtained experimentally from pull-out specimens with L_d of 25 mm were used to quantify the interface parameters. The FEA results were then validated versus the experimental results that were obtained from specimens with L_d of 51 mm and 102 mm. Based on the results of the FEA the following conclusions were drawn:

- A trilinear bond-slip relationship is proposed to represent the interface between NiTiNb SMA and CFRP taking into account the cohesive and frictional components of stress transfer at the interface.
- The debonding mechanism predicted by the FEA matches well with the experimental test observations using conventional instruments and the DIC system.

7.5. Performance of the patch during activation and under monotonic tensile loading

Two self-stressing patches were tested to evaluate: (a) the maximum recovery force that the patches can generate upon activation, and (b) the monotonic tensile response of the activated patches. These tests provided an opportunity to evaluate whether or not the prestressing force that can be achieved is proportional to the number of wires in the patch or if there are unanticipated losses in the system.

- Targeted heating of the NiTiNb wires using electrical conduction or forced air direct heating was shown to be an effective means to activate the wires without softening the adhesive or causing debonding of the SMA wires from the CFRP tabs.
- The maximum load carrying capacity of the tested patches when subjected to monotonic tensile loading was nearly twice the measured prestressing force. Failure occurred by debonding of the SMA wires from the CFRP anchorages.
- During activation the behavior of the self-stressing patch is similar to the behavior of a single wire. The recovery stress was 370 MPa and 390 MPa for the self-

stressing patch and a single wire, respectively. The stress that caused complete debonding was 705 MPa, 710 MPa and 800 MPa for the self-stressing patches, single-wire pull-out specimens, and multiple wire pull-out specimens, respectively. The results suggest that no loss of prestress occurred during activation. The results suggest that the prestressing force was proportional to the number of NiTiNb wires in the patch.

- Scaling up the patch to achieve a double-sided repair using two 85 mm wide patches with 37 wires each would generate prestressing force of 12 kN, which is comparable to the configuration that has been previously used to extend the fatigue life of cracked steel element tested by Taljsten et al. (2009).

7.6. Performance of the patch under fatigue loading

In this research a self-stressing SMA/FRP patch was tested under fatigue loading to examine the stability of the prestressing force that was generated by activating the NiTiNb SMA wires. Two different prestressing levels and three force ranges were considered in this study. Based on these tests the following conclusions can be drawn:

- A stable prestress can be achieved when the NiTiNb SMA wires are partially activated to 250 MPa such that the maximum stress during the application of fatigue loading is less than the stress required to initiate debonding of the wire. In this case a minimal loss of prestress can be expected after 2 million loading cycles.
- A sudden loss of 40% of the prestressing occurred for the specimens which were partially activated to 250 MPa and tested such that the maximum applied load was greater than the load at the onset of debonding. The loss of prestress force

gradually decreased and stabilized at 60,000 cycles at 60%. Rupture of the first SMA wire was observed after 106,000 and 109,000 cycles for the two tested specimens. Rupture of one of the wires occurred accompanied by a sudden decrease of the residual prestressing force and rupture of subsequent wires due to the increased demand on the intact wires. Complete debonding was observed after 117,000 and 115,000 cycles for the two tested specimens.

- Specimens with full activation of the wires exhibited a sudden loss in the prestress as soon as the fatigue loading was applied as debonding initiated. The prestress was completely lost after 24,000 and 33,000 loading cycles for the two tested specimens. Complete failure occurred by rupture of one or more of the wires at 58,900 and 49,600 cycles for the two tested specimens.
- An empirical model was presented which can be used to predict the degradation of the prestressing force based on the stress range and the initial prestress level. The proposed model along with the bond study presented in this dissertation can be used to facilitate the design a self-stressing repair system.

7.7. Limitations

This dissertation presents the pilot study to develop the self-stressing patch. The limitations of this study are as the following:

- In this research the recovery force was found to be proportion to the number of wires in the self-stressing patch. However, the maximum number of wires was limited to 10 wires. The scaling effect should be evaluated for larger number of wires.

- The stability of the thermomechanical properties of the NiTiNb wires and resin were not evaluated when subjected to cyclic sub-zero temperatures. The sub-zero temperature could lead to a reduction of the prestressing force in the wires and embrittlement of the resin which may compromise the efficiency of the proposed repair system.
- The suitability of applying the self-stressing patch to a cracked steel member in confined areas was not evaluated.

7.8. Recommended future work

While the current research led to the development of the self-stressing patch additional research work is needed to increase the efficiency of the proposed repair system and to deepen the understanding of the behavior of the patch. Recommended topics for future research include:

- Based on the experimental results obtained in this research the self-stressing patch was developed. The performance of the patch under monotonic and fatigue loading is satisfactory. However, the effectiveness of using the patch to increase the fatigue life of cracked members needs to be examined.
- The proposed system was developed specifically with the target application of repairing cracked steel structures in mind. The potential to use this or a similar patch configuration for other similar prestressing applications should be investigated.
- Different techniques to increase the bond capacity of the SMA wires to FRP patches, such as modifying the wire geometry in the anchorage zone or selecting

different adhesives, should be investigated with the objective of increasing the efficiency of the proposed self-stressing patch.

- The quantification of the CZM parameters for NiTiNb wires embedded in FRP neglected any interdependencies between the parameters. Further investigation is needed to study any possible interdependencies between the parameters, which could lead to better predictions of the debonding behavior.
- More specimens need to be tested to validate the loss of prestress when the applied load is less than the load at onset of debonding. The model was developed based on specimens with a partial prestress of 250 MPa only. Other initial prestressing level and applied stress ranges should be considered to make the predictions more robust.
- A physics-based model should be developed to predict the fatigue degradation of the prestressing force in the NiTiNb wires. Such a model would facilitate the development of a more comprehensive platform for the design of the proposed patches.
- The research findings indicate that the NiTiNb wire could fail by rupture under fatigue loading. The fatigue behavior of a single wire should be investigated to evaluate the fatigue lives at different stress range.

References

Alam, M., Youssef, M., and Nehdi, M. (2007). Utilizing shape memory alloys to enhance the performance and safety of civil infrastructure: A review. *Canadian Journal of Civil Engineering*, 34(9), 1075-1086.

Almar-Naess, A., Haagensen, P., Lian, B., Moan, T., and Simonsen, T. (1984). Investigation of the Alexander L. Kielland failure metallurgical and fracture analysis. *Journal of Energy Resources Technology*, 106(1), 24-31.

Andrawes, B., and Shin, M. (2008). Seismic retrofitting of bridge columns using shape memory alloys. *Proceedings of the SPIE - The International Society for Optical Engineering*, 9 pages.

Andrawes, B., Shin, M., and Wierschem, N. (2010). Active confinement of reinforced concrete bridge columns using shape memory alloys. *Bridge Engineering*, 15(1), 81-89.

ASTM International. (2014). F2516 Standard test method for tension testing of nickel-titanium superelastic materials. West Conshohocken, PA, USA.

ASTM International. (2014). D3039/D3039M Standard test method for tensile properties of polymer matrix composite materials. West Conshohocken, PA, USA.

ASTM International. (2014). D638-14 Standard test method for tensile properties of plastics. West Conshohocken, PA, USA.

Bassetti, A., Nussbaumer, A., and Hirt, M. (2000). Crack repair and fatigue life extension of riveted bridge members using composite materials. *Proceedings of the Bridge Engineering Conference*, Sharm El Sheikh, Egypt, 375-380.

Baz, A., Chen, T., and Ro, J. (2000). Shape control of NITINOL-reinforced composite beams. *Composites Part B: Engineering*, 31(8), 631-642.

Chang, B., Phares, B., Sarkar, P., and Wipf, T. (2009). Development of a procedure for fatigue design of slender support structures subjected to wind-induced vibration. Transportation Research Record 2131, *Transportation Research Board*, Washington, DC, 23–33.

Chen, Q., Shin, M., and Andrawes, B. (2014). Experimental study of non-circular concrete elements actively confined with shape memory alloy wires. *Construction and Building Materials*, 61, 303-11.

Choi, E., Cho, S., Hu, J., Park, T., and Chung, Y. (2010). Recovery and Residual Stress of SMA Wires and Applications for Concrete Structures. *Smart Materials and Structures*, 19(9), 10 pages.

Choi, E., Chung, Y., Kim, Y., and Kim, J. (2011). Monotonic and cyclic bond behavior of confined concrete using NiTiNb SMA wires. *Smart Material and Structures*, 20(7), 11 pages.

Cladera, A., Weber, B., Leinenbach, C., Czaderski, C., Shahverdi, M., and Motavalli, M. (2014). Iron-based shape memory alloys for civil engineering structures: An overview. *Construction and Building Materials*, 63, 281-93.

Colombi, P., Fava, G., and Sonzogni, L. (2015). Fatigue crack growth in CFRP-strengthened steel plates. *Composites Part B: Engineering*, 72, 87-96

Czaderski, C., Hahnebach, B., and Motavalli, M. (2006). RC beam with variable stiffness and strength. *Construction & Building Materials*, 20(9), 824-33.

Czaderski, C., Shahverdi, M., Bronnimann, R., Leinenbach, C., and Motavalli, M. (2014). Feasibility of iron-based shape memory alloy strips for prestressed strengthening of concrete structures, *Construction and Building Materials*, 56, 94-105.

Dassault Systèmes Simulia Corp. (2012). *Abaqus 6.12-1 Analysis User`s Manual*. Providence, RI: Dassault Systèmes Simulia Corp.

Dawood, M., El-Tahan, M., and Zheng, B. (2015). Bond behavior of superelastic shape memory alloys to carbon fiber reinforced polymer composites. *Composites Part B: Engineering*, 77, 238-247.

Domazet, Z. (1996). Comparison of fatigue crack retardation methods. *Engineering Failure Analysis*, 3(2), 137-147

Dommer, K., and Andrawes B. (2012). Thermomechanical Characterization of NiTiNb Shape Memory Alloy for Concrete Active Confinement Applications, *Materials in Civil Engineering*, 24(10), 16-24.

Dong, Z., Klotz, U., Leinenbach, C., Bergamini, A., Czaderski, C., and Motavalli, M. (2009). A novel Fe-Mn-Si shape memory alloy with improved shape recovery properties by VC precipitation, *Advanced Engineering Materials*, 11(1-2), 40-4.

Emdad, R., and Al-Mahaidi, R. (2015). Effect of prestressed CFRP patches on crack growth of centre-notched steel plates. *Composite Structures*, 123, 109-122.

Epps, J., and Chandra, R. (1997). Shape memory alloy actuation for active tuning of composite beams. *Smart Materials and Structures*, 6(3), 251-264.

Fam, A., MacDougall, C., and Shaat, A. (2009). Upgrading steel-concrete composite girders and repair of damaged steel beams using bonded CFRP laminates. *Thin-Walled Structures*, 47(10), 1122-1135.

Fisher, J., Kulak, G., and Smith, I. (1998). A fatigue primer for structural engineers. *National steel bridge alliance.*

Foley, C., Fournelle, R., Ginal, S., and Peronto, J. (2004). Structural analysis of sign bridge structures and luminaire supports, *Wisconsin DOT*, Madison, WI.

Gao, F., Wang, Z., Wang, Y., Wang, Y., and Li, J. (2014). A Prototype of a biomimetic mantle jet propeller inspired by cuttlefish actuated by SMA wires and a theoretical model for its jet thrust. *Bionic Engineering*, 11(3), 412-422.

Ghafoori, E., and Motavalli, M. (2013). Flexural and interfacial behavior of metallic beams strengthened by prestressed bonded plates. *Composite Structures*, 101, 22-34.

Ghafoori, E., Motavalli, M., Botsis, J., Herwig, A., and Galli, M. (2012a). Fatigue strengthening of damaged metallic beams using prestressed unbonded and bonded CFRP plates. *International Journal of Fatigue*, 44, 303-315

Ghafoori, E., Motavalli, M., Nussbaumer, A., Herwig, A., Prinz, G., and Fontana, M. (2015a). Design criterion for fatigue strengthening of riveted beams in a 120-year-old railway metallic bridge using pre-stressed CFRP plates. *Composites Part B: Engineering*, 68, 1-13.

Ghafoori, E., Motavalli, M., Nussbaumer, A., Herwig, A., Prinz, G., and Fontana, M. (2015b). Determination of minimum CFRP pre-stress levels for fatigue crack prevention in retrofitted metallic beams. *Engineering Structures*, 84, 29-41.

Ghafoori, E., Schumacher, A., and Motavalli, M. (2012b). Fatigue behavior of notched steel beams reinforced with bonded CFRP plates: Determination of prestressing level for crack arrest. *Engineering Structures*, 45, 270-283.

GOM mbH. (2011). *ARAMIS User Manual-Software*. Braunschweig, Germany: GOM mbH.

Goode, J., and Van De Lindt, J. (2007) development of a semi-prescriptive selection procedure for reliability-based fatigue design of high mast lighting structural supports. *Performance of constructed facilities*, 21(3), 193-206.

Goodman, J. (1899). *Mechanics applied to engineering*. London, Longman, Green & Company.

Huawen, Y., Konig, C., Ummenhofer, T., Shizhong, Q., and Plum, R. (2010). Fatigue Performance of Tension Steel Plates Strengthened with Prestressed CFRP Laminates. *Composites for Construction*, 14(5), 609–615.

Icardi, U. (2001). Large bending actuator made with SMA contractile wires: Theory, numerical simulation and experiments. *Composites Part B: Engineering*, 32(3), 259-267

Jang, B., and Kishi, T. (2005). Adhesive strength between TiNi fibers embedded in CFRP composites. *Materials Letters*, 59(11), 1338-1341.

Janke, L., Czaderski, C., Motavalli, M., and Ruth, J. (2005). Applications of shape memory alloys in civil engineering structures - Overview, limits and new ideas, *Materials and Structures*, 38(279), 578-592.

Jiao, H., Mashiri, F., and Zhao, X. (2012). A comparative study on fatigue behaviour of steel beams retrofitted with welding, pultruded CFRP plates and wet layup CFRP. *Thin-Walled Structures*, 59, 144-152.

Johnsom, J. (1899). *The materials of construction*. 1st edition. New York, John Wiley and Sons.

Jones, R. (1999). Mechanics of composite materials. *Hemisphere publishing corporation.*

Jones, S., and Civjan, S. (2003). Application of fiber reinforced polymer overlays to extend steel fatigue life. *Journal of Composites for Construction*, 7(4), 331-338.

Jonnalagadda, K., Kline, G., and Sottos, N. (1997). Local displacements and load transfer in shape memory alloy composites. *Experimental Mechanics*, 37(1), 78-86.

Koller, R., Stoecklin, I., Valet, S., and Terrasi, G. (2014). CFRP-Strengthening and Long-Term Performance of Fatigue Critical Welds of a Steel Box Girder. *Polymers*, 6(2), 443-463.

Lagoudas, D., Mayes, J., and Khan, M. (2001). Simplified shape memory alloy (SMA) material model for vibration isolation, *Proceedings of the SPIE - The International Society for Optical Engineering*, 4326, 452-61.

Lam, A., Cheng, J., Yam, M., and Kennedy, G. (2007). Repair of steel structures by bonded carbon fibre reinforced polymer patching: Experimental and numerical study of carbon fibre reinforced polymer - Steel double-lap joints under tensile loading. *Canadian Journal of Civil Engineering*, 34(12), 1542-1553.

Lau, K., Chan, A., Shi, S., and Zhou, L. (2002). Debond induced by strain recovery of an embedded NiTi wire at a NiTi/epoxy interface: micro-scale observation. *Materials and Design*, 23(3), 265-270.

Liu, M., Li, H., Song, G., and Ou, J. (2007). Investigation of vibration mitigation of stay cables incorporated with superelastic shape memory alloy dampers. *Smart Materials and Structures*, 16(6), 2202-2213.

Loughlan, J., Thompson, S., and Smith, H. (2002). Buckling control using embedded shape memory actuators and the utilization of smart technology in future aerospace platforms. *Composite structures*, 58, 319–347.

Maji, B., Das, C., Krishnan, M., and Ray, R. (2006). The corrosion behaviour of Fe-15Mn-7Si-9Cr-5Ni shape memory alloy. *Corrosion Science*, 48(4), 937-949.

Melton, K., and Mercier, O. (1981). Mechanical properties of NiTi-based shape memory alloys. *Acta Metallurgica*, 29(2), p 393-398.

Melton, K., Simpson, J., and Duerig, T. (1986). A new wide hysteresis based shape memory alloy and its applications. *Proceedings of the international conference on martensitic transformation*, 1053-1058.

Melton, K., Proft, J., and Duerig, T. (1989). Wide hysteresis shape memory alloys based on the NiTINb system. *Materials research society international symposium proceedings*.

Moser, K., Bergamini, A., Christen, R., and Czaderski, C. (2005). Feasibility of concrete prestressed by shape memory alloy short fibers. Materials and Structures, 38(279), 593-600.

Moser, K., Bergamini, A., Christen, R., and Czaderski, C. (2004). Feasibility of concrete prestressed by shape memory alloy short fibers. *Materials and Structures*, 38(5), 593-600.

Nakamura, H., Jiang, W., Suzuki, H., Maeda, K., and Irube, T. (2009). Experimental study on repair of fatigue cracks at welded web gusset joint using CFRP strips. *Thin-Walled Structures*, 47(10), 1059-1068

NDC (2015a). Material data sheet: shape memory Nitinol alloys, accessed from http://www.nitinol.com/wp-content/uploads/2012/01/Material-Data-Sheet-Shape-Memory.pdf on April 19, 2015.

NDC (2015b). Material data sheet: superelastic Nitinol alloys, accessed from http://www.nitinol.com/wp-content/uploads/2012/01/Material-Data-Sheet-Superelastic.pdf on April 19, 2015.

Payandeh, Y., Meraghni, F., Patoor, E., and Eberhardt, A. (2010). Debonding initiation in a NiTi shape memory wire-epoxy matrix composite. Influence of martensitic transformation. *Materials and Design*, 31(3), 1077-1084.

Payandeh, Y., Meraghni, F., Patoor, E., and Eberhardt, A. (2009). Effect of martensitic transformation on the debonding propagation in Ni-Ti shape memory wire composite. *Materials Science and Engineering A*, 518(1-2), 35-40.

Payandeh, Y., Meraghni, F., Patoor, E., and Eberhardt, A. (2012). Study of the martensitic transformation in NiTi-epoxy smart composite and its effect on the overall behavior. *Materials and Design*, 39, 104-110.

Poon, C., Zhou, L., Jin, W., and Shi, S. (2005a). Interfacial debond of shape memory alloy composites. *Smart Materials and Structures*, 14(4), N29-N37.

Poon, C., Lau, k., and Zhou, L. (2005b). Design of pull-out stresses for prestrained SMA wire/polymer hybrid composites. *Composites Part B: Engineering*, 36(1), 25-31.

Raghavan, J., Bartkiewicz, T., Boyko, S., Kupriyanov, M., Rajapakse, N., and Yu, B. (2010). Damping, tensile, and impact properties of superelastic shape memory alloy (SMA) fiber-reinforced polymer composites. *Composites Part B: Engineering*, 41(3), 214-222.

Rossi, C., Colorado, J., Coral, W., and Barrientos, A. (2011). Bending Continuous Structures with SMAs: a Novel Robotic fish Design. *Bioinspiration & Biomimetics*, 6(4), 15 pages.

Rovere, C., Alano, J., Silva, R., Nascente, P., Otubo, J., and Kuri, S. (2012). Influence of alloying elements on the corrosion properties of shape memory stainless steels, *Materials Chemistry and Physics*, 133(2-3), 668-73.

Sadrnezhaad, S., Nemati, N., and Bagheri, R. (2009). Improved adhesion of NiTi wire to silicone matrix for smart composite medical applications. *Materials and Design*, 30(9), 3667-3672.

Schnerch, D., and Rizkalla, S. (2008). Flexural strengthening of steel bridges with high modulus CFRP strips. *Journal of Bridge Engineering*, 13(2), 192-201.

Sharp, P., Clayton, J., and Clark, G. (1994). The fatigue resistance of peened 7050-T7541 aluminum alloy repair and treatment of a component surface. *Fatigue & Fracture of Engineering Materials & Structures*, 17(3), 243–252, March 1994

Shin, M., and Andrawes, B. (2010). Experimental investigation of actively confined concrete using shape memory alloys. *Engineering Structures*, 32(3), 656-664.

Shin, M., and Andrawes, B. (2011). Lateral cyclic behavior of reinforced concrete columns retrofitted with shape memory spirals and FRP wraps. *Structural Engineering*, 137(11), 1282-1290.

Shin, M., and Andrawes, B. (2011a). Emergency repair of severely damaged reinforced concrete columns using active confinement with shape memory alloys. *Smart Materials and Structures*, 20(6), 9 pages.

Shin, M., and Andrawes, B. (2011b). Lateral Cyclic Behavior of Reinforced Concrete Columns Retrofitted with Shape Memory Spirals and FRP Wraps. *Journal of Structural Engineering*, 137(11), 1282–1290.

Simpson, J., Melton, K., and Duerig, T. (1986). *US Patent No. 4,631,094.* Accessed from http://patft.uspto.gov/ on April 2, 2015.

Sippola, M., and Lindeoos, T. (2007). Adaptive composite structures in shape control application. *Structural mechanics*, 40(1), 65-79.

Sittner, P., and Stalmans, R. (2000). Developing hybrid polymer composites with embedded shape memory alloy wires. *JOM*, 52(10), 15-20.

Song, G., Hu, Z., Sun, K., Ma, N., Economides, M., Robello, S., and Ehlig-Economides, C. (2008). An Innovative ultradeepwater subsea blowout preventer control system using shape-memory alloy actuators. *Energy Resources Technology*, 130(3), 7 pages.

Song, G., Kelly, B., and Agrawal, B. (2000a). Active position control of a shape memory alloy wire actuated composite beam. *Smart Materials and Structures*, 9(5), 711-716.

Song, G., Kelly, B., Agrawal, B., Lam, P., and Srivatsan, T. (2000b). Application of Shape Memory Alloy Wire Actuator for Precision Position Control of a Composite Beam. *Journal of Materials Engineering and Performance*, 9(3), 330-333.

Song, G., Ma, N., Lee, H., and Arnold, S. (2007). Design and control of a proof-of-concept variable area exhaust nozzle using shape-memory alloy actuators. *Smart Materials and Structures*, 16(4), 1342-7.

Taljsten, B., Hansen, C., and Schmidt, J. (2009). Strengthening of old metallic structures in fatigue with prestressed and non-prestressed CFRP laminates. *Construction and Building Materials*, 23(4), 1665–1677.

Tavakkolizadeh, M., and Saadatmanesh, H. (2003). Fatigue strength of steel girders strengthened with carbon fiber reinforced polymer patch. *Journal of Structural Engineering*, 129(2), 186-196.

Turner, T. (2005). SMA hybrid composites for dynamic response abatement applications. *Journal of Vibration and Acoustics*, 127(3), 273-279.

Walbridge, S., Soudki, K., and Vatandoost, F. (2011). Fatigue retrofitting of welded steel cover plates using pre-stressed carbon fiber reinforced polymer strips. *Structural Engineering International*, 21(3), 279-284.

Wang, H., Wu, G., and Wu, A. (2014). Effect of FRP configurations on the fatigue repair effectiveness of cracked steel plates. *Composites for Construction*, 18(1), 11 pages.

Wang, Y., Zhou, L., Wang, Z., Huang, H., and Ye, L. (2011). Analysis of internal stresses induced by strain recovery in a single SMA fiber-matrix composite. *Composites Part B: Engineering*, 42(5), 1135-1143.

Wierschem, N., and Andrawes, B. (2010). Superelastic SMA-FRP composite reinforcement for concrete structures. *Smart Materials and Structures*, 19(2), 13 pages

Wu, C., Zhao, X., AI-Mahaidi, R., Emdad, M., and Duan, W. (2012). Fatigue Tests of Cracked Steel Plates Strengthened with UHM CFRP Plates. *Advances in Structural Engineering*, 15(10), 1801-1815.

Wu, G., Wang, H., Wu, Z., Liu, H., and Ren, Y. (2012). Experimental study on the fatigue behavior of steel beams strengthened with different fiber-reinforced composite plates. *Composites for Construction*, 16(2), 127-137.

Ying, C., Hai-chang, J., Li-jian, R., Li, X. and Xin-qing, Z. (2011). Mechanical behavior in NiTiNb shape memory alloys with low Nb content. *Intermetallics*, 19(2), 217-220.

Yuse, K. and Kikushima, Y. (2005). Development and experimental consideration of SMA/CFRP actuator for vibration control. *Sensors and Actuators A (Physical)*, 122(1), 99–107.

Zafar, A. and Andrawes, B. (2014). Fabrication and Cyclic Behavior of Highly Ductile Superelastic Shape Memory Composites. *Materials in Civil Engineering*, 26(4), 622-32.

Zhao, L., Duerig, T., and Wayman, C. (1989). Transformation and Mechanical Behaviour of a Ni47Ti44Nb9 Shape Memory Alloy. *Proceedings of the MRS international meeting on advanced materials "Shape memory materials"*, 9, 171-176.

Appendices

Appendix A: Detailed Results of the Epoxy Tensile Tests

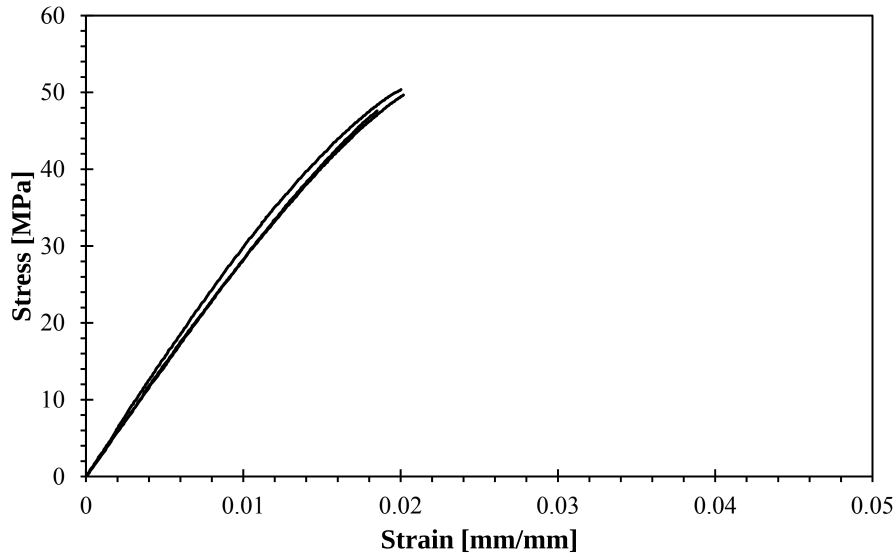

Figure A.1. Stress-strain curves for Tyfo S epoxy coupons cured and tested at 25°C

Table A.1. Test results of Tyfo S epoxy specimens

Post cure temperature [°C]	Test temperature [°C]	Tensile strength [MPa]	Tensile modulus [MPa]	Elongation [mm/mm]
25	24.4	50	2800	0.020
	24.4	48	2775	0.019
	24.3	50	3000	0.020
	44.4	5	---[1]	---[1]
	44.1	5	---[1]	---[1]
	44.2	5	---[1]	---[1]

---[1]: The specimen was too soft to mount an extensometer

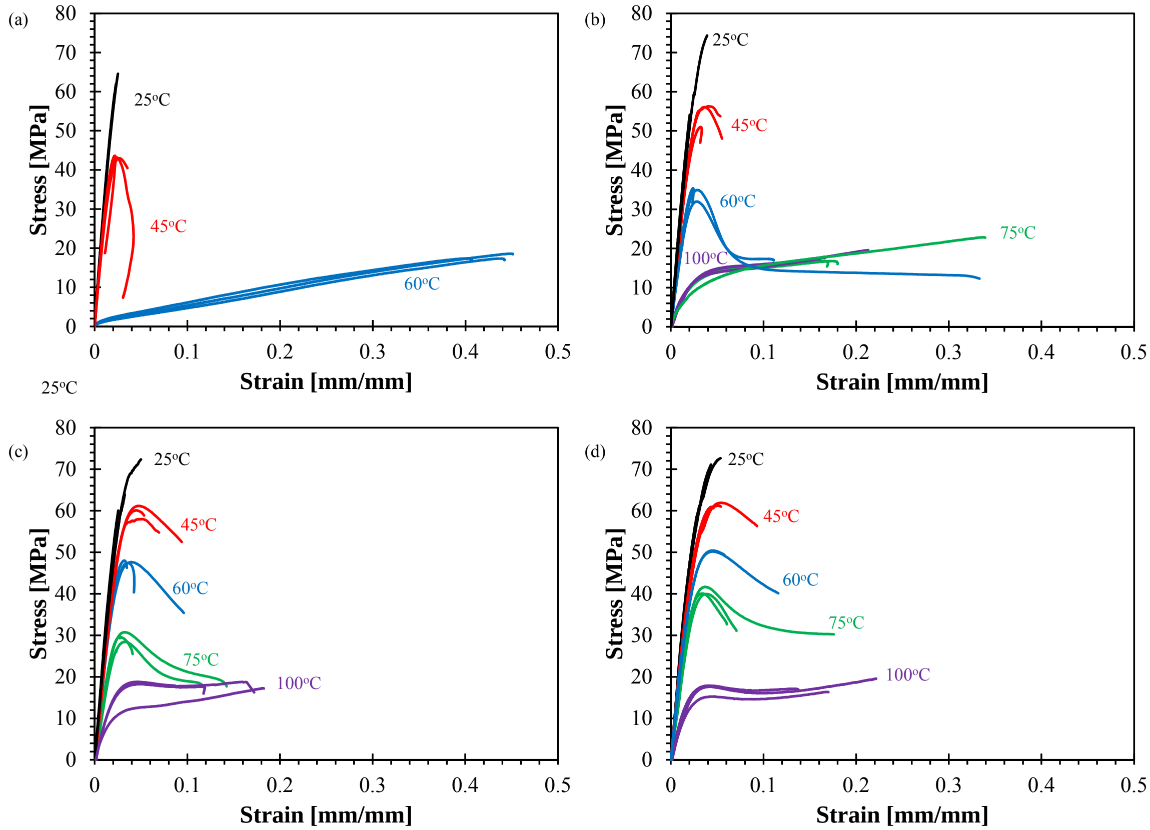

Figure A.2. Stress-strain curves for Araldite epoxy coupons cured at: (a) 25°C, (b) 25°C + post cured at 45°C, (c) 25°C + post cured at 60°C, and (d) 25°C + post cured at 75°C; and tested at various temperatures

Table A.2. Test results of Araldite epoxy specimens cured at 25°C and tested at different ambient temperatures

Post cure temperature [°C]	Test temperature [°C]	Tensile strength [MPa]	Tensile modulus [MPa]	Elongation [mm/mm]
25	24.3	56	2615	0.025
	24.3	52	2720	0.021
	24.2	54	2655	0.023
	44.4	38	2330	0.042
	44.6	38	2490	0.023
	44.6	38	2260	0.035
	60.6	15	40	0.408
	60.6	15	40	0.408
	60.4	16	35	0.451

Table A.3. Test results of Araldite epoxy specimens post cured at 45^{o}C and tested at different ambient temperatures

Post cure temperature [^{o}C]	Test temperature [^{o}C]	Tensile strength [MPa]	Tensile modulus [MPa]	Elongation [mm/mm]
45	24.6	74	2555	0.039
	25.9	44	2785	0.016
	25.7	54	2830	0.020
	44.4	56	2345	0.055
	44.8	56	2320	0.053
	46.1	51	2325	0.033
	62.4	32	1720	0.333
	61.8	35	1845	0.111
	61.1	35	1900	0.025
	75.5	16	980	0.118
	75.5	17	550	0.170
	75.6	17	640	0.180
	99.4	18	510	0.167
	98.6	20	540	0.213
	99.8	17	670	0.160

Table A.4. Test results of Araldite epoxy specimens post cured at 60^{o}C and tested at different ambient temperatures

Post cure temperature [^{o}C]	Test temperature [^{o}C]	Tensile strength [MPa]	Tensile modulus [MPa]	Elongation [mm/mm]
60	24.3	64	2400	0.032
	26.3	60	2675	0.025
	26.1	72	2400	0.050
	45.7	61	2090	0.094
	45.8	58	2210	0.069
	45.7	60	2215	0.053
	61.0	47	2050	0.043
	60.5	48	2040	0.096
	60.2	48	2255	0.035
	75.8	30	1450	0.041
	75.5	28	1250	0.117
	75.5	31	1375	0.142
	97.9	19	765	0.172
	102.0	17	690	0.183
	98.4	18	760	0.119

Table A.5. Test results of Araldite epoxy specimens post cured at 75°C and tested at different ambient temperatures

Post cure temperature [°C]	Test temperature [°C]	Tensile strength [MPa]	Tensile modulus [MPa]	Elongation [mm/mm]
75	26.2	71	2485	0.043
	26.3	73	2545	0.054
	25.9	72	2330	0.051
	45.4	61	2285	0.046
	45.2	62	2185	0.093
	45.3	61	2035	0.054
	60.4	50	2010	0.058
	60.3	50	2275	0.116
	60.8	28	2145	0.014
	75.3	42	1750	0.176
	75.4	40	1595	0.071
	76.2	40	1850	0.060
	98.0	18	870	0.138
	99.4	16	675	0.170
	98.7	19	720	0.210

Appendix B: Detailed Results of the Bond Behavior of the Superelastic NiTi SMA Wires Embedded in CFRP Composite

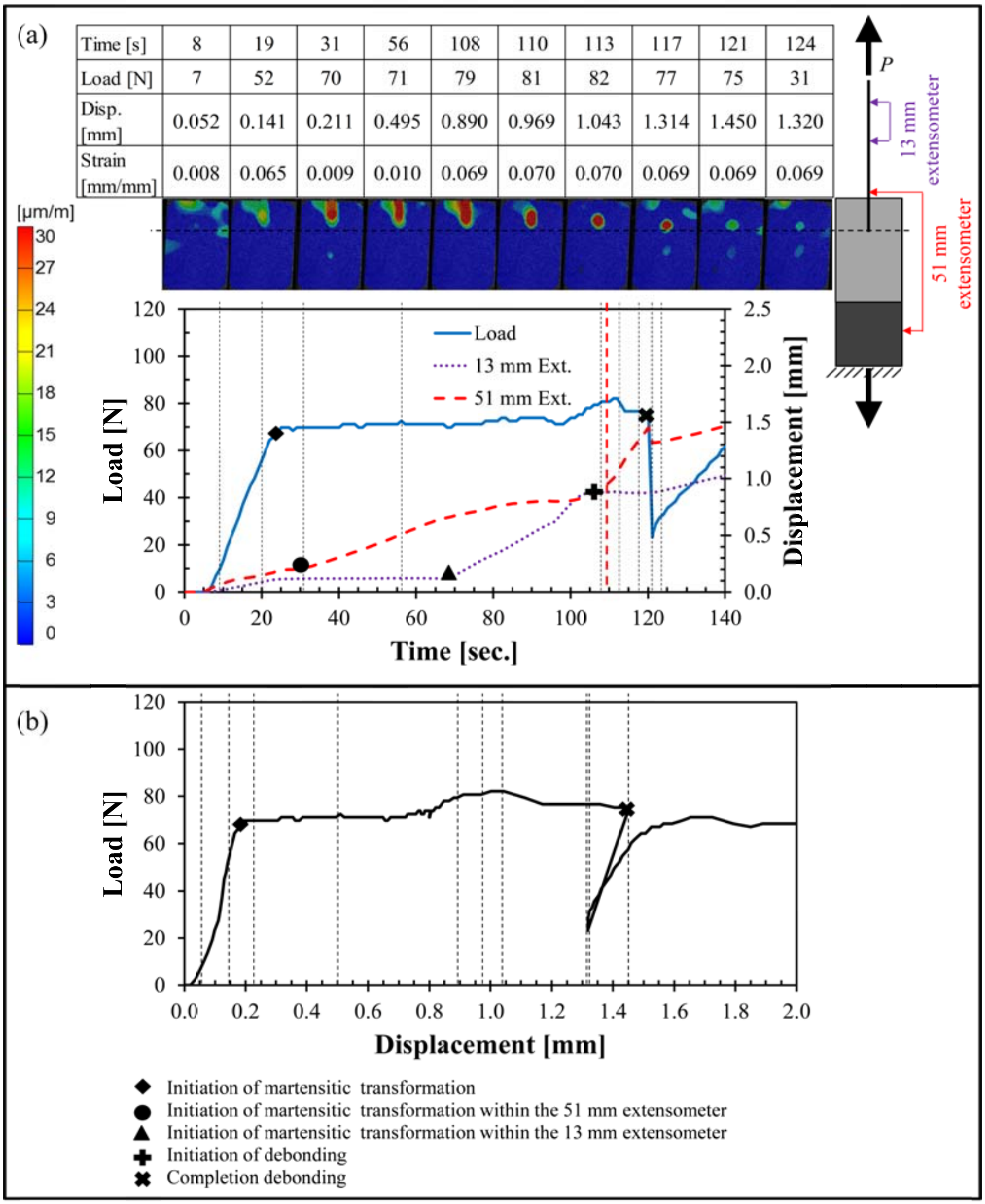

Figure B.1. (a) Load and displacement histories and DIC contours; and (b) Load-displacement relationship for a specimen with L_d of 13 mm and d_b of 0.47 mm, repetition# 1

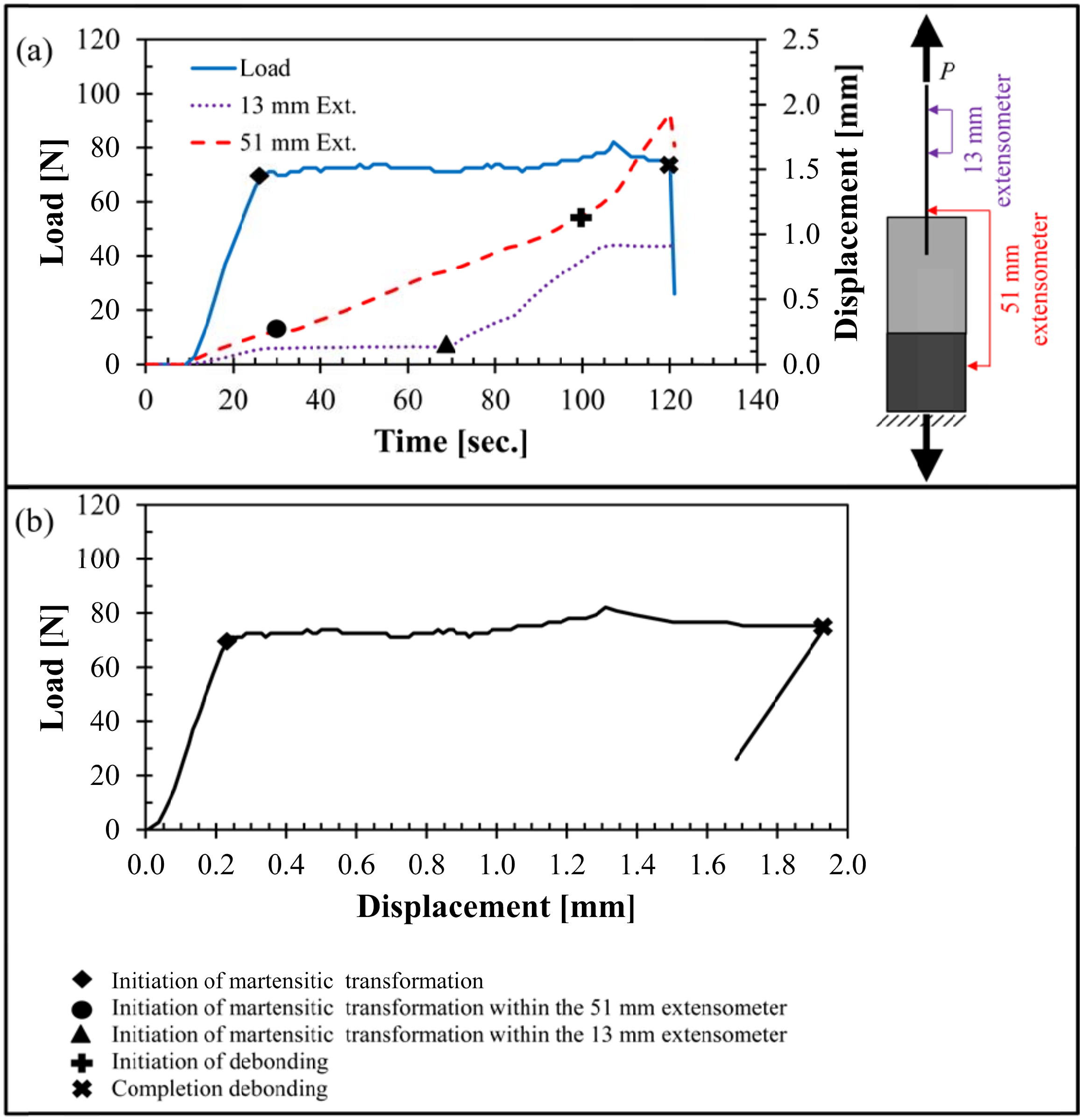

Figure B.2. (a) Load and displacement histories; and (b) Load-displacement relationship for a specimen with L_d of 13 mm and d_b of 0.47 mm, repetition# 2

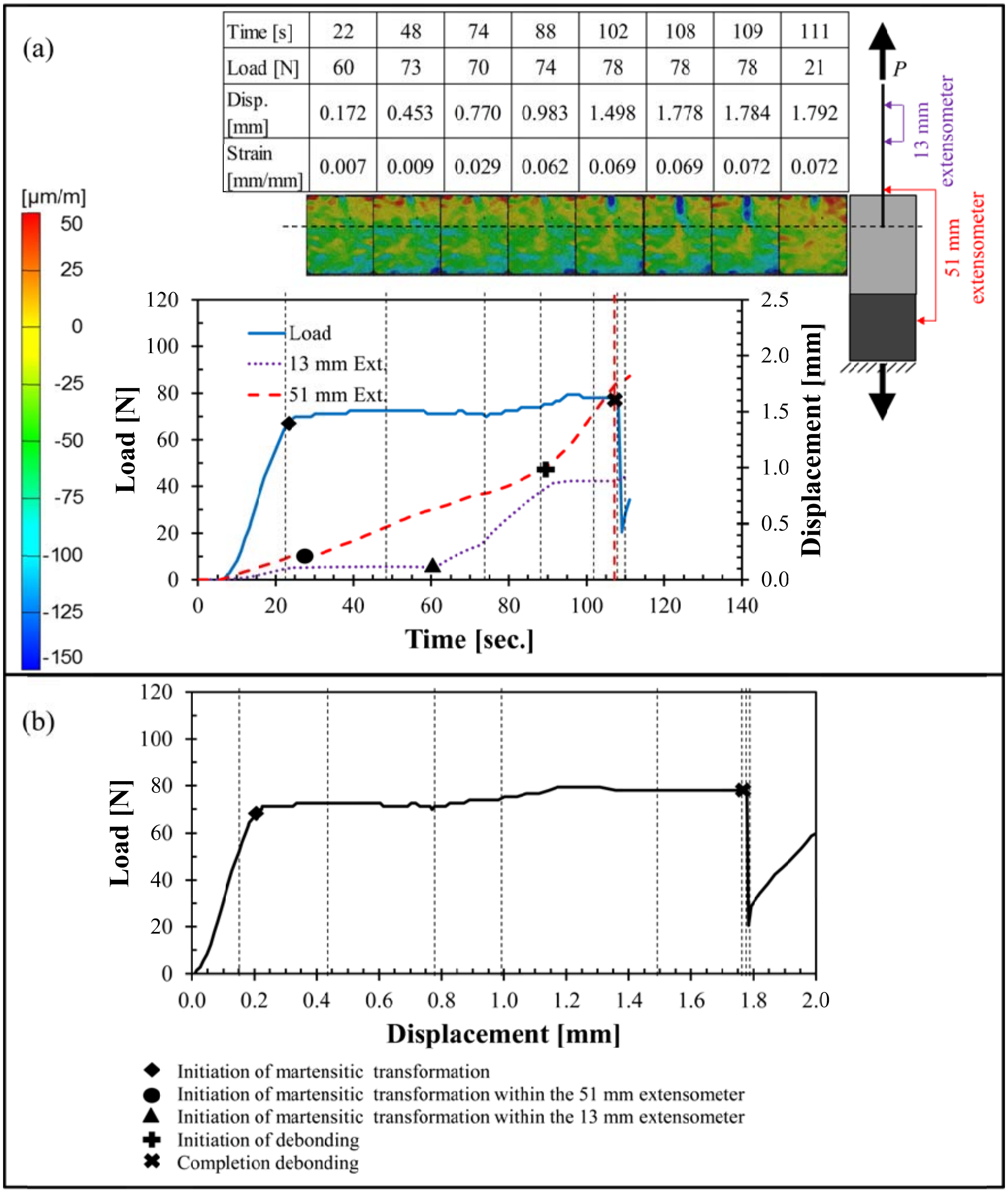

Time [s]	22	48	74	88	102	108	109	111
Load [N]	60	73	70	74	78	78	78	21
Disp. [mm]	0.172	0.453	0.770	0.983	1.498	1.778	1.784	1.792
Strain [mm/mm]	0.007	0.009	0.029	0.062	0.069	0.069	0.072	0.072

Figure B.3. (a) Load and displacement histories and DIC contours; and (b) Load-displacement relationship for a specimen with L_d of 13 mm and d_b of 0.47 mm, repetition# 3

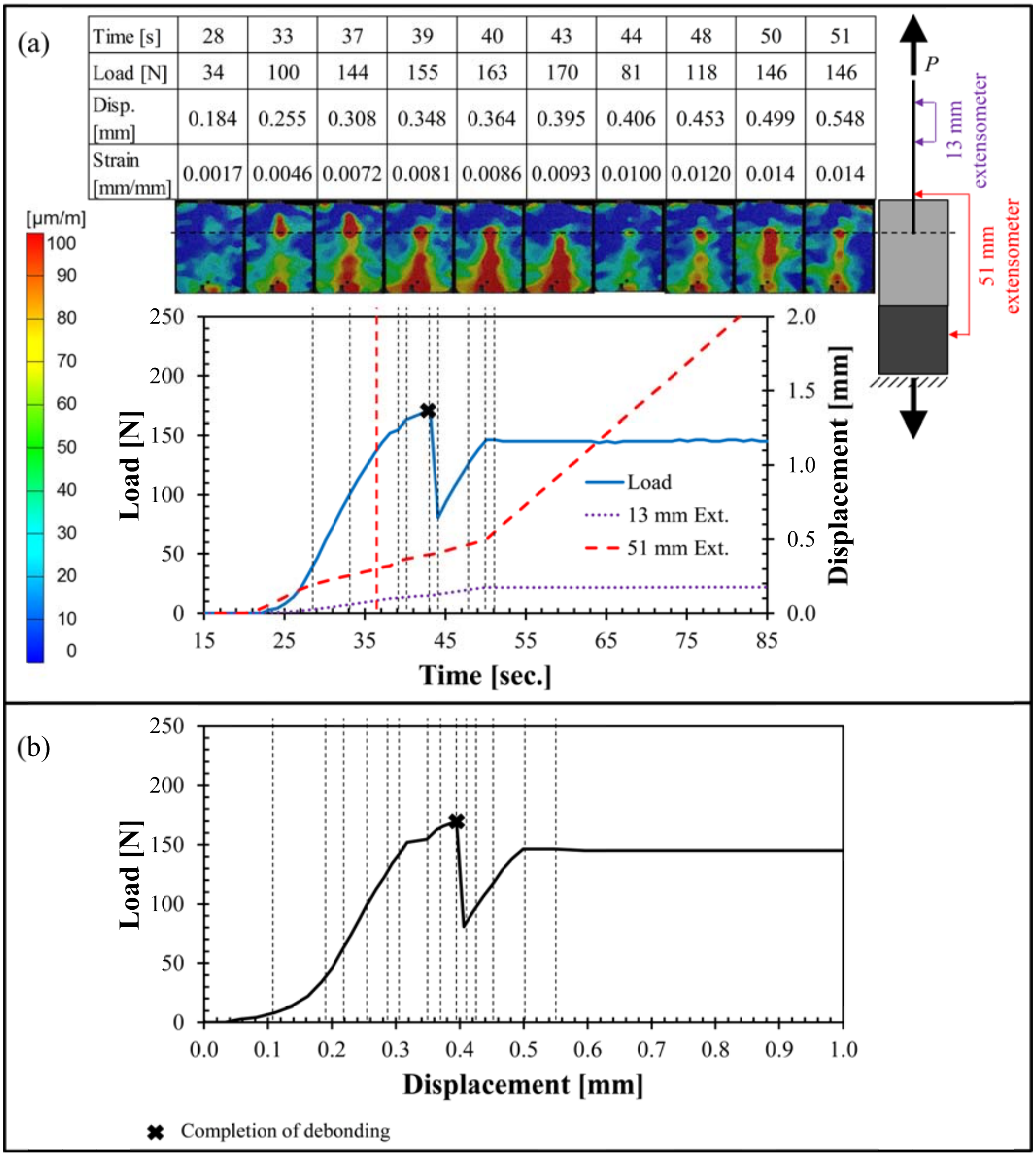

Figure B.4. (a) Load and displacement histories and DIC contours; and (b) Load-displacement relationship for a specimen with L_d of 13 mm and d_b of 0.66 mm, repetition# 1

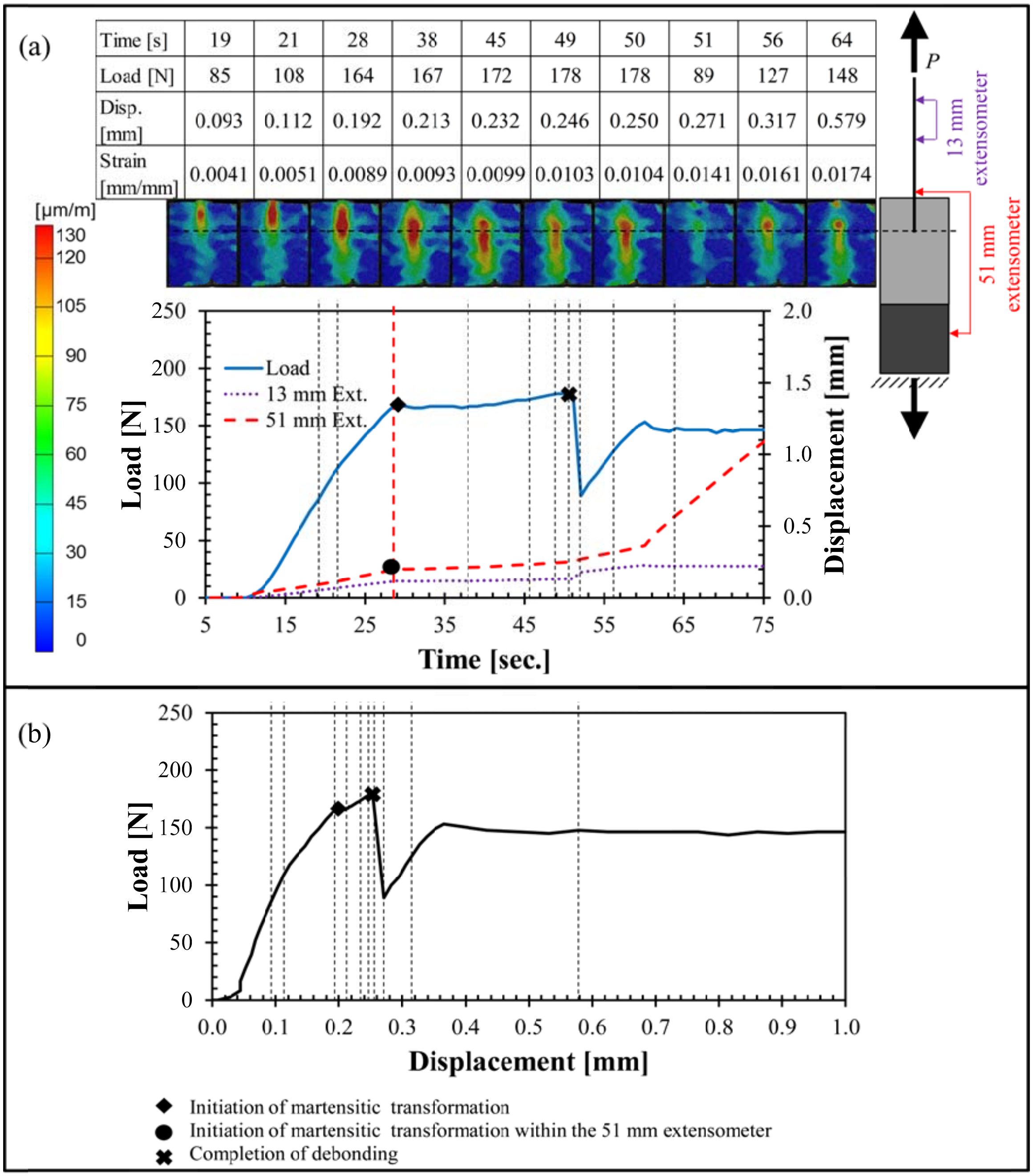

Time [s]	19	21	28	38	45	49	50	51	56	64
Load [N]	85	108	164	167	172	178	178	89	127	148
Disp. [mm]	0.093	0.112	0.192	0.213	0.232	0.246	0.250	0.271	0.317	0.579
Strain [mm/mm]	0.0041	0.0051	0.0089	0.0093	0.0099	0.0103	0.0104	0.0141	0.0161	0.0174

Figure B.5. (a) Load and displacement histories and DIC contours; and (b) Load-displacement relationship for a specimen with L_d of 13 mm and d_b of 0.66 mm, repetition# 2

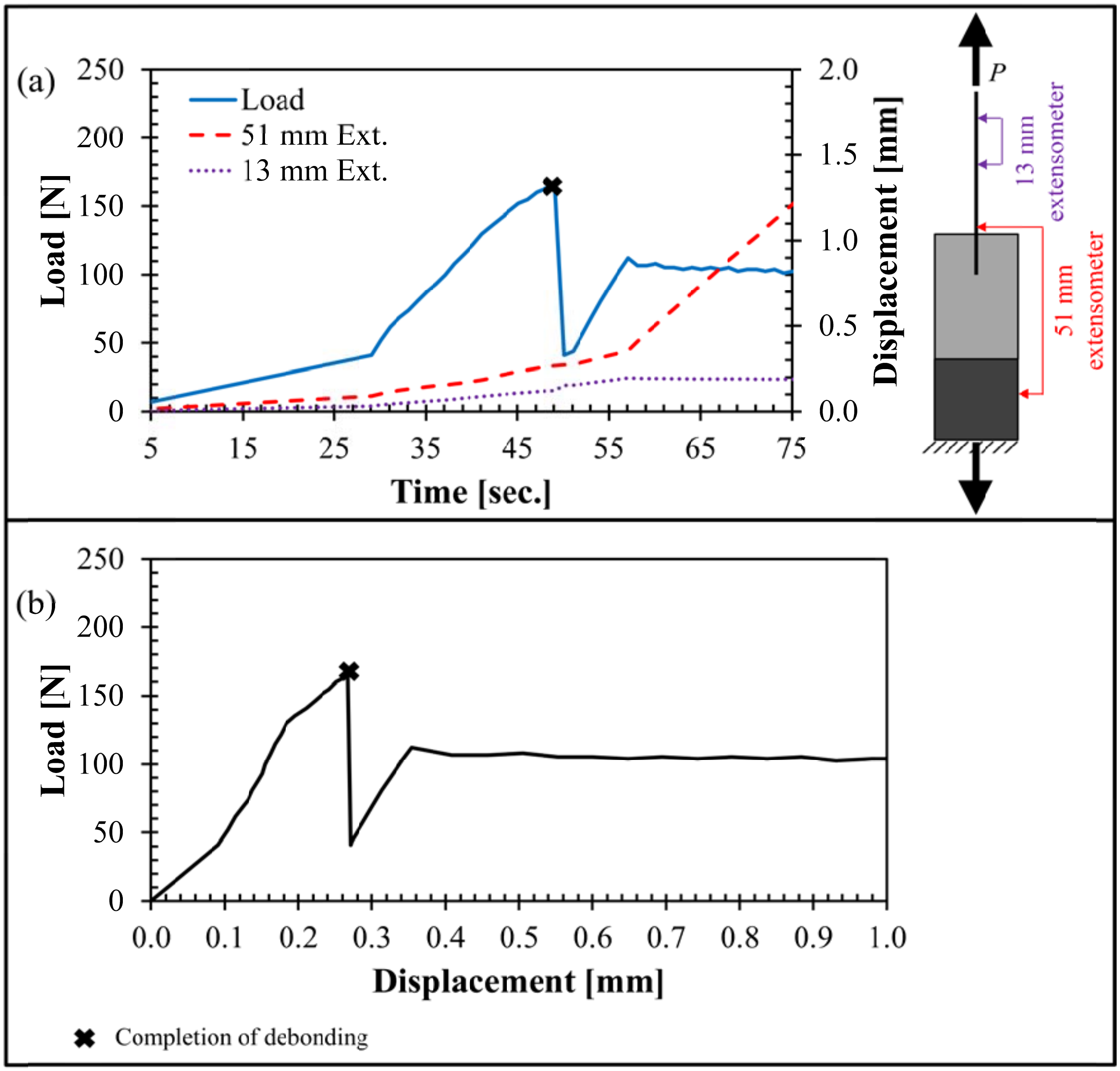

Figure B.6. (a) Load and displacement histories; and (b) Load-displacement relationship for a specimen with L_d of 13 mm and d_b of 0.66 mm, repetition# 3

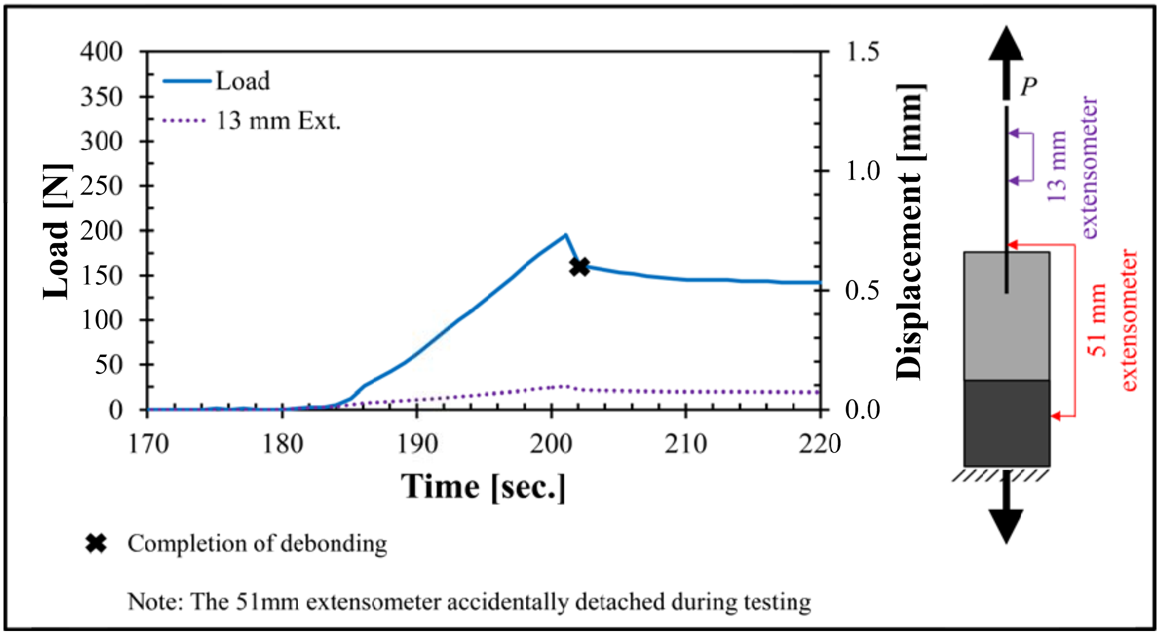

Figure B.7. Load and displacement histories for a specimen with L_d of 13 mm and d_b of 0.89 mm, repetition# 1

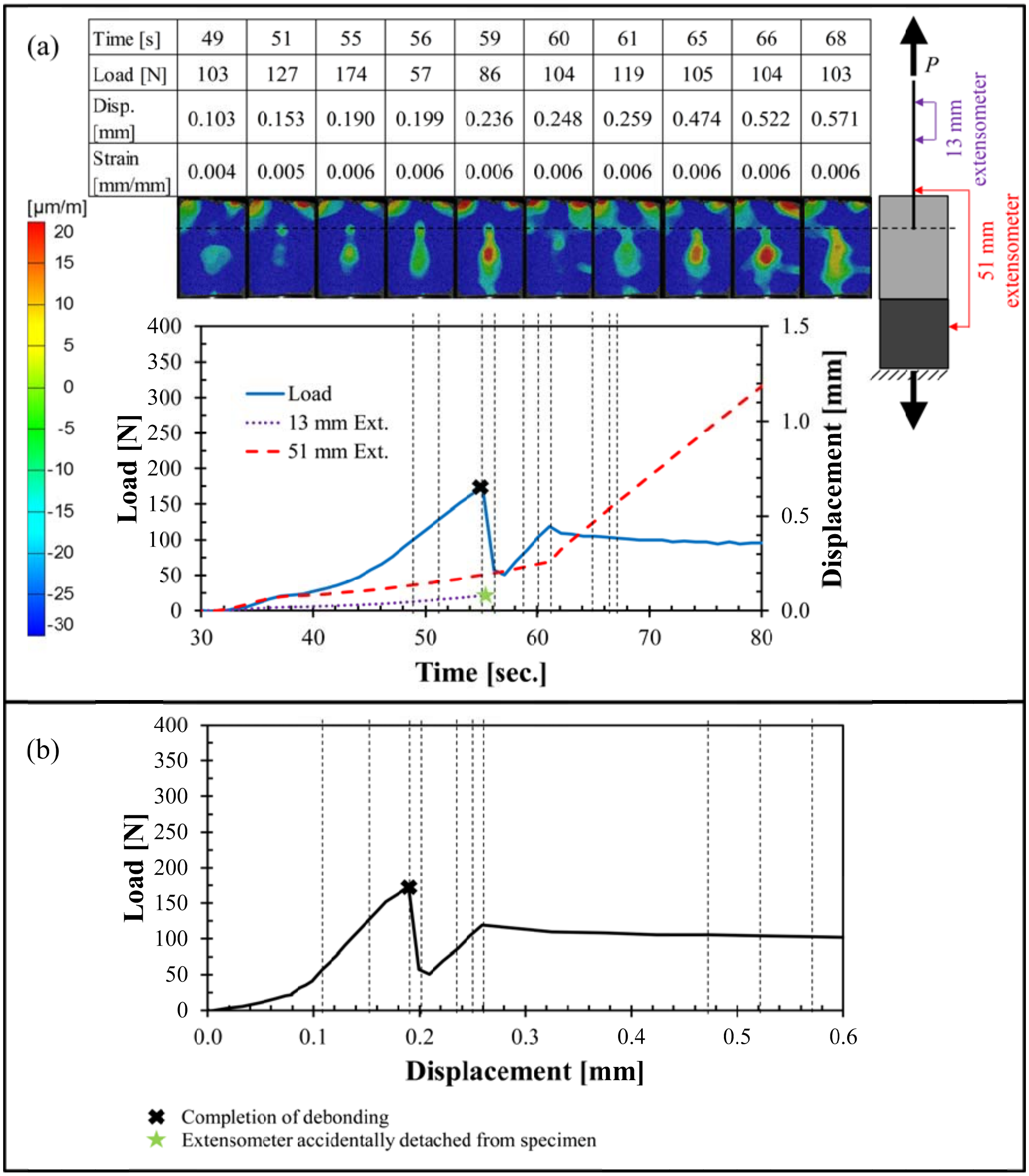

Time [s]	49	51	55	56	59	60	61	65	66	68
Load [N]	103	127	174	57	86	104	119	105	104	103
Disp. [mm]	0.103	0.153	0.190	0.199	0.236	0.248	0.259	0.474	0.522	0.571
Strain [mm/mm]	0.004	0.005	0.006	0.006	0.006	0.006	0.006	0.006	0.006	0.006

Figure B.8. (a) Load and displacement histories and DIC contours; and (b) Load-displacement relationship for a specimen with L_d of 13 mm and d_b of 0.89 mm, repetition# 2

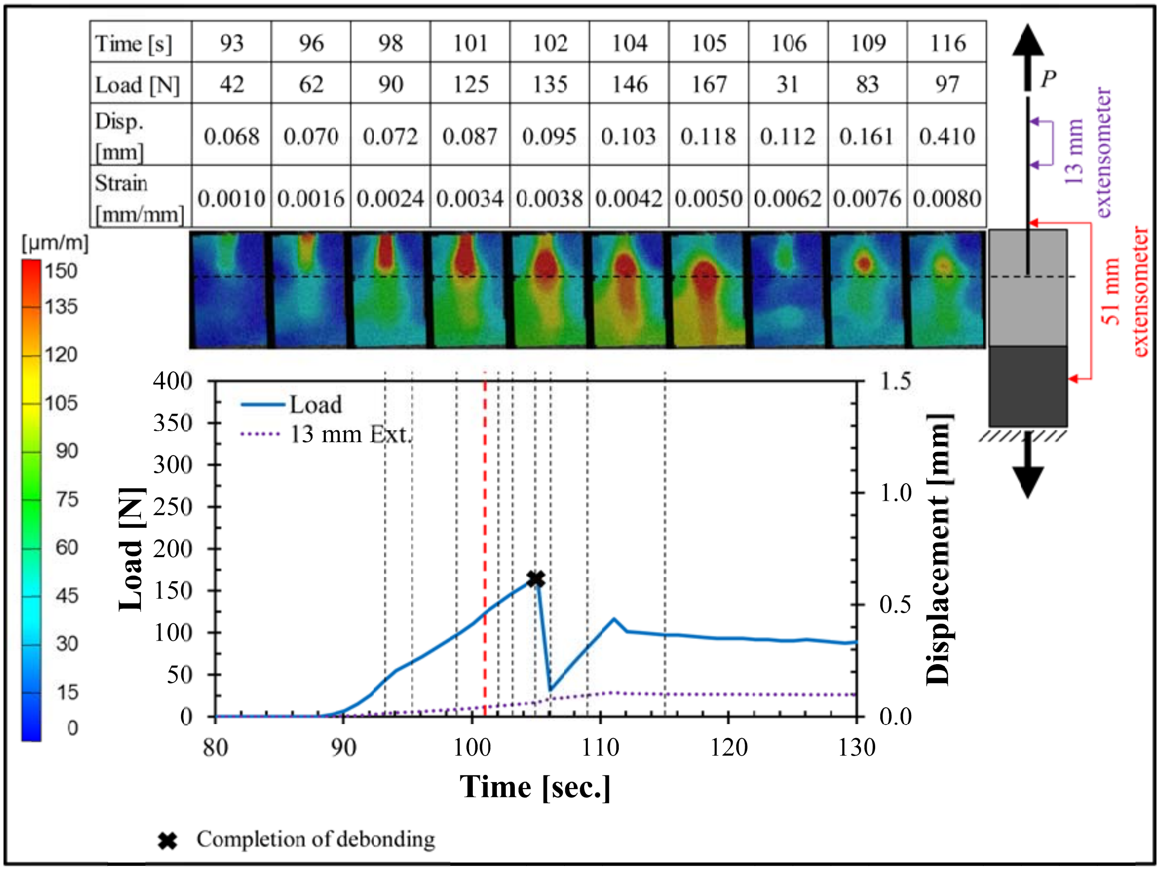

Time [s]	93	96	98	101	102	104	105	106	109	116
Load [N]	42	62	90	125	135	146	167	31	83	97
Disp. [mm]	0.068	0.070	0.072	0.087	0.095	0.103	0.118	0.112	0.161	0.410
Strain [mm/mm]	0.0010	0.0016	0.0024	0.0034	0.0038	0.0042	0.0050	0.0062	0.0076	0.0080

Figure B.9. Load and displacement histories and DIC contours for a specimen with L_d of 13 mm and d_b of 0.89 mm, repetition# 3

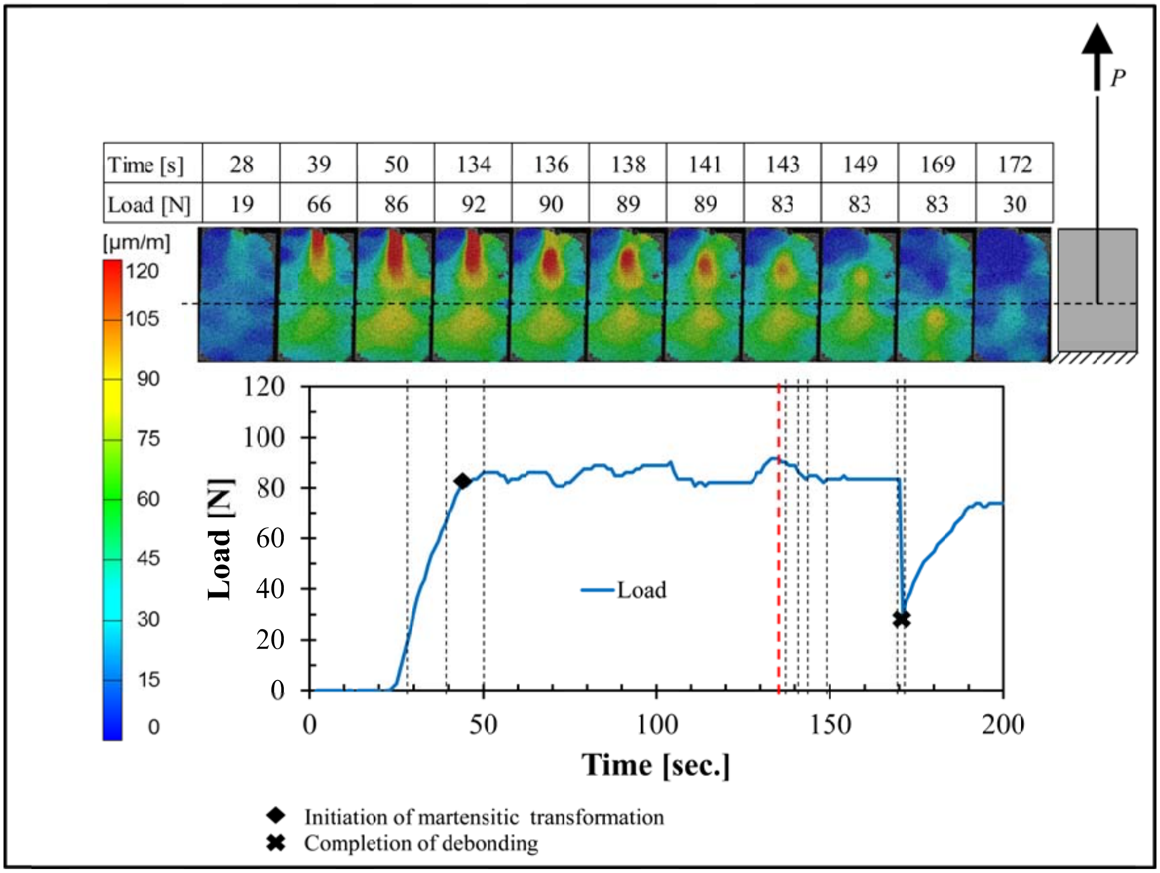

Figure B.10. Load history and DIC contours for a specimen with L_d of 25 mm and d_b of 0.47 mm, repetition# 1

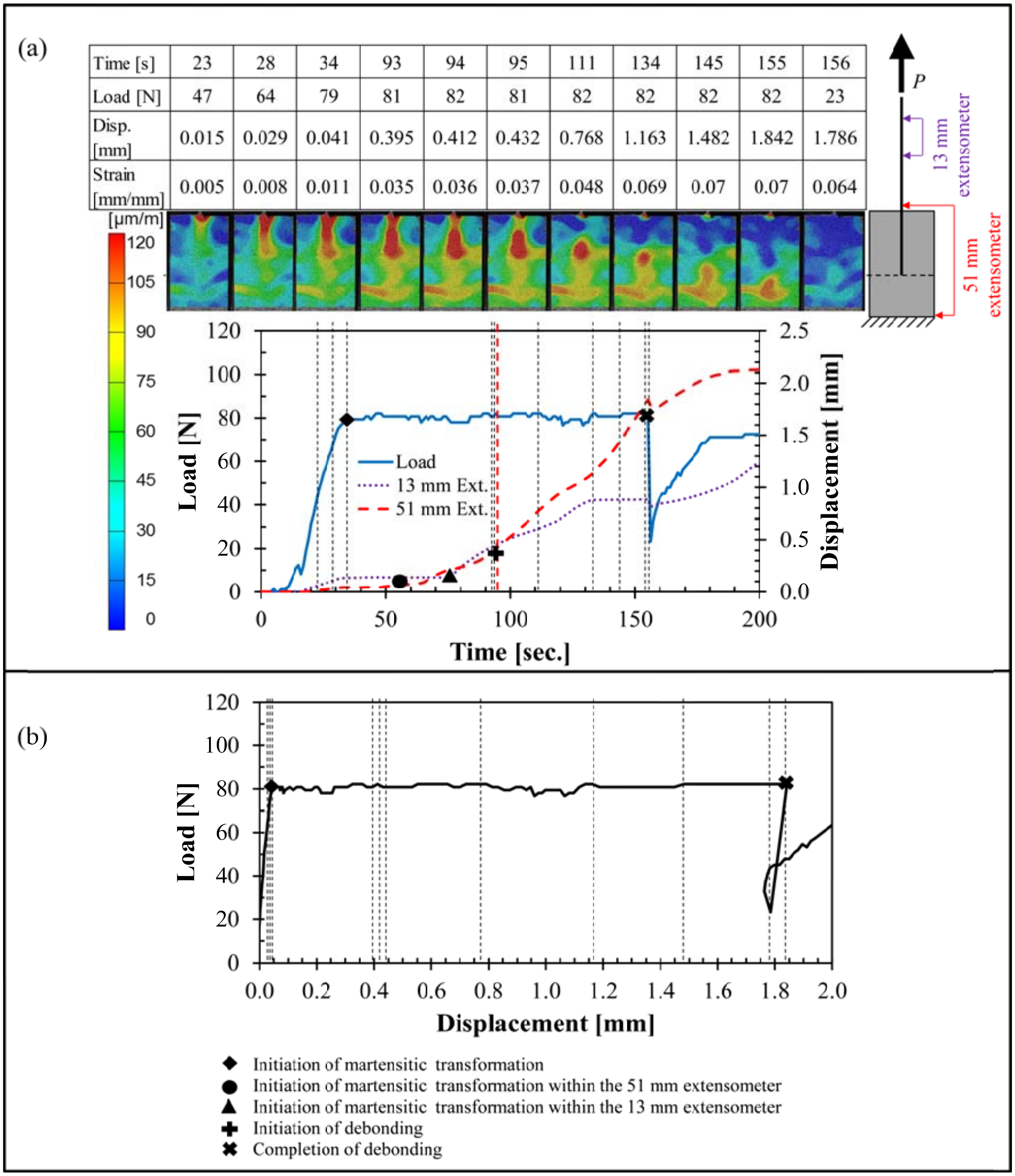

Figure B.11. (a) Load and displacement histories and DIC contours; and (b) Load-displacement relationship for a specimen with L_d of 25 mm and d_b of 0.47 mm, repetition# 2

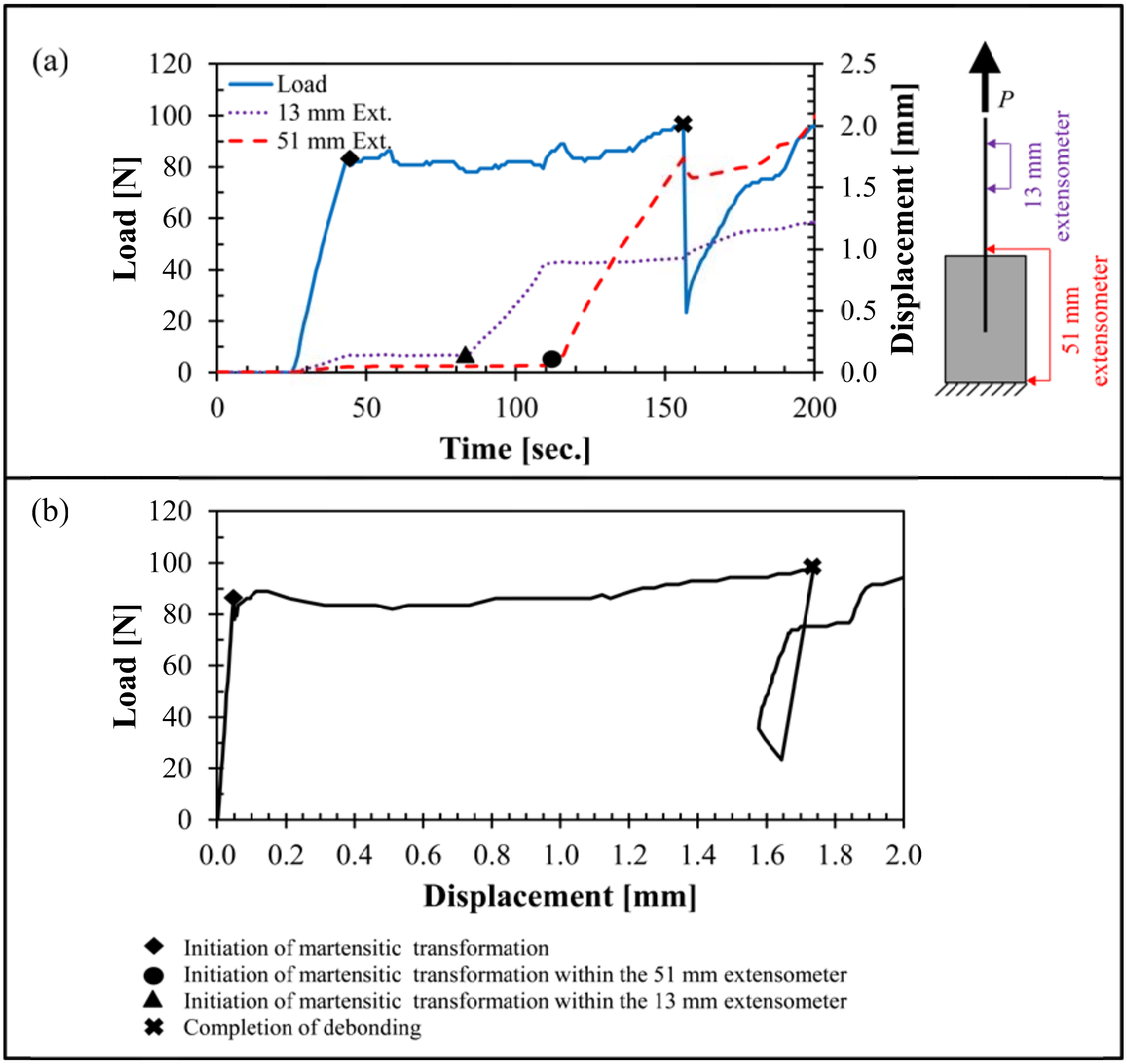

Figure B.12. (a) Load and displacement histories; and (b) Load-displacement relationship for a specimen with L_d of 25 mm and d_b of 0.47 mm, repetition# 3

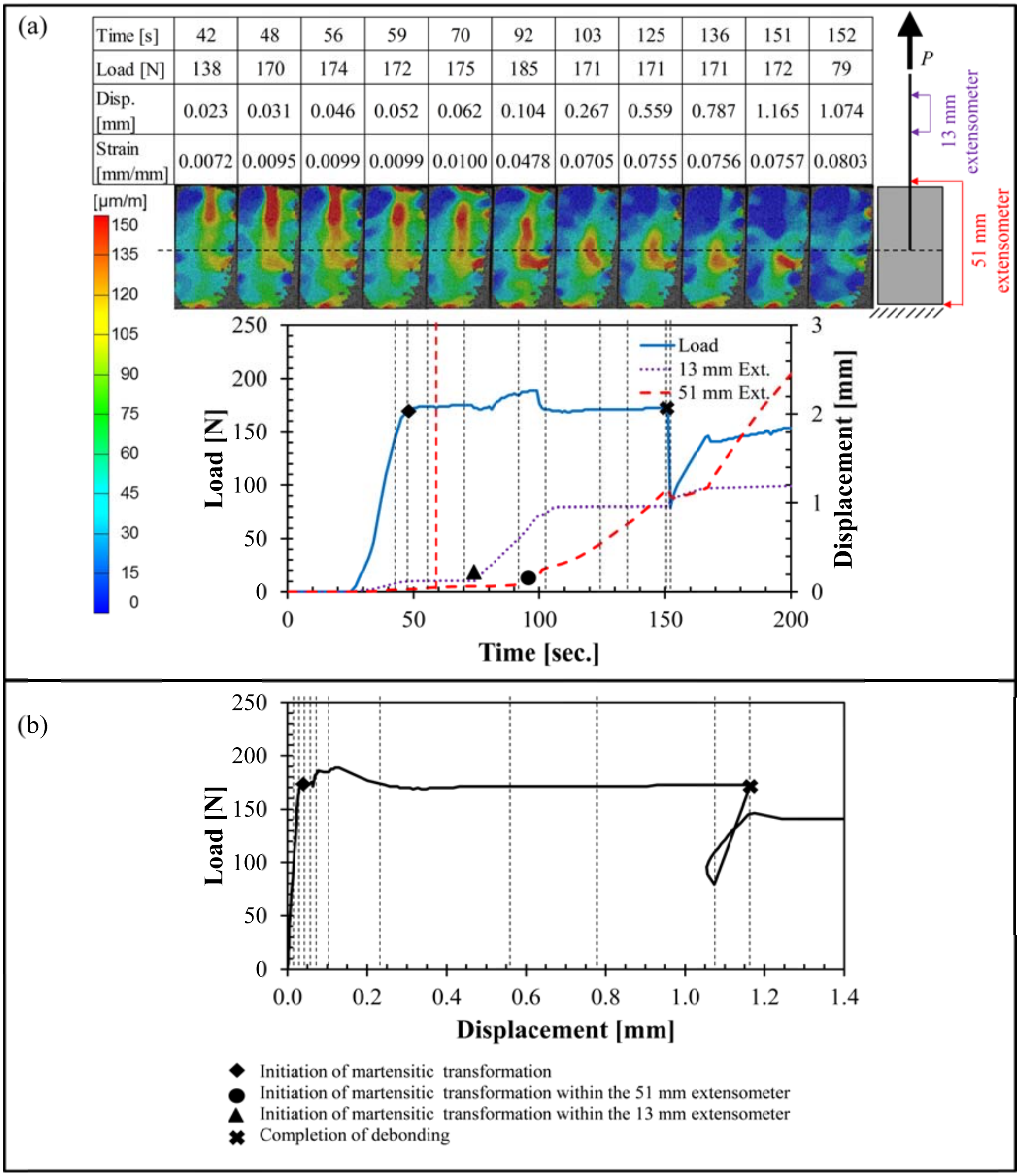

Figure B.13. (a) Load and displacement histories and DIC contours; and (b) Load-displacement relationship for a specimen with L_d of 25 mm and d_b of 0.66 mm, repetition# 1

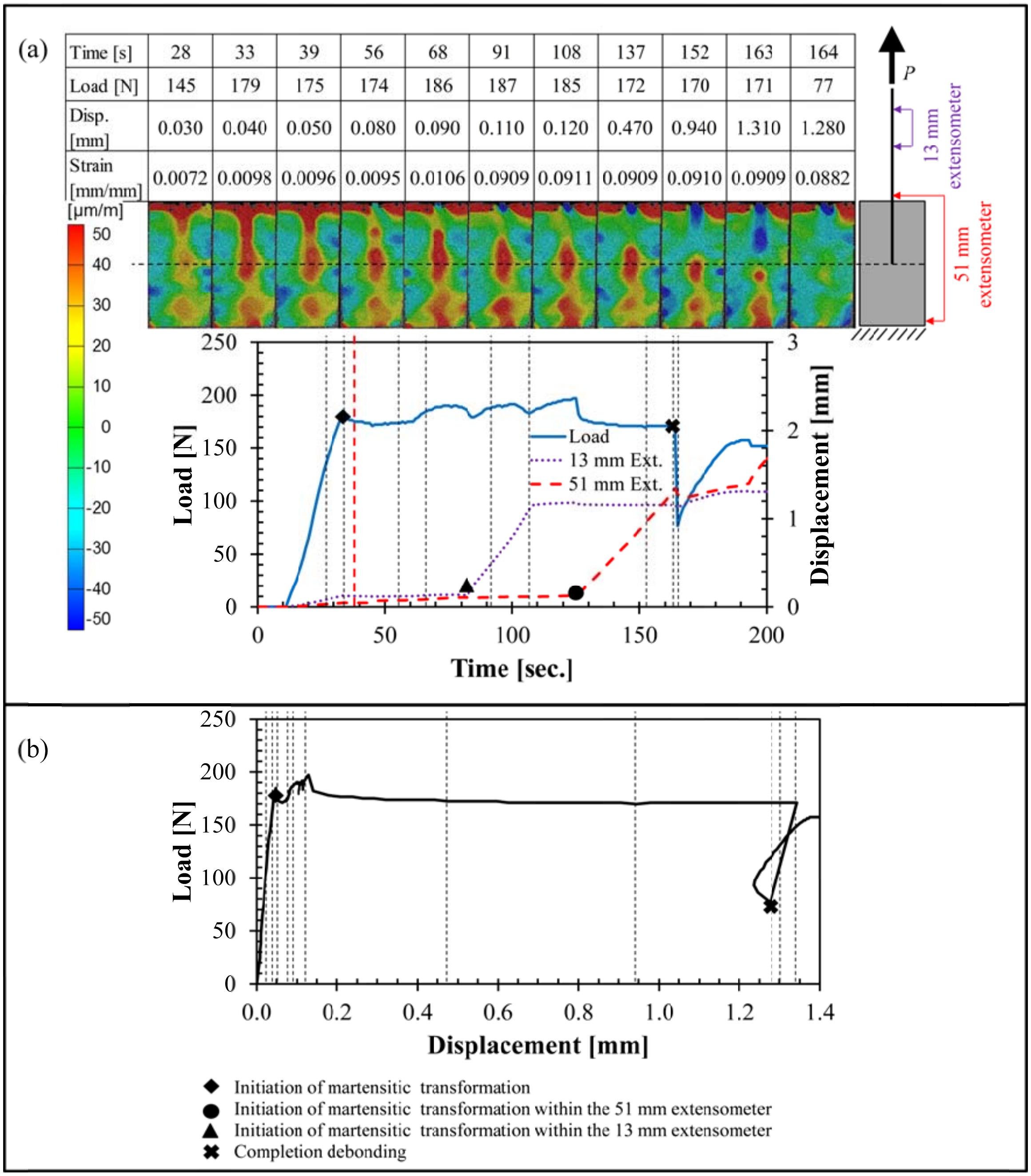

Figure B.14. (a) Load and displacement histories and DIC contours; and (b) Load-displacement relationship for a specimen with L_d of 25 mm and d_b of 0.66 mm, repetition# 2

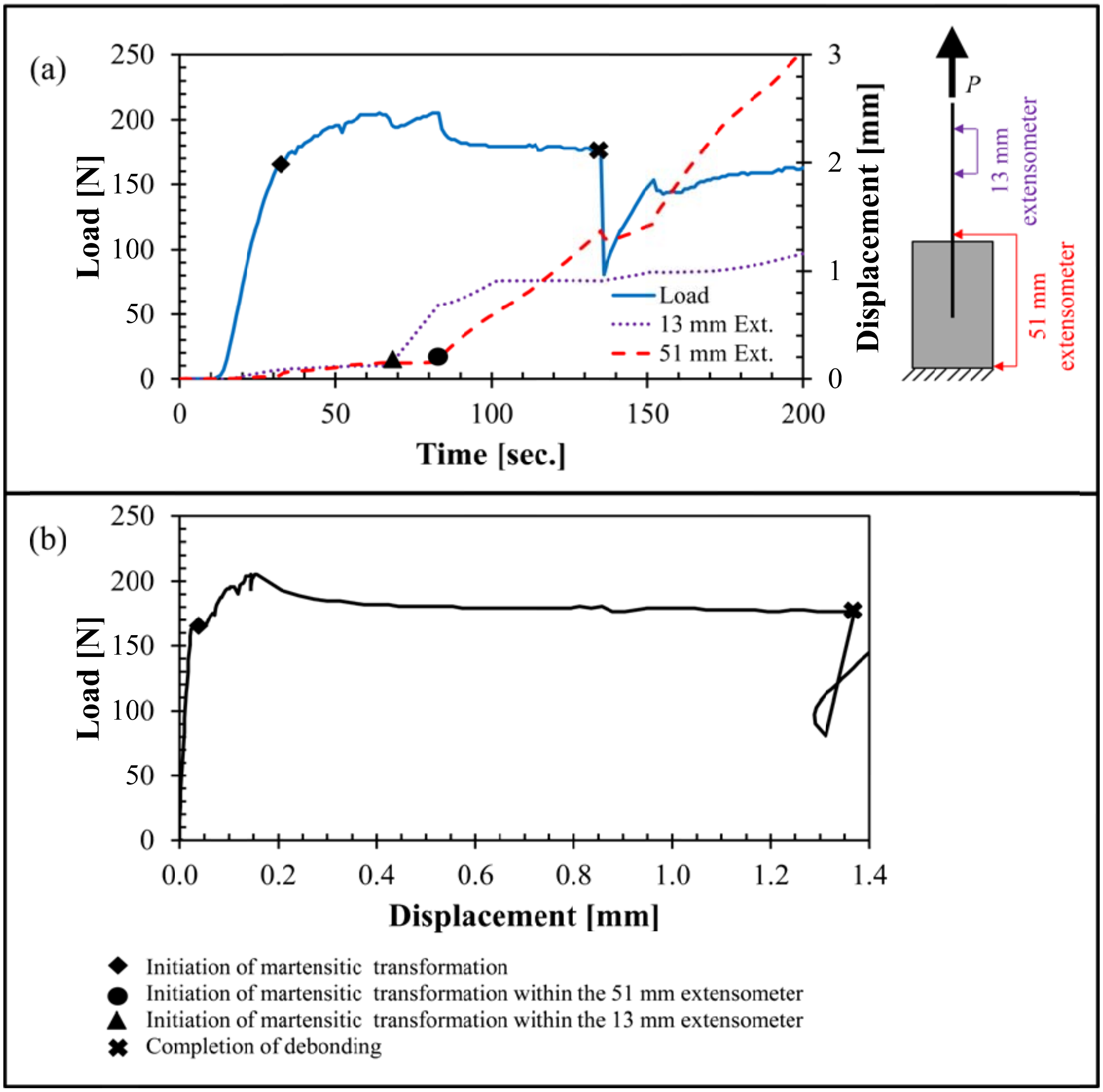

Figure B.15. (a) Load and displacement histories; and (b) Load-displacement relationship for a specimen with L_d of 25 mm and d_b of 0.66 mm, repetition# 3

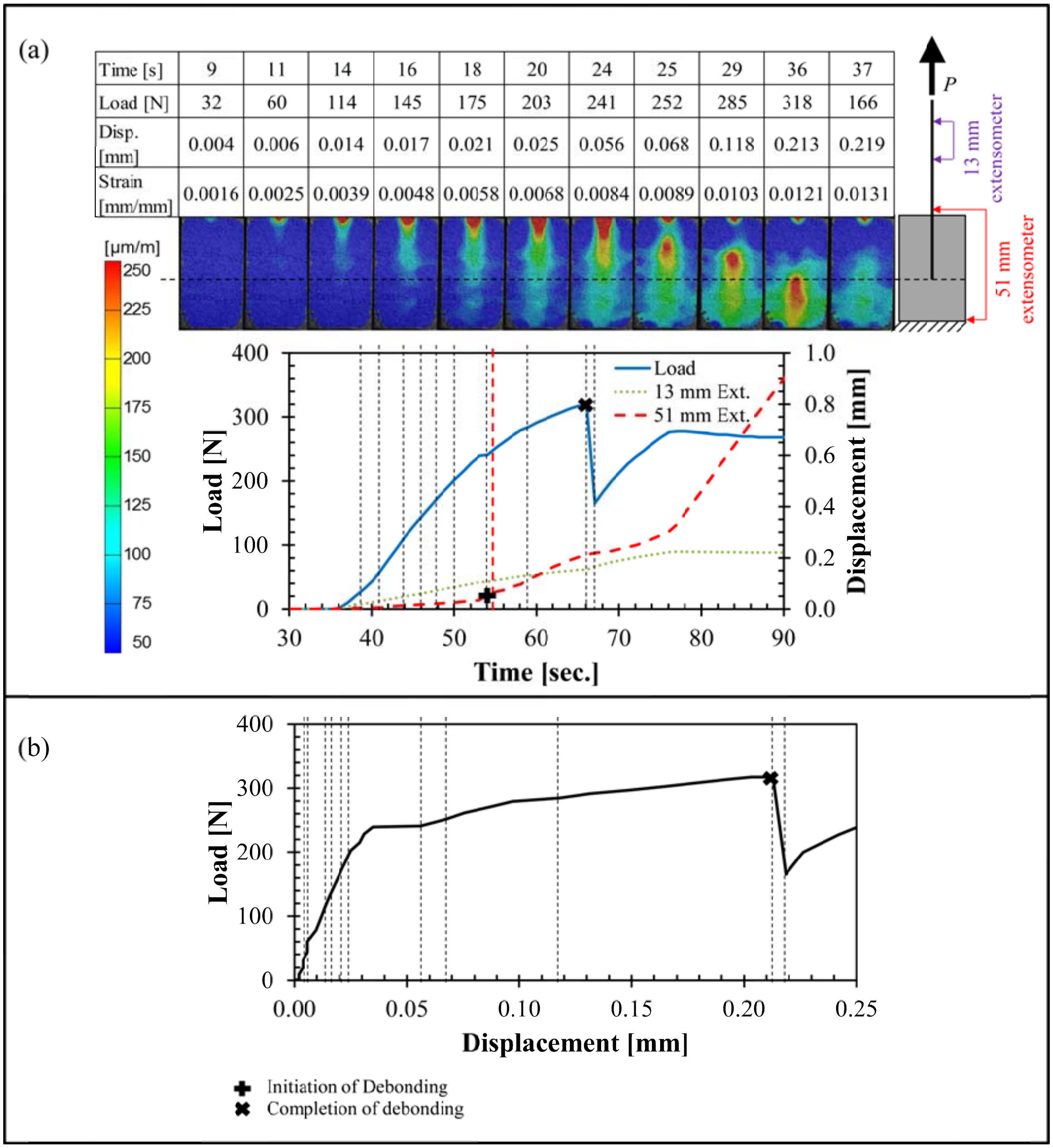

Time [s]	9	11	14	16	18	20	24	25	29	36	37
Load [N]	32	60	114	145	175	203	241	252	285	318	166
Disp. [mm]	0.004	0.006	0.014	0.017	0.021	0.025	0.056	0.068	0.118	0.213	0.219
Strain [mm/mm]	0.0016	0.0025	0.0039	0.0048	0.0058	0.0068	0.0084	0.0089	0.0103	0.0121	0.0131

Figure B.16. (a) Load and displacement histories and DIC contours; and (b) Load-displacement relationship for a specimen with L_d of 25 mm and d_b of 0.89 mm, repetition# 1

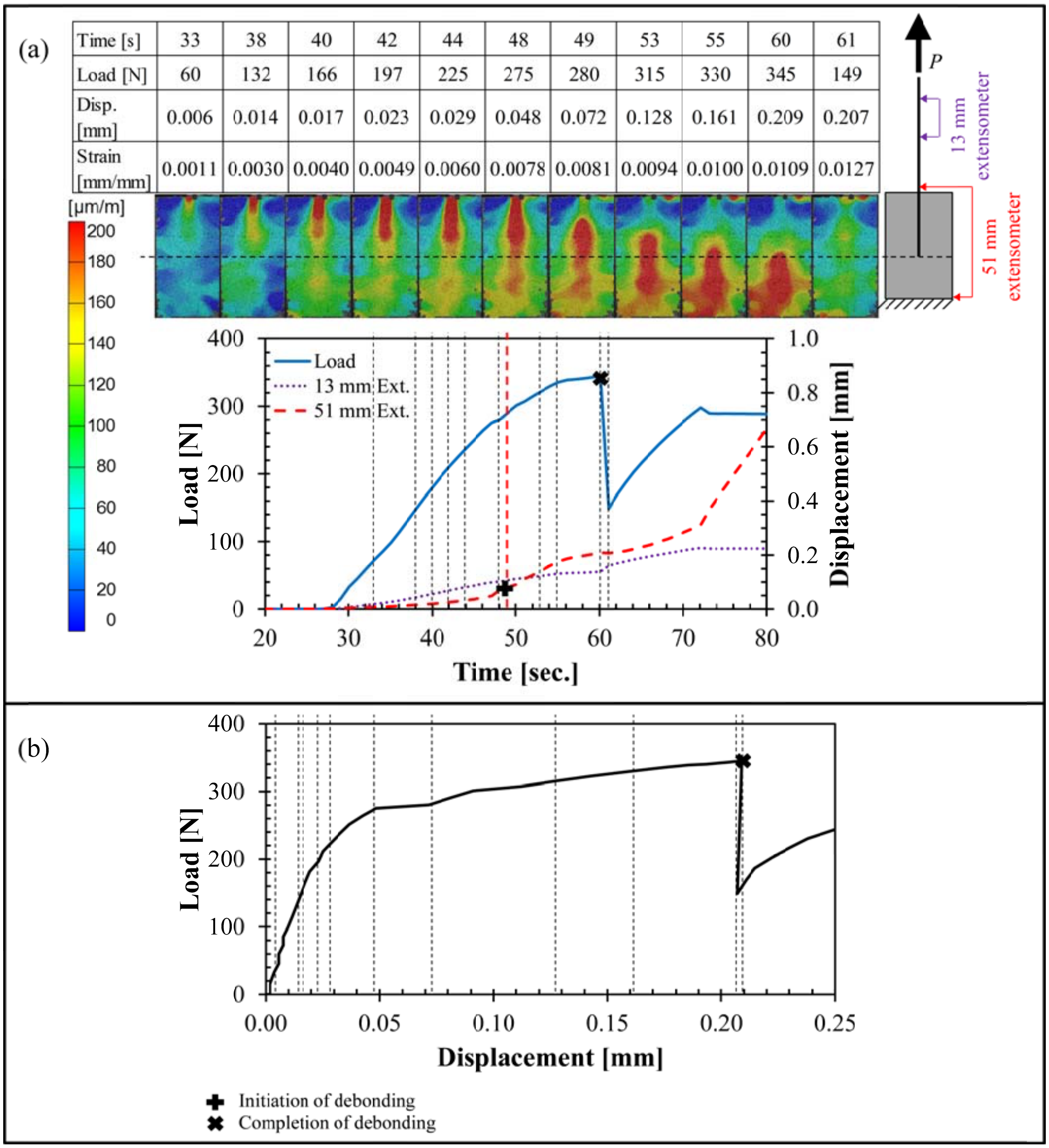

Time [s]	33	38	40	42	44	48	49	53	55	60	61
Load [N]	60	132	166	197	225	275	280	315	330	345	149
Disp. [mm]	0.006	0.014	0.017	0.023	0.029	0.048	0.072	0.128	0.161	0.209	0.207
Strain [mm/mm]	0.0011	0.0030	0.0040	0.0049	0.0060	0.0078	0.0081	0.0094	0.0100	0.0109	0.0127

Figure B.17. (a) Load and displacement histories and DIC contours; and (b) Load-displacement relationship for a specimen with L_d of 25 mm and d_b of 0.89 mm, repetition# 2

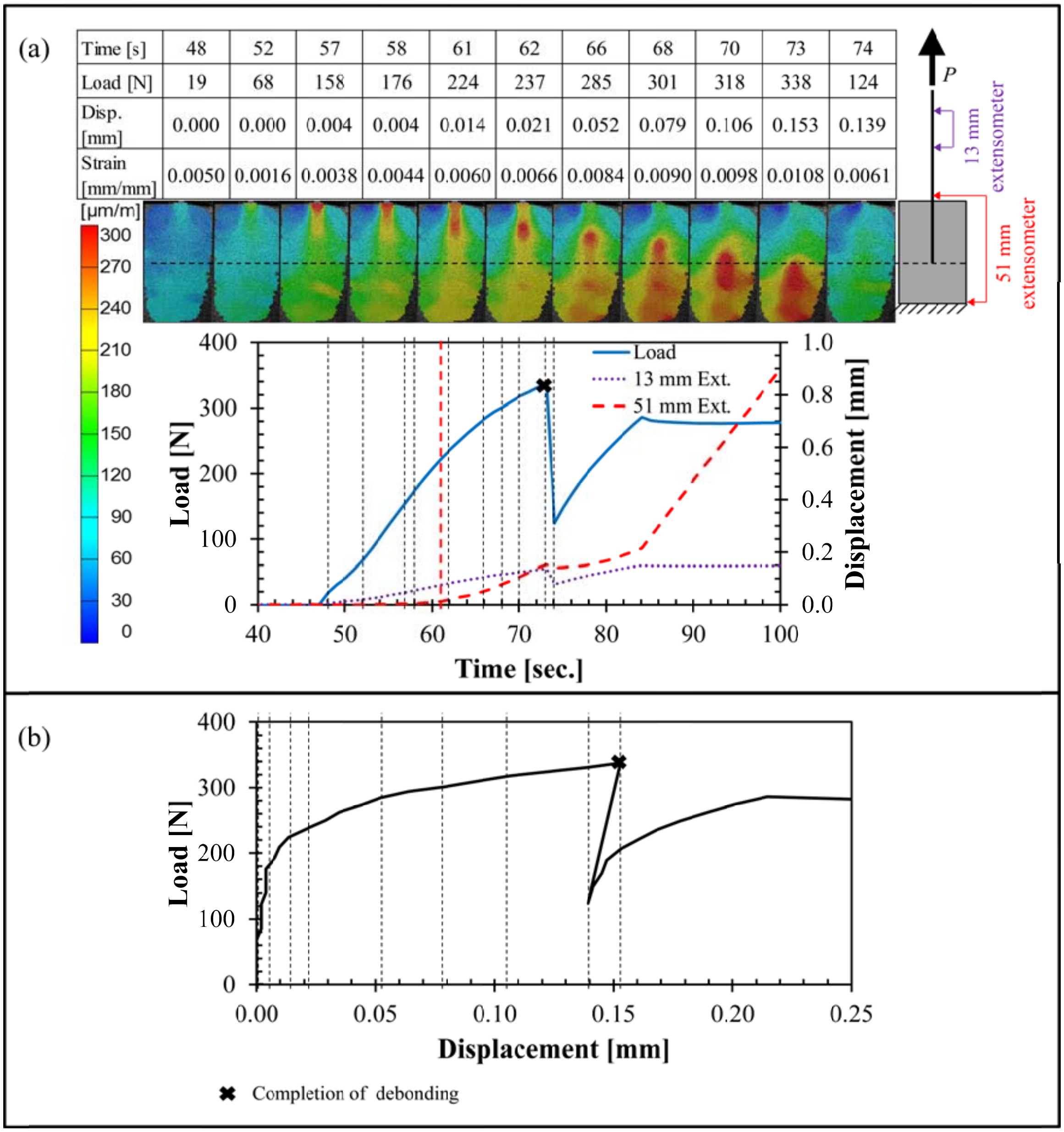

Time [s]	48	52	57	58	61	62	66	68	70	73	74
Load [N]	19	68	158	176	224	237	285	301	318	338	124
Disp. [mm]	0.000	0.000	0.004	0.004	0.014	0.021	0.052	0.079	0.106	0.153	0.139
Strain [mm/mm]	0.0050	0.0016	0.0038	0.0044	0.0060	0.0066	0.0084	0.0090	0.0098	0.0108	0.0061

Figure B.18. (a) Load and displacement histories and DIC contours; and (b) Load-displacement relationship for a specimen with L_d of 25 mm and d_b of 0.89 mm, repetition# 3

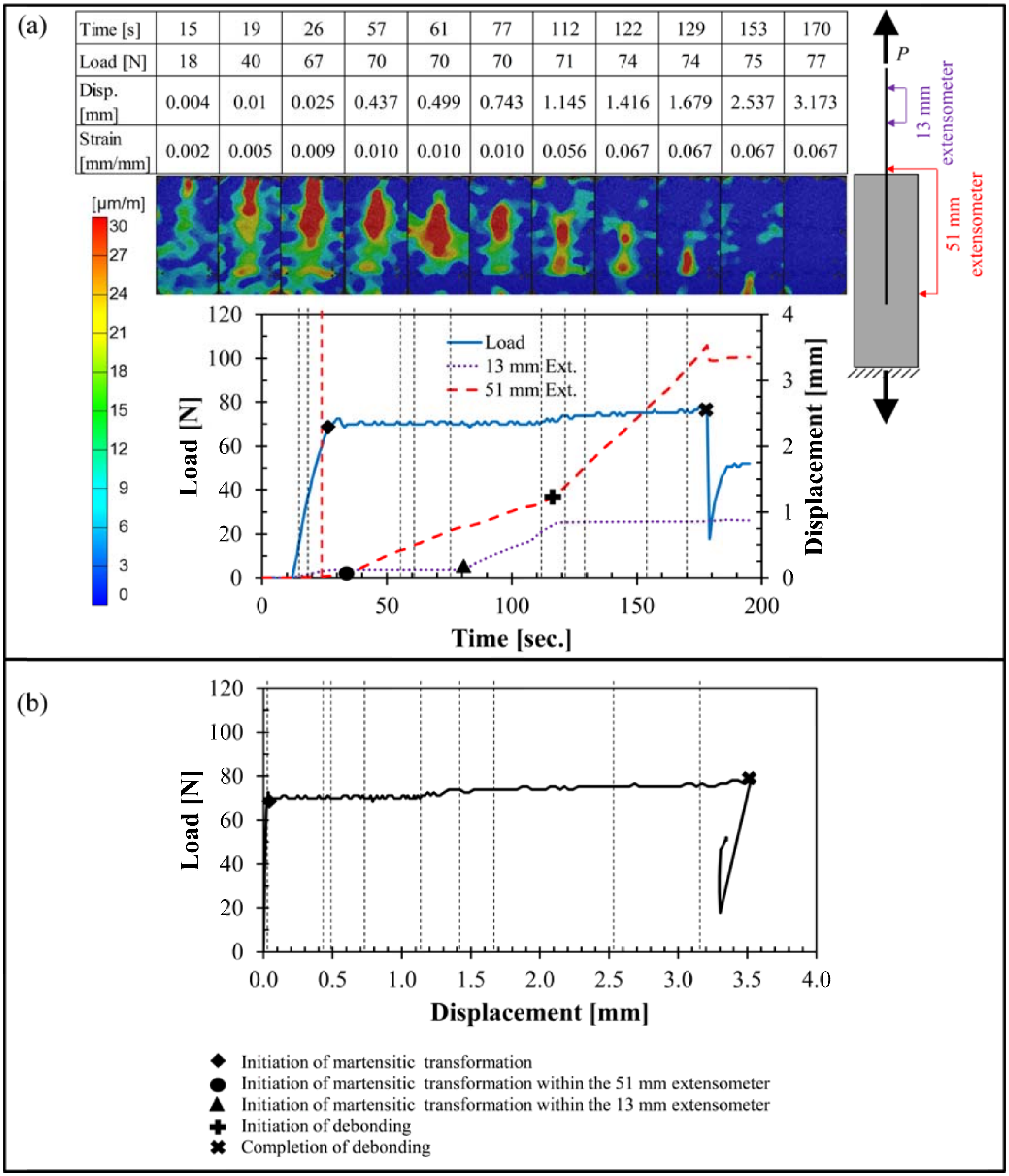

Time [s]	15	19	26	57	61	77	112	122	129	153	170
Load [N]	18	40	67	70	70	70	71	74	74	75	77
Disp. [mm]	0.004	0.01	0.025	0.437	0.499	0.743	1.145	1.416	1.679	2.537	3.173
Strain [mm/mm]	0.002	0.005	0.009	0.010	0.010	0.010	0.056	0.067	0.067	0.067	0.067

Figure B.19. (a) Load and displacement histories and DIC contours; and (b) Load-displacement relationship for a specimen with L_d of 51 mm and d_b of 0.47 mm, repetition# 1

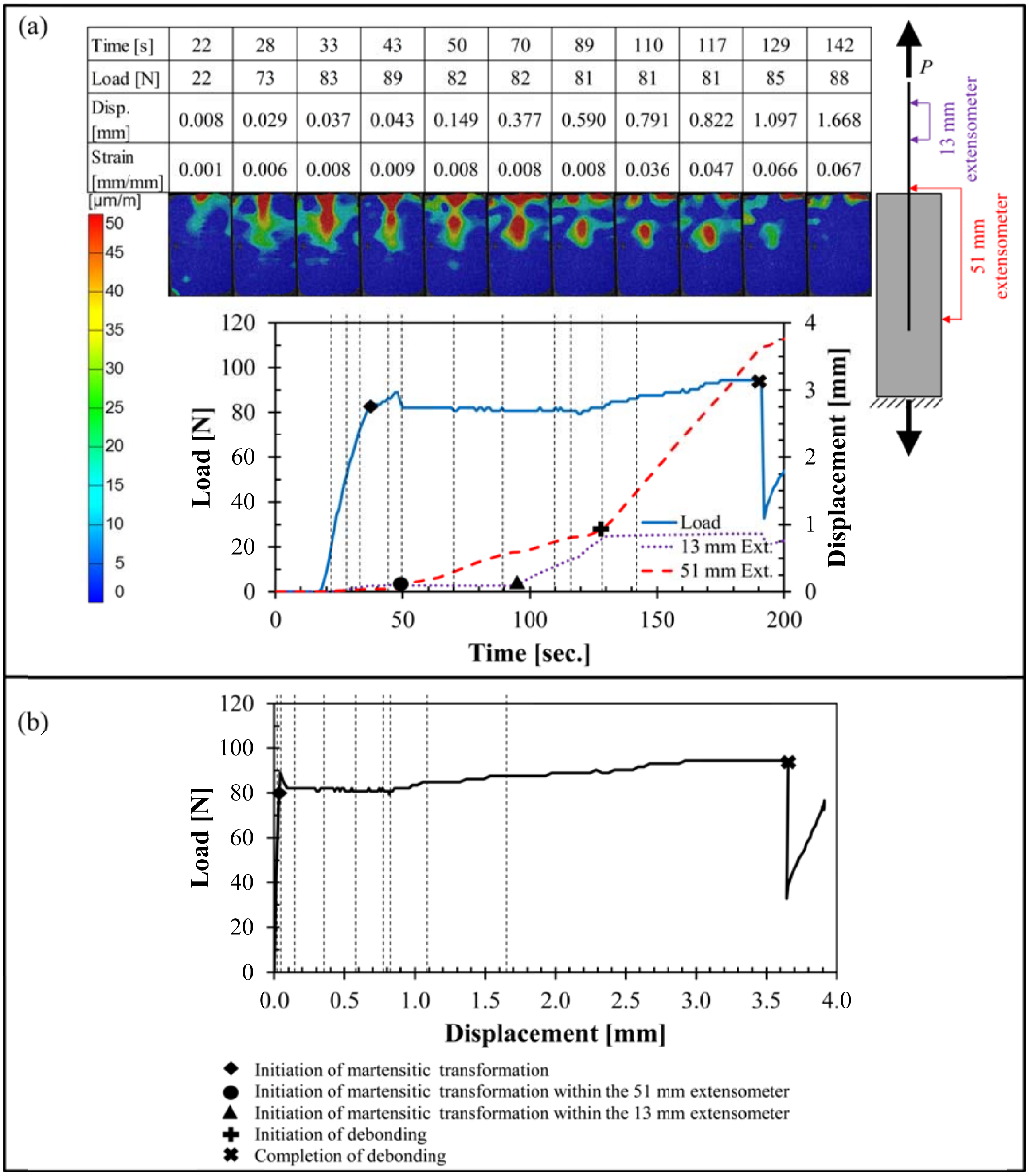

Figure B.20. (a) Load and displacement histories and DIC contours; and (b) Load-displacement relationship for a specimen with L_d of 51 mm and d_b of 0.47 mm, repetition# 2

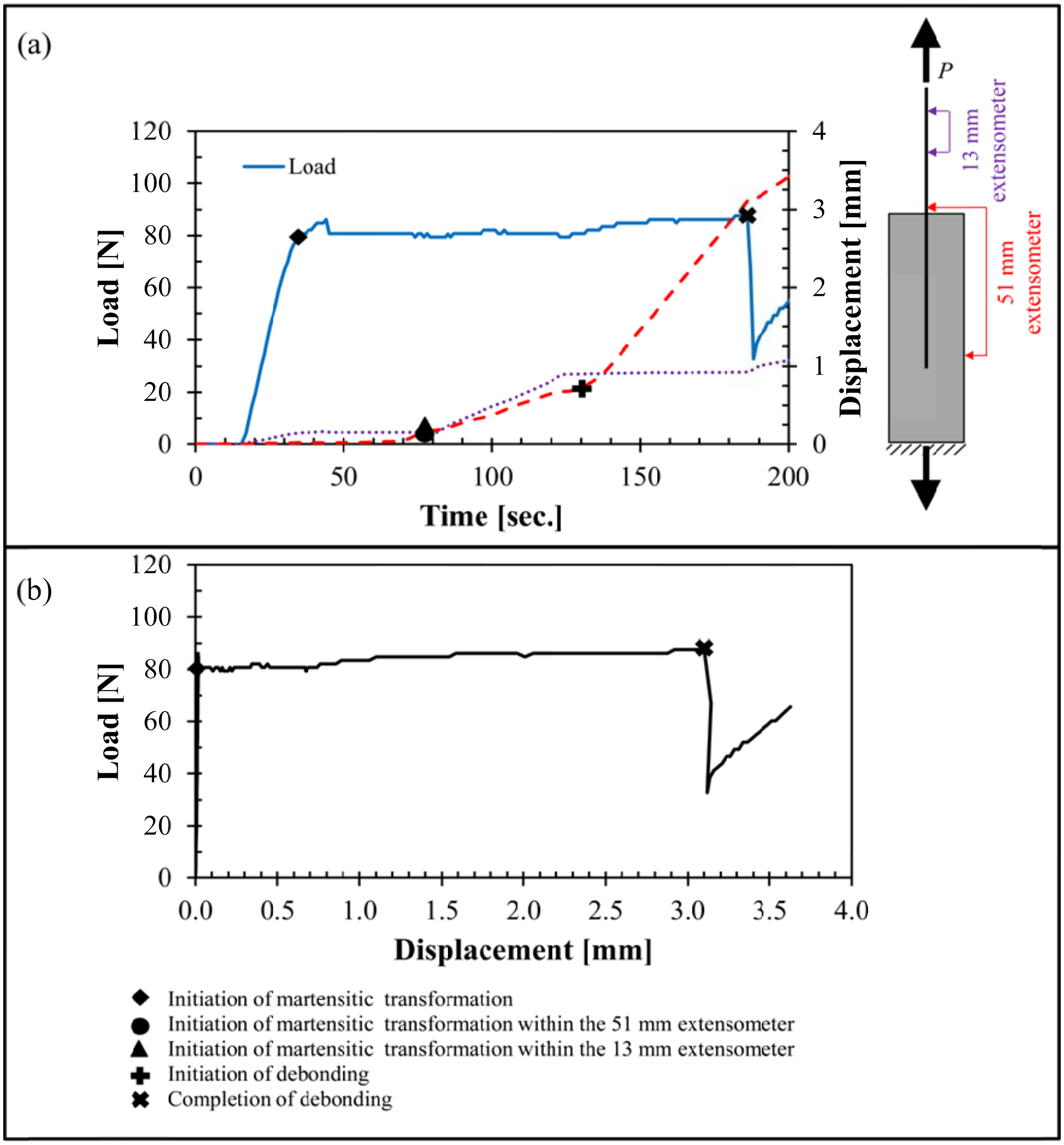

Figure B.21. (a) Load and displacement histories and DIC contours; and (b) Load-displacement relationship for a specimen with L_d of 51 mm and d_b of 0.47 mm, repetition# 3

Time [s]	22	25	31	40	81	96	100	117	126	146	159
Load [N]	96	123	164	174	166	166	166	164	166	166	164
Strain [mm/mm]	0.004	0.006	0.009	0.01	0.01	0.01	0.01	0.017	0.028	0.051	0.067

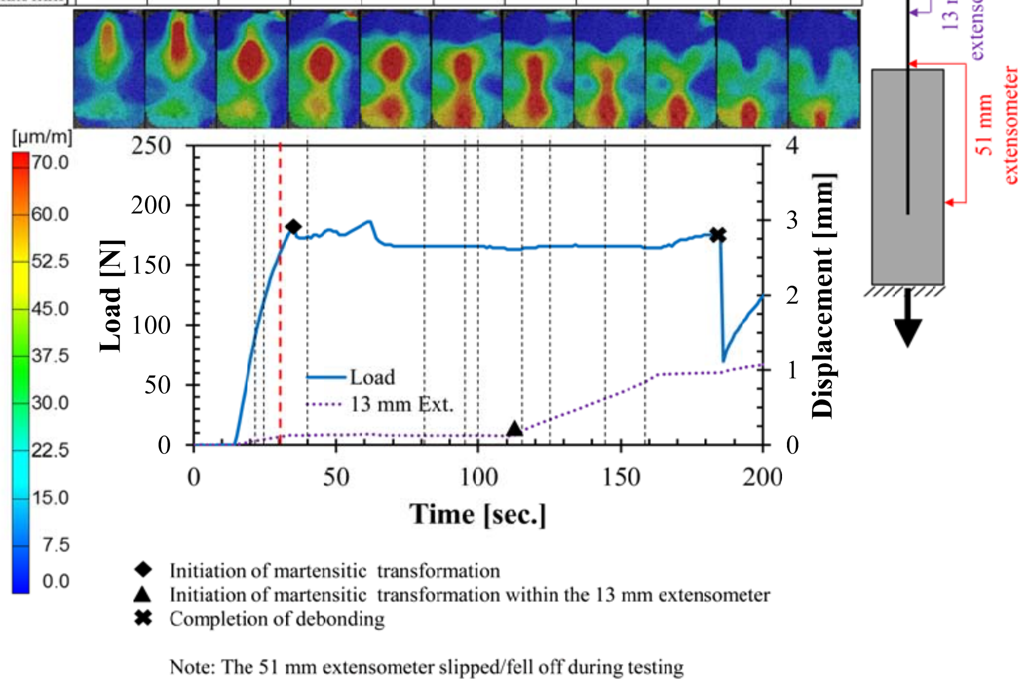

Figure B.22. (a) Load and displacement histories and DIC contours for a specimen with L_d of 51 mm and d_b of 0.66 mm, repetition# 1

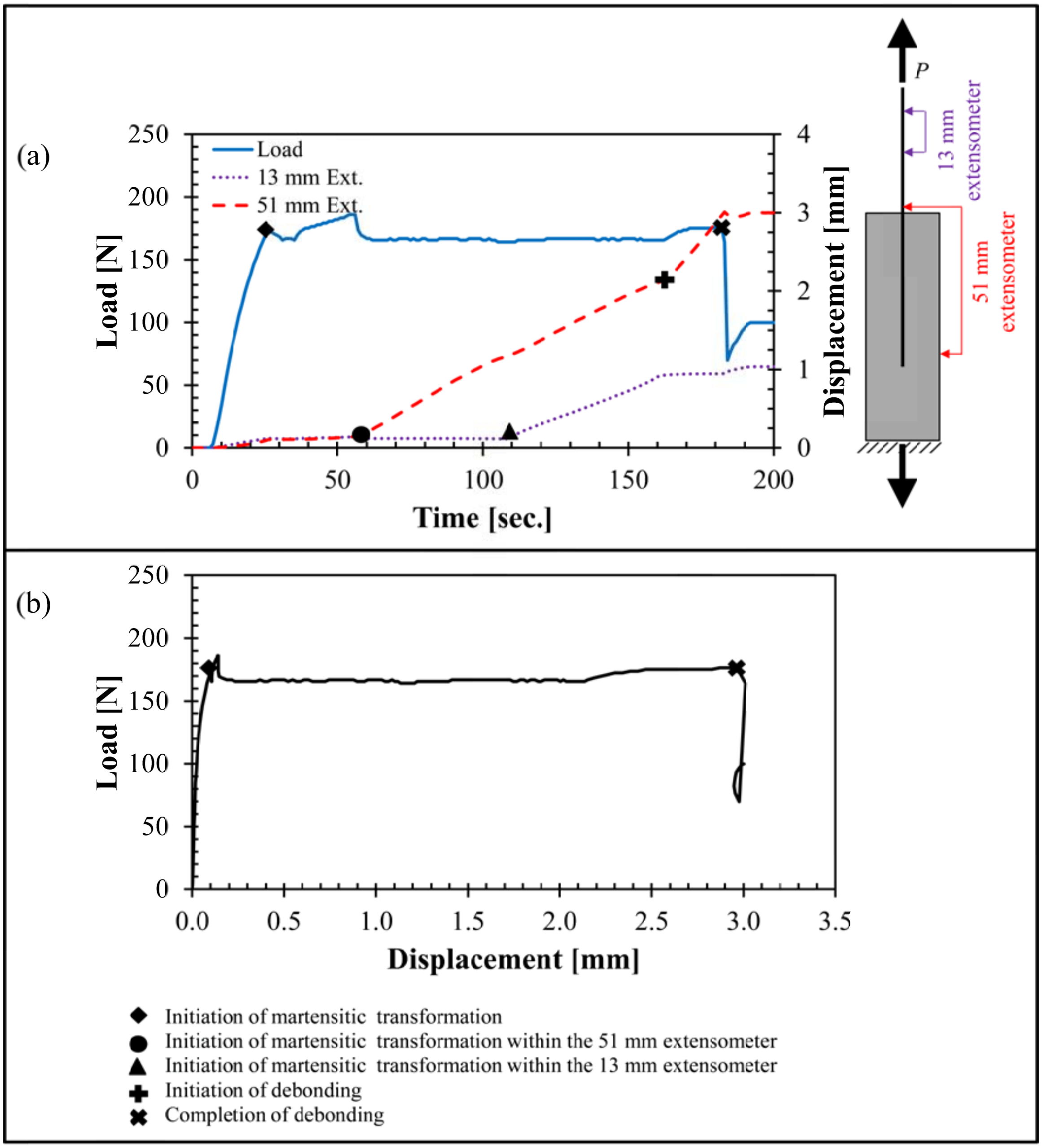

Figure B.23. (a) Load and displacement histories and (b) Load-displacement relationship for a specimen with L_d of 51 mm and d_b of 0.66 mm, repetition# 2

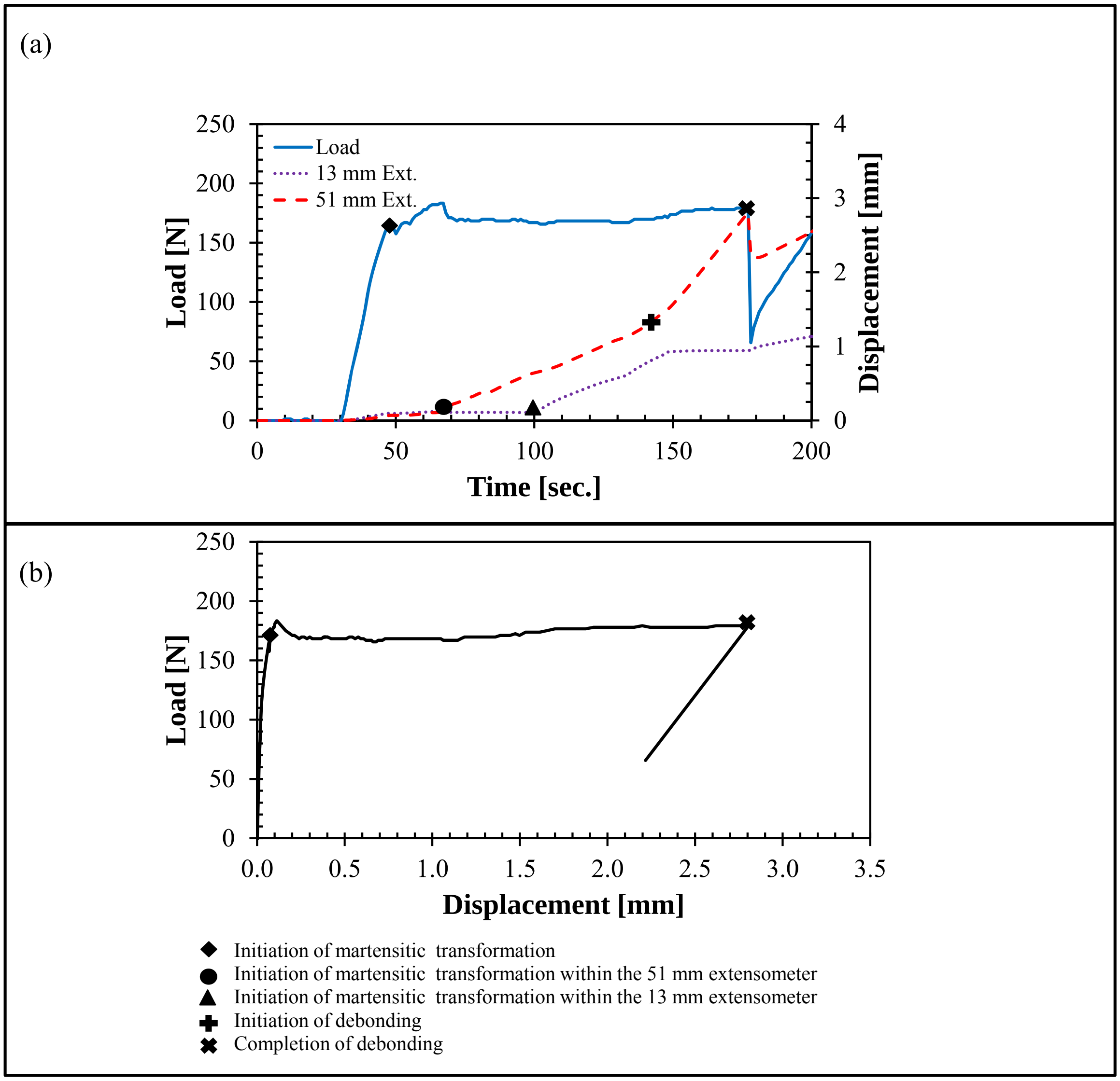

Figure B.24. (a) Load and displacement histories and (b) Load-displacement relationship for a specimen with L_d of 51 mm and d_b of 0.66 mm, repetition# 3

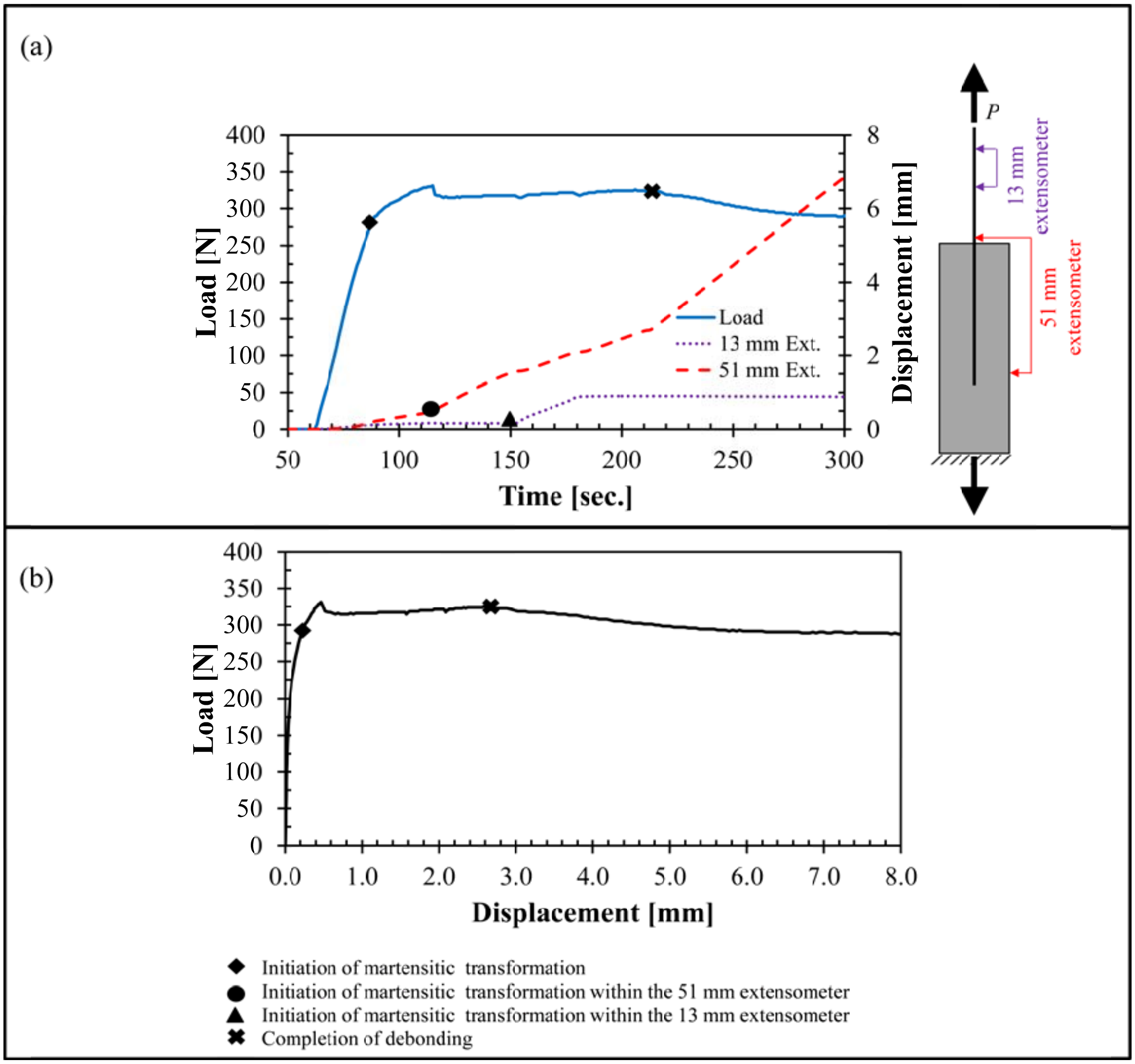

Figure B.25. (a) Load and displacement histories and (b) Load-displacement relationship for a specimen with L_d of 51 mm and d_b of 0.89 mm, repetition# 1

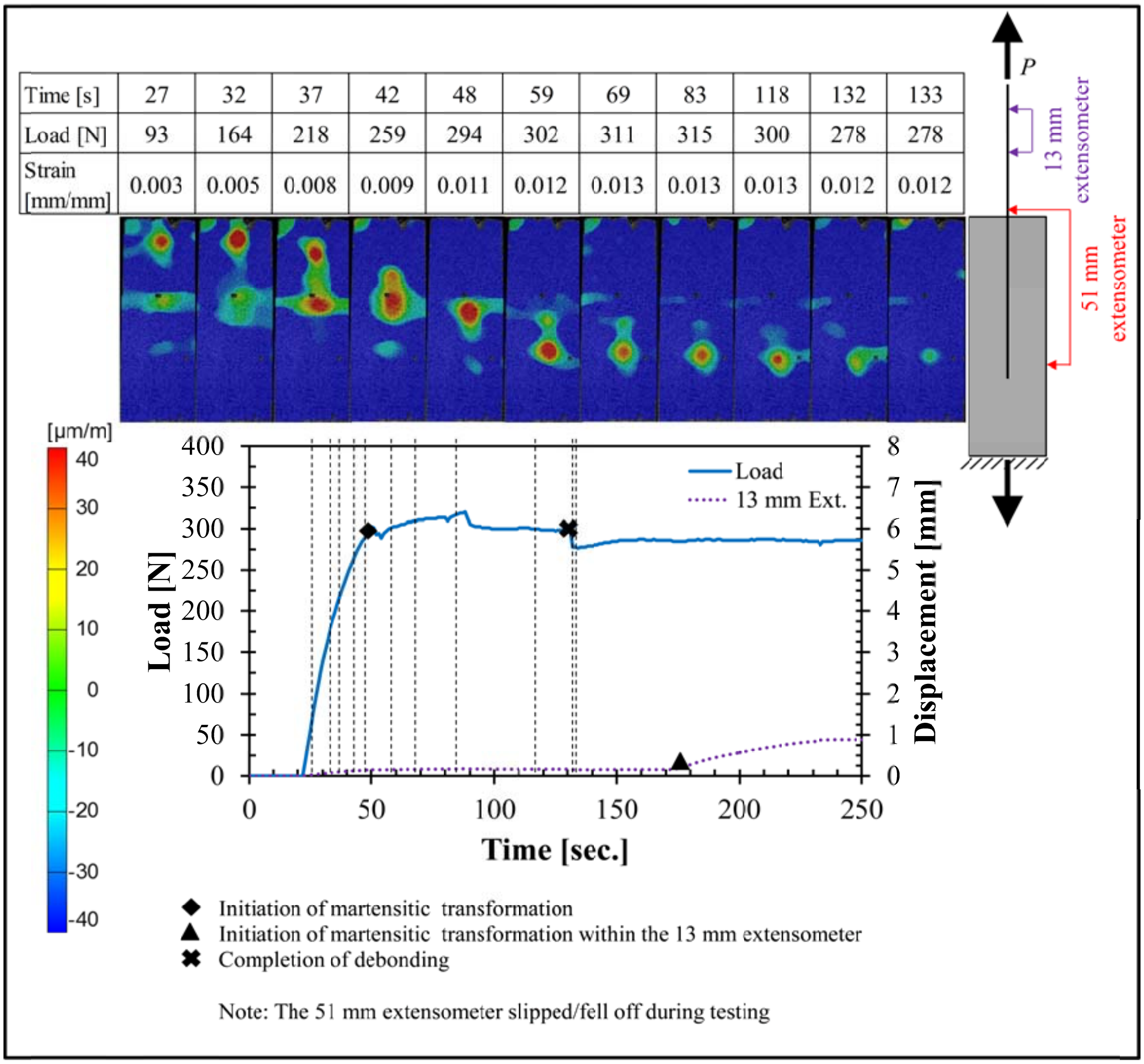

Time [s]	27	32	37	42	48	59	69	83	118	132	133
Load [N]	93	164	218	259	294	302	311	315	300	278	278
Strain [mm/mm]	0.003	0.005	0.008	0.009	0.011	0.012	0.013	0.013	0.013	0.012	0.012

Figure B.26. Load and displacement histories and DIC contours for a specimen with L_d of 51 mm and d_b of 0.89 mm, repetition# 2

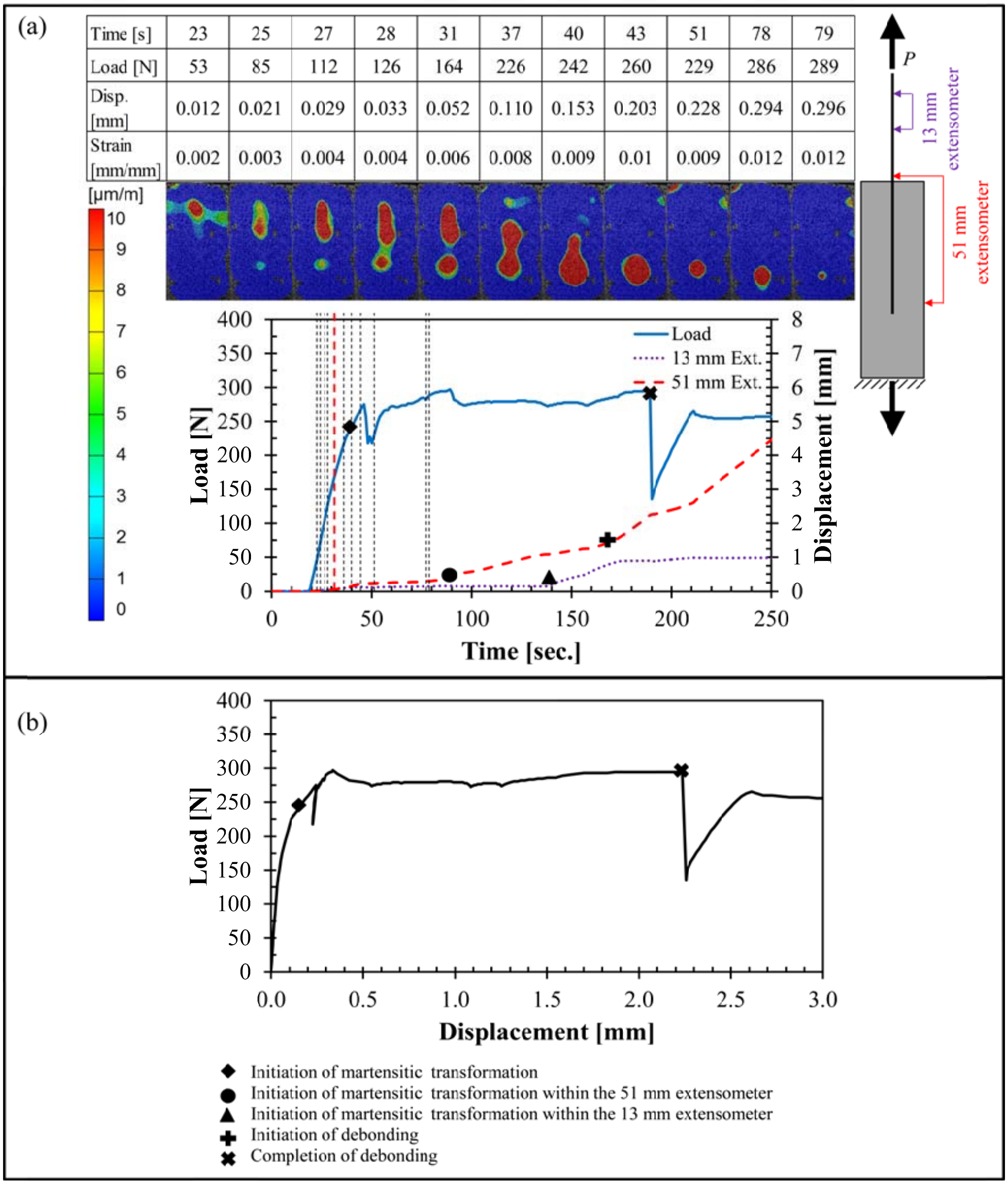

Figure B.27. (a) Load and displacement histories and DIC contours; and (b) Load-displacement relationship for a specimen with L_d of 51 mm and d_b of 0.89 mm, repetition# 3

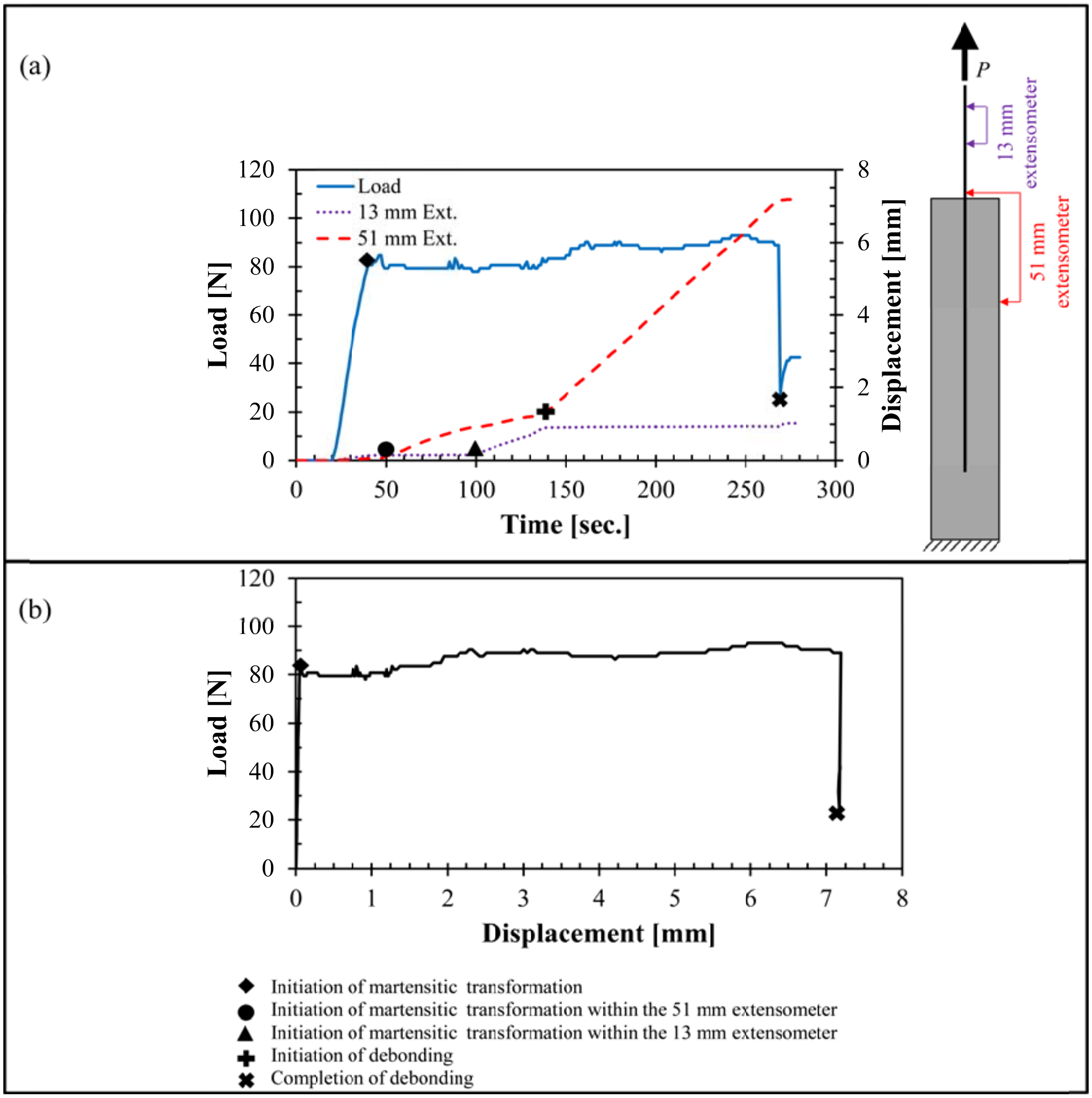

Figure B.28. (a) Load and displacement histories and (b) Load-displacement relationship for a specimen with L_d of 102 mm and d_b of 0.47 mm, repetition# 3

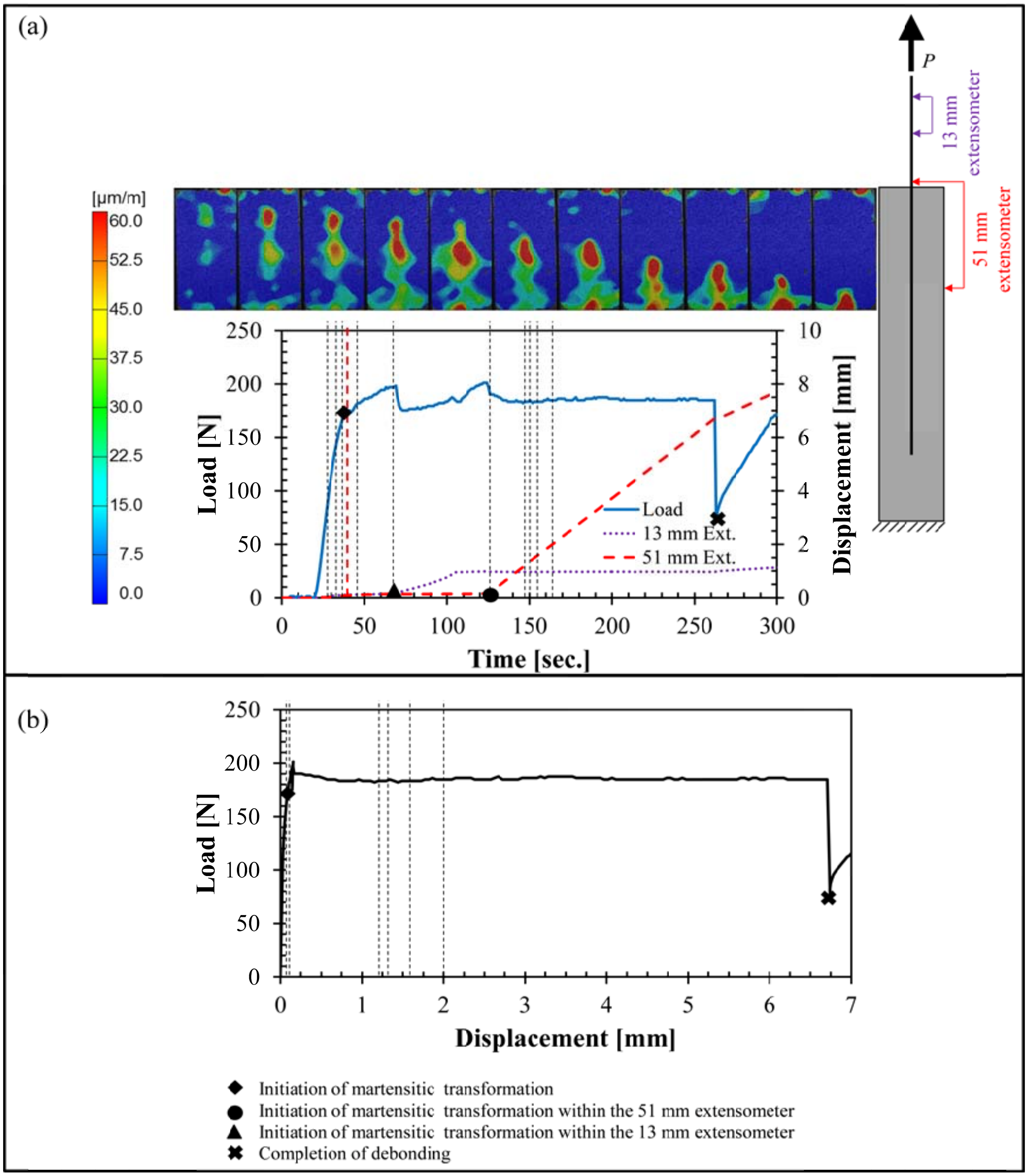

Figure B.29. (a) Load and displacement histories and DIC contours; and (b) Load-displacement relationship for a specimen with L_d of 102 mm and d_b of 0.66 mm, repetition# 1

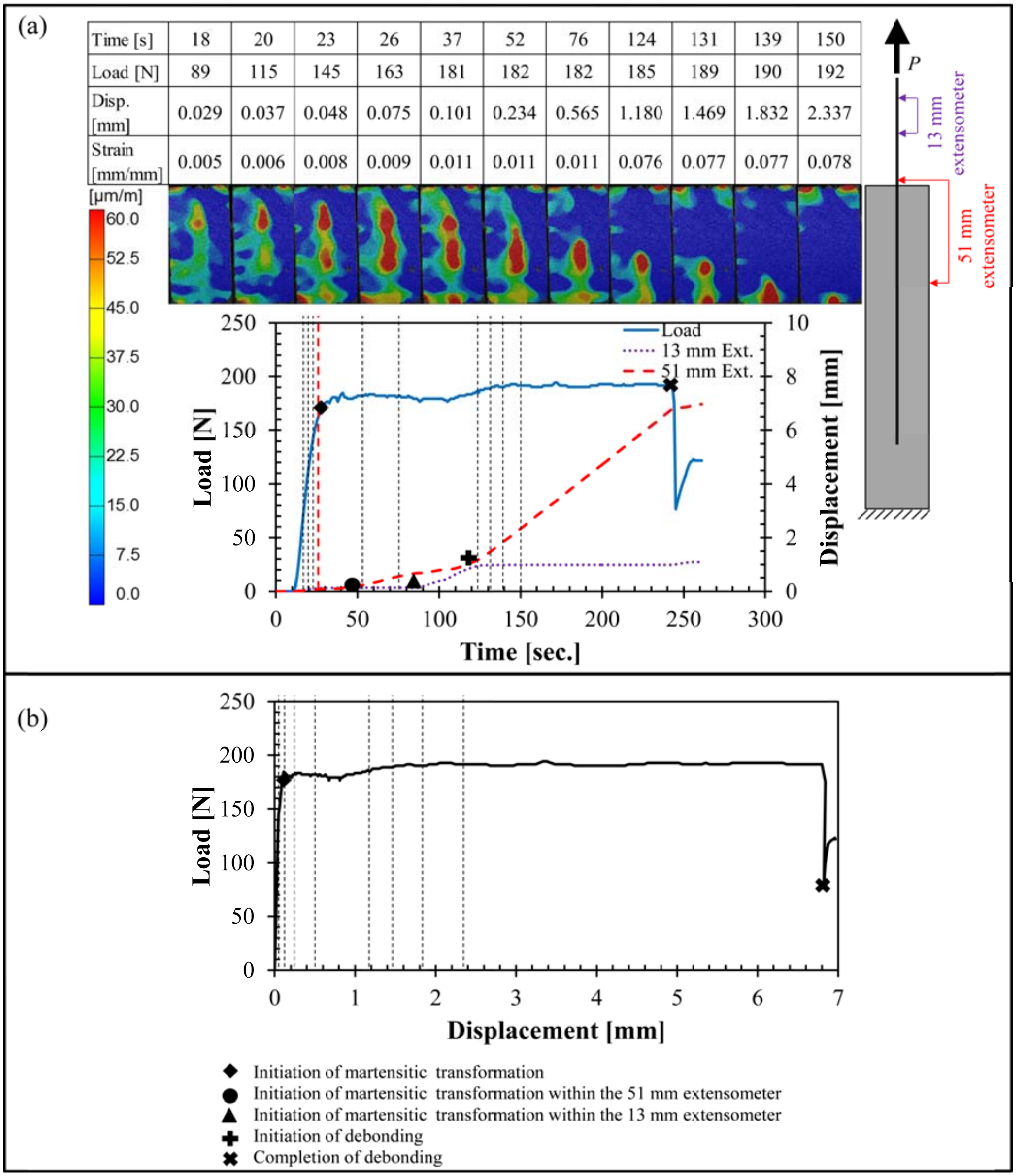

Time [s]	18	20	23	26	37	52	76	124	131	139	150
Load [N]	89	115	145	163	181	182	182	185	189	190	192
Disp. [mm]	0.029	0.037	0.048	0.075	0.101	0.234	0.565	1.180	1.469	1.832	2.337
Strain [mm/mm]	0.005	0.006	0.008	0.009	0.011	0.011	0.011	0.076	0.077	0.077	0.078

Figure B.30. (a) Load and displacement histories and DIC contours; and (b) Load-displacement relationship for a specimen with L_d of 102 mm and d_b of 0.66 mm, repetition# 2

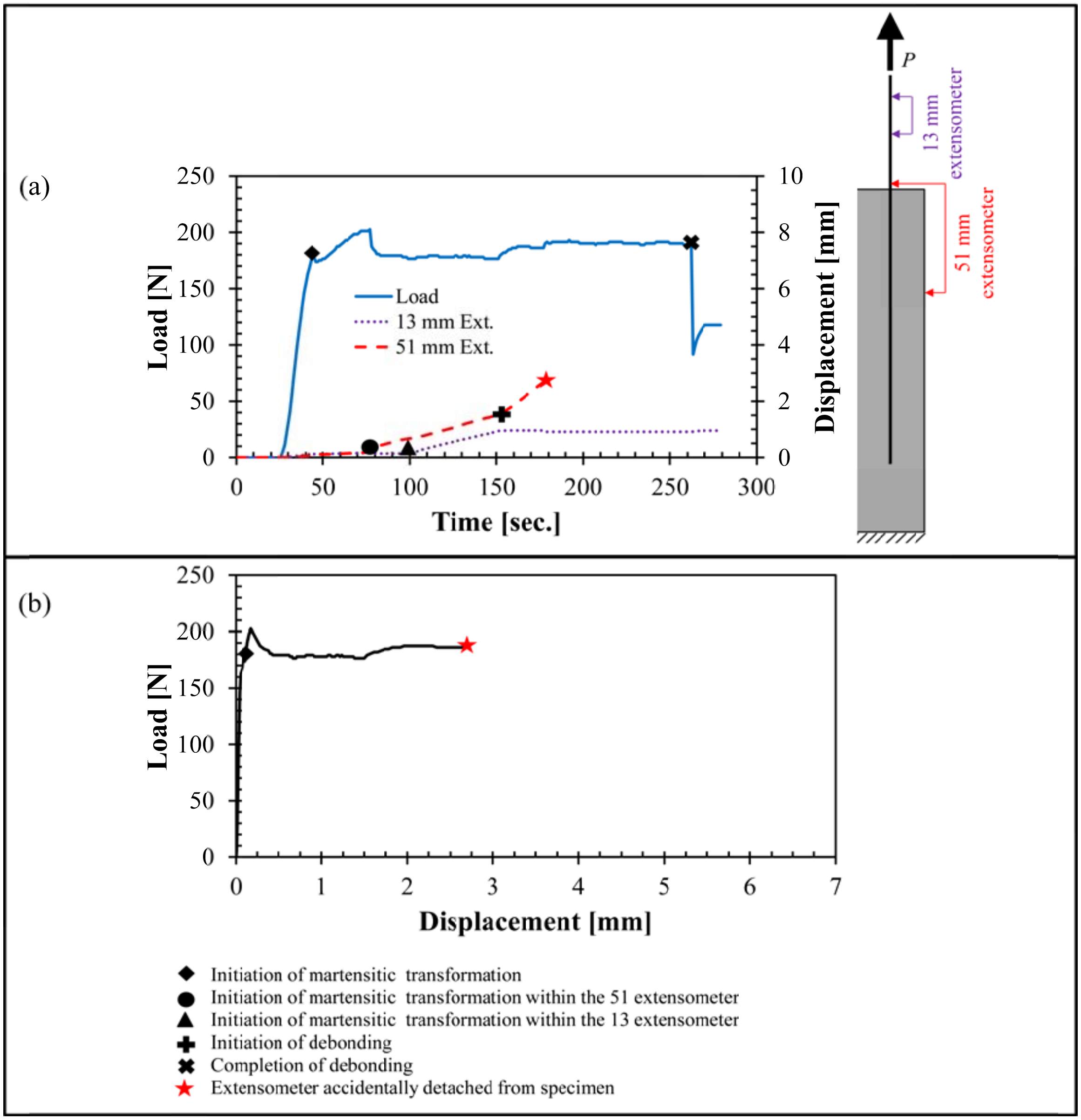

Figure B.31 (a) Load and displacement histories and (b) Load-displacement relationship for a specimen with L_d of 102 mm and d_b of 0.66 mm, repetition# 3

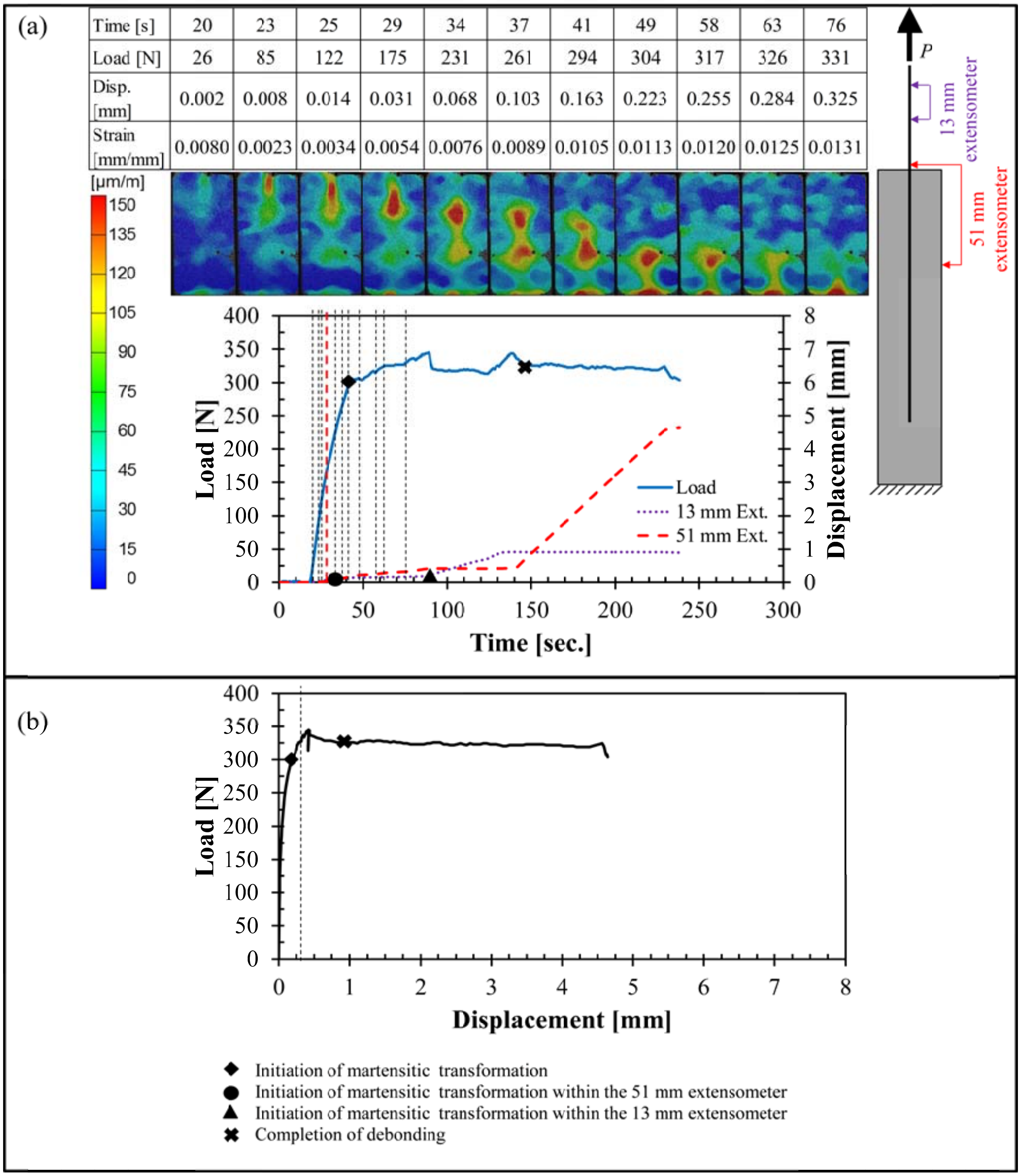

Time [s]	20	23	25	29	34	37	41	49	58	63	76
Load [N]	26	85	122	175	231	261	294	304	317	326	331
Disp. [mm]	0.002	0.008	0.014	0.031	0.068	0.103	0.163	0.223	0.255	0.284	0.325
Strain [mm/mm]	0.0080	0.0023	0.0034	0.0054	0.0076	0.0089	0.0105	0.0113	0.0120	0.0125	0.0131

Figure B.32. (a) Load and displacement histories and DIC contours; and (b) Load-displacement relationship for a specimen with L_d of 102 mm and d_b of 0.89 mm, repetition# 1

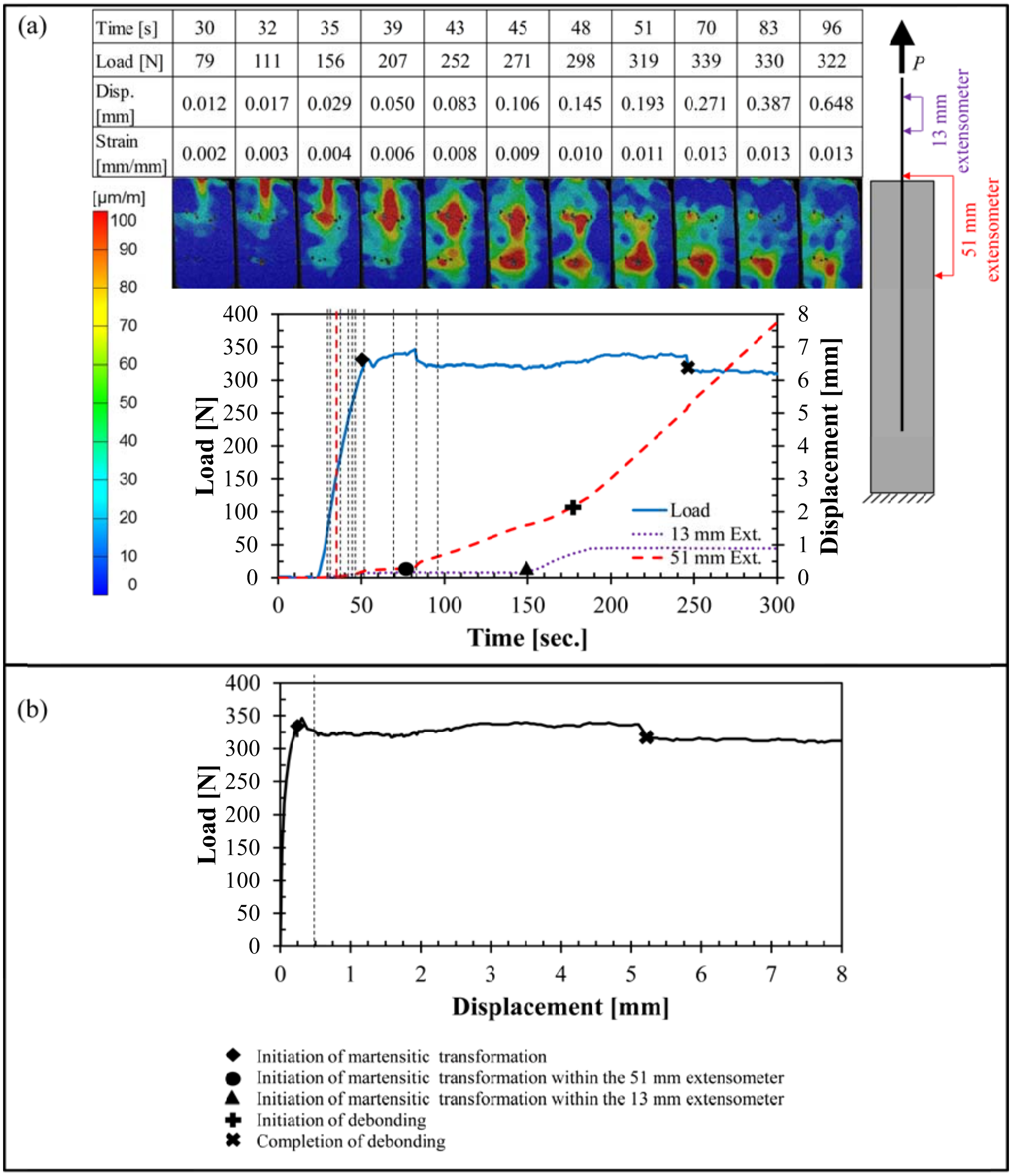

Figure B.33. (a) Load and displacement histories and DIC contours; and (b) Load-displacement relationship for a specimen with L_d of 102 mm and d_b of 0.89 mm, repetition# 2

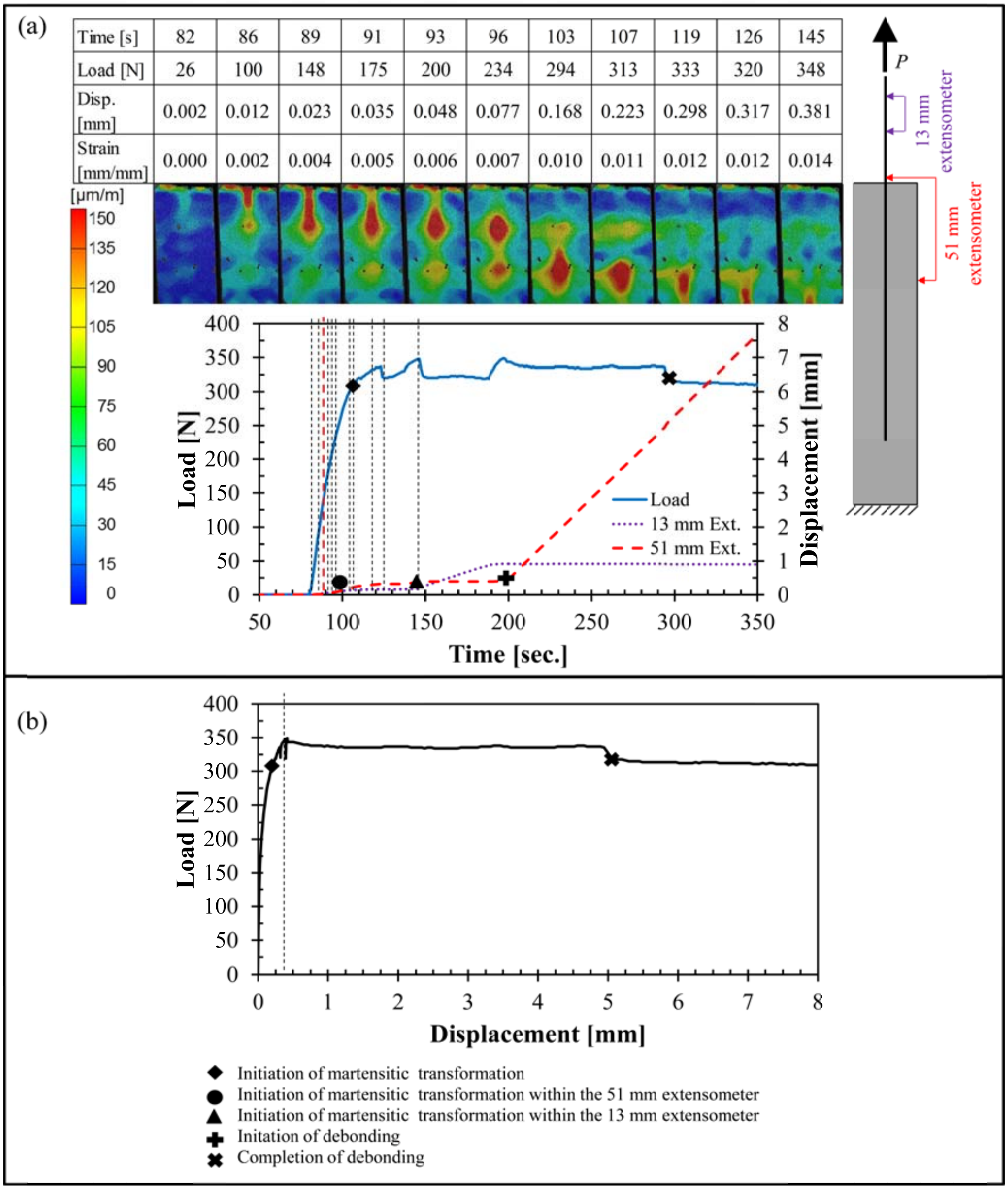

Time [s]	82	86	89	91	93	96	103	107	119	126	145
Load [N]	26	100	148	175	200	234	294	313	333	320	348
Disp. [mm]	0.002	0.012	0.023	0.035	0.048	0.077	0.168	0.223	0.298	0.317	0.381
Strain [mm/mm]	0.000	0.002	0.004	0.005	0.006	0.007	0.010	0.011	0.012	0.012	0.014

Figure B.34. (a) Load and displacement histories and DIC contours; and (b) Load-displacement relationship for a specimen with L_d of 102 mm and d_b of 0.89 mm, repetition# 3

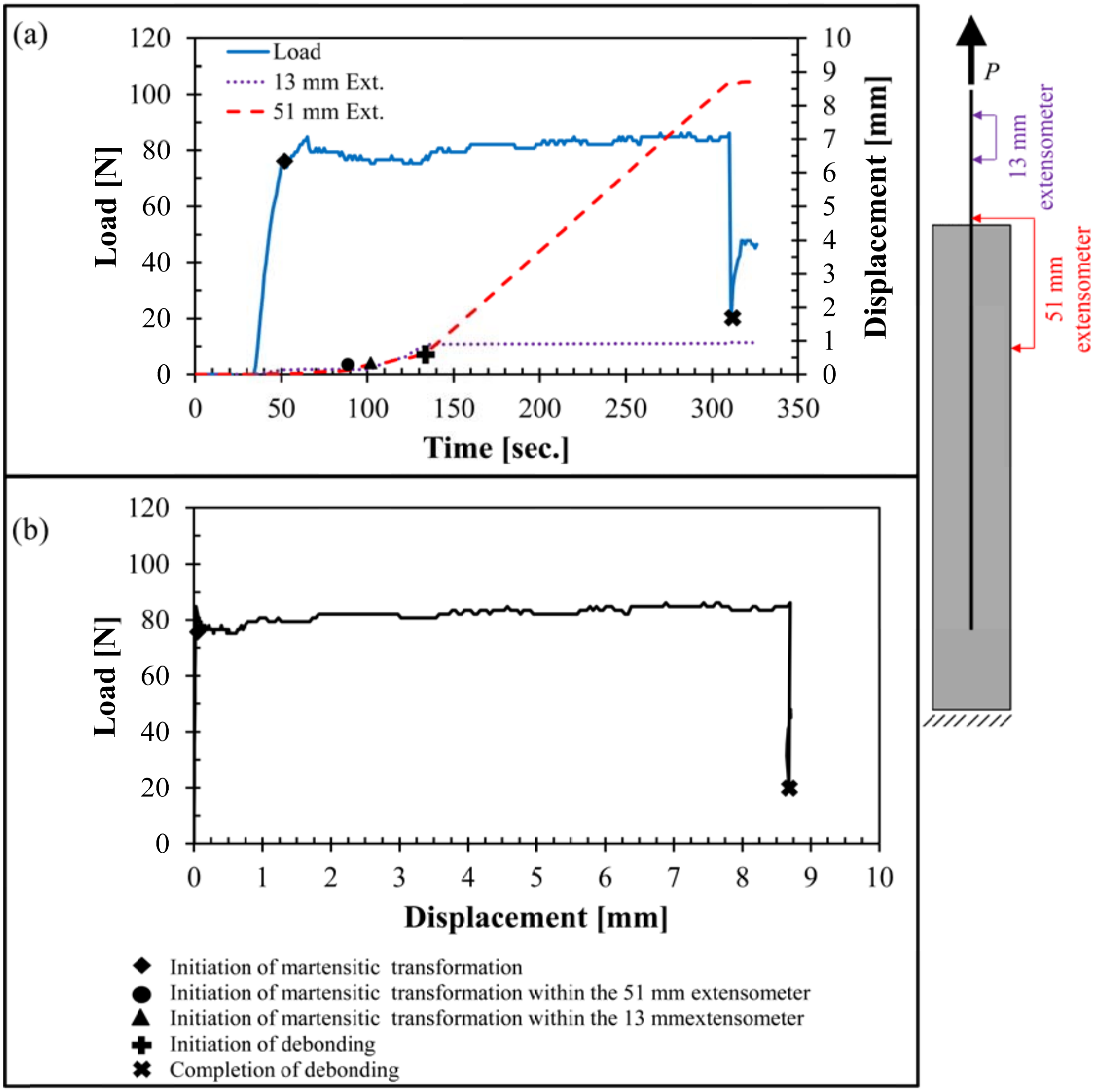

Figure B.35. (a) Load and displacement histories and (b) Load-displacement relationship for a specimen with L_d of 127 mm and d_b of 0.47 mm, repetition# 1

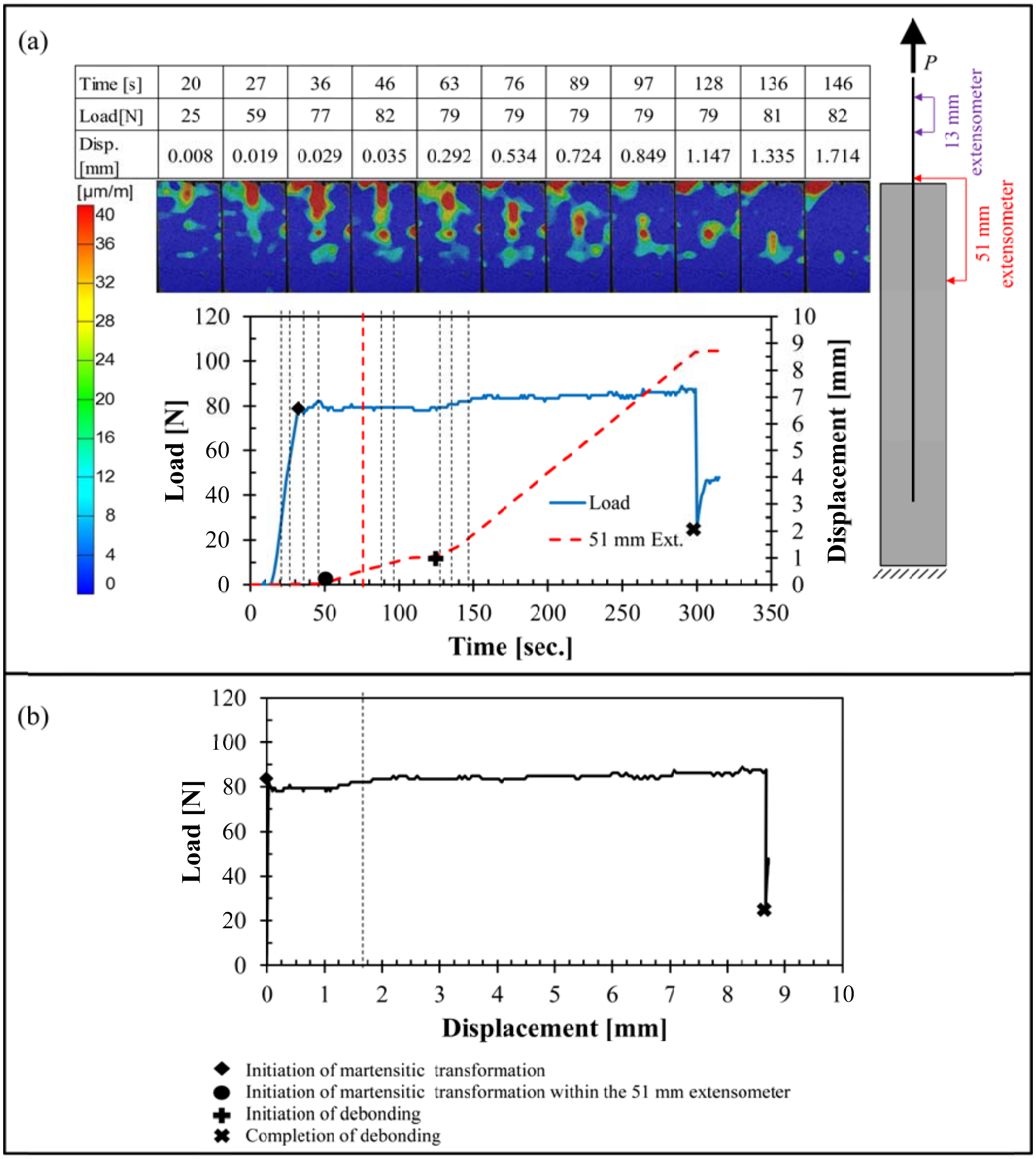

Figure B.36. (a) Load and displacement history and DIC contours; and (b) Load-displacement relationship for a specimen with L_d of 127 mm and d_b of 0.47 mm, repetition# 2

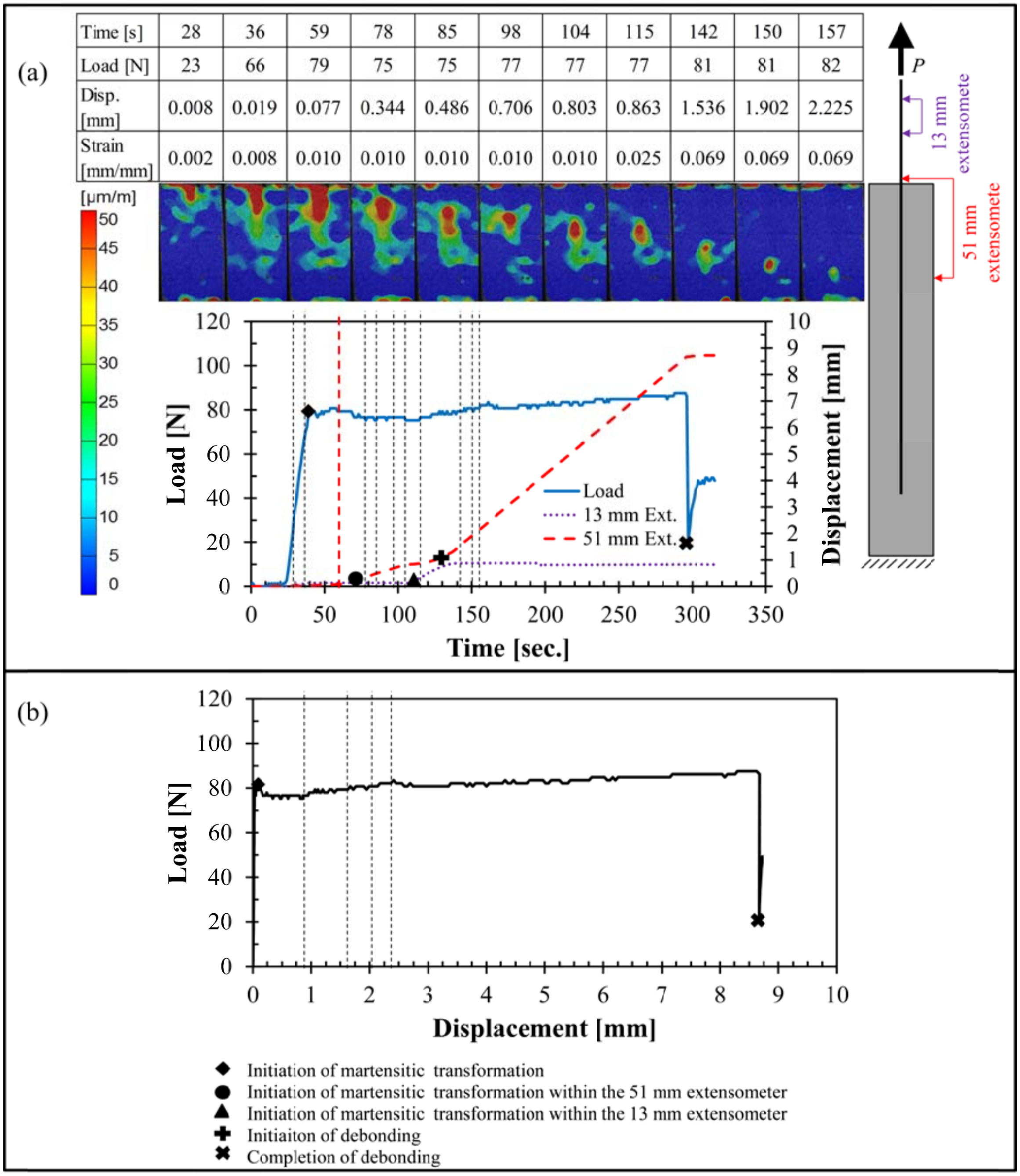

Figure B.37. (a) Load and displacement histories and DIC contours; and (b) Load-displacement relationship for a specimen with L_d of 127 mm and d_b of 0.47 mm, repetition# 3

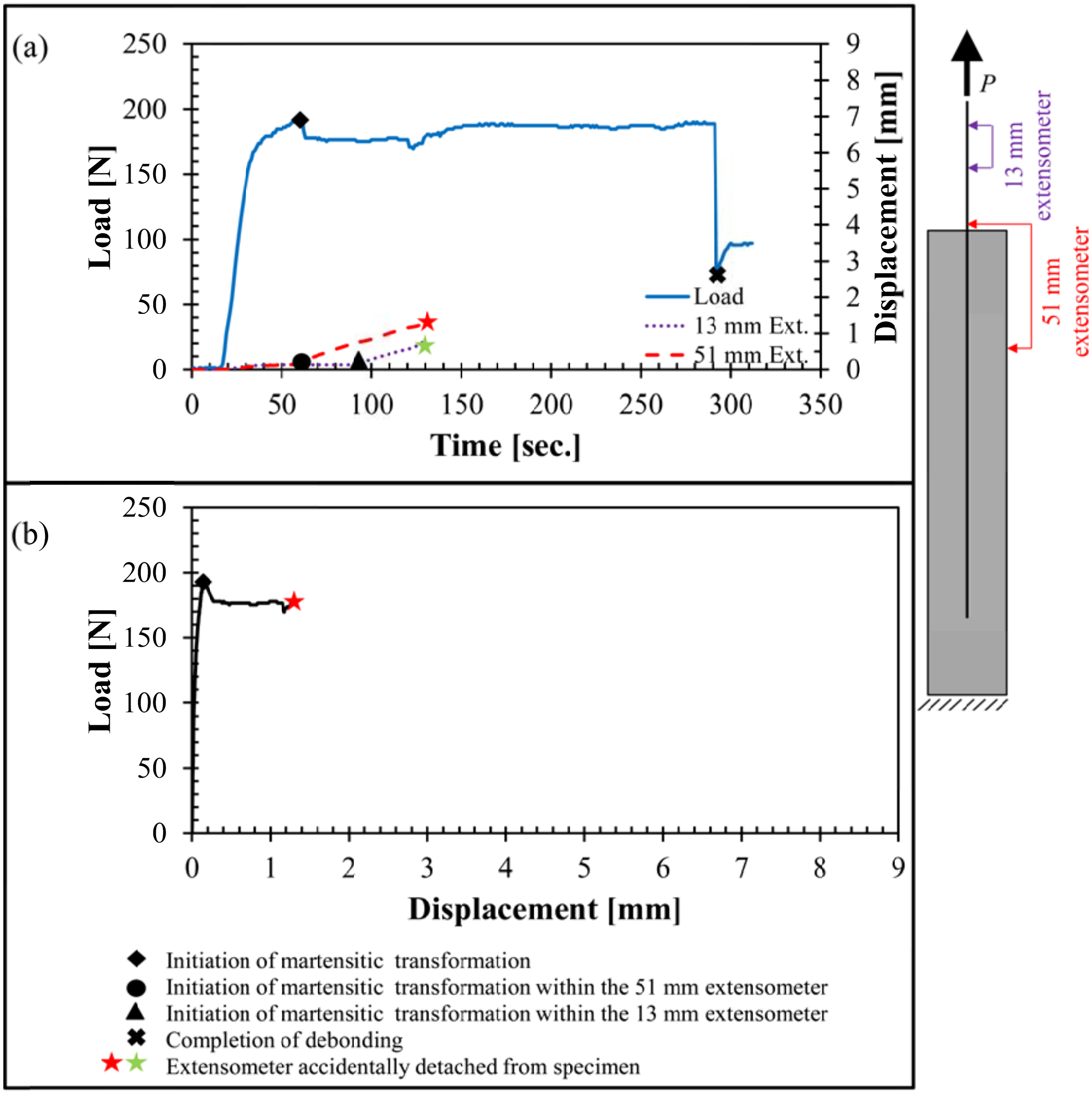

Figure B.38. (a) Load and displacement histories and (b) Load-displacement relationship for a specimen with L_d of 127 mm and d_b of 0.66 mm, repetition# 1

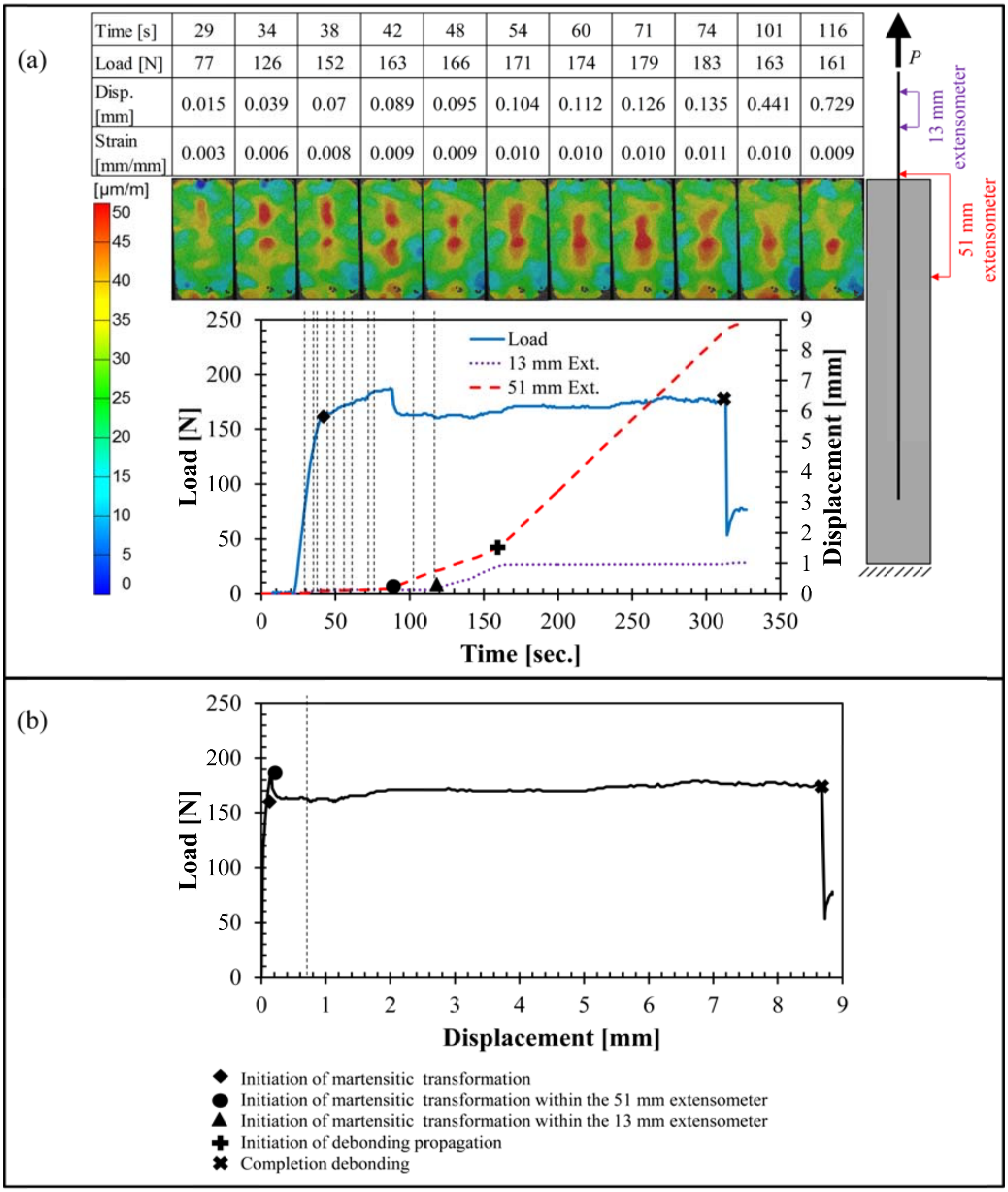

Figure B.39. (a) Load and displacement histories and DIC contours; and (b) Load-displacement relationship for a specimen with L_d of 127 mm and d_b of 0.66 mm, repetition# 2

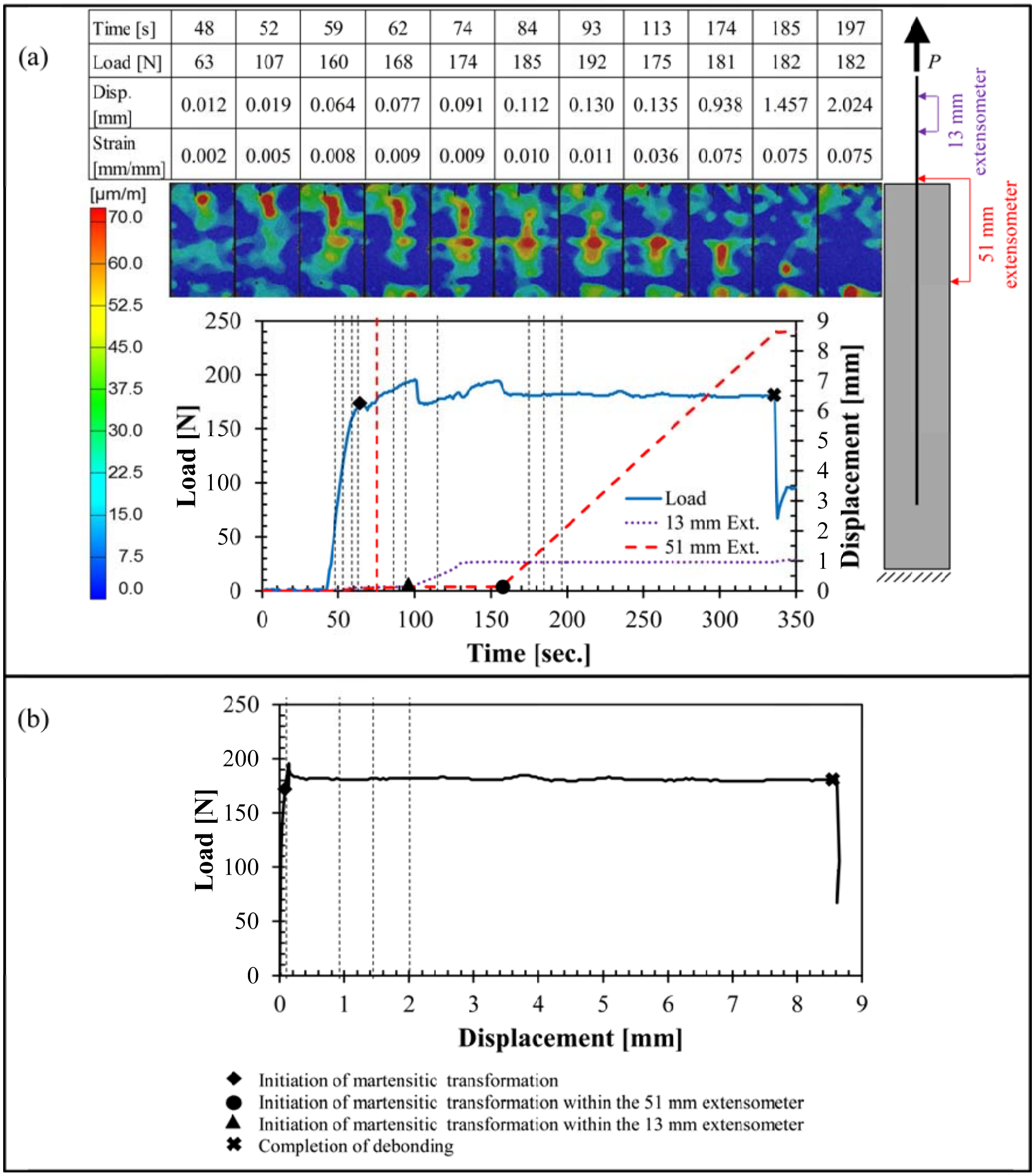

Time [s]	48	52	59	62	74	84	93	113	174	185	197
Load [N]	63	107	160	168	174	185	192	175	181	182	182
Disp. [mm]	0.012	0.019	0.064	0.077	0.091	0.112	0.130	0.135	0.938	1.457	2.024
Strain [mm/mm]	0.002	0.005	0.008	0.009	0.009	0.010	0.011	0.036	0.075	0.075	0.075

Figure B.40. (a) Load and displacement histories and DIC contours; and (b) Load-displacement relationship for a specimen with L_d of 127 mm and d_b of 0.66 mm, repetition# 3

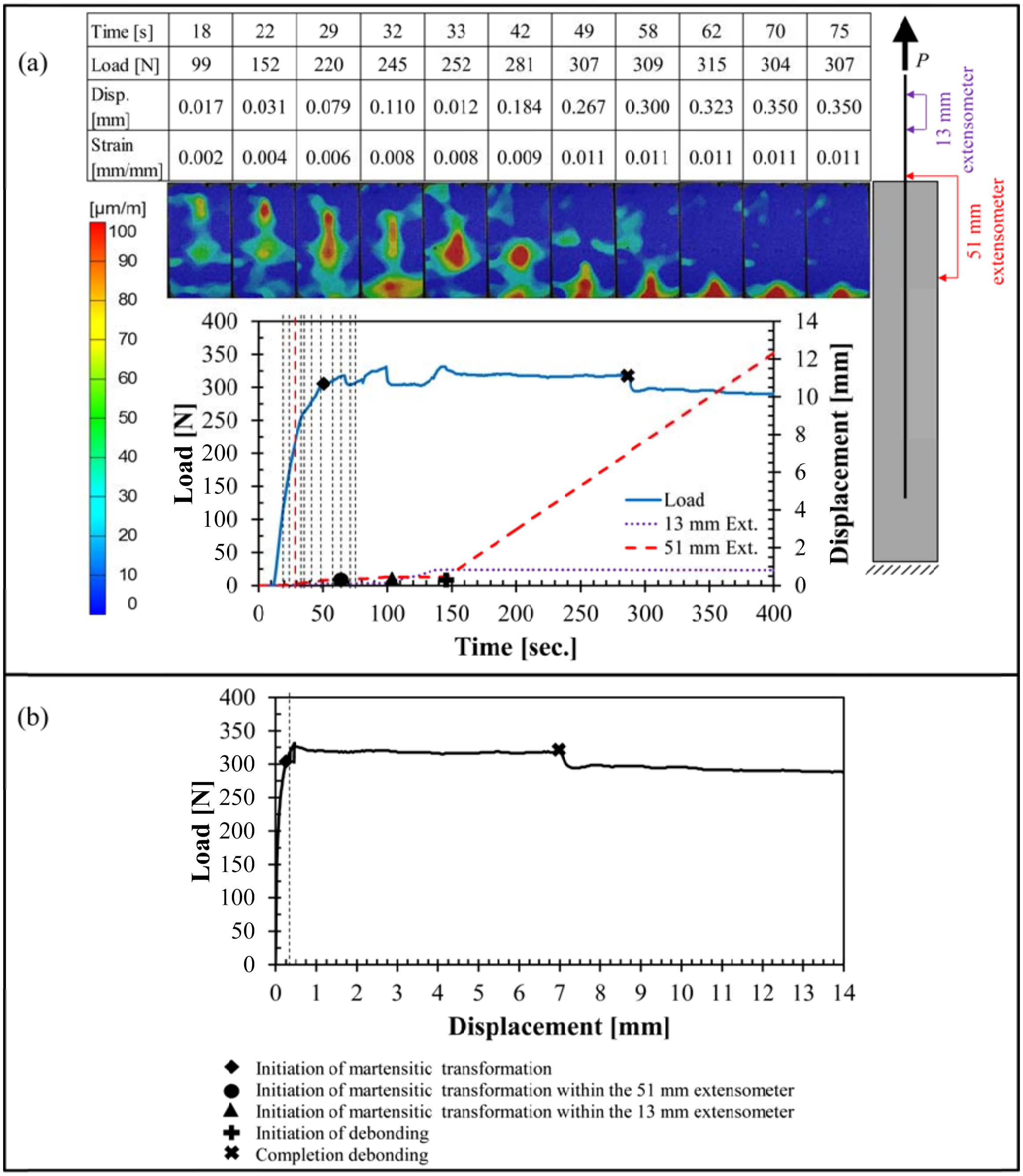

Figure B.41. (a) Load and displacement histories and DIC contours; and (b) Load-displacement relationship for a specimen with L_d of 127 mm and d_b of 0.89 mm, repetition# 1

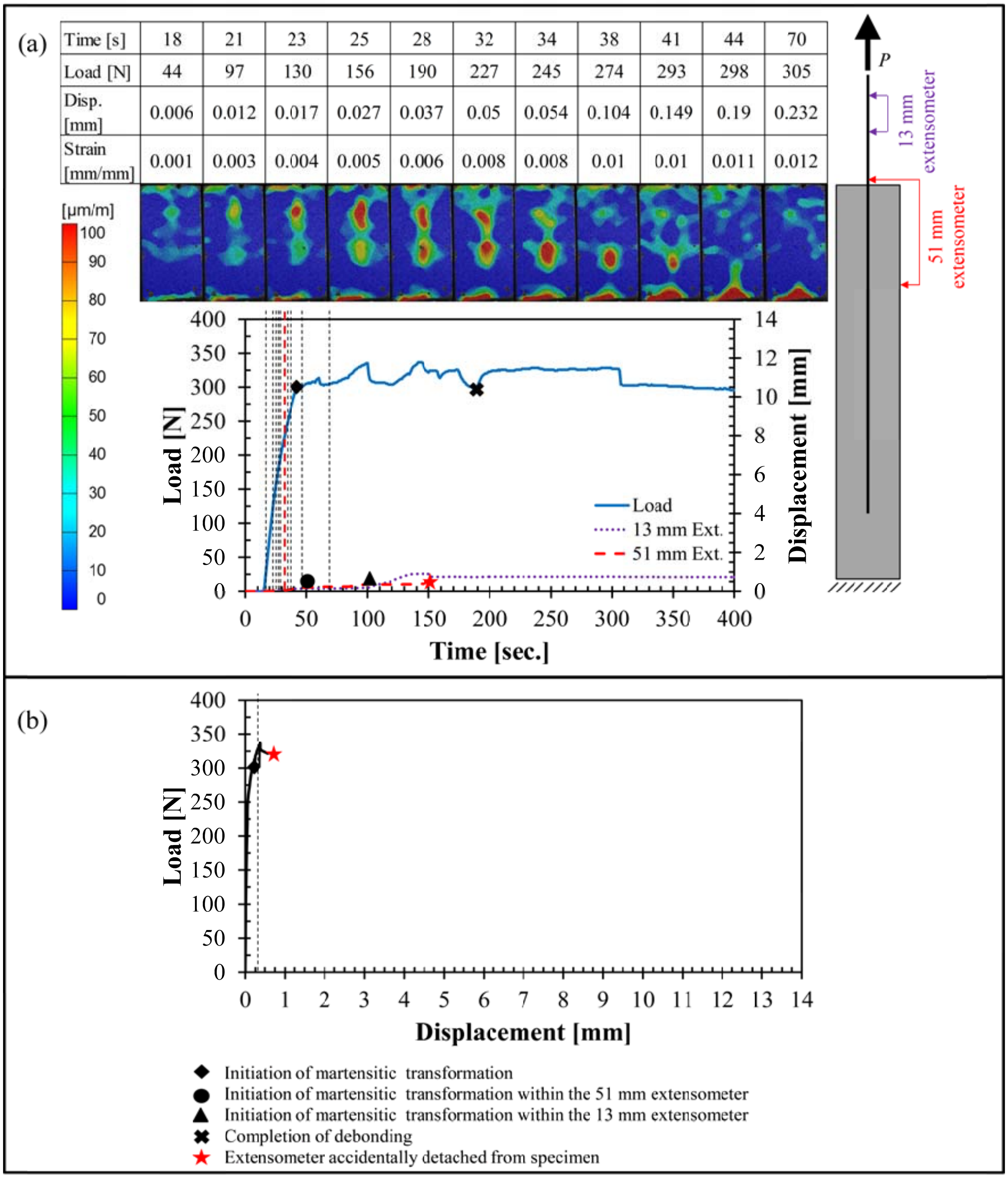

Time [s]	18	21	23	25	28	32	34	38	41	44	70
Load [N]	44	97	130	156	190	227	245	274	293	298	305
Disp. [mm]	0.006	0.012	0.017	0.027	0.037	0.05	0.054	0.104	0.149	0.19	0.232
Strain [mm/mm]	0.001	0.003	0.004	0.005	0.006	0.008	0.008	0.01	0.01	0.011	0.012

Figure B.42. (a) Load and displacement histories and DIC contours; and (b) Load-displacement relationship for a specimen with L_d of 127 mm and d_b of 0.89 mm, repetition# 2

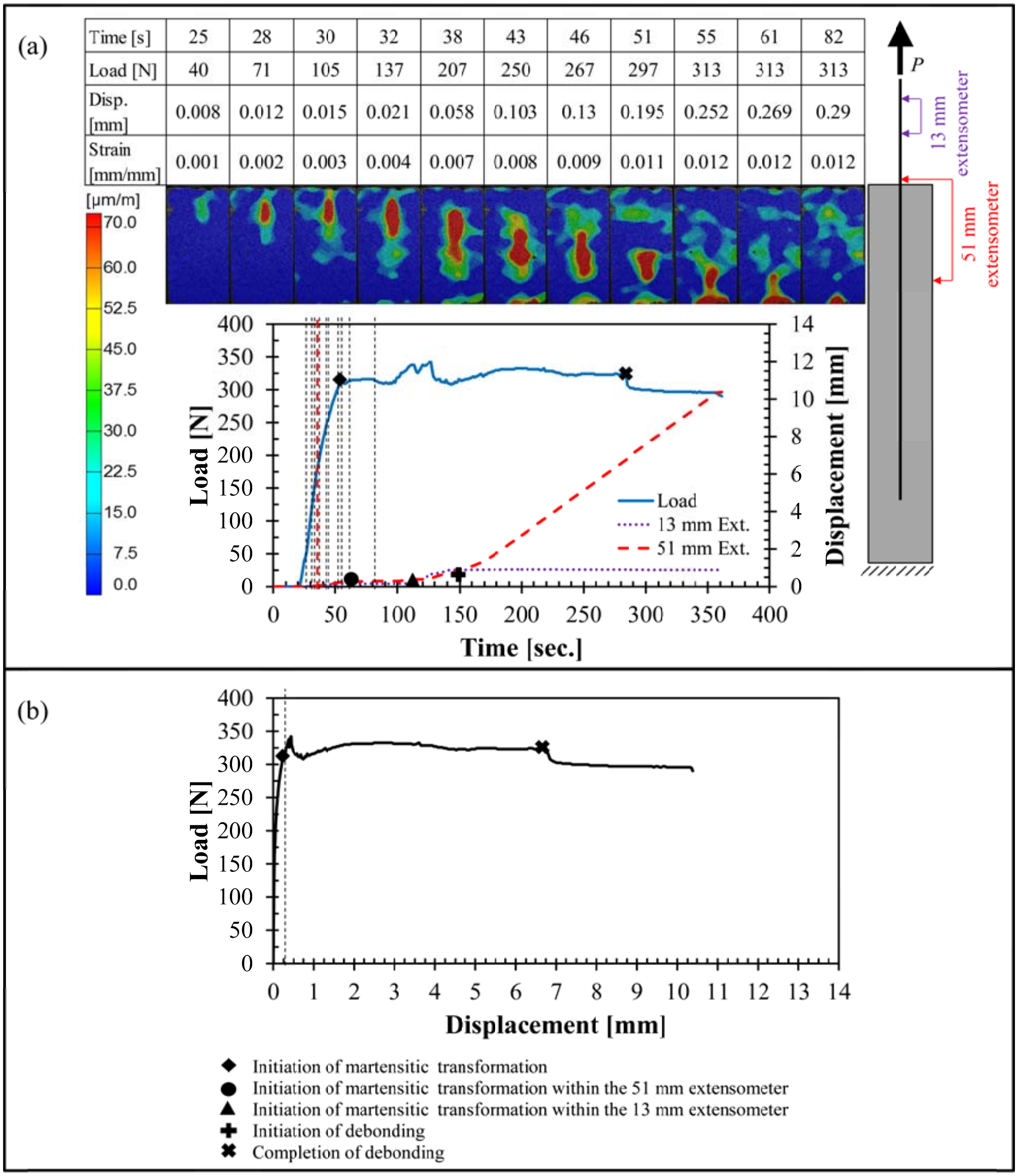

Time [s]	25	28	30	32	38	43	46	51	55	61	82
Load [N]	40	71	105	137	207	250	267	297	313	313	313
Disp. [mm]	0.008	0.012	0.015	0.021	0.058	0.103	0.13	0.195	0.252	0.269	0.29
Strain [mm/mm]	0.001	0.002	0.003	0.004	0.007	0.008	0.009	0.011	0.012	0.012	0.012

Figure B.43. (a) Load and displacement histories and DIC contours; and (b) Load-displacement relationship for a specimen with L_d of 127 mm and d_b of 0.89 mm, repetition# 3

Appendix C: Detailed Results of the Bond Behavior of the NiTiNb SMA Wires Embedded in FRP Composite

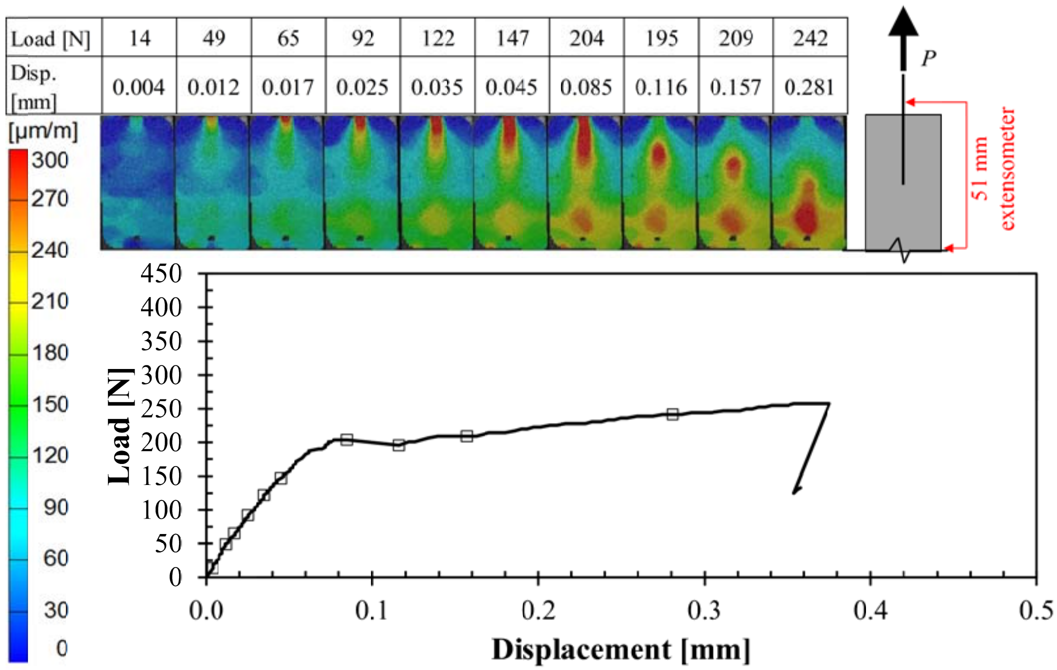

Figure C.1. Load versus relative displacement and DIC contours for pull-out specimen with 1 NiTiNb wire and embedment length of 25 mm embedded in CFRP patch, repetition #1

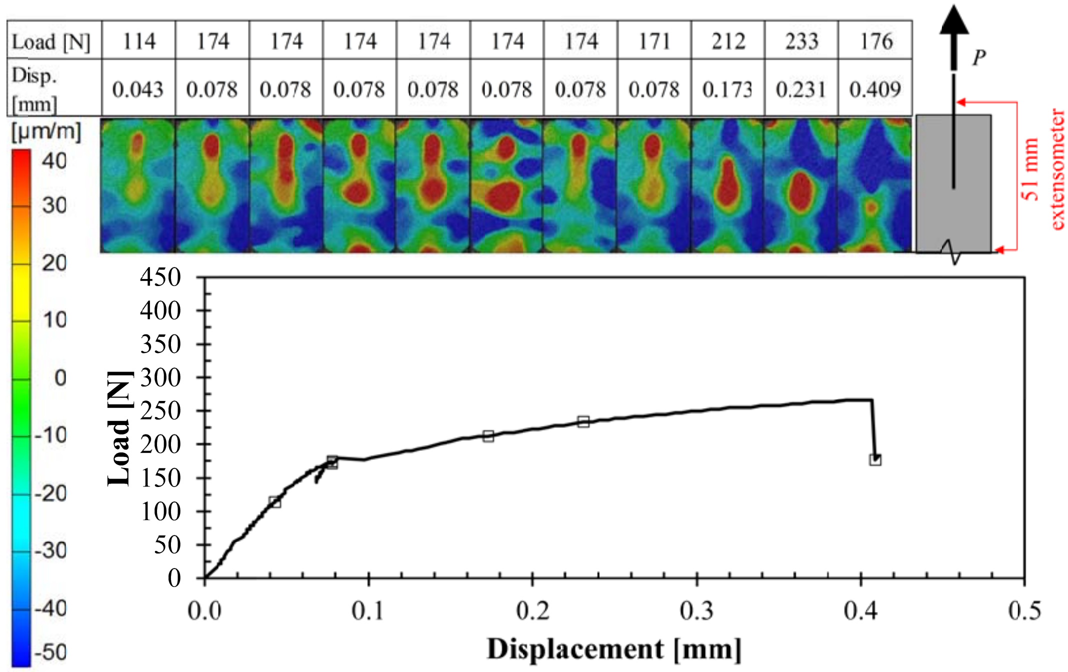

Figure C.2. Load versus relative displacement and DIC contours for pull-out specimen with 1 NiTiNb wire and embedment length of 25 mm embedded in CFRP patch, repetition #2

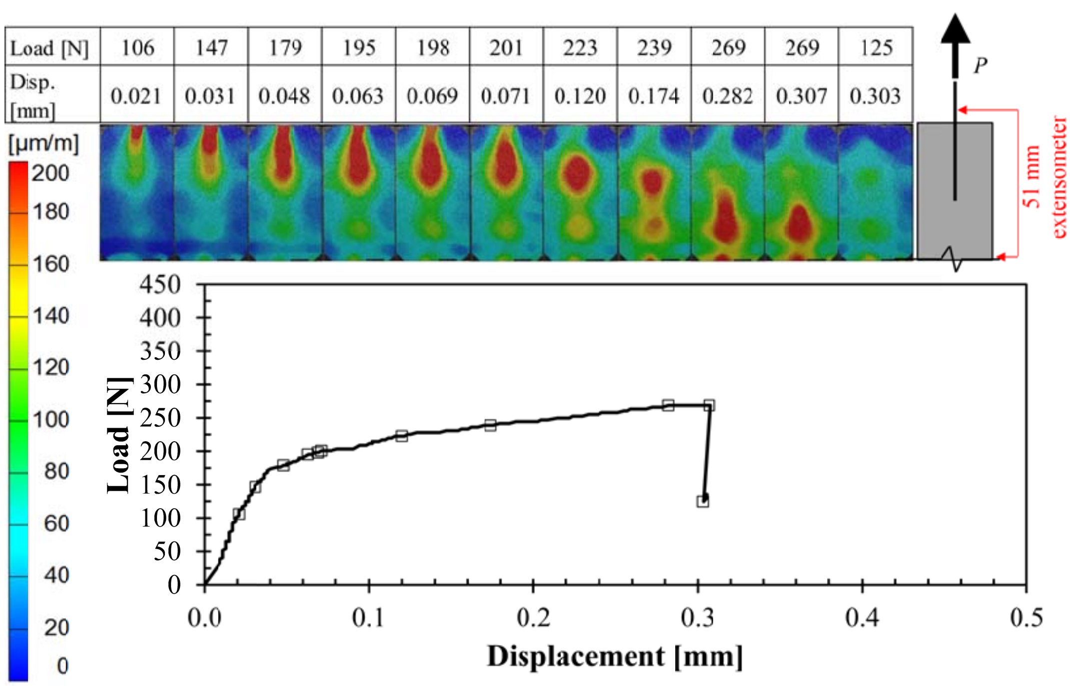

Figure C.3. Load versus relative displacement and DIC contours for pull-out specimen with 1 NiTiNb wire and embedment length of 25 mm embedded in CFRP patch, repetition #3

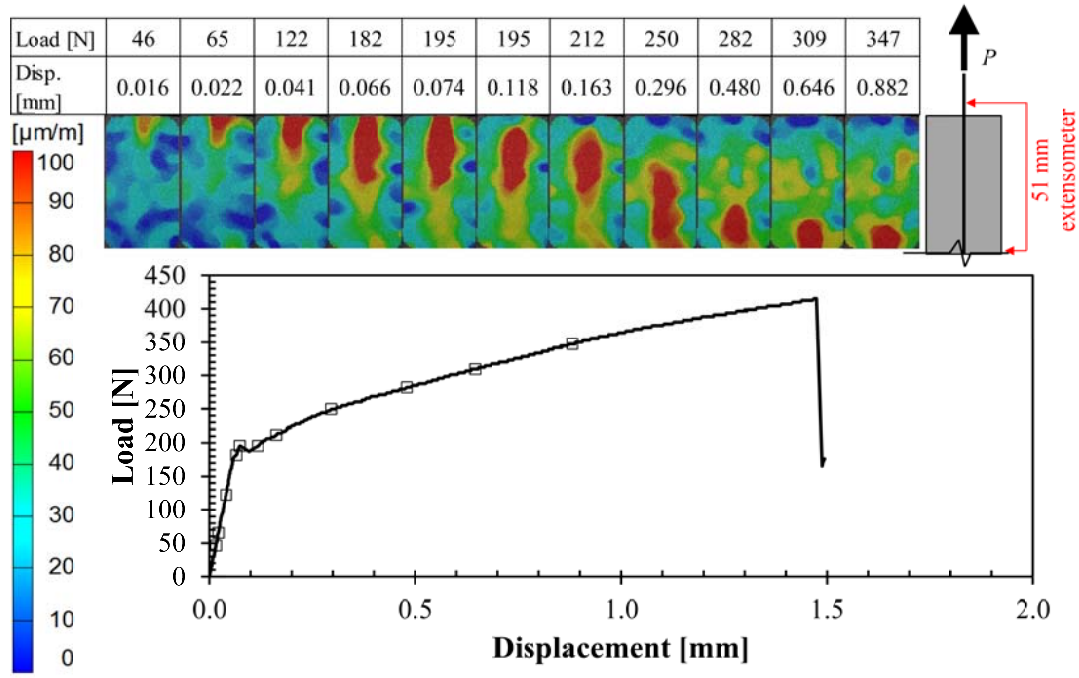

Figure C.4. Load versus relative displacement and DIC contours for pull-out specimen with 1 NiTiNb wire and embedment length of 51 mm embedded in CFRP patch, repetition #1

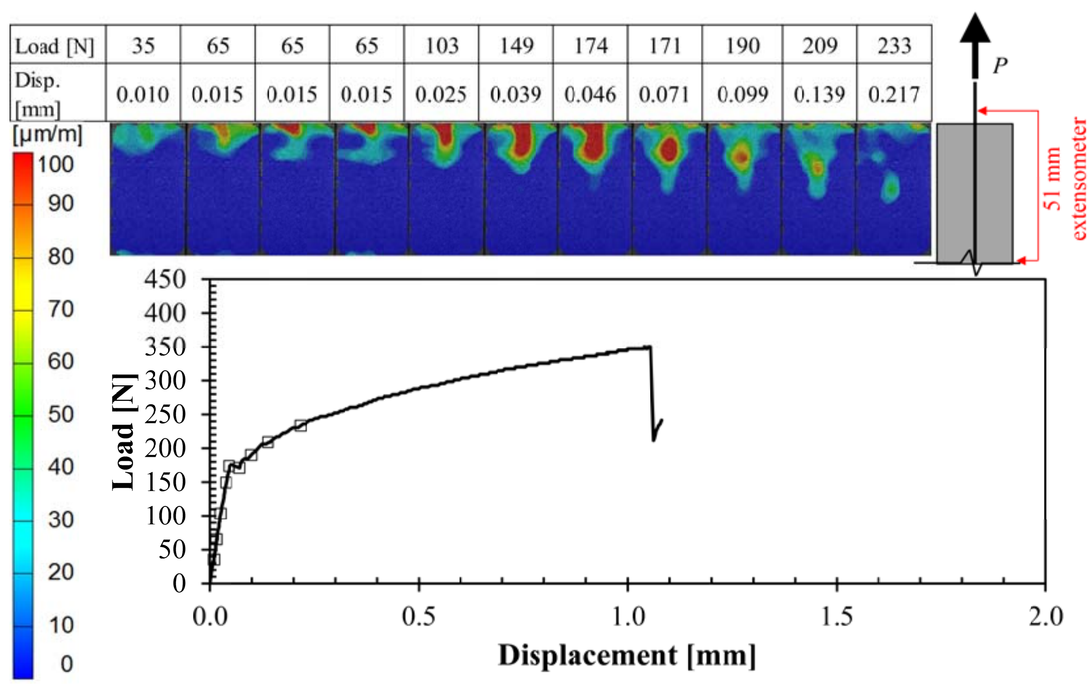

Figure C.5. Load versus relative displacement and DIC contours for pull-out specimen with 1 NiTiNb wire and embedment length of 51 mm embedded in CFRP patch, repetition #2

Load [N]	46	65	100	136	141	174	187	193	209	233	247
Disp. [mm]	0.018	0.023	0.037	0.050	0.052	0.070	0.112	0.126	0.172	0.246	0.312

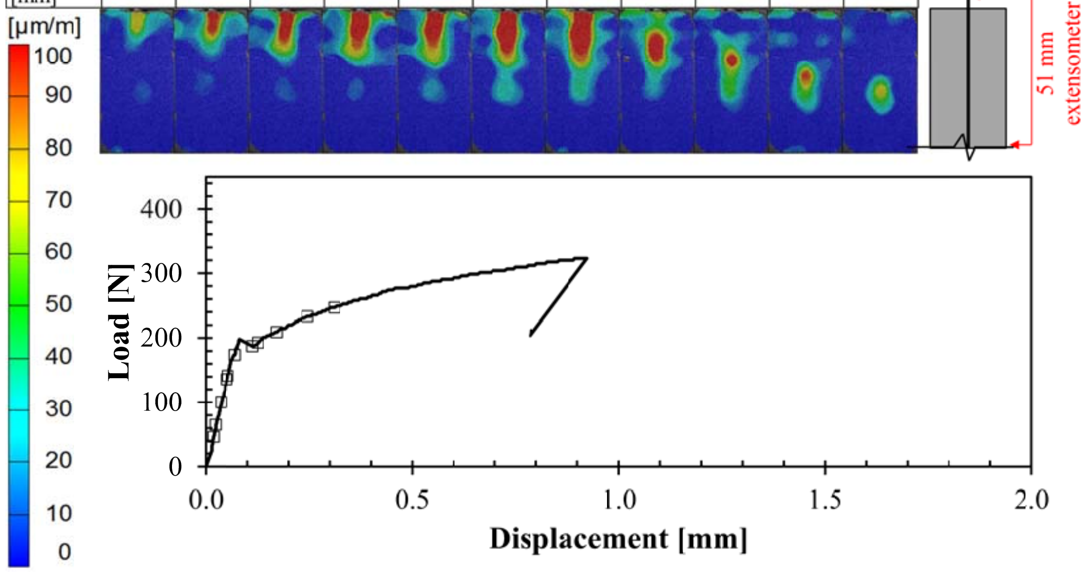

Figure C.6. Load versus relative displacement and DIC contours for pull-out specimen with 1 NiTiNb wire and embedment length of 51 mm embedded in CFRP patch, repetition #3

Load [N]	24	46	79	133	147	157	163	168	171	206	217
Disp. [mm]	0.010	0.017	0.029	0.046	0.052	0.058	0.060	0.062	0.068	0.168	0.201

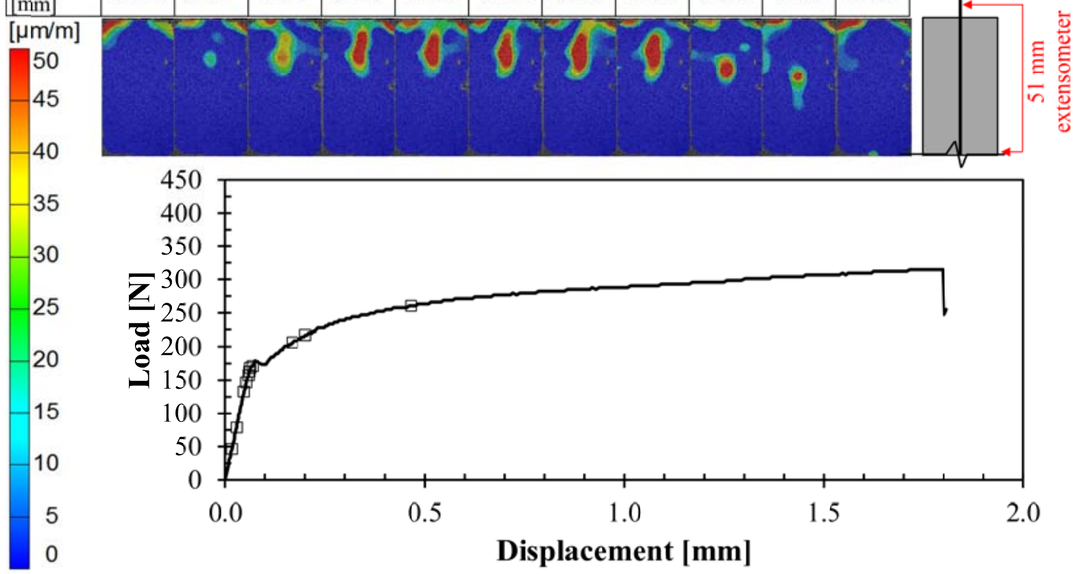

Figure C.7. Load versus relative displacement and DIC contours for pull-out specimen with 1 NiTiNb wire and embedment length of 102 mm embedded in CFRP patch, repetition #1

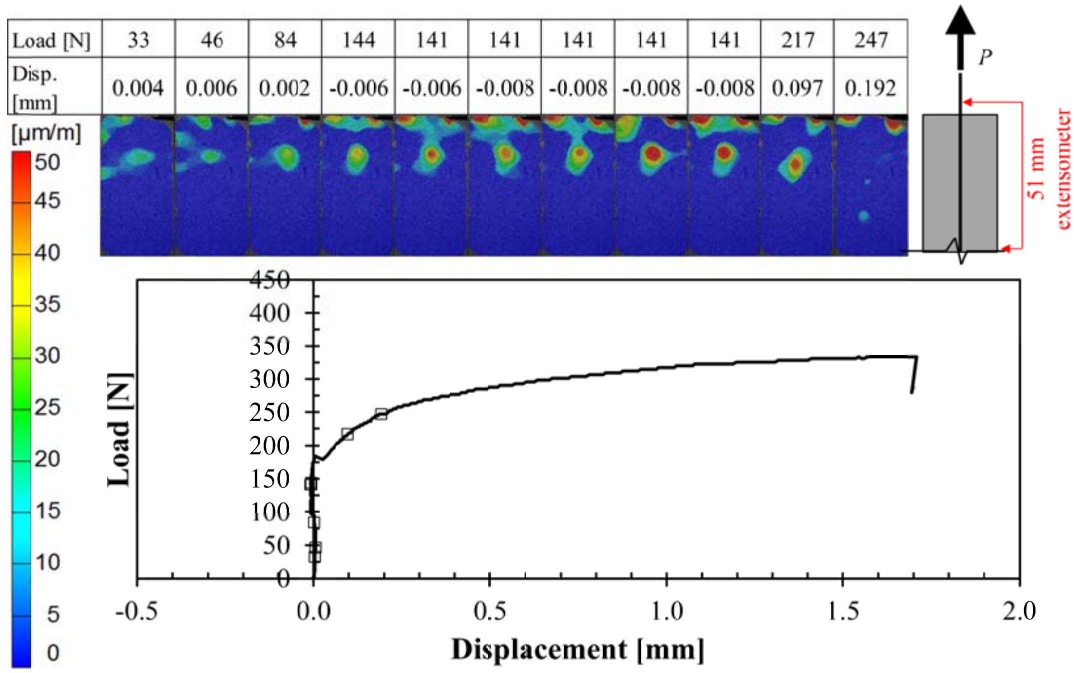

Figure C.8. Load versus relative displacement and DIC contours for pull-out specimen with 1 NiTiNb wire and embedment length of 102 mm embedded in CFRP patch, repetition #2

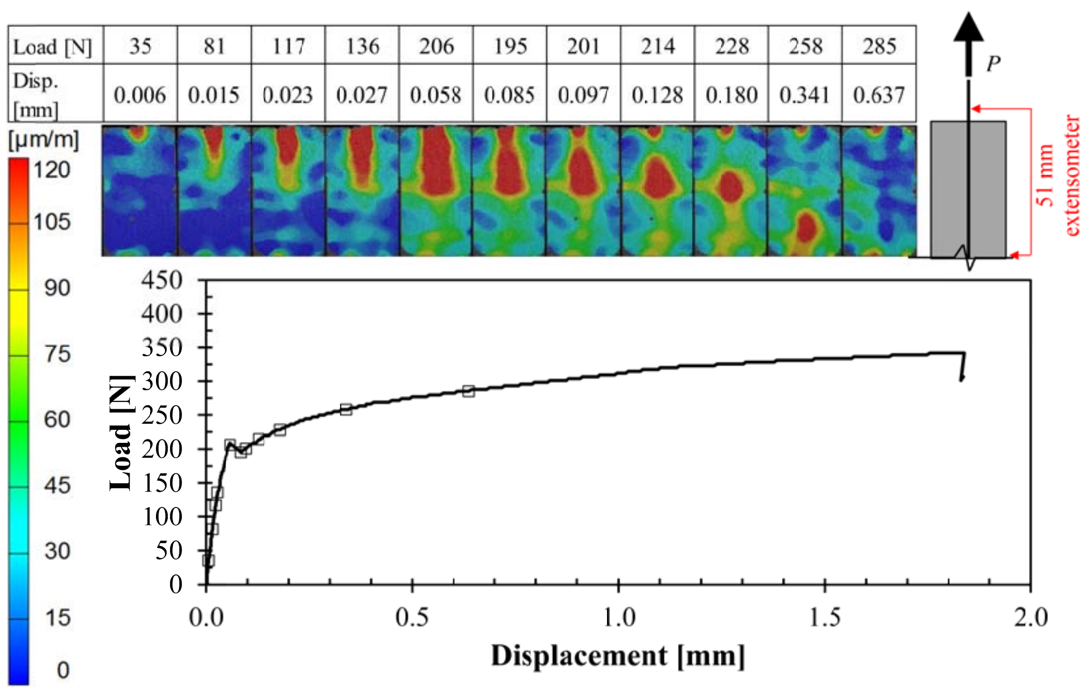

Figure C.9. Load versus relative displacement and DIC contours for pull-out specimen with 1 NiTiNb wire and embedment length of 102 mm embedded in CFRP patch, repetition #3

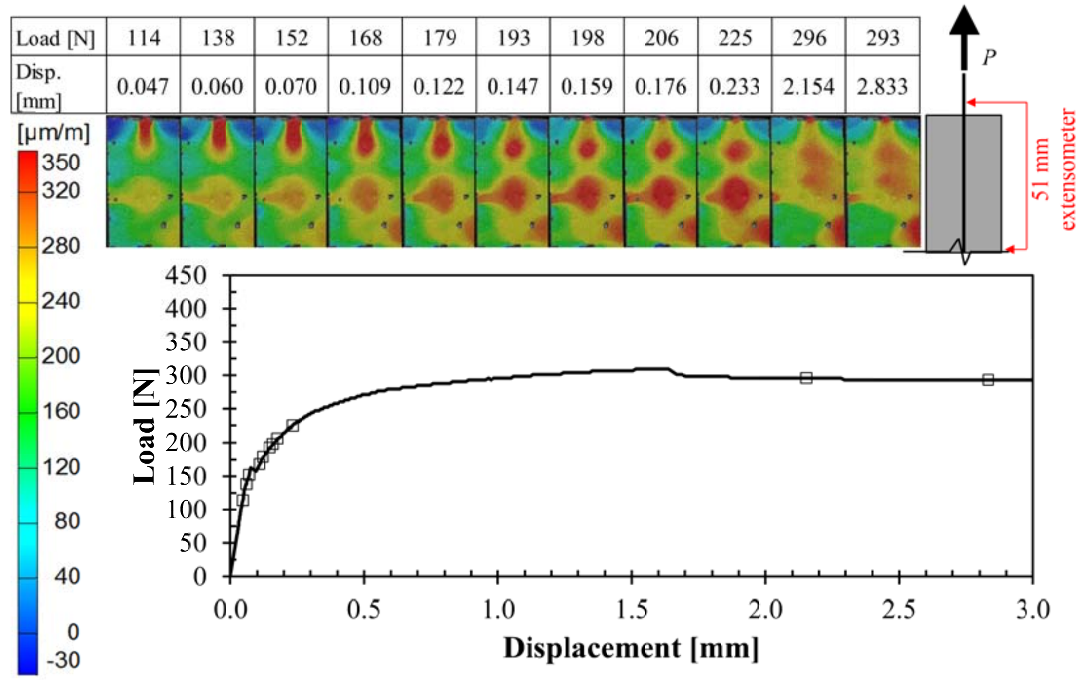

Figure C.10. Load versus relative displacement and DIC contours for pull-out specimen with 1 NiTiNb wire and embedment length of 102 mm embedded in GFRP patch, repetition #1

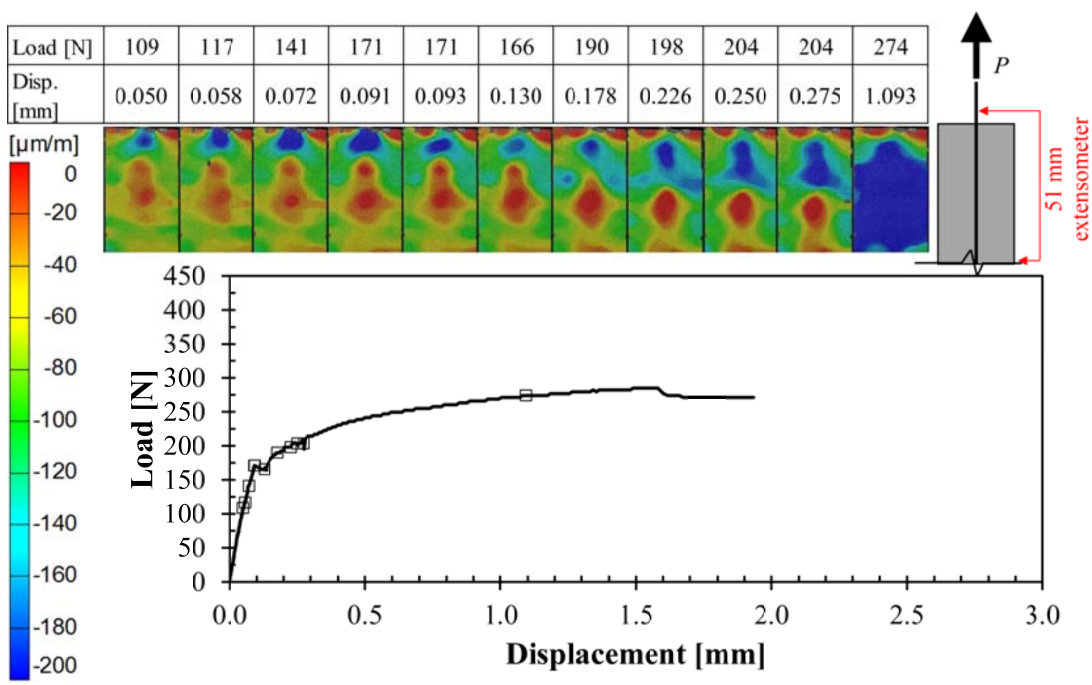

Figure C.11. Load versus relative displacement and DIC contours for pull-out specimen with 1 NiTiNb wire and embedment length of 102 mm embedded in GFRP patch, repetition #2

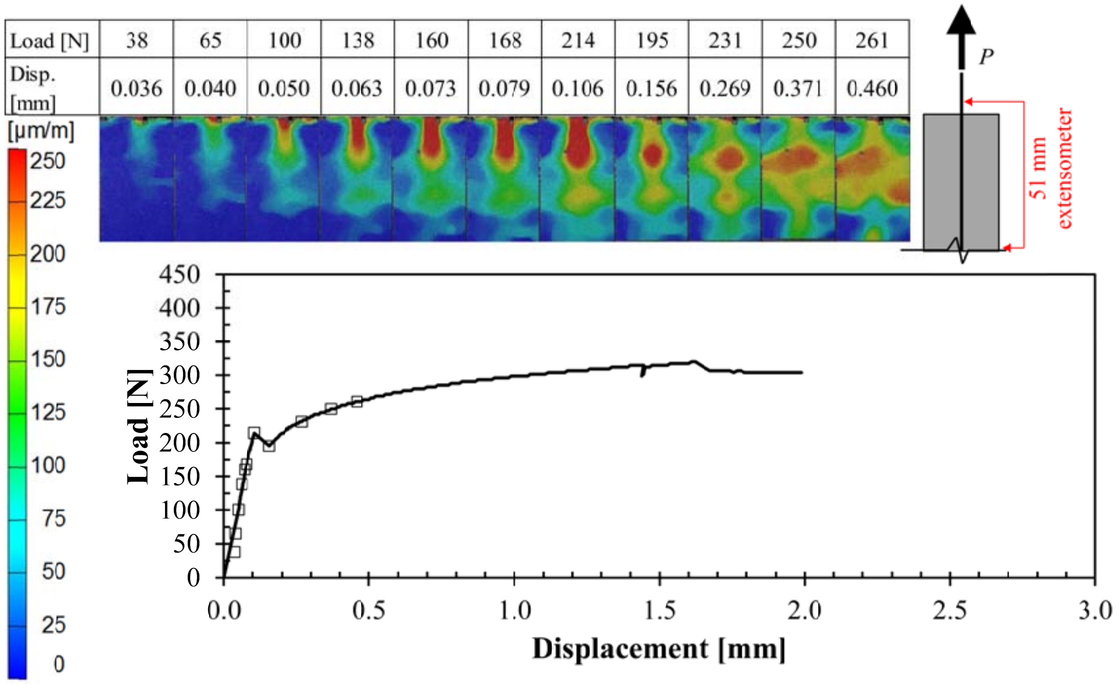

Figure C.12. Load versus relative displacement and DIC contours for pull-out specimen with 1 NiTiNb wire and embedment length of 102 mm embedded in GFRP patch, repetition #3

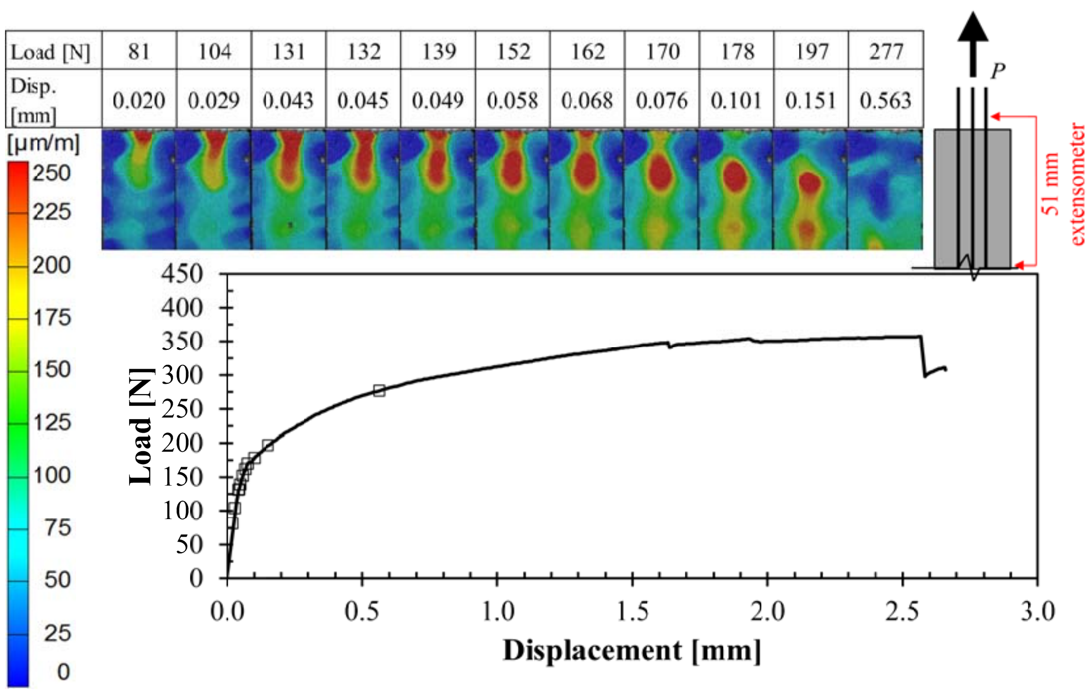

Figure C.13. Load versus relative displacement and DIC contours for pull-out specimen with 3 NiTiNb wires and embedment length of 102 mm embedded in CFRP patch, repetition #1

Load [N]	115	139	158	181	189	205	237	261	272	287	311
Disp. [mm]	0.063	0.094	0.114	0.151	0.170	0.211	0.352	0.528	0.625	0.746	1.023

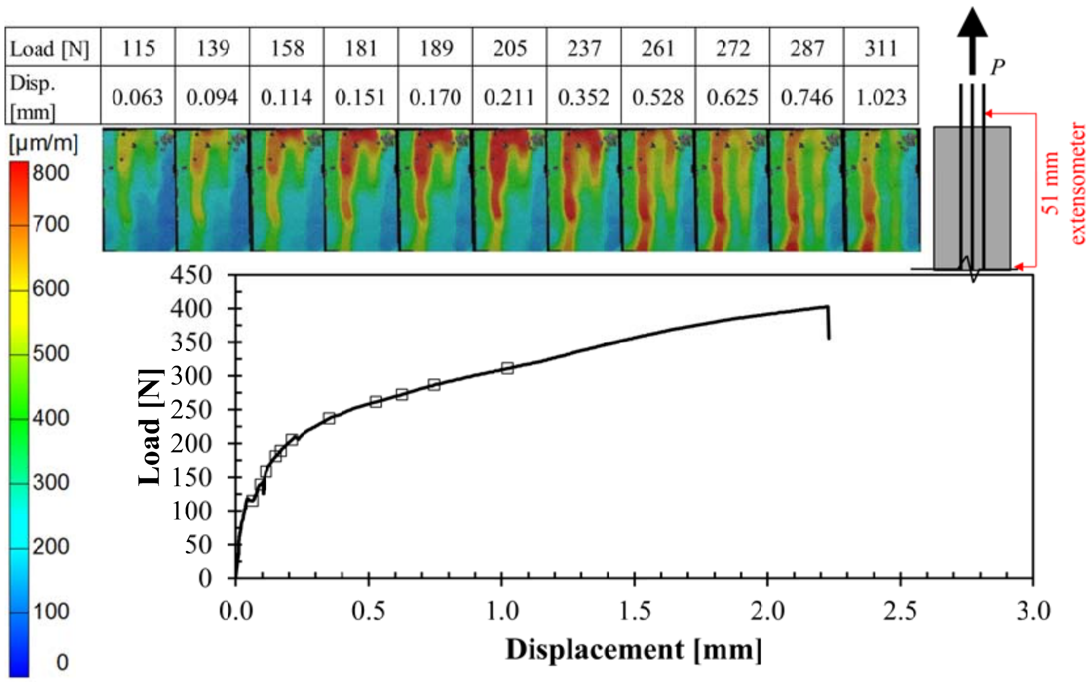

Figure C.14. Load versus relative displacement and DIC contours for pull-out specimen with 3 NiTiNb wires and embedment length of 102 mm embedded in CFRP patch, repetition #2

Load [N]	92	128	171	199	214	235	245	262	275	295	310
Disp. [mm]	0.032	0.044	0.061	0.141	0.205	0.276	0.325	0.435	0.539	0.739	0.932

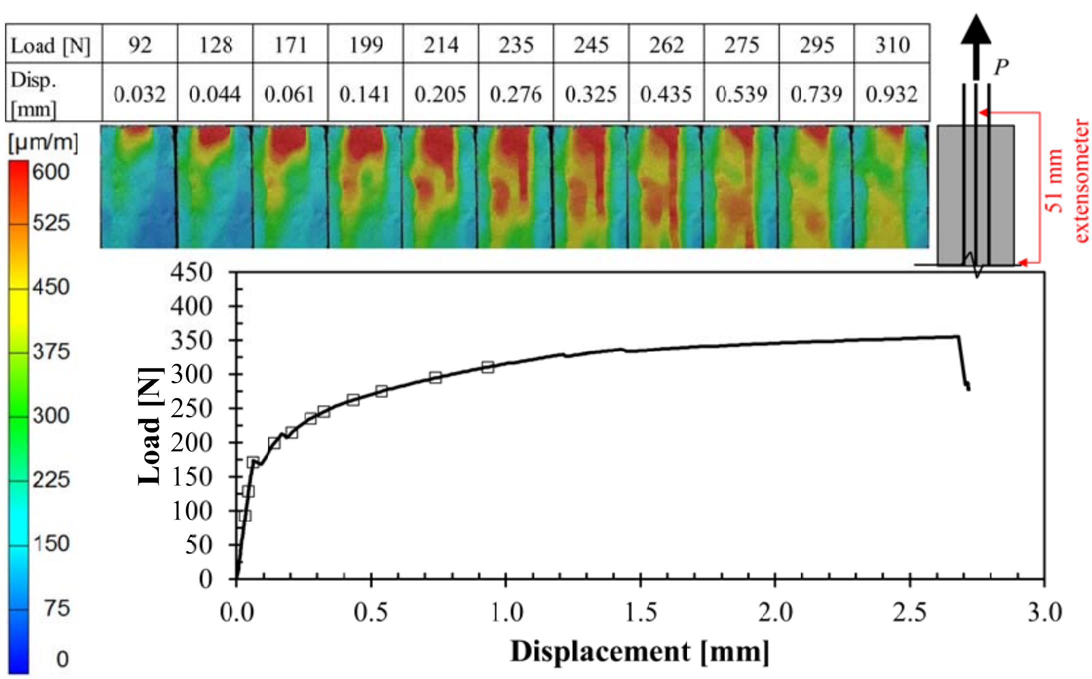

Figure C.15. Load versus relative displacement and DIC contours for pull-out specimen with 3 NiTiNb wires and embedment length of 102 mm embedded in CFRP patch, repetition #3